Combining CryoSat-2 Data with Ocean-Sea-Ice Models to Improve the Understanding of Arctic Sea Ice Thickness

Sievers, Imke

DOI (link to publication from Publisher):
10.54337/aau745674256

Publication date:
2024

Document Version
Publisher's PDF, also known as Version of record

COMBINING CRYOSAT-2 DATA WITH OCEAN-SEA-ICE MODELS TO IMPROVE THE UNDERSTANDING OF ARCTIC SEA ICE THICKNESS

BY
IMKE SIEVERS

PhD Thesis 2024

AALBORG UNIVERSITY
DENMARK

Combining CryoSat-2 Data with Ocean-Sea-Ice Models to Improve the Understanding of Arctic Sea Ice Thickness

Ph.D. Dissertation

Imke Sievers

PhD Thesis 2024

Aalborg University
Department of Electronic Systems
Fredrik Bajers Vej 7B
DK-9220 Aalborg

Submitted: May 2024

Main Supervisor: Associate Professor Ming Shen
Aalborg University

Assessment: Professor Ehsan Forootan (chairman)
Aalborg University, Denmark

Senior Researcher Francois Counillon
Nansen Environmental and Remote Sensing Centre (NERSC), Norway

Associate Professor Jack Christopher Landy
UiT The Arctic University of Norway, Norway

PhD Series: Technical Faculty of IT and Design, Aalborg University

Department: Department of Electronic Systems

ISSN: 2446-1628
ISBN: 978-87-94563-49-9

Published by:
Aalborg University Open Publishing
Kroghstræde 1-3
DK – 9220 Aalborg Øst
aauopen@aau.dk

Abstract

Sea ice plays a major role in the global climate system. Its presence governs the radiation budget and determines how much heat and momentum can be transferred between ocean and atmosphere. In order to monitor sea ice and analyse how it has changed over the recent past, different satellite observations are used. Sea ice area is monitored by passive microwave and optical sensors. To make accurate estimates of the sea ice volume, sea ice thickness (SIT) estimates are also needed. The monitoring and estimation of SIT from satellite observations is an active area of research. This thesis contributes to this research by developing sea ice model-based parameterizations for satellite radar observations and an assimilation framework for these observations, with the aim of improving our understanding of Arctic SIT. The work presented here concentrates on CryoSat-2 freeboard observations.

When estimating SIT from space, only the part above the sea surface, called freeboard (FB), can be observed. To convert FB to SIT, assumptions about sea ice density, snow thickness, snow density and water density are made. These assumptions are known to introduce errors, and the work presented here introduces a model-based approach to estimating them. The main novelty is the derivation of a sea ice density and the use of ocean model water density.

Further, this thesis introduces a Kalman Filter-based approach to assimilate FB to improve SIT. One challenge in retrieving CryoSat-2 FB is to know where the radar signal is reflected. CryoSat-2 carries a Ku-band radar, which prior to launch was assumed to penetrate the snow and to be reflected at the ice snow interface. Later studies found that this is not the case and that the scattering horizon varies depending on the region and season. Comparing the SIT from a classically-derived SIT product to the SIT-derived from the FB assimilation framework, presented here, shows that the assimilation gives better results in two regions where independent SIT observations were available.

Finally, this thesis analyses the sea ice model used to derive the FB and the influence different model parameterizations have on the SIT, sea ice concentration and snow thickness. The form drag parameterisation is found to have the largest influence on the sea ice volume and snow thickness. More work is needed to determine which form drag parameterisation is best suited for the model FB parametrisation.

Resumé

Havis spiller en stor rolle i det globale klimasystem. Dens tilstedeværelse styrer hvor meget varme og momentum der kan overføres mellem havet og atmosfæren inklusiv strålingsbudgettet. For at overvåge og analysere ændringer i havisen siden 1970'erne anvendes forskellige satellitobservationer. Havisens udbredelse bestemmes med passive mikrobølger og optiske sensorer. For at få den fulde beskrivelse af havis er det også nødvendigt at lave præcise skøn over havisens tykkelse og volumen, hviket eksempelvis gøres ved brug af altimeter målinger.

Overvågning og estimater af havistykkelsen baseret på satellitobservationer er et aktivt forskningsområde. Denne afhandling bidrager ved at integrere fribords observationer i en fysisk havis model baseret på assimilering af fribord. Samtidig er der udviklet parameteriseringer til at bestemme de variable der bliver anvendt til at konverterer fribord til havistykkelse og omvendt. Formålet er at forbedre vores forståelse af havistykkelsen i Arktis. Hovedfokus er på CryoSat-2 altimeter observationer og det deraf afledte fribord. Det er kun den del af fribordet der er over havniveau der bliver observeret. For at konvertere fribord til havis laver man nogle antagelser om massefylden af havis, sne og havvand. Derudover laver man et estimat af sneens tykkelse. Det er velkendt at disse antagelser introducerer usikkerheder og fejl. Denne afhandling introducerer en fysisk modelbaseret tilgang til at estimere disse variable i stedet for den klassiske konstante/klimatologiske tilgang. Dette studie har introduceret en ny formulering for havisens massefylde og brug af havmodellens massefylde for vand til udledning af havistykkelsen.

Yderligere introducerer denne afhandling en Kalman Filter-baseret tilgang til at assimilere fribord med henblik på at forbedre havistykkelsen. En udfordring ved at anvende CryoSat-2 fribord er at vide hvor radar signalet afspejles. CryoSat-2 bruger en Ku-band radar. Før opsendelsen var antagelsen at signalet trænger igennem sneen og bliver reflekteret ved is/sne grænsefladen. Efterfølgende undersøgelser fandt at dette ikke er tilfældet og at spredningshorisonten varierer afhængigt af region og sæson. Sammenligning af havistykkelsen fra et klassisk afledt havistykkelses produkt og det der er udviklet her baseret på assimilering af fribord i en "state of the art" ismodel viser, at assimileringen giver bedre resultater i to regioner. Sammenligningen er baseret på

tilgængelige uafhængige havistykkelses observationer. Til sidst analyserer afhandlingen den havis model, der er anvendt til at udlede fribord og indflydelsen af forskellige model parameteriseringer på den modellerede havis og sne. Den såkaldte "form drag" parameterisering har vist sig at have den største indflydelse på havis volumen og snetykkelse. Det kræver stadig mere arbejde at bestemme, hvilken parameterisering der bedst egnet til at parameterisere modelleret fribord.

Contents

Thesis Details

Thesis Title:	Combining CryoSat-2 Data with Ocean-Sea-Ice Models to Improve the Understanding of Arctic Sea Ice Thickness
Ph.D. Student:	Imke Sievers
Supervisors:	Assoc. Prof. Ming Shen, Aalborg University PhD Researcher Till Soya Rasmussen, Danish Meteorological Institute Prof. Lars Stenseng, Danish Technical University

The main body of this thesis consists of the following papers.

[1] Imke Sievers, Till A. S. Rasmussen and Lars Stenseng, "Assimilating CryoSat-2 freeboard to improve Arctic sea ice thickness estimates," *The Cryosphere*, no.17, pp. 3721–3738, 2023, https://doi.org/10.5194/tc-17-3721-2023.

[2] Imke Sievers, Henriette Skourup, and Till A. S. Rasmussen, "Impact assessment of snow thickness, sea ice density and water density in CryoSat-2 derived sea ice thickness," *The Cryosphere*, Discussion, 2023, https://doi.org/10.5194/tc-2023-122.

[3] Imke Sievers, Andrea M. U. Gierisch, Till A. S. Rasmussen, Robinson Hordoir, and Lars Stenseng, "Arctic sea ice and snow from different ice models: A CICE–SI3 intercomparison study," *The Cryosphere*, Discussion, Withdrawn, 2022, https://doi.org/10.5194/tc-2022-84.

This thesis has been submitted for assessment in partial fulfilment of the PhD degree. The thesis is based on the submitted or published scientific papers which are listed above. Parts of the papers are used directly or indirectly in the extended summary of the thesis. As part of the assessment, co-author statements have been made available to the assessment committee and are also available at the Faculty. The thesis is not in its present form acceptable for open publication but only in limited and closed circulation as copyright may not be ensured.

Acknowledgement

I'd like to thank my supervisors for their support and guidance. Most of all, I'd like to thank Till A. Soya Rasmussen for his patience and for doing everything in his power to help me through the process, as well as providing scientific and technical guidance. Further, I'd like to thank Nicolaj Hansen, Renée Mie Fredensborg Hansen, Lea Poropat, Ida Margrethe Ringgaard, Marina Georgati, Henriette Skourup and most of all Ole Krarup Leth for proofreading parts or even the entire thesis. My colleges at DMI, I'd like to thank for their encouragement and providing such a nice and fun work environment. In Winter 2022 I had the opportunity to spend three months in Lars Nerger's Data Assimilation Team at Alfred Wegener Institute, where I learned a lot about PDAF and Ensemble Kalman filters. For this opportunity, and his support, I'd like to thank Lars Nerger. For adopting me into their community, despite technically not being affiliated with them, I'd like to thank the DTU Space PhD committee and fellow PhD students. Without you, I would have felt a bit lost at times. Finally, I'd like to thank my friends and family for their emotional support and encouragement.

Imke Sievers
Aalborg University, May 8, 2024

Acronyms

AOA Arctic Ocean Atlas

ASAR advanced SAR

ASD Altimetric Snow Depth

AWI Alfred Wegener Institute

BGEP Beaufort Gyre Exploration Project

BGrun model run from 1995-2020 without assimilation

C3S Dayly sea ice surface temperature

C6N4$_{J21}$ Model run from Paper 2 with improved sea ice desnity parameterisation

CAFS Coupled Arctic Forecast System

CCMEP Canadian Centre for Meteorological and Environmental Prediction

CICE Community Ice CodE

CICEfd SI3 reference run in paper 3 with constant neutral drag

CICEref CICE reference run in paper 3

CICEref model run for SI3 comparison in paper 3 from 2007-2020

CICEs CICE reference run in paper 3 with increased snow forcing and constant drag

CICEtN CICE reference run in paper 3 with freezing point from NEMO

CMIP Coupled Model Intercomparison Project

CPOM Center for Polar Observation and Modelling

CS2SMOS SMOS/CryoSat-2 merged SIT product

DMI Danish Meteorological Institute

DORIS Doppler Orbitography and Radiopositioning Integrated by Satellite

EASE Equal-Area Scalable Earth

EASE2-Grid Equal-Area Scalable Earth Grid

ECCC Environment and Climate Change Canada

ECMWF European Centre for Medium-Range Weather Forecasts

EnKF Ensemble based Kalman Filter

ENVISAT Environmental Satellite

ERA5 ECMWF Reanalysis v5

ERS European Remote Sensing

ESA European Space Agency

EUMETSAT European Organisation for the Exploitation of Meteorological Satellites

EVP Elastic-Viscous-Plastic

FB Freeboard

fbRun model run from 2018-2020 with SIC and FB assimilation

FYI First Year Ice

GLORYS Global Ocean Physics Reanalysis

GODAR Global Oceanographic Data Archaeology and Rescue

HYCOM Hybrid Coordinate Ocean Model

ICESat Ice, Cloud and land Elevation Satellite

IMB Ice mass balance bouy

IPCC International Panel on Climate Change

JPL Jet Propulsion Laboratory

LEGOS Laboratoire d'Etudes en Géophysique et Océanographie Spatiales

LESTKF Local Error Subspace Transform Kalman Filter

LRM Low Resolution Mode

LRR Laser Retro-Reflector

MOSAiC Multidisciplinary drifting Observatory for the Study of Arctic Climate

MPI Message Passing Interface

MW99 Modified Warren et al. (1999) snow climatology

MYI Multi Year Ice

NASA National Aeronautics and Space Administration

NEMO Nucleus for European Modelling of the Ocean

NOAA National Oceanic and Atmospheric Administration

ORAS5 Ocean Reanalysis System 5

OSISAF Ocean and Sea Ice Satellite Application Facility

Paper 1 Sievers et al. (2023a)

Paper 2 Sievers et al. (2023b)

Paper 3 Sievers et al. (2022)

PDAF Parallel Data Assimilation Framework

PHC3 Polar Science Center Hydrographic Climatology version 3

refRun reference run from 2018-2020 (subset of BGrun)

RIOPSv2 Regional Ice Ocean Prediction System version 2

RMSE Root Mean Square Error

SAR Synthetic Aperture Radar

SARAL Satellite with ARgos and ALtiKa

SARin Synthetic Aperture Radar interferometry

SI3 Sea Ice Modelling Integrated Initiative

SI3fd SI3 reference run in paper 3 with constant neutral drag

SI3nb SI3 reference run in paper 3 without blowing snow

SI3ref SI3 reference run, used in work in progress section

SIC Sea Ice Concentration

sicRun model run from 2018-2020 with SIC assimilation only

SIMIP Sea-Ice Model Intercomparison Project

SIRAL Synthetic Aperture Radar Interferometric Radar Altimeter

SIT Sea Ice Thickness

SMMR Scanning Multichannel Microwave Radiometer

SMOS Soil Moisture and Ocean Salinity Satellite

SSMI Special Sensor Microwave Imager

SSMIS Special Sensor Microwave Imager Sounder

TFMRA Threshold First Maximum Retracker Algorithm

TPXO Tidal model

W99 Warren et al. (1999) snow climatology

WMO World Meteorological Organisation

WOA World Ocean Atlas

Nomenclature

$\bar{\mathbf{x}}_i$	mean model state
$\bar{\mathbf{x}}_m$	array holding mean of the pre run model states
$\mathbf{H}$	observation operator
$\mathbf{K}$	Kalman gain
$\mathbf{P}_i^f$	covariance matrix of the model ensemble error
$\mathbf{R}_i$	observation error covariance matrix
$\mathbf{x}^a$	array holding state analysis
$\mathbf{x}^f$	array holding model forecast
$\mathbf{x}_i$	model state ensemble
$\mathbf{x}_i^h$	array holding model state combining pre run model states with current assimilation step
$\mathbf{x}_m^h$	array holding single member of the pre run model states
$\mathbf{x}_{mi}$	array holding model state from current assimilation step
$\mathbf{y}^o$	array holding observations
∇H_0	surface slope
ψ	ridging redistribution function
ρ_b	density of the brine content
ρ_i	sea ice density
ρ_s	sonw density

ρ_w	water density
ρ_a	air density
ρ_{fresh}	density of fresh ice
ρ_{new}	sea ice density of fresh FYI ice
ρ_{old}	sea ice density of fresh MYI ice
ρ_w	water density
σ	internal stress
τ_a	stresses from atmosphere
τ_b	basal stress
τ_w	stresses from ocean
$\vec{U}_a$	atmosphere velocity
$\vec{U}_i$	ice velocity
$\vec{U}_w$	ocean velocity
$\vec{k}$	unit vector
$\vec{u}$	horizontal velocity
a_b	brine content of the ice
a_{FYI}	FYI fraction per grid cell
c	speed of light in vacuum
C_a	air drag coefficient
C_f	drag contribution from the ice flow eges (FB)
C_r	drag contribution from the sail or keel
C_s	drag contribution from the ice flow surface skin
c_s	speed of light in snow
C_w	ocean drag coefficient
C_{fd}	sea ice edge contribution for neutral drag coefficient following Lüpkes et al. (2012)

C_{ice}	sea ice skin contribution for neutral drag coefficient following Lüpkes et al. (2012)
C_{mp}	drag contribution from the melt pond edges
cat	sea ice category
cp_O	ocean heat capacity
f	thermodynamic growth and melt
f_c	Coriolis term
FB_0	Freeboard prior to assimilation
FB_i	ice freeboard
FB_r	radar freeboard
$fmpot$	freeze and melt potential
g	gravitational acceleration
g_h	ice thickness distribution function
H_s	snow thicknes
H_{0_w}	sea surface layer thickness
Hs_{cat}	snow thickness in category cat
Hs_i	snow thickness from the initialisation
i	assimilation step
Inc_{FB}	Freeboard increment
Inc_{sic}	SIC increment
Inc_{sit}	SIT increment
$IncF_{sic}$	fractal SIC increment
$IncF_{sit}$	fractal SIT increment
M	combined mass of ice and snow per unit area
m	number of observations
N	ensemble of size

n	model size (grid points)
N_t	time steps in one assimilation period
SIC_0	SIC prior to assimilation
SIC_{cat}	sea ice concentration in category *cat*
SIC_i	sea ice concentration from the initialisation
SIT_0	SIT prior to assimilation
SIT_b	sea ice thickness upper limit in category *cat*
SIT_{cat}	sea ice thickness in category *cat*
SIT_i	sea ice thickness from the initialisation
SST	sea surface temperature
t	time
t_0	first time step of assimilation period
t_i	time at assimilation step i
t_m	time in month
TI_{melt}	ice melting temperature
TO_{freeze}	ocean freezing temperature

Chapter 1

Introduction

1 Aim and Objectives of this Thesis

The overall aim of this thesis is to improve our understanding of Arctic sea ice thickness (SIT) and quantify and reduce the uncertainties of it by combining observations and sea ice models. Apart from SIT being an important variable to estimate the currently present sea ice volume in the Arctic, a good estimate can also be used to improve sea ice predictions (Blockley and Peterson, 2018; Guemas et al., 2016; Ordoñez et al., 2018). This thesis aims to bridge the gap between observed parameters and modelled parameters. In particular, this thesis focuses on the relationship between CryoSat-2 radar freeboard (FB) observations and simulated sea ice thickness from numerical sea ice models. The method for this is to develop a framework for radar FB assimilation.

Satellite-based SIT is calculated from radar satellite-derived FB, and FB is the distance between the water line and the ice surface. Radar FB is the FB measured by radar satellites and converted to FB by applying a correction term for slower wave propagation in the snow pack (Ricker et al., 2014). To assimilate it, it has to be derived from model values. In this work, the values investigated to do so are snow thickness, SIT, sea ice density and water density. The hypothesis is that sea ice model output can be used to derive radar FB, which can be used to assimilate CryoSat-2 radar FB to improve modelled SIT, and that model variables for snow thickness, sea ice density and water density can be derived that are closer to observations compared to the values used in currently available CryoSat-2 SIT products.

One motivation for this work is that the commonly assimilated CryoSat-2 SIT depends on uncertain snow thickness, sea ice density and water density values. Several studies have found the sea ice density and snow thickness values, currently used, to be uncertain and potentially biased (Ji et al., 2021; Jutila et al., 2022; Zhou et al., 2021). Further, there is a need to reassess the uncertainty of water density, since the claim that

it can be neglected emerges from a study that only considered seasonal variability, not spatial variability (Wadhams et al., 1992).

To achieve that, the main objectives of this thesis are to:

1. Understand the parameterisation in the model and determine their influence on SIT and snow thickness. This is done by investigation of different sea ice model parametrization. As the model-derived radar FB is calculated from model SIT and snow thickness, understanding the origin of their variability in between different model parameterisations is relevant to the developed assimilation framework and the derived radar FB. This objective is addressed in Sievers et al. (2022) and the work in progress section.

2. Prove that model-derived sea ice density, snow thickness and water density values can substitute the values used in currently available CryoSat-2 SIT products. Coupled sea ice - ocean models already include parameters for snow thickness and water density. These can be used but need to be evaluated. The snow density and sea ice density are constant in current model simulations. Alexandrov et al. (2010) showed that the sea ice density should be varied when used to convert FB to SIT. Therefore, a new parameterisation will be derived in this work. For the snow density, a simple time-dependent parameterisation following Mallett et al. (2020) will be used. This objective is addressed in Sievers et al. (2023b).

3. Assess the SIT differences based on changing the snow thickness, sea ice density and water density used in available CryoSat-2 SIT products with modelled values. This is achieved by substituting the values of snow thickness, sea ice density and water density used in available CryoSat-2 SIT products with model values. This objective is addressed in Sievers et al. (2023b). Since Sievers et al. (2023b) finds that the model values can be used as an alternative to the value used currently in available CryoSat-2 SIT products, it needs to be assessed if the new values influence the derived SIT and to which degree.

4. Demonstrate that the assimilation of radar FB can improve SIT estimates. This is achieved with a model and assimilation system for the radar FB assimilation. The motivation for this objective is that there has not been any system assimilating radar FB to date, and it has to be proven that assimilating radar FB can improve the modelled SIT. This objective is addressed in Sievers et al. (2023a).

2 Motivation

Arctic sea ice plays an important role in the global climate system. It influences atmospheric circulation patterns (Budikova, 2009; Liang et al., 2020; Stroeve et al., 2011), changes the global radiation budget (Cohen et al., 2014; Serreze et al., 2007), alters the

Arctic fresh water cycle (Rabe et al., 2014; Wang et al., 2018) and has a major impact on the local biology (Boetius et al., 2013; Hop et al., 2020; Lannuzel et al., 2020). It is well known that there has been a rapid loss of ice volume over recent decades (Kinnard et al., 2008; Simmonds, 2015; Walsh et al., 2017). Satellite measurements have played a key role in observing this loss. The longest ongoing satellite sea ice observations are sea ice area observations, which have been conducted since the 1970s (Johannessen et al., 1999; Sissala et al., 1972; Stroeve et al., 2008). However, to make meaningful statements about the development of the Arctic sea ice volume, SIT estimates are needed in addition to sea ice area estimates.

Arctic-wide SIT observation on high temporal frequencies can only be achieved by satellite. The satellite observation systems from which most currently available SIT data products are derived are: passive microwave (Tian-Kunze et al., 2014), laser altimetry (Martino et al., 2019) and radar altimetry (Wingham et al., 2006). Passive microwave SIT is, for example, derived from the Soil Moisture and Ocean Salinity SMOS mission (Huntemann et al., 2014; Tian-Kunze et al., 2014), laser altimetry-based SIT from the Ice, Cloud and land Elevation Satellite (ICESat) mission (Petty et al., 2020) and radar altimetry based SIT from CryoSat-2 (Hendricks et al., 2021; Landy et al., 2022; Tilling et al., 2018), Satellite with ARgos and ALtiKa (SARAL) (Joshi et al., 2020), ENVISAT Advanced Synthetic Aperture Radar (ASAR) (Nakamura et al., 2009), and European Remote Sensing Satellites ERS-1 and ERS-2 (Laxon et al., 2003). SIT from SMOS is only valid for thin ice (Tian-Kunze et al., 2014), and IceSat observations are only available on limited time scales. Therefore, this thesis focuses on radar-derived SIT, specifically on the relation between radar-derived CryoSat-2 FB and SIT.

Laxon et al. (2003) were the first to derive SIT from satellite observations and levelled the ground for the European Space Agency's (ESA) CryoSat mission, dedicated to observing the cryosphere (Wingham et al., 2006). To derive SIT, Laxon et al. (2003) used radar altimetry-based FB observations. CryoSat-2 also carries a radar altimeter, but with an improved footprint to better distinguish between leads and ice flows (Wingham et al., 2006). To derive SIT from FB, hydro-static balance is assumed and the FB is related to the ice thickness through assumptions made for the values of snow density, sea ice density, snow thickness and water density. In the last decade, both the accuracy of the observed FB (King et al., 2018; Kwok, 2014; Ricker et al., 2015; Willatt et al., 2011) and the adequacy of the values of sea ice density and snow thickness used to derive SIT from FB (Glissenaar et al., 2021; Ji et al., 2021; Jutila et al., 2022; Kern et al., 2015; Mallett et al., 2021a) have been discussed.

Several uncertainty sources of radar satellite-derived SIT have been discussed in recent years. For example, the accuracy of the FB observations has been evaluated regarding where the radar signal is reflected (reflection horizon). Studies found that snow temperature, snow thickness, moisture content and snow density layering lead to dislocation of the reflection horizon and thereby introduce errors in the FB measurements (King et al., 2018; Kwok, 2014; Ricker et al., 2015; Willatt et al., 2011). This can

result in up to 1.7 m biases in the derived SIT (King et al., 2018). Another source of uncertainty in the retrieved radar FB originates from the interpretation of the received radar signal. Studies have found that the technique called retracking (fitting a curve to the received signal to interpret it) can lead to biases in the resulting radar FB (Landy et al., 2020; Xia and Xie, 2018). The values typically used in the hydro-static balance equation to derive SIT from FB for snow thickness, snow density and sea ice density have also been investigated by several studies (Alexandrov et al., 2010; Ji et al., 2021; Jutila et al., 2022; King et al., 2018; Kurtz and Farrell, 2011; Kwok and Cunningham, 2015). In particular, sea ice density and snow thickness have been proven to introduce large uncertainties in the FB to SIT conversion.

Another tool that has been widely used to understand Arctic SIT are numerical sea ice models (Hunke et al., 2020; Long et al., 2021; Notz et al., 2016). In contrast to satellite observations, sea ice models are based on physical equations solving thermodynamic and dynamic equations of ice, forced by ocean and atmospheric input (Hunke et al., 2021a; Rousset et al., 2015; Vancoppenolle et al., 2023; Zhang and Rothrock, 2001). They are limited by our understanding of the physical system driving sea ice growth melt and dynamics, technical implementations and forcing data. Therefore, model-derived sea ice thickness differs from model to model (Kumar et al., 2021; Long et al., 2021).

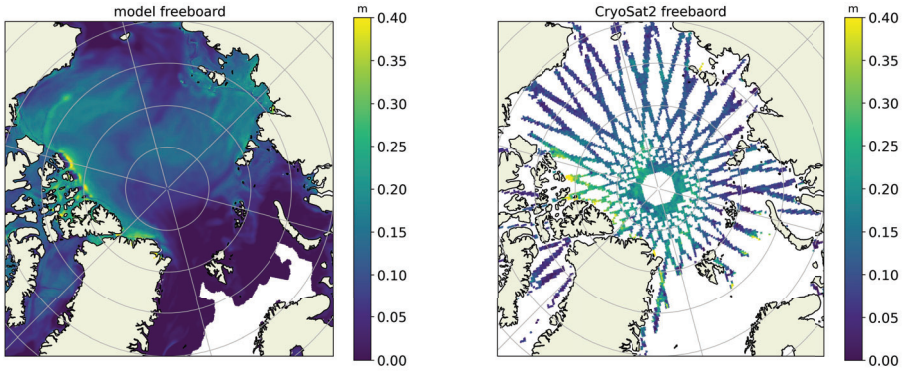

Fig. 1.1: Example of one week FB from sea ice models (left) and CryoSat-2 observations (right) for the first week of January 2018.

One approach to exploit the advantages of both sea ice models and satellite-based SIT observations is data assimilation (Fiedler et al., 2022; Mignac et al., 2022; Xie et al., 2018). Data assimilation combines models and observations and their uncertainties in order to provide the best estimate of the system one aims to predict. For forecasting the sea ice state, or improving the estimate of the past state, it is common practice to assimilate SIT or sea ice concentration (SIC) (Chen et al., 2017a; Collow et al., 2015;

Mignac et al., 2022; Ponsoni et al., 2023; Posey et al., 2015; Shu et al., 2021; Smith et al., 2021). The work presented here will explore different aspects of assimilating radar FB to improve SIT estimates.

The assimilation technique chosen in this thesis is the Kalman Filter, which assumes that both model and observation errors are unbiased, Gaussian distributed and uncorrelated in time (Kalman and Bucy, 1961). It is however known that sea ice models often come with a bias in, for example, ice extent (Fiedler et al., 2022; Ponsoni et al., 2023; Zhang and Rothrock, 2003) and that, especially, the SIC error is not Gaussian distributed. Despite the approximations made, prior studies show that assimilating sea ice using Kalman Filters improves the modelled sea ice estimates (Cheng et al., 2023; Lisæter et al., 2003; Mathiot et al., 2012).

To our knowledge, this thesis includes the first assimilation approach for radar FB. Several publications have mentioned FB assimilation previously (Chenal et al., 2022; Kaminski et al., 2018; Mathiot et al., 2012; Vernieres et al., 2016). Vernieres et al. (2016) and Chenal et al. (2022) have not yet published their methods, Kaminski et al. (2018) only theoretically investigate the effect of FB assimilation on SIT. The first ever assimilating FB study by Mathiot et al. (2012) assimilated ICESat monthly snow FB (FB plus snow thickness). They found that the assimilation of snow FB improves the central Arctic mean SIT by 50 cm. They also used an Ensemble based Kalman Filter (EnKF). However, their method differs from the approach taken in this thesis on two points. First, they assimilated snow FB from ICESat, not FB from CryoSat-2. The difference here is that snow FB is the distance from the water surface to the snow surface, and the FB is the distance from the water surface to the ice-snow interface. Second, their assimilation system is a multivariate Ensemble Kalman filter. In contrast, the setup presented here is single variate and uses a historical run to estimate the background error instead of running a full ensemble. The simplifications were made to ensure that the assimilation setup was feasible to be conducted within the timeframe of this thesis and to keep computational costs low.

3 Structure of the Thesis

This thesis is based on a collection of Papers, but the model coupling and assimilation framework development were central parts of the work carried out. Therefore, this thesis includes an extensive method chapter (chapter 2) where the developed assimilation system is described. This section also includes a more detailed introduction to CryoSat-2 FB, sea ice models and Kalman Filter assimilation. In chapter 3, the included Papers are summarised, and some unpublished results are shown in a work in progress section (chapter 3 section 3). Here, only a brief overview of the Papers is included.

In the first study included in this thesis, a Kalman Filter-based assimilation setup for the radar FB is tested to investigate if the derived FB improves the modelled SIT. Since the satellite-derived FB comes with the above-mentioned uncertainties and the aim of

deriving modelled FB is to improve our understanding of the satellite-derived FB, it can not be used to evaluate the modelled FB. Instead, this study uses independent SIT observations. In theory, if the modelled radar FB was derived correctly, assimilating it and converting the assimilated FB back to SIT should improve the modelled SIT, under the condition that the observations come with realistic error estimates.

In the second study included in this thesis, the model parameters for snow thickness, water density and sea ice density used to derive the model FB are investigated. Three main points are addressed in this study: a new sea ice density parameterisation is introduced, the commonly neglected variability of the water density is investigated, and how the derived SIT would be influenced, on average, when exchanging the commonly used values of snow thickness, sea ice density and water density with the values from the model setup is evaluated. The model setup allows for a multi-variable comparison, while earlier studies only investigated one of the values at a time. Earlier studies discussed either the influence of changing sea ice density (Ji et al., 2021; Jutila et al., 2022) or snow thickness (Mallett et al., 2021b) separately.

In the third study of this thesis, the effect of different model parameterisation on modelled SIT and snow thickness are tested. This is of relevance for the model-derived FB, because the modelled FB is derived based on model SIT and snow thickness.

For further details, all Papers are attached in the appendix. In chapter 4, the results from the included Papers and the work in progress are discussed and related to the overall aim and objective of the thesis. Chapter 5 highlights the overall outcome of the included studies and outlines a path forward based on the discussed results from the included studies.

Chapter 2

Method and Background

The following sections give a more detailed introduction to the satellite data assimilated, sea ice models and the EnKF. Furthermore, it describes the overall setup, consisting of: the assimilated data, the ice model used in the assimilation setup, the ocean-sea ice model coupling and the software used to implement the assimilation. The data sets assimilated in this study are described in section 1. The section covers the SIC data and the CryoSat-2 FB data, as well as an overview of the techniques, which are typically used to derive SIT from CryoSat-2 FB. Section 2 provides an overview of sea ice models in general and the sea ice model used in this study, Community Ice CodE (CICE). It also includes a list of all runs discussed in the thesis. Section 3 provides a brief introduction to Kalman Filters and to the software used to implement the assimilation framework. 3.4 brings all parts discussed in chapter 2 together and describes the overall assimilation framework. The final part, section 4, serves as a technical reference for the coupling between the ocean model Nucleus for European Modelling of the Ocean (NEMO) and CICE, and further model development carried out as part of this thesis.

1 Sea Ice Satellite Observations

1.1 Ocean and Sea Ice Satellite Application Facility (OSISAF)

The assimilated SIC data is the European Organisation for the Exploitation of Meteorological Satellites (EUMETSAT) Ocean and Sea Ice Satellite Application Facility (OSISAF) daily climate data record product OSI-430-a (OSISAF, 2022), which can be downloaded from the Norwegian Meteorological Institute FTP server. The data set is provided on a 25x25 km Equal-Area Scalable Earth (EASE) grid with a daily frequency. The OSI-430-a data set is based on passive microwave observations from the satellite-based instruments Scanning Multichannel Microwave Radiometer (SMMR), Special Sen-

sor Microwave Imager (SSMI) and Special Sensor Microwave Imager Sounder (SSMIS). It has an uncertainty of up to 15%. More details can be found in the scientific validation report by Saldo (2022).

In the very first setup of the assimilation framework, the finer resolution SIC product OSI-401-d (OSISAF, 2017) was used. The grid resolution of OSI-401-d is 10x10 km and matches the sea ice model grid resolution used in this study better than OSI-430-a's 25x25 km grid resolution. However, it was found that OSI-401-d included error estimates of up to 15% in areas which are ice-free all year. The same is not the case in OSI-430-a, where the error estimate was processed with an ice mask, ensuring that the error in ice-free areas is 0%. OSI-430-a was therefore chosen due to its better error estimate.

Even though the main focus of this work is to develop an assimilation framework for FB observations, the SIC biases discussed in the current chapter, section 3, indicated the need for assimilation of SIC as well.

1.2 Freeboard Observations

The first conversion of FB to SIT conducted by Laxon et al. (2003) derived its FB from the European Remote Sensing satellites ERS-1 and ERS-2. The ERS satellites operated from 1991 to 2000 and from 1995 to 2011, respectively, and covered areas up to 81.5° N (Attema et al., 2000). The successful retrieval of SIT from the ERS satellites lay the foundation for the ESA mission CryoSat-2, which provided the measurements that are assimilated in this thesis. CryoSat-2 orbits the earth in polar orbit, covering the Arctic up to 88°N and carries a Ku-band radar altimeter with a frequency of 13.6 GHz. The major improvement from the ERS satellites to CryoSat-2, apart from a smaller polar gap, is the synthetic aperture technique, which reduces the radar's along-track footprint from about 5 to 10 km to around 250 m resolution (Wingham et al., 2006). The higher resolution allows for more unambiguous radar return.

CryoSat-2 is not the only satellite that observes FB from space. The National Aeronautics and Space Administration (NASA) mission ICESat (Ice, Cloud and land Elevation Satellite) (2003–2009) and its follow-up mission ICESat-2 (2018-present) (Abdalati et al., 2010) also observes FB, however, they use a laser technique in contrast to ESA's ERS and CryoSat-2 missions. ICESat-2s laser is reflected from the snow-air interface and the measured FB is called snow FB or total FB, whereas CryoSat-2's radar is reflected closer to, or at, the snow-ice interface (Ricker et al., 2014). ICESat's snow FB was in the first study that assimilates FB (Mathiot et al., 2012).

ESA's satellites Sentinel-3 (Donlon et al., 2012) and ENVISAT (Louet and Bruzzi, 1999) are also used to derive FB (Louet and Bruzzi, 1999). Sentinel-3 (2016-present) carries a radar altimeter with Synthetic Aperture Radar (SAR) capabilities similar to CryoSat-2. Lawrence et al. (2021) showed that FB could be derived from it, similarly, as from CryoSat-2. Sentinel-3 has a larger polar gap; thus, there are no observations north of 81.5 °N. This also limits ENVISAT (2002–2012), which similar to the ERS satellites

and CryoSat-2 carried a Ku-band radar, but without SAR capabilities. Guerreiro et al. (2017), Zhang et al. (2021) and Wang et al. (2022) have successfully derived FB from it. Compared with CryoSat-2, it has the disadvantage of a poorer resolution, no SAR mode and therefore, a bigger footprint as well as a large polar gap. Comparing all the above-mentioned FB measurements, CryoSat-2 provides the longest record of FB measurements with high latitude coverage.

The Definition of Freeboard

As mentioned above, several different satellites observe FB, but their sensors differ. This leads to several different definitions of FB. In this text, three different FB definitions are used:

1. FB: Here describing the distance between the ocean and the snow-ice interface.
2. snow FB: Here describing the distance between the ocean and the snow-air interface.
3. radar FB: Here describing the FB plus a correction term accounting for the slow-down of the radar signal in snow, following Ricker et al. (2014).

Other studies define other names and sometimes even switch out some of the above definitions. They will not be detailed here to not confuse the reader. Figure 2.1 shows the different kinds of FB introduced above. Snow FB is measured by, for example, ICESat-2 (Martino et al., 2019). The advantage of the laser, in contrast to the radar altimeter, is that it is unambiguously reflected from the snow-air interface. The disadvantage of this method is that it depends on cloud-free conditions and has a shorter data record than CryoSat-2. In this study, we concentrate on CryoSat-2 data and the radar and FB.

When the CryoSat-2 mission was designed, it was assumed that it would measure FB based on Beaven et al. (1995). However, soon it was discovered that this is not always the case and that especially thick, wet and warm snow interferes with the radar signal (King et al., 2018; Kwok, 2014; Kwok et al., 2011; Ricker et al., 2015; Willatt et al., 2011). Ricker et al. (2014) defined the radar FB as the distance between the radar scattering horizon and the sea surface. The radar scattering horizon is the surface from where the radar signal actually is reflected. To convert the radar FB into FB, Tilling et al. (2018) introduced a correction term depending on the speed of light in snow, which is subtracted from the FB. It is based on the following equation:

$$FB_r = FB - (\frac{c}{c_s} - 1) * H_s \tag{2.1}$$

Here FB_r is the radar FB, FB the FB, c the speed of light in vacuum ($c = 3 \times 10^8$m/s), c_s the speed of light in snow and H_s the snow thickness. In Tilling et al. (2018) ($\frac{c}{c_s} - 1$)

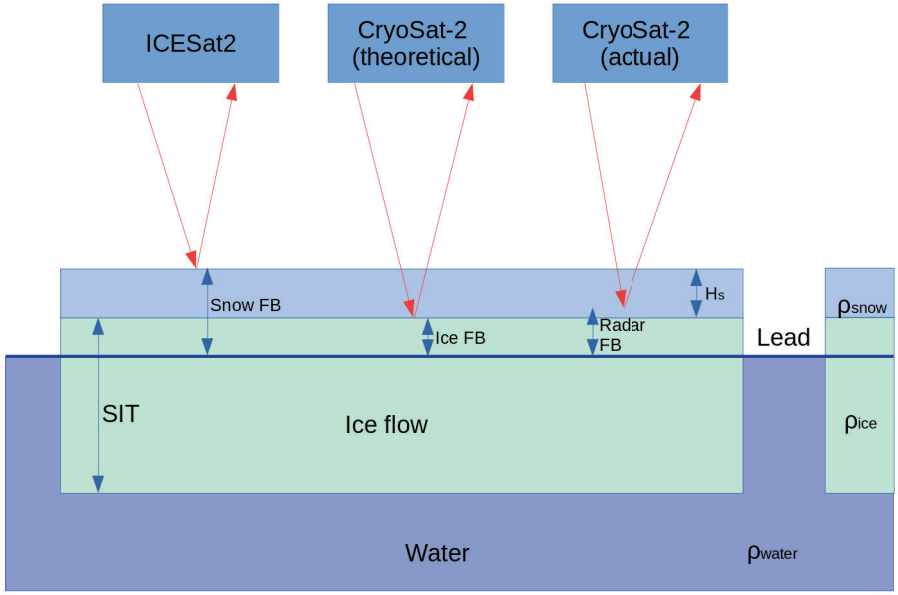

Fig. 2.1: Overview of FB definitions commonly used. The blue arrows indicate the different FB definitions, and ice thickness (SIT) and snow thickness (H_s), and the red arrows indicate the satellite signal used to measure FB. The blue boxes in the upper part of the figures indicate the satellites ICESat and CryoSat-2. Here, CryoSat-2 appears twice to show the difference between radar FB and FB. FB is the FB that it was designed to measure (Wingham et al., 2006) and radar FB is the FB that it actually measures (Ricker et al., 2014).

was approximated to 0.25, but recently Mallett et al. (2020) suggested calculating c_s depending on the snow density as follows:

$$c_s = c(1 + 0.51 \times \rho_s)^{-1.5} \tag{2.2}$$

They suggested using a linear function (equation 2.3) derived from the Warren et al. (1999) (W99) climatology to estimate ρ_s and found that this leads to an up to 0.15 m SIT improvement.

$$\rho_s = 6.5t + 274.51 \tag{2.3}$$

The linear function depends on month since October (t in equation 2.3) and is only valid for the month October to April. This conversion of radar FB to FB does not take into account the uncertainties based on reflection from within the snow pack.

There is an ongoing debate whether the correction of the Ku-band radar speed in snow is sufficient (Gerland et al., 2012; King et al., 2018; Kwok, 2014; Ricker et al., 2015). Overall, there is consensus that Ku-band radar penetrates dry, thin and cold

snow better than warm, wet and thick snow (Giles and Hvidegaard, 2006; King et al., 2018; Willatt et al., 2011). Due to the lack of better understanding of the temporal and spatial scale of the issues, it is here assumed to be sufficient to correct for the radar speed reduction in snow from equation 2.2 when deriving FB from FB_r (Hendricks et al., 2021).

1.3 CryoSat-2

CryoSat-2 carries the following instruments: The Synthetic Aperture Radar Interferometric Radar Altimeter (SIRAL), the Doppler navigation system DORIS (Doppler Orbitography and Radiopositioning Integrated by Satellite), the Star Tracker and the Laser Retro-Reflector (LRR). The DORIS, Star Tracker and LRR instruments mainly ensure accurate knowledge of the location and orientation of the satellite and will not be further discussed. SIRAL can operate in three different modes: Low resolution mode (LRM), which is mainly used over open ocean, and the central parts of Greenland and Antarctic, SAR interferometry (SARin) mode, used at the ice sheet margins, and SAR mode, used over sea ice. The following section will give a brief overview of the processing needed to derive FB from CryoSat-2 radar observations.

In the SAR mode, the radar transmits a burst of pulses, which are used to decrease the satellite's footprint in the flight direction by means of Doppler processing. To do so, the frequency shift of the reflected signal due to the satellite's flight velocity is used to separate the overlapping footprints into thin "slices" and determine if the "slice" was reflected from a location ahead or behind the satellite.

These "slices" are then stacked to one return signal, which is less noisy and has a higher resolution than echoes from the low resolution mode. The shape of this return signal differs depending on which surfaces the radar was reflected from, ice, ocean or a mix of the two. To derive FB, a return signal from a lead is necessary to determine the sea surface height. Leads are openings within the ice pack. Their radar return signal is characterised by higher power of the reflected signal and is typically more narrow in range than a return signal from an ice floe. More detail about lead detention can be found in Quartly et al. (2019), as well as typical error sources resulting from lead detection discussed.

To derive where in the return signal the surface in the nadir direction (direction below the satellite) is located, a process called retracking is applied to the return signal. There are a multitude of different retrackers, but mainly two groups of retrackers are used for CryoSat-2 FB retrievals. The two main groups of retrackers are physical retrackers (Laforge et al., 2021; Landy et al., 2020; Villadsen et al., 2016) and threshold retrackers (Davis, 1997; Laxon et al., 2013; Ricker et al., 2014; Tilling et al., 2018). Physical retrackers model the surface from which the signal was reflected and determine the point on the received return signal, locating the surface from this (Kurtz et al., 2014).

Threshold retrackers set a percentage of the leading edge of the received return

signal to be the surface (Davis, 1997). Overall physical retrackers are found to be more representative, but also more computational expensive (Laforge et al., 2021), than threshold retrackers. Landy et al. (2020) identified that the way the return signal is retracked can lead to significant errors in the derived FB. After additional processing of the signal, taking, for example, the sea surface high into account, or the atmospheric conditions, the FB is then determined by subtracting distance estimates from ice floes and leads. The above description of the CryoSat-2 signal processing is only intended to give an overview. Processing CryoSat-2 return signals to determine the FB is an active area of research, and the different steps described above only scratch at the surface of ongoing discussions. Additional post-processing is further discussed in, for example, Dawson et al. (2022), Tilling et al. (2018), Laxon et al. (2013), Quartly et al. (2019) and Landy et al. (2020).

The FB assimilated in this study is the weekly CryoSat-2 radar FB from the Alfred Wegener Institute (AWI) weekly gridded CryoSat-2 SIT product (Hendricks et al., 2021). This product uses a 50% Threshold First Maximum Retracker Algorithm (TFMRA) (Ricker et al., 2014). As an input to their algorithm, they use ESA's Level 1 Baseline-D ICE data (Meloni et al., 2020). It comes on a 25 km Equal-Area Scalable Earth Grid version 2 (EASE2-Grid) and on a weekly frequency. Several other similar data sets exist. These include for example, the Center for Polar Observation and Modelling (CPOM) data set described by Tilling et al. (2018), or the Jet Propulsion Laboratory (JPL) data set described by Kwok and Cunningham (2015), or the Laboratoire d'Études en Géophysique et Océanographie Spatiales (LEGOS) Altimetric SIT Data described in Guerreiro and Fleury (2017). The reason the AWI data set was chosen is its high temporal frequency and the fact that it also contains all variables used to derive SIT from the radar FB as described in the following section.

From CryoSat-2 Freeboard to Sea Ice Thickness

The following section describes how FB is converted into SIT.

Assuming hydrostatic balance, the relationship between FB and SIT can be described by:

$$SIT = \frac{FB\rho_w}{(\rho_w - \rho_i)} + \frac{H_s\rho_s}{(\rho_w - \rho_i)} \tag{2.4}$$

Where FB is the FB, ρ_w is the density of water, ρ_i is the density of sea ice, ρ_s is the density of snow and H_s is the snow thickness. Most available CryoSat-2 SIT products calculate SIT based on equation 2.4 (or a variation of it) estimating ρ_w, ρ_i, ρ_s and H_s from climatologies or empirical values depending on the ice type (Guerreiro and Fleury, 2017; Hendricks et al., 2021; Kurtz et al., 2013; Kwok and Cunningham, 2015; Tilling et al., 2018). The ice types in these products are first year ice (FYI) and multi-year ice (MYI). The distinction between FYI and MYI is in most cases done with the help of passive microwave satellite products (Sallila et al., 2019). This method, based on

ice type depending on values for ρ_i and H_s to derive SIT from CryoSat-2, will in the following text be called the classical approach. Below is a brief overview of how the approach was developed and the values that are typically used for ρ_w, ρ_i, ρ_s and H_s.

In the early days of satellite-derived SIT, it was assumed that these values could be substituted by climatological and empirical values. This was the first time that Arctic-wide SIT was derived from radar satellite FB. The uncertainties of ρ_w, ρ_i, ρ_s and H_s were estimated to result in an SIT uncertainty in the order of 0.1 m (Laxon et al., 2003).

Alexandrov et al. (2010) conducted a study on in situ SIT, snow thickness and FB observations, which showed that the sea ice density error was significantly underestimated by Laxon et al. (2003). Alexandrov et al. (2010) proposed to differentiate between sea ice density values FYI and MYI. Their proposed value for FYI is 916.7 $\pm$ 35.7 kg/m^3. It is based on the assumption of hydrostatic balance and snow, ice and FB measurements from the Sever expedition (Romanov, 2004). Their value for MYI is 882 $\pm$ 23 kg/m^3 based on measurements from Khohlov (1978). These values are the ones most commonly used to date (Fiedler et al., 2022; Hendricks et al., 2021; Landy et al., 2022; Sallila et al., 2019).

In recent years, new estimates of sea ice density have been derived. Ji et al. (2021) suggested a statistical approach using a comprehensive amount of Arctic field observations from 2001 to 2015, which were mostly taken during summer. They also find that there is an annual variability in sea ice density. The fact that most observations were taken during summer raises the question of if it is suitable for wintertime FB to SIT conversion. Jutila et al. (2022) derived sea ice density from airborne snow, total snow and ice thickness and snow FB observations to derive sea ice density. Based on the airborne observations, Jutila et al. (2022) derived sea ice density from a fitted curve, relating FB to sea ice density. Their observations are based on two field companies from the west Arctic in April 2017 and 2019. They acknowledge that more research is needed before their methodology can be used to derive sea ice density for FB to SIT conversion.

Snow thickness introduces uncertainty to the conversion of FB to SIT in two different ways. The first contribution is the snow load, which determines how much ice sticks out of the water, as illustrated by equation 2.4. The other contribution is the uncertainty introduced by snow to the scattering horizon and the reduction of speed of light (Kwok, 2014; Ricker et al., 2014). The uncertainty of FB to SIT conversion, due to snow thickness, has made snow thickness the most discussed uncertainty in SIT retrievals from CryoSat-2 (Fiedler et al., 2022; Kern et al., 2015; Kurtz and Farrell, 2011; Kwok, 2014; Mallett et al., 2020; Ricker et al., 2014; Tilling et al., 2018).

For a long time, this discussion was held back by the fact that no Arctic-wide snow thickness estimate exists on the same spatial and temporal resolution as CryoSat-2 data, except W99. Recently, several satellite- or model-based snow products have been published (Lawrence et al., 2018; Liston et al., 2020; Petty et al., 2018; Rostosky et al., 2018; Shi et al., 2020). Zhou et al. (2021) performed an intercomparison study that considers most of the above-cited snow products and W99. They found that they agree

on the general spatial thickness distribution but significantly differ in the annual cycle, magnitude and inter-annual trend. The researchers concluded that more research is needed in order to produce reliable Arctic-wide snow products.

The snow thickness that most CryoSat-2-derived SIT products use to date is therefore still based on W99 (Warren et al., 1999). W99 was derived from snow measurements from the late 1950s to the late 1980s. Since the measurements were obtained, Arctic sea ice has changed dramatically from being dominated by MYI to being dominated by FYI (Stroeve and Notz, 2018; Tschudi et al., 2016). Kurtz and Farrell (2011) found that snow on FYI differs significantly from snow on MYI and proposed to use a 50% reduced W99 snow thickness over FYI. Some products still use this modified W99 (MW99) (Ricker et al., 2017; Tilling et al., 2018). Others have proceeded to partially substitute FYI snow cover with snow depth climatologies from Advanced Microwave Scanning Radiometer satellite-derived snow thickness (Hendricks et al., 2021). The climatological snow product lacks inter-annual variability, and several studies have shown that this leads to a significant SIT error (Kern et al., 2015; Zygmuntowska et al., 2014). Recent studies by Fiedler et al. (2022) and Landy et al. (2022) substituted the entire W99 climatology with snow model values.

Similar to snow thickness values, snow density values for equation 2.4 are often taken from W99 or derived from it (Hendricks et al., 2021; Mallett et al., 2020; Tilling et al., 2018). Alexandrov et al. (2010) concluded that the snow density only leads to small uncertainties in the FB to SIT conversion.

Water density contributions are in general neglected (Kurtz et al., 2013; Ricker et al., 2014) when the uncertainty of SIT retrievals is calculated. This is done under the assumption that the water density has an uncertainty of $\pm$ 0.5 kg/m^3 (Alexandrov et al., 2010; Hendricks et al., 2021; Kurtz et al., 2013). The water density depends on salinity and temperature. Particularly, salinity varies greatly within the Arctic Ocean's top layers, with low values close to the Russian river outlets (Janout et al., 2020; Shiklomanov et al., 2021) and high values close to Fram Straight (Zweng et al., 2019). Based on this, the uncertainty of $\pm$ 0.5 kg/m^3 might be underestimated.

Even though snow thickness, snow density, sea ice density, snow density and water density might contribute to SIT uncertainties in different ways, all variables have one thing in common: their values are estimated on rather crude assumptions. In the presented thesis, this issue is addressed by the replacement of the traditional values with values derived from a sea ice model. The model will be described in section 2.1 and the variables introduced to derive SIT from FB will be described in section 4.2.

2 Sea Ice Models

Sea ice models numerically solve the dynamics and thermodynamics of sea ice. Based on the sea ice model CICE, a description of the main equations is presented in the next section. Numerical sea ice models have three main applications (Hunke et al., 2020):

1. Simulating the heat exchange between the ocean and the atmosphere in climate models, where sea ice plays an important part in the radiation budget. As part of the World Climate Research Program, sea ice models even have their own intercomparison project: The SIMIP - Sea-Ice Model Intercomparison Project (Notz et al., 2016).

2. Sea ice forecasts, used for everything from route planning for ships to climate adaptation. Many countries bordering the Arctic run short-term forecasts of Arctic sea ice conditions. Examples of such forecast systems are: the HYCOM-CICE model run operationally at the Danish Meteorological Institute (DMI) (Ponsoni et al., 2023), the Regional Ice Ocean Prediction System version 2 (RIOPSv2) developed at the Canadian Centre for Meteorological and Environmental Prediction (CCMEP) (Smith et al., 2021), and the Coupled Arctic Forecast System (CAFS) run at the National Oceanic and Atmospheric Administration (NOAA) (Maslowski et al., 2012).

3. Study of sea ice in a controlled environment to deepen and test our understanding of it. Studies often aim at development for the above two applications, for example, Tsamados et al. (2015) investigated melt from different sources, Zhang et al. (2018) explored the impact of including melt ponds and Roach et al. (2019) researched the effect of waves on the ice in the marginal ice zone.

SIT is a central property of numerical sea ice models. The first sea ice models described sea ice thickness as the average thickness of the sea ice present within one grid cell (Maykut and Untersteiner, 1971). Later, it was shown that models that included a subgrid parameterization of SIT into several categories improved the simulation of the sea ice significantly (Björk, 1992; Holland et al., 2006; Schramm et al., 1997; Walsh et al., 1985). As a consequence, most sea ice models today use a multicategory approach (Lipscomb and Hunke, 2004; Mélia, 2002; Rousset et al., 2015). The introduction of sub grid scale SIT distributions not only have a significant influence on the sea ice simulated, but it also impacts the ocean and the atmosphere by influencing the boundary layers temperature, density and salinity concentration (Bitz et al., 2001; Holland et al., 2006).

Over the past 20 years, many more parameterizations for sub-grid-scale processes have been added. For example: surface type varying ocean and atmospheric drag formulations that better resolve the energy transfer between the atmosphere and ice, and ocean and ice (Lüpkes et al., 2012; Tsamados et al., 2014); multi-scattering albedo formulations depending on snow and ice physical parameters (Briegleb and Light, 2007); transport of biological matter (Duarte et al., 2017); sub–grid–scale transport of snow (Hunke et al., 2021a); and sub-gird-scale ice flow size distribution (Roach et al., 2018), to only name a few.

2.1 CICE

The primary sea ice model in this study is the Community Ice CodE (CICE) (Hunke et al., 2021c), which is a widely used sea ice model. For example, was CICE in the latest version of the Coupled Model Intercomparison Project (CMIP), the most used sea ice component (Long et al., 2021). The CMIP models are the models that are used in the International Panel on Climate Change (IPCC) reports, advising governments worldwide on issues concerning climate change. Apart from being frequently used in climate models, CICE is also a component in several operational sea ice forecast systems as, for example, in the HYCOM-CICE model operating at DMI (Ponsoni et al., 2023) and the RIOPSv2 developed at CCMEP (Smith et al., 2021).

The fundamental equation CICE is solving is:

$$\frac{\partial g_h}{\partial t} = -\nabla \cdot (g_h \vec{u}) - \frac{\partial (f g_h)}{\partial SIT} + \psi \tag{2.5}$$

Where g_h is the ice thickness distribution function, t is time, $\vec{u}$ the horizontal velocity in x and y direction, ψ the ridging redistribution function and f the thermodynamic growth and melt. On the right-hand side, the first and second terms (counting the nabla operator as one) of equation 2.5 describe the horizontal transport, the third term the thickness change due to thermal processes and the fourth the thickness change due to mechanical process like ridging and rafting (Hunke et al., 2017). Each of the three terms is solved separately. Various options for parameterization are available, and the ones used in this study will be described in the following.

The default advection scheme, which is used in this study, was introduced by Lipscomb and Hunke (2004) and is an incremental remapping scheme. CICE also comes with the option of using an upwind transport scheme (Smolarkiewicz, 1996). The incremental remapping scheme has the advantage of being more efficient for multicategory models and conserves tracers (Lipscomb and Hunke, 2004).

The thermodynamic growth and melt described by f are computed by Icepack, which is developed separately by the CICE consortium and can also be run as a standalone 1-D sea ice model (Hunke et al., 2021b). Icepack computes the thickness distribution based on the number of categories listed in table 2.1. In this study, the lower bounds defined by the World Meteorological Organization (WMO) for five sea ice categories are used.

The thermodynamic formulation of this study is the mushy layer theory option (Turner et al., 2013), which allows for brine drainage and the calculation of ice ages.

The dynamics of sea ice is described in CICE by:

$$M \frac{\partial \vec{u}}{\partial t} = \nabla \sigma + \vec{\tau}_a + \vec{\tau}_w + \vec{\tau}_b - \vec{k} \times M f_c \vec{u} - M g \nabla H_0 \tag{2.6}$$

Here, M is the combined mass of ice and snow per unit area. The first term on the right-hand side in equation 2.6 is the divergence of the internal stress (σ). To calculate

Table 2.1: Sea ice categories (*cat*) bounds following the WMO definition for sea ice models with 5 categories.

category *cat*	upper bound
1	0.3 m
2	0.7 m
3	1.2 m
4	2.0 m
5	∞

this term, an Elastic-Viscous-Plastic (EVP) rheology is used, which assumes an elliptic yield curve (Hunke and Dukowicz, 1997). The second and third terms are the stresses from atmosphere and ocean ($\vec{\tau}_{a,w}$). They are calculated as follows:

$$\vec{\tau}_{a,w} = \rho_{a,w} C_{a,w} \|\vec{U}_{a,w} - \vec{U}_i\|^2 \tag{2.7}$$

Here $\rho_{a,w}$ is the air or water density, C_a and C_w the air or ocean drag coefficient and $\vec{U}_{a,w}$ the atmosphere and ocean velocity and $\vec{U}_i$ the ice velocity. The ocean and air densities are constants, the atmosphere and ocean velocities are boundary conditions and the ice velocity is calculated by CICE itself. The drag coefficients are by default in CICE set to constant values. Tsamados et al. (2014) argue that with thinning ice in the Arctic, the ice pack has become more mobile and the surface rougher, thus a constant drag coefficient is not sufficient anymore. They suggest using a variable drag coefficient. This is the form drag parametrization, which is calculated with dependencies on the surface type as follows:

$$C_a = C_f + C_r + C_s + C_{mp} \tag{2.8}$$

$$C_w = C_f + C_r + C_s \tag{2.9}$$

Here C_f is the drag associated with the ice flow edges or FB, C_r the drag component introduced by the sail or keel of the ice flow, C_s is the contribution from the ice flow surface skin and C_{mp} the contribution from the melt pond edges, which is only relevant for the atmospheric drag. This formulation allows the drag coefficient to vary in time and space and is the formulation used in this study.

The fourth term in equation 2.6 is the seabed stress. The seabed stress depends on the SIT. The fifth and the sixth term of equation 2.6 are the Coriolis term and the sea surface slope. Here $\vec{k}$ is the unit vector, f_c the Coriolis term, $\vec{u}$ the velocity field, g the gravitational acceleration, τ_b the basal stress and ∇H_0 the surface slope.

2.2 Model Setup

This section describes the model configurations used in all included studies (Sievers et al., 2022, 2023a,b).

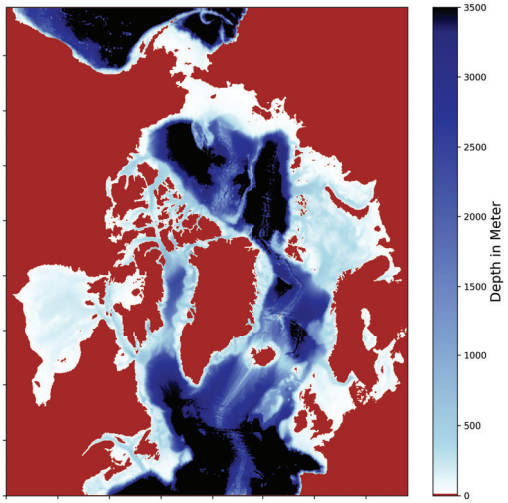

Fig. 2.2: Model domain bathymetry

The model domain is the 10 x 10 km pan Arctic domain displayed in figure 2.2. The grid was adapted by Hordoir et al. (2022) and originates from Bentsen et al. (1999). Both the ocean and the ice model run with a 600-second time step, and they exchange information at every time step. The NEMO ocean setup follows Hordoir et al. (2022) except for adjustments required for a change of version from NEMO3.6 to NEMO4 into account (for more technical details, see section 4).

All forcing and boundary conditions are handled by NEMO. At the lateral boundaries, the model is forced by monthly temperature, salinity, sea surface height and velocity fields from the Global Ocean Physics Reanalysis (GLORYS) (Lellouche et al., 2021). The atmospheric forcing is from ECMWF Reanalysis v5 (ERA5) (Hersbach et al., 2017), which has a frequency of three hours. The ERA5 fields used are 2-m temperature, 2-m specific humidity, 10-m winds components, incoming short and long wave radiation, total precipitation, snowfall and sea level pressure. The river run-off consists of a monthly climatology from Day et al. (2014). Tidal forcing at the boundaries is provided by TPXO 7.2 harmonic tidal constituents (Egbert and Erofeeva, 2002). The CICE runs included in this thesis are:

- BGrun: running from 1995-2020, ocean initialised from temperature and salinity fields from Ocean Reanalysis System 5 (ORAS5) Zuo et al. (2019), ice initialised depending on sea surface temperate and latitude. The run was utilised to calculate the Kalman filter background error in Sievers et al. (2023a) and the model values in Sievers et al. (2023a).

Model Option	
Time step	600 s
Ice categories	5
Ice layers	7
Snow layers	1
wind-ice drag	form drag (Tsamados et al., 2014)
ocean-ice drag	form drag (Tsamados et al., 2014)
dynamics solver	EVP (Hibler, 1979)
land fast ice	yes
melt ponds	yes
ridging/rafting	yes
heat diffusion in ice	mushy layer (Feltham et al., 2006)
Albedo	delta Eddington (Joseph et al., 1976)
Sea ice salinity	mushy layer (Feltham et al., 2006)

Table 2.2: CICE settings of all model runs

- refRun: subset of model run BGrun from 2018-01-01 to 2020-01-01. The run was used in Sievers et al. (2023a).
- sicRun: running from 2018-2020, restarted from BGrun restart files at 2018-01-01, assimilating SIC. The run was used in Sievers et al. (2023a).
- fbRun: running from 2018-2020, restarted from BGrun restart files at 2018-01-01, assimilating both FB and SIC. The run was used in Sievers et al. (2023a).
- CICEref: running from 2007-01-09 to 2020-01-09, ocean initialised from temperature and salinity fields from Ocean Reanalysis System 5 (ORAS5) Zuo et al. (2019), ice and snow also initialised from the ORAS5. The run was used in the model intercomparison study in Sievers et al. (2022).
- CICEtN: same as CICEref, but only running from 2007-01-09 to 2010-01-09 and with SST calculated following Commission et al. (2015). Discussed in Chapter 3 to 5.
- CICEfd: same as CICEref, but only running from 2007-01-09 to 2010-01-09 with constant drag coefficients instead of Tsamados et al. (2014) form drag formulation. Discussed in Chapter 3 to 5.
- CICEs: same as CICEref, but only running from 2007-01-09 to 2010-01-09, with the original snow forcing increased by 1.22 times. Discussed in Chapter 3 to 5.

All simulations ran with the CICE settings discussed in section 2.1. An overview of the CICE settings is also listed in table 2.2.

In Sievers et al. (2022) and Chapter 3, additional model runs from a different sea ice model are included. These runs originate from the NEMO default sea ice model Sea Ice Modelling Integrated Initiative (SI3). Sievers et al. (2022) compares these model runs to the above-mentioned CICE runs. SI^3 was developed as a combination of the three most commonly run sea ice models with NEMO: CICE (Hunke et al., 2017), Louvain-La-Neuve sea ice model (LIM) (Rousset et al., 2015) and (GELATO) (Salas Mélia, 2002). Many of the fundamental assumptions are similar to the ones taken in CICE. A detailed description of the SI^3 setup would exceed the scope of this thesis. For further details on these runs, please see Sievers et al. (2022) or Vancoppenolle et al. (2023) for further details on the model and table 3.1 for differences between CICEref and SI3ref. Since these runs are, however, discussed in Chapter 3 a list of the relevant runs and their differences follows:

- SI3ref: running from 2007-01-09 to 2020-01-09, ocean initialised from temperature and salinity fields from (ORAS5) Zuo et al. (2019), ice and snow also initialised from the ORAS5. See also table 3.1 in chapter 3.
- SI3nb: as SI3ref, but without reduction of snow, by blowing snow parameterisation.
- SI3fd: as SI3ref, but with constant form drag parameters identical to CICEfd.

3 Data Assimilation

Data assimilation in geoscience originates from numerical weather prediction, but it is also used in other geophysical modelling applications, including sea ice forecasts and hindcasts (Chen et al., 2017b; Mu et al., 2018; Shu et al., 2021; Yang et al., 2020). It is used in reanalysis to derive the optimal state of a system based on both observations and models, as well as their uncertainties. The three most used assimilation methods are nudging, variational methods and Kalman filtering.

The difference between a nudging scheme and the Kalman Filter is that the Kalman Filter takes both the model and the observation error into account. The difference between the Kalman Filter and the variational approaches is that the model errors evolve over time in the Kalman Filter and that the Kalman Filter is simpler to implement because no tangent linear model or adjoint model is needed. The variational approach is more physically consistent than the Kalman Filter, which constrains its solution by mean and variance, but not physical dependence (Wang et al., 2023). This work uses a Kalman Filter-based algorithm.

3.1 Sea Ice Assimilation

There are several studies that have assimilated sea ice variables into an ocean sea ice model with an EnKF prior to the work presented here. Many of these systems are multivariate, meaning that their state vector $\mathbf{x}$ consists of several model state variables, of which not all necessarily need to be observed. Which variables are in the state vector differs. Mu et al. (2020) state vector consists of SIC, SIT, sea ice drift, and temperature and salinity in the mixed layer, Lisæter et al. (2003) state vector consists of the ocean variables: salinity, temperature, layer thickness, velocities, barotropic velocity and barotropic pressure, and for the ice of SIC and SIT, Mathiot et al. (2012) state vector consists of all ocean and ice model state variables plus snow freeboard except ice temperature and heat content, Liang et al. (2019) state vector consists of sea surface temperature and SIC and SIT; and Yang et al. (2014) state vector consists of SIT and SIC. The state vector in the current thesis only consists of either FB or SIC. The multivariate approach of the studies above is often preferred because variables that are physically dependent on another are updated simultaneously through cross co-variances. Particularly, upper ocean temperature and the sea ice edge have been found to be strongly correlated (Lisæter et al., 2003; Yang et al., 2014). The FB assimilation study of Mathiot et al. (2012), assimilating snow FB from ICESat, used the cross correlations between snow FB to update the model SIT without directly observing it.

The aim of the current work is to understand the relationship between the FB and SIT. Therefore, the approach that Mathiot et al. (2012) followed was not applied. Rather, the Kalman Filter is used as a tool to derive the best estimate of FB and investigate its physical relationship with the model SIT. The derived modelled radar FB could, however, in the future be used as an observation operator in a multivariate system. An example of an observation operator to assimilate lower level satellite observation is the brightness temperature observation operator developed in Burgard et al. (2020) to improve SIC.

3.2 Kalman Filter

A Kalman filter is a sequential assimilation method, which means that a sequence of steps is repeated in order to estimate the model state and error development. The sequential steps of the Kalman filter are:

- an initialisation of the model (only done in the first step)
- a forecast of the model ($\mathbf{x}^f$)
- an analysis in which the model state and observations ($\mathbf{y}^o$) including their errors are analysed to calculate the optimal state ($\mathbf{x}^a(t_i)$)
- model correction towards the found optimal state and the sequel is repeated

In the analysing step, the best estimate is calculated based on the assumption that the assimilated data is Gaussian distributed and therefore can be described by their mean and variance, and that the model and observation errors are unbiased and uncorrelated (Wang et al., 2023). The optimal state is found by solving the following (Evensen, 1994):

$$\mathbf{x}^a(t_i) = \mathbf{x}^f(t_i) + \mathbf{K}_i(\mathbf{y}_i^o - \mathbf{H}_i\mathbf{x}^f(t_i)) \tag{2.10}$$

$\mathbf{H}$ is the observation operator mapping the observations on the model field and $\mathbf{K}$ is the Kalman gain calculated as follows:

$$\mathbf{K}_i = \mathbf{P}^f(t_i)\mathbf{H}_i^T(\mathbf{H}_i\mathbf{P}^f(t_i)\mathbf{H}_i^T + \mathbf{R}_i)^{-1} \tag{2.11}$$

Where $\mathbf{R}_i$ is the observation error covariance matrix and $\mathbf{P}_i^f$ the covariance matrix of the model ensemble error.

In this study, an adaption of the EnKF is used. The EnKF first introduced by Evensen (1994) is a variation of the extended Kalman filter (Kalman and Bucy, 1961). The difference between the extended Kalman filter and the EnKF is that the extended Kalman filter integrates the error covariance matrix, while the EnKF uses a Monte Carlo approach. Evensen (1994) showed that it is more efficient and more stable to use a Monte Carlo approach to calculate the error covariance for large non-linear systems such as, for example, ocean models. This approach is based on the assumption that the error covariance of the forecast model state can be described by the mean and covariance of an ensemble of model forecasts.

The Monte Carlo approach here is that $\mathbf{P}_i^f$ is not explicitly solved but calculated from the covariance matrix of an ensemble of models, which are all run over a forecast time t. The mean model state ($\bar{\mathbf{x}}_i$) is given by the mean of the ensemble of N members:

$$\bar{\mathbf{x}}_i = \frac{1}{N}\sum_{h=1}^{N}\mathbf{x}_i^h \tag{2.12}$$

The state error covariance matrix can be calculated from the ensemble members as follows:

$$\mathbf{P}_i = \frac{1}{N-1}(\mathbf{x}_i - \bar{\mathbf{x}}_i)(\mathbf{x}_i - \bar{\mathbf{x}}_i)^T \tag{2.13}$$

In this setup, $\mathbf{x}_i \in \mathbb{R}^{n\times N}$ is a matrix containing the ensemble of size N of model states of size n and $\mathbf{P}_i \in \mathbb{R}^{n\times n}$ is the model background error. In the EnKF, the dimensions of the other terms in equation 2.11 are: $\mathbf{R}_i \in \mathbb{R}^{m\times m}$, with m being the number of observations and $\mathbf{H}_i \in \mathbb{R}^{m\times n}$.

This study assumes that the ensemble can be approximated by inter-annual variability. $\mathbf{P}_i^f$ consists of historical fields from a pre-run model experiment (BGrun). This means that the assimilation in principle is not an EnKF. The background error covariance matrix, though, is calculated based on the same assumptions, namely that variability in the model reflects its error. In this case, the inter-annual variability is used instead

of perturbed forcing introduced variability (Cheng et al., 2023). The EnKF uses several model realisations to forecast the mean state and calculates the model background error from the variance of the different runs; likewise, the increment is applied to all model runs in the ensemble. In the approach presented here, the model background is calculated from the inter-annual variability around the date of the forecast. Only one model realisation is run and updated with the increment. The approach is significantly less computationally expensive but does not reflect the time evolving error of the model.

For a model of the dimensions used in this study (n=693528, N=80, m<693528), the full matrix of $\mathbf{K}_i$ would still be too large to be calculated. This is a common problem, and it can be solved in a multitude of ways (Hunt et al., 2007; Nerger et al., 2012; Pham, 2001), the detailed description of which exceeds the scope of this work. In this study, the Parallel Data Assimilation Framework (PDAF) Local Error Subspace Transform Kalman Filter (LESTKF) (Nerger et al., 2012) has been used to solve equation 2.10. PDAF is a FORTRAN-based software package including a collection of different Kalman filter solutions for geophysical models. It has been used successfully in the past to assimilate sea ice by, for example, Shu et al. (2021), Yang et al. (2020) and Mu et al. (2018). The strategy for the LESTKF computational implementation is described in Nerger and Hiller (2013). PDAF has different implementation strategies. The steps taken to implement it are described in the following paragraph.

3.3 PDAF Implementation

Several implementation strategies are supported by PDAF. Here the parallelised offline version was chosen. This terminology follows the PDAF implementation guide (Nerger, 2024). In the offline coupling, the model is first run and stopped, and then the SIC and FB states are written to files, which are then read by PDAF to calculate the error covariance matrix of the model state. To do so, the model ensemble from the BGrun is read. The observations and associated errors are also read and have prior to this step been interpolated onto the model grid. To calculate equations 2.10 and 2.11, the model and files are converted into 1-D arrays.

To ensure that the model state and observations are cohesive, the observation operator $\mathbf{H}$ was introduced. $\mathbf{H}$ is an array containing 1 where observations exist and 0 where no observations exist. While the observation array $\mathbf{y}_i$ is smaller than the model state $\mathbf{x}_i$, $\mathbf{H}$ has the same dimensions as the model state and maps $\mathbf{y}_i$ onto $\mathbf{x}_i$.

To reduce computation costs, the ensemble only has one member that is updated with the analysed field and $\mathbf{x}_i^h$ is calculated from snapshots from the BGrun. The ensemble used to calculate the model error covariance matrix in equation 2.13 is calculated from an ensemble of pre run model states ($\mathbf{x}_m^h$). This method has been used by, for example, Aubert and Fournier (2011). The ensemble is calculated as follows:

$$\mathbf{x}_i^h = \mathbf{x}_m^h - \bar{\mathbf{x}}_m + \mathbf{x}_{ms} \tag{2.14}$$

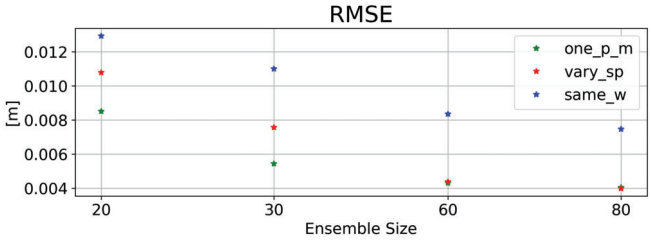

Fig. 2.3: RMSE between one week forecast and observations for three different ensemble compositions. The three different ensemble compositions are listed below.

$\bar{\mathbf{x}}_m$ is the mean pre run model states, $\mathbf{x}_m^h$ one single member of the pre run model states and $\mathbf{x}_{ms}$ the model state from the assimilation run. From the BGrun, it was known that the model overestimates the ice edge. This is also discussed in Sievers et al. (2022). To take this bias into consideration when creating the ensemble, the different configurations of the ensemble were tested. In figure 2.3, the root-mean-square error (RMSE) between the FB forecast and observations for three different constructions of the ensemble are shown for four different ensemble sizes. The three ensembles are constructed as follows:

- one_p_m: the members $\mathbf{x}_m^h$ are taken from all different months throughout the 20 years of pre run.
- vary_sp: $\frac{2}{3}$ of the ensembles are taken from the same date as the current assimilation step, $\frac{1}{6}$ from two months before and $\frac{1}{6}$ from two months after the current assimilation step.
- same_w: all members $\mathbf{x}_m^h$ were taken from the same day as the current assimilation step. For the ensembles with a larger seize than the years available, the following and prior days were chosen.

Figure 2.3 shows the smallest errors for 60 and 80 ensemble members for the one_p_m and vary_sp option. one_p_m and vary_sp were introduced to increase the ensemble spread, by taking more model states into account than those that reflect the inter-annual variability (same_w). This was done, as mentioned above, to account for known biases. For the final assimilation setup, vary_sp was chosen to ensure that the ensemble spread used to calculate the model error is not so large that it would lead to an overestimation of the model error.

The filter used is the Local Error Subspace Transform Kalman Filter (LESTKF) (Nerger et al., 2012). The localisation refers to the fact that the filter only takes observations in a certain radius into account. The impact from the observations on the model location is weighted depending on the distance between the observation and the current model location. In figure 2.4, the RMSE between one week forecast and observations

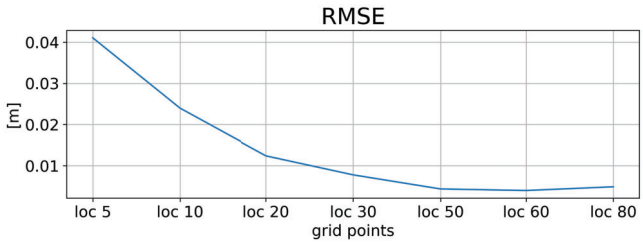

Fig. 2.4: RMSE between one week forecast and observations for different localisation radii in grid points.

for different localisation radii is shown. The radius is given in grid cells between five and 80. The lowest error is shown for 60 grid cells, which is also the localisation radius the with which the assimilation was run.

3.4 Assimilation Setup

The previous sections of this chapter described the individual components of the full assimilating system. This section describes how the components are tied together, as illustrated by figure 2.5.

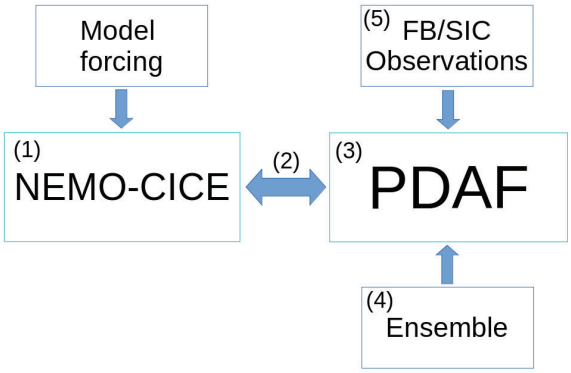

Fig. 2.5: Schematic overview of the assimilation system. The smaller blue boxes (4 and 5) indicate inputs, the larger turquoise boxes separately executed programs and the blue arrows file exchange. The numbers are used to link the graph with the description in section 3.4.

The numbers below are references to figure 2.5. The assimilation cycles are seven days. The run starts with one week of forecast based on the NEMO-CICE (1) setup described in chapter 2, section 2.2. This run is initialised with restart files from the

BGrun. At the end of the assimilation cycle, weekly means of SIC and FB are written to file (2) as well as the ocean and sea ice restart files. Then the filtering step by PDAF (3) is performed as described in chapter 2 section 3 and 3.3. The filter uses the weekly means of SIC and FB as well as the ensemble files (4) and the observations (5) as input. All input files are provided on the model grid. The ensemble (4) was created as described in chapter 2, section 3.3 by the vary_sp method.

The observations (5) are weekly averages of SIC and FB covering the same week as the model was run during the forecast step. The assimilated SIC data is the OSISAF OSI-430-a SIC described in chapter 2, section 1.1. The assimilated FB data was introduced at the end of chapter 2, section 1.3 and will be referred to as AWI FB in the following chapters. The AWI FB comes in weekly averages, the OSISAF SIC is averaged over the current week at assimilation time. PDAF is run twice, once for FB, and once for SIC, to avoid unrealistic cross correlations. In a test with a state vector containing both FB and SIT, unrealistic FB changes appeared in central Arctic regions. The resulting increments are written to two separate files as part of the offline PDAF-model coupling (2). The model is restarted from the ocean and ice restart files. Right after the initialisation, the increment is read in to the model (1) and applied as described in section 4.2. The assimilation is run November to March, whereas the model runs free from April to October due to lack of observations. Sievers et al. (2023a) provide further details on the assimilation routine described in this chapter and the resulting SIT.

4 Model Development and Coupling

This section describes the modifications to the original model code, which are needed to perform the studies included in this thesis. First the coupling of the ocean model NEMO and the sea ice model CICE is described (section 4.1), and next all subroutines needed for the FB assimilation and their functions (section 4.2). This section is intended to act as a reference for technical details.

4.1 Coupling CICE and NEMO

The coupling of NEMO and CICE in this thesis is based on previous coupled systems with earlier versions of the same models. The previous system from the Environment and Climate Change Canada (ECCC) is based on NEMO3.6-CICE4 and described in Smith et al. (2021). The general strategy of the coupling is to compile both models in one executable and call CICE as a submodule of NEMO.

The coupled models are parallelised. The distribution and communication are done with the help of the FORTRAN Message Passing Interface (MPI). Each of the two model components has its own strategy on how to distribute the domain to the processors. Figure 2.6 shows a schematic example of the model domain with the two different MPI distributions. At each coupling step, the fields must be communicated from one model's

local distribution to global fields and back to the other model's local distribution. This is known to be a bottleneck as this is not a parallel process.

To update the coupled system to NEMO4 and CICE6.2 two system updates had to be considered: all Icepack modules and some variables from CICE4 to CICE6.2 had changed names and NEMO4 included an updated MPI processor distribution strategy. Changing the names of routines and variables from CICE4 to CICE6.2 was straightforward. To account for the changes in the MPI routines of NEMO4, the indexing in the routines that collect the CICE decomposition, shown in figure 2.6, to the global domain and on to the NEMO domain, had to be adjusted.

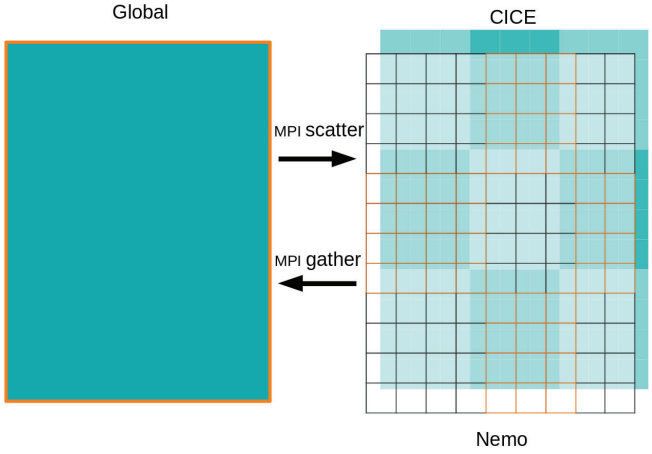

Fig. 2.6: MPI decomposition of CICE and NEMO. The MPI decomposition of CICE is schematically indicated by filled turquoise boxes, and the MPI decomposition of NEMO by transparent black and orange outlined boxes.

In addition, the freeze and melt potential was updated according to changes described in Ponsoni et al. (2023). The freezing point of the ocean and melt temperature of ocean/ice is a function of the salinity. Seawater is typically significantly more saline than sea ice, and therefore it has a lower freezing point than the melt point of sea ice. The freeze and melt potential ($fmpot$), which determines how much ice potentially can freeze or melt, depends on the freezing point temperature of the ocean and the melt point temperature of sea ice. The new formulation of the freeze and melt potential is

defined in equation 2.15.

$$fmpot = \begin{cases} \dfrac{\rho_w cp_O H_{0_w}(TI_{melt} - SST)}{2\Delta t}, & \text{if } TI_{melt} > TO_{freez} \text{ and } SST > TO_{freez}. \\ 0, & \text{if } TI_{melt} > TO_{freez} \text{ and } SST > TO_{freez} \\ & \text{and } TI_{melt} <= SST. \\ \dfrac{\rho_w cp_O H_{0_w}(TO_{freez} - SST)}{2\Delta t}, & \text{else.} \end{cases} \tag{2.15}$$

Here ρ_w is the water density, cp_O is the ocean heat capacity, H_{0_w} is the ocean surface layer thickness, SST is the sea surface temperature and Δt is the ocean model time step. The only thermodynamic option where the salinity of sea ice is the mushy layer theory option (Turner et al., 2013). In the original formulation, both the freezing point temperature and the melt point temperature were based on the ocean salinity.

With the original calculation of $fmpot$, ice was melted as soon as the surface temperature is above the freezing point, no matter what the melting point of the ice is. Ponsoni et al. (2023) found that this leads to too high amount of melt in warm waters (personal communication with M. Hvid Ribergaard).

4.2 CICE Development

This section describes the development of CICE. All subroutines added to CICE as part of this thesis and their purpose are listed in table 2.3. In the following text, namelist parameters are written in italics, and subroutine and module names in quotation marks.

The comparison of CICE and SI^3 required an option to start CICE from initial conditions. The added routine was used in (Sievers et al., 2022). The option to start CICE from initial files is set in the namelist with the option *ice_data_type*; additionally, the name of the file name of the initial condition is set there. The fields used are: SIC, SIT and snow thickness. The fields need to be on the model grid and have one value per grid cell. The values are distributed to the categories in 'ice_init'. The fields are read-in in a new CICE routine 'isc_from_file' which is called in the CICE routine 'ice_init'. At each grid cell, the input variables are put into one category only, see equation 2.16.

$$SIT_{cat}, Hs_{cat}, SIC_{cat} = \begin{cases} SIT_i, Hs_i, SIC_i, & \text{if } SIT_i > SIT_b(cat-1) \text{ and } SIT_i < SIT_b(cat). \\ 0, & \text{else.} \end{cases} \tag{2.16}$$

Here SIT_i, Hs_i and SIC_i is the SIT, snow thickness and SIC from the initial files, SIT_{cat}, Hs_{cat} and SIC_{cat} the SIT, snow thickness and SIC in category cat and SIT_b the categories upper SIT bound.

Table 2.3: Modified and added model routines, their purpose and the studies in which they were used.

new subroutines	purpose	used in
'isc_from_file'	read in sea ice initial conditions for snow thickness, SIT and SIC	Sievers et al. (2022)
'read_inc'	read in routine for the FB and SIC increment files	Sievers et al. (2023a)
'do_fb_assim'	routine determining if conditions allow for FB assimilation	Sievers et al. (2023a)
'ice_fb_radar'	module calculating radar FB, ρ_i and SIT from radar FB	Sievers et al. (2023a,a)
'rfb_inout'	routine included in 'ice_fb_radar' calculating radar FB	Sievers et al. (2023a)
existing subroutines	purpose of addition	used in
'ice_init'	An additional option for the name list parameter *ice_data_type* was added to allow for restart from file.	Sievers et al. (2022)
'ice_relaxcon'	This routine was introduced by Rasmussen et al. (2018) for the DMI nudging scheme. All routines for the FB assimilation are called from here.	Sievers et al. (2023a)

The assimilation required that several new variables be introduced. These are sea ice density, radar FB and snow density. In addition, several new routines are introduced to perform the assimilation discussed in chapter 2, section 3.

In the following paragraphs, the separate subroutines (table 2.3) that were introduced to perform the FB assimilation will be described (the yellow squares in figure 2.7). All steps necessary for the assimilation will be discussed in the order indicated by figure 2.7 in the following paragraphs.

The subroutine called 'read_inc' reads the increment calculated in the Kalman filter described in chapter 2 section 3. The increment is the change of one variable that needs to be added to the model state in order to be equal to the optimal state estimate from the Kalman filter. To avoid chock, the increments are linearly spread over the time of the assimilation cycle of one week. This method was introduced by Bloom et al. (1996) and called incremental analysis updating. This means if data is assimilated each week, the variable is read in at the first time step of assimilation period (t_0) and divided by

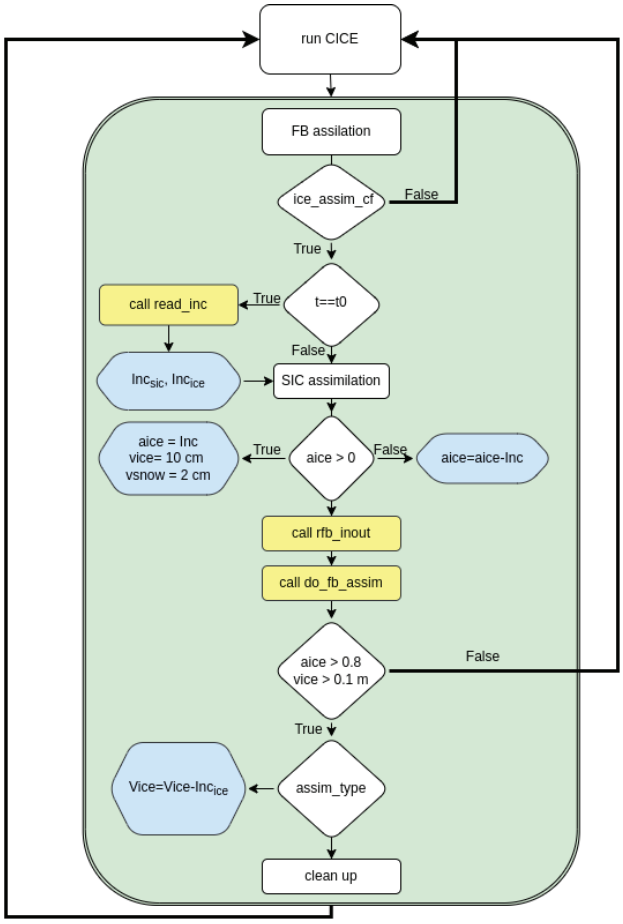

Fig. 2.7: Flow chart of assimilation implemented in CICE. Green background marks existing routines that were extended, and yellow background marks routines subroutine calls within new (white square) routines. The white rhombuses mark conditional statements, squares subroutines and blue hexagons changes to the model state.

the number of time steps the model runs per week.

Since incremental increment sounds repetitive, it will be referred to as a fractal increment in this study. The fractal increments calculated are the SIC fractal increment $IncF_{sic}$ and the SIT fractal increment $IncF_{sit}$. To calculate $IncF_{sic}$, the SIC increment

is divided by the number of time steps N_t, as follows:

$$IncF_{sic} = \frac{Inc_{sic}}{N_t} \tag{2.17}$$

To calculate Inc_{ice}, the FB increment is read, and then it is subtracted from the model radar FB. This new FB is converted into ice thickness by the subroutine 'rfb_inout'. This ice thickness is subtracted from the ice thickness at t_0 and the resulting SIT increment is divided by the number of time steps to get the fractal increment $IncF_{sit}$. The step of converting the FB into ice thickness has to be done at t_0. If it were not done at t_0, the snow thickness, sea ice density or water density might change and result in an inconsistent calculation of SIT, when FB increments are converted to SIT increments.

The calculation of the fractal SIT increment at t_0 ensures that the change in SIT are related to the results from the Kalman filter analysis step. To calculate the SIT increment, the ratio of the FB increment Inc_{FB} to the old FB (FB_0) is calculated, and the current SIT is multiplied by it (equation 2.18).

$$IncF_{sit} = SIT\frac{Inc_{FB}}{FB_0}\frac{1}{N_t} \tag{2.18}$$

This approach assumes that all changes in FB thickness are caused by SIT changes.

After the increments have been read and the fractal increments $IncF_{sit}$ and $IncF_{sic}$ are calculated, the assimilation routine continues with applying $IncF_{sic}$ at each time step. This is done in two different ways, depending on whether ice exists in the current grid cell. If ice already exists, SIC in all five categories is changed according to:

$$SIC(cat) = SIC_0(cat) - SIC_0(cat)\frac{IncF_{sic}}{SIC_0} \tag{2.19}$$

Here *cat* refers to the SIT categories from table 2.1 and SIC_0 the SIC prior to the assimilation. If there was no ice prior to the assimilation, new sea ice is created. The new SIC is equal to $IncF_{sic}$, the SIT to 0.1 m and the snow to 0.02 m, and the ice and snow enthalpy is calculated according to Turner and Hunke (2015).

In preparation for the FB assimilation, the radar FB is calculated by combining equation 2.1 and 2.4 to:

$$FB_r = \frac{SIT(\rho_w - \rho_i) - H_s\rho_s}{\rho_w} - H_s(\frac{c}{c_s} - 1) \tag{2.20}$$

The variables SIT, H_s and ρ_w are defined in the model, c_s is defined in equation 2.2 and c is constant as defined in section 1.3. ρ_s and ρ_i are constant in the original CICE code. Initial experiments showed that space and time dependent ρ_i and ρ_s values were necessary to yield realistic results. To simulate the seasonal variability of ρ_s, Mallett et al. (2020) was followed:

$$\rho_s = 6.5t_m + 274.51 \tag{2.21}$$

with t_m the time in month linearly increasing from 0 on the first of October to 6 at the 30th of April. ρ_i is calculated as follows:

$$\rho_i = a_b \rho_b + (1. - a_b)\rho_{fresh} \tag{2.22}$$

Here a_b is the brine content of the ice, ρ_b the density of the brine and ρ_{fresh} the density of fresh ice. ρ_{fresh} was set to 882 kg/m^3, which is the value typically used for MYI in conventional CryoSat-2-derived SIT following Alexandrov et al. (2010). As an upper bound for the sea ice density, the water density was set. The evaluation of the resulting ice densities will be discussed in chapter 4.

The subroutine 'do_fb_assim' consists of two options to check whether the FB assimilation should be carried out or not. The FB increment is only applied if model SIC is above 0.8 and SIT above 0.1 m. These thresholds were chosen to ensure stability. However, they also have a physical motivation. The threshold of 0.1 m SIT was chosen because CryoSat-2 was specifically designed to measure thick sea ice and is less accurate in thin ice areas (Wingham et al., 2006). The threshold of 80% SIC was chosen because the CryoSat-2 backscatter from open water is stronger than from sea ice, which makes it difficult to distinguish leads from ice floes at low SIC.

The *assim_type* parameter was introduced to test different ways of applying the FB increment. Currently, only one of these options runs stable and gives realistic results. The option that runs stable and gives realistic results is $assim\_type == 3$. This option is based on the assumption that the correction for the increments is only caused by SIT differences, and its results will be discussed in chapter 4. The other options tested were one based on the assumption that the FB increment carries information about both the SIT change and snow thickness change, and another distributing the ice into the thickness categories following Gupta et al. (2021). Neither run stable and so were not further developed due to a lack of time.

The ice thickness is now calculated from the $IncF_{ice}$, similar to equation 2.19:

$$SIT(cat) = SIT_0(cat) - SIT_0(cat)\frac{IncF_{ice}}{SIT_0} \tag{2.23}$$

Here SIT_0 is the SIT prior to the assimilation, $SIT(cat)$ the SIT depending on the category (thickness categories in table 2.1) and $SIT_0(cat)$ the SIT prior to the assimilation depending on the category prior to the assimilation. As a last step, the routine 'cleanup_itd' is run to re-bin the ice into their correct thickness categories.

Chapter 3

Summary of Papers

This thesis is a collection of papers. The papers considered in this study are:

- Paper 1: Sievers, I., Rasmussen, T. A., and Stenseng, L. (2023). Assimilating CryoSat-2 freeboard to improve arctic sea ice thickness estimates. The Cryosphere, 17(9):3721–3738.
- Paper 2: Sievers, I., Skourup, H., and Rasmussen, T. A. S. (2023b). Impact assessment of snow thickness, sea ice density and water density in CryoSat-2 derived sea ice thickness. The Cryosphere Discussions, 2023:1–25.
- Paper 3: Sievers, I., Gierisch, A. M., Rasmussen, T. A., Hordoir, R., and Stenseng, L. (2022). Arctic sea ice and snow from different ice models: A CICE–SI^3 intercomparison study. The Cryosphere Discussions, pages 1–34.

The overall aim of the thesis is to improve our understanding of Arctic sea ice thickness by investigating the relationship between FB and SIT from CryoSat-2 and sea ice models. The following section summarises the included studies and highlights their link to the overall topic. Additional discussions are found in chapter 4.

Paper 1 is published, Paper 2 is under review and Paper 3 has been in review but was withdrawn. The main reason to withdraw Paper 3 was that one central requirement of the reviewers could not be met. The requirement was to set up a base model run in which both models perform similarly. A substantial effort to tune the models to provide similar results while avoiding downgrading their results was unsuccessful, which motivated the withdrawal. The results of the tuning are presented in the work in section 3.1 of this chapter. The latest versions of the papers can be found in the appendix.

1 Paper 1: Assimilating CryoSat-2 Freeboard to Improve Arctic Sea Ice Thickness Estimates

Paper 1 introduces the assimilation described in section 3.4 and evaluates the results in three steps against in-situ observations and classical-derived SIT from CryoSat-2. The runs discussed in Paper 1 are the runs fbRun, refRun and sicRun introduced in section 2.2.

First, the fbRun's and refRun's FB were compared to the assimilated FB, in order to demonstrate that the assimilation works. Comparing the AWI FB (the assimilated FB) and the fbRun's FB showed that the assimilated FB is closer to the AWI FB than the refRun FB. This demonstrates that the assimilation works as expected.

Secondly, the fbRun's and refRun's SIT were compared to the classically-derived SIT. The classical derived SIT from CryoSat-2 is the SIT included in the weekly AWI data (Hendricks et al., 2021), which was introduced as one of the CryoSat-2 SIT data products mentioned in section 1.3. This comparison showed that the fbRun's SIT is closer to the AWI SIT than the refRun's SIT. The AWI SIT is, however, not independent of the fbRun SIT, since the fbRun includes assimilated FB from the same data set as the AWI SIT is based upon.

Third, the refRun and the fbRun SIT are compared to independent in-situ observations from the Beaufort Gyre Exploration Project (BGEP) and the Multidisciplinary drifting Observatory for the Study of Arctic Climate (MOSAiC) expedition. BGEP are sea ice draft measurements and the SIT measurements from MOSAiC are based on Ice Mass Balance buoys (Lei et al., 2021). In the Beaufort Gyre, the fbRun SIT is clearly closer to the observations than the refRun SIT. In the MOSAiC locations, however, the refRun and the sicRun are close to the observations, while the fbRun SIT differs significantly from the observations. Paper 1 links the overestimation of the FB, and resulting SIT overestimation in the fbRun, to the assimilated AWI FB data. Paper 1 shows that both the AWI SIT and the fbRun SIT compare equally well to the BGEP in-situ observations and that the fbRun SIT compares significantly better to the MOSAiC observations.

2 Paper 2: Impact Assessment of Snow Thickness, Sea Ice Density and Water Density in CryoSat-2 Derived Sea Ice Thickness

The assimilation method presented in Paper 1 converts the assimilated FB to SIT under the same assumptions as the classical approach but it uses model values instead of empirical and climatological values. The model output is from the BGrun that did not include data assimilation. The objectives of Paper 2 are to (1) compare the snow

thickness, sea ice density and water density from the model and those from a CryoSat-2 SIT product to independent observations, (2) present alternative model values were needed and (3) assess to how much SIT difference using the model values instead of the CryoSat-2 product values leads.

The Altimetric Snow Depth (ASD) from Garnier et al. (2021) is used to evaluate the snow thickness. Overall, the validation shows that the model snow thickness compares better to ASD snow thickness than the AWI snow thickness compares to the ASD snow thickness. There is a regional and seasonal variability in the comparison. In the Canadian Arctic in early winter, the model has too thin snow compared to ASD, while the modelled snow in late winter in all regions is thicker than the ASD snow.

The sea ice density is evaluated with airborne sea ice density measurements from Jutila et al. (2022) and sea ice densities from ice cores from the MOSAiC expedition (Oggier et al., 2023a,b). The model sea ice density is closer to the Jutila et al. (2022) sea ice density than the AWI sea ice density is. For the MOSAiC sea ice density, the AWI sea ice density compares better than the model sea ice density.

To create a meaningful SIT comparison, a new model-derived sea ice density is presented, called C6N4$_{J21}$ in the following. This density varies by FYI area, which is a model diagnostic. The derived sea ice density is closer to observations than the original model sea ice density, and overall closer to the observations than the AWI sea ice density is.

The water density is validated against World Ocean Atlas (WOA) (Zweng et al., 2019) derived water density. The water density values from the model compare better to the WOA water density than the single value AWI water density does. The water density leads to the smallest SIT differences of up to 0.33 m between the AWI constant value water density and the modelled water density.

Paper 2 finds that the SIT difference resulting from exchanging the CryoSat-2 values with model values are highest for snow thickness and sea ice density but that their effect overall is lower when all three values are substitute together. The SIT value from the water density is with a maximum of 0.33 m higher than expected, which is why an additional analysis was conducted.

An additional SIT comparison between the WOA and the model and CryoSat-2 water density was conducted. This comparison shows that on average, the constant CryoSat-2 value leads to 0.02 m and the model water density to 0.01 m SIT difference and their maximum differences to 0.13 m and 0.16 m respectively. These differences are small compared to the differences introduced by the snow thickness and the sea ice density, but not negligible, as many classical-derived CryoSat-2 SIT products state (Hendricks et al., 2021; Kurtz et al., 2013; Tilling et al., 2018).

Paper 2 traces back the origin of the water density error estimate to Wadhams et al. (1992) and finds that the variability only account for the seasonal variability of the water density but not for the regional variability. Paper 2 suggests a new error estimate of 2.6 kg/m^3 instead of the commonly used $0.5kg/m^3$. The new error estimate is based

on the standard deviation between the AWI single value and the WOA data.

3 Work in Progress (Paper 3)

As mentioned in the introduction to this chapter, Paper 3 was withdrawn in line with the recommendations of the editor. Based on the recommendations from the reviewers, additional work has been carried out. This section will first summarise the original paper and then present the additional work that was carried out in response to the review.

3.1 Paper 3: Arctic Sea Ice and Snow from Different Ice Models: A CICE–SI^3 Intercomparison Study

Paper 3 compares two sea ice - ocean model setups based on the same grid, coupled to the same ocean model (NEMO), forced by the same atmospheric forcing (Hersbach et al., 2017), boundary conditions (Lellouche et al., 2021) and started from the same initial conditions. The only difference is the sea ice model. The two sea ice models are the NEMO default sea ice model SI^3 and CICE. The aim is to evaluate how the simulations with the two sea ice models differ with a focus on the sea ice and the snow, and to evaluate the coupling of CICE and NEMO described in section 4.1.

The model inter comparison differences were found to be small in comparison to the CMIP6 sea ice component model intercomparison study by Long et al. (2021). The model differences were found to be comparable to a similar regional model intercomparison study comparing CICE and Budgell (Kumar et al., 2021). The main differences in the ice extent were found in the East Greenland Sea, where CICE modelled a larger sea ice extent. The central Arctic showed the biggest difference of snow and sea ice thickness.

The snow thickness differences were unexpected since both models were forced by the same snow fall data. Paper 3 further shows that the snow and sea ice thickness differences are correlated, especially over FYI. This finding led to an analysis of which model settings forced the differences between the two models. Paper 3 attributes the differences in thickness, and extent, to the differences in albedo calculation and drag formulation. Further, Paper 3 concludes that the snow thickness differences are caused by the "blowing snow" parameterisation, which reduces the snow volume in SI^3.

The study finds that the snow and ice volume differences between the models are correlated, in particular typical thin ice areas. The model with the thicker snow layer has the lower ice volume and vice versa. The study only investigated the correlation but not what the correlation's cause.

The main point of criticism from the reviewers was that the models should start from one common reference run in which the model results are close to identical. This comment was made based on the assumption that the models are rather similar, while

in reality, they are somewhat different. An effort was made to tune the models to give similar results, without any success. This was the main reason the paper was withdrawn. Another point of criticism from the reviewers was that the analysis of the differences in model settings should have been tested more. This point will be addressed in the next section.

3.2 Model Differences

The main differences of the runs from Paper 3 are listed in table 3.1. The settings that were further investigated are discussed below. The settings which were investigated in more detail are: the drag formulation, the blowing snow parameterisation and the freezing point. The settings were chosen based on the possibility of unifying the model settings. The drag formulation and the blowing snow parameterisation can be set to the same parameterisation without substantial changes to the model code. The freezing point was set as part of the performed model coupling. In contrast, extensive modifications to the model code would be needed to unify the parameterisation governing the heat and salt content, the basal stress and the albedo. Since the aim of this study was to compare the existing models and not to modify them to be the same, only the drag formulation, the blowing snow parameterisation and the freezing point were modified. The results of unifying these settings will be discussed in the following paragraphs.

Model Option	CICE	SI^3
wind–ice drag	following Tsamados et al. (2014)	Lüpkes et al. (2012)
ocean–ice drag	following Tsamados et al. (2014)	constant: 5e-3
blowing snow	no	yes (rn_blow_s = 0.66)
freezing point	Assur (1958)	Commission et al. (2015)
Sea ice salinity	mushy layer (Feltham et al., 2006)	Vancoppenolle et al. (2005)
heat diffusion in ice	mushy layer (Feltham et al., 2006)	Bitz and Lipscomb (1999)
Albedo	delta Eddington (Joseph et al., 1976)	0.61–0.8 (surface type)
Maximum depth of basal stress	threshold_hw = 30 m	∞
Advection scheme	"Remap" Lipscomb and Hunke (2004)	Prather (1986)

Table 3.1: Significant CICE and SI^3 model differences for the runs CICEref and SI3ref.

Blowing Snow

Paper 3 concludes that the SI^3 blowing snow parameterisation is the only parameterisation that modifies the snow and differs between the models. Both models are forced by the same atmospheric forcing, including snow fall. The blowing snow setting in SI^3 reduces the snow volume by "blowing" some of the snow into leads. How much snow is blown into leads is set by a namelist parameter. The CICE version used has no comparable settings. Based on this, Paper 3 suggested that the differences in snow thickness are caused by the blowing snow parameter. This hypothesis was tested by running a

SI^3 run without blowing snow, and the results are shown in figure 3.1. The model runs from Paper 3 are called CICEref and SI3ref, and the SI^3 run without blowing snow is called SI3nb.

Figure 3.1 shows the monthly ice volume in the upper panel the monthly snow volume in the middle panel, and the differences between the SI3ref and SI3nb run in the bottom panel. The upper panel demonstrates that the ice volume difference between SI3ref, and SI3nb is small compared to the difference between the SI^3 runs and CICEref. The middle panel in figure 3.1 shows that the difference between the CICEref snow volume and the SI3ref snow volume is significantly larger than the snow volume difference between the SI3ref and SI3nb run. This indicates that the blowing snow parameterisation is only responsible for a small part of the snow thickness differences between the CICEref and SI3ref.

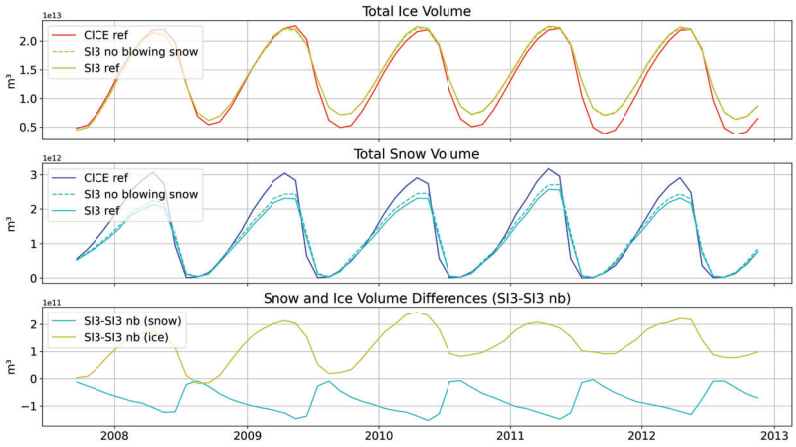

Fig. 3.1: Model snow and sea ice volume differences between CICE and SI^3 with and without blowing snow over five years. The upper panel shows the Arctic total ice volume from CICEref, SI3nb and SI3ref, the middle panel the Arctic total Snow volume from CICEref, SI3nb and SI3ref; and the lower panel the differences between SI3ref and SI3nb in snow and ice volume. Be aware of the difference in scale of the y-axes.

Paper 3 found that snow volume and sea ice volume differences between the models are correlated and argues that one reason for the thinner ice in CICE could be due to its thicker snow layer. The lower panel of figure 3.1 shows that the ice and snow volume differences between SI3ref and SI3nb are also correlated, and that the ice volume in SI3ref increases more over the years compared to the SI3nb run. As expected, the snow

volume in the SI3ref run is lower than in the SI3nb run, supporting the hypothesis of Paper 3 connecting the snow thickness difference to the ice thickness difference. However, figure 3.1 also demonstrates that the difference in snow between CICE and SI^3 can not be explained by blowing snow parameterisation alone.

The blowing snow parameterisation leads to a sea ice volume difference of 84.8 km^3 after running the model for five years. This difference is significantly lower than the ice volume difference between SI3ref and CICEref as shown in figure 3.1's upper panel.

Freezing Point

In Paper 3, it was assumed that CICE calculates the freezing point following the salinity dependent calculation from Assur (1958) and SI^3 calculated the freezing point following salinity and pressure dependent calculation from Fofonoff and Millard Jr (1983). This is based on the settings used in CICE and SI^3. During the revision of Paper 3, it was found that CICE's actual freezing point is constantly -1.8 ^{o}C. The reason for this is that the coupling is executed before the CICE thermodynamic routine is called, in which the freezing point is calculated following Assur (1958). Prior to the thermodynamic routine, the freezing point is set to its initial value given in the initialisation routine, which is equal to -1.8 ^{o}C. The freezing point influences the freezing and melting of ice in CICE. In the CICE-NEMO coupling, the heat transport between CICE and NEMO is calculated as a freezing and melting potential (introduced in chapter 2 section 4.1) depending on the freezing point of seawater and the sea surface temperature.

To evaluate how much the freezing point influences the formation of ice, CICE was run with the freezing point calculated following Fofonoff and Millard Jr (1983), which is the same formulation as used in SI^3. This run will hereafter be called CICEtN. Figure 3.2 shows the snow and ice volume and their differences for the runs CICEref, CICEtN and SI3ref from the initialisation in September 2007 until September 2010. The upper panel shows the total ice volume, the middle panel shows the total snow volume, and the lower panel shows the differences in snow and ice volume between CICEref and CICEtN. The total sea ice volume in CICEtN is lower than in CICEref. The difference is of the same magnitude as the SI^3 sea ice volume difference caused by the blowing snow parameterisation (comp. fig. 3.1).

The freeze and melt potential described by equation 2.15 calculates how much ice is melted. If fmpot is negative, ice is melted. In the CICEref run, the freezing point was rather low, at -1.8 ^{o}C. In the CICEtN run the freezing point is in most places higher, resulting in less sea ice volume. Figure 3.2's middle panel shows that the snow volume differs between CICEref and CICEtN but significantly less than the snow volume between the CICE runs and SI3ref. The lower panel shows no clear correlation between the snow and ice volume differences, which indicates no link between the snow and ice volume differences.

The low sea ice and snow volume differences between CICEref and CICEtN in figure 3.2 indicate that the freezing point differences between SI3ref and CICEref most likely

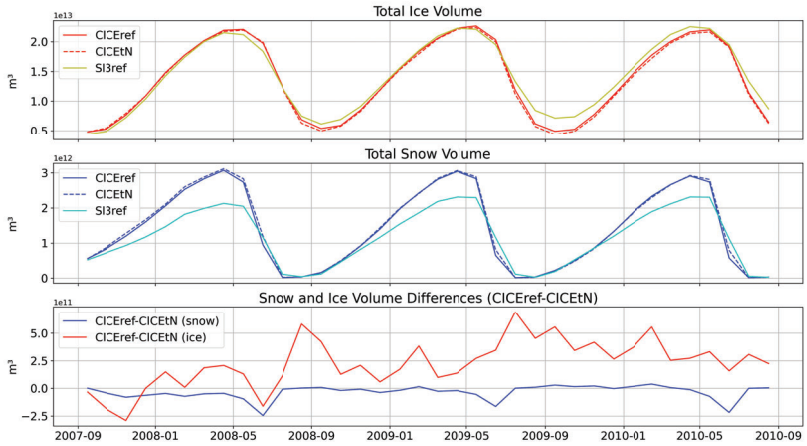

Fig. 3.2: Model snow and sea ice volume differences between CICEref and SI3ref and CICEtN, with differing freezing points in CICE. The upper panel shows the total ice volume, the middle panel the total snow volume, and the lower panel the snow and ice volume differences between CICEref and CICEtN. Be aware of the difference in scale of the y-axes.

do not cause the snow and ice volume differences between the models.

Ice-Ocean and Ice-Atmosphere Drag

Drag coefficients in sea ice modelling are used to parameterise the transfer of momentum between the ocean and the ice and the atmosphere and the ice. In CICE, the ice and ocean drag coefficients are either constant values or dependent on the shape and amount of ice present following Tsamados et al. (2014). This parameterisation is also known as form drag and was described in detail in chapter 2 section 2.1. SI^3 also includes one constant option and one form drag option, where the latter follows Lüpkes et al. (2012). The form drag formulation in CICE (Tsamados et al., 2014) calculates values for both the ocean-ice drag and the atmosphere-ice drag, while the form drag formulation in SI^3 (Lüpkes et al., 2012) only calculates values for the atmospheric drag coefficient. Lüpkes et al. (2012) atmosphere-ice form drag calculation only depends on the SIC:

$$C_a = C_{ice} + C_{fd} \tag{3.1}$$

$$C_{ice} = 1.4e - 3 \tag{3.2}$$

$$C_{fd} = 2.2310^{-03} \cdot (1 - SIC)^{1.1} \tag{3.3}$$

They base their formulation of the atmosphere-ice drag coefficient (C_a) on splitting the drag into a contribution from the sea ice skin (C_{ice}) and one from the ice edge (C_{fd}). The ocean-ice drag coefficient (C_w) is set to $C_w = 5e-3$. Tsamados et al. (2014) developed a formulation for C_a and C_w also under the assumption that C_a and C_w can be calculated by splitting C_a and C_w into several contributions. Further, Tsamados et al. (2014) calculate the transfer coefficients of latent and sensible heat depending on the drag coefficient C_a and the ice bottom growth on the drag coefficient C_w. C_a and C_w are calculated following equation 2.8 and 2.9. To calculate each of the contributions C_f, C_r, C_s and C_{mp}, several new parameters were introduced and calculated, such as, for example, the sail and keel of the ice flow. Introducing each of them here would go beyond the scope of this thesis, for which it is sufficient to point out that the Lüpkes et al. (2012) formulation depends on significantly fewer parameters than the Tsamados et al. (2014) formulation, which also alters the latent and sensible heat transfer.

Both models also allow setting both the atmosphere-ice and ocean-ice drag coefficient to constant values. To evaluate the influence of the different form drag formulations, two additional runs were run, SI3fd and CICEfd. In these two runs, the drag coefficients were set to $Cd_a = 1.4e-3$ and $Cd_w = 5e-3$. Figure 3.3's upper panel shows the total

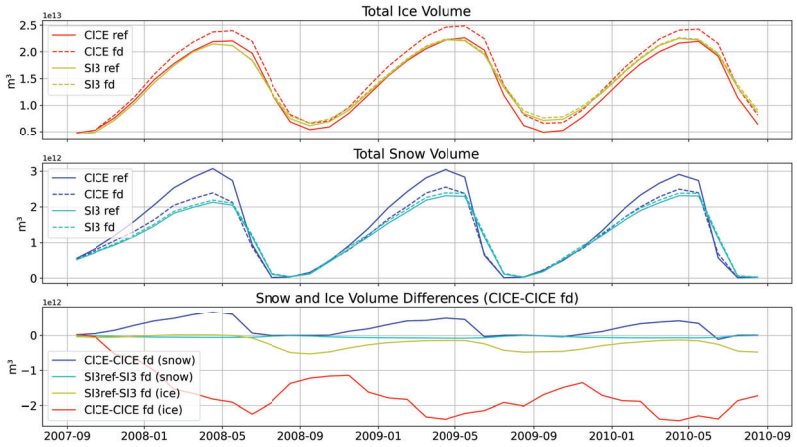

Fig. 3.3: The upper panel shows the Arctic total ice volume from CICEref, CICEfd, SI3ref and SI3fd, the middle panel the Arctic total snow volume from CICEref, CICEfd, SI3ref and SI3fd, and the lower panel the snow and ice volume differences between CICEref and CICEfd, and SI3ref and SI3fd. Be aware of the difference in scale of the y-axes.

sea ice volume from CICEref, CICEfd, SI3ref and SI3fd. CICEref and CICEfd differ

more than SI3ref and SI3fd. The same is shown in the middle panel for the snow volume difference. The CICEfd run has overall the largest ice volume, and the CICEref has over all the largest snow volume. The snow volume of the SI^3 runs is almost identical, and the CICEfd run is closer to the SI^3 runs than to the CICEref run. The Tsamados et al. (2014) form drag formulation influences not only the momentum transfer from the wind to the ice but also the latent and sensible heat transfer. This could be one reason why the Tsamados et al. (2014) form drag formulation has such a strong influence on the snow volume.

Paper 3 correlates the snow volume differences with the ice volume differences. Calculating the correlation of the SI^3 and CICE snow and ice volume differences in figure 3.3, gives low values in comparison to the ones found in Paper 3 (p-value CICE: 0.14, p-value SI^3 0.004). The pattern of opposing snow and ice volume differences, which motivated the calculation of the correlation in Paper 3, though is visible in figure 3.3 lower panel, as well as in figure 3.1 lower panel. The reason for the low correlation between the snow and ice volume differences from figure 3.3 lower panel could be the shorter time over which the correlation was calculated, the inclusion of the spin up, as well as the change in form drag influencing both the formation and melt of snow and ice. As Paper 3 discusses, the snow thickness is not the only parameter in the model influencing the sea ice volume, but it does seem to have some influence on the ice formation.

The CICE snow and sea ice volume differences in figure 3.3 lower panel are the largest differences compared to the volume differences of SI^3 in the same figure and the CICE differences in figure 3.2 lower panel and the SI^3 differences in figure 3.1 lower panel. This shows that the form drag formulation from Tsamados et al. (2014) leads to the largest differences in sea ice and snow volume, considering the investigated model parametrisations.

3.3 Snow on Sea Ice and the Form Drag Formulation

Since the drag formulation in CICE leads to the largest differences in snow and ice volume, the origins of these differences were investigated further. The origin of the sea ice volume differences between the form drag and the constant drag formulation in CICE were studied among other parametrisation by Tsamados et al. (2015). They relate the thicker ice volume resulting from the constant drag parametrisation to lower summer melt when comparing it to the form drag run. From figure 3.3, it is clear that both the snow and the ice volume differences already build up over the first winter, and as discussed above, there are several indicators that the snow plays an important role. Snow is not analysed by Tsamados et al. (2015). Tsamados et al. (2015) analysed a 24-year mean growth and melt rates excluding the 10-year spin up. The annual cycles in figures 3.1, 3.2 and 3.3 reveal that the largest difference between the snow and ice volume already evolves during the first year. This would mean that the melt is not the main cause for the lower SIT in runs using the form drag formulation.

Paper 3 concludes that the snow might have a large influence on the sea ice volume. The explanation for this is that a higher snow volume insulates the ice from the cold atmosphere and causes lower ice growth. This conclusion is solely based on the correlation, but no physical parameters were analysed. To test if the additional snow causes the lower ice growth in CICEref, or if there are other causes for the reduced sea ice growth in the form drag formulation, an additional run with increased snow forcing and constant form drag parameterisation was run. This run will hereafter be called CICEs. The snow forcing in CICEs was multiplied by 1.22, which is about the amount of March snow difference between CICEref and CICEfd.

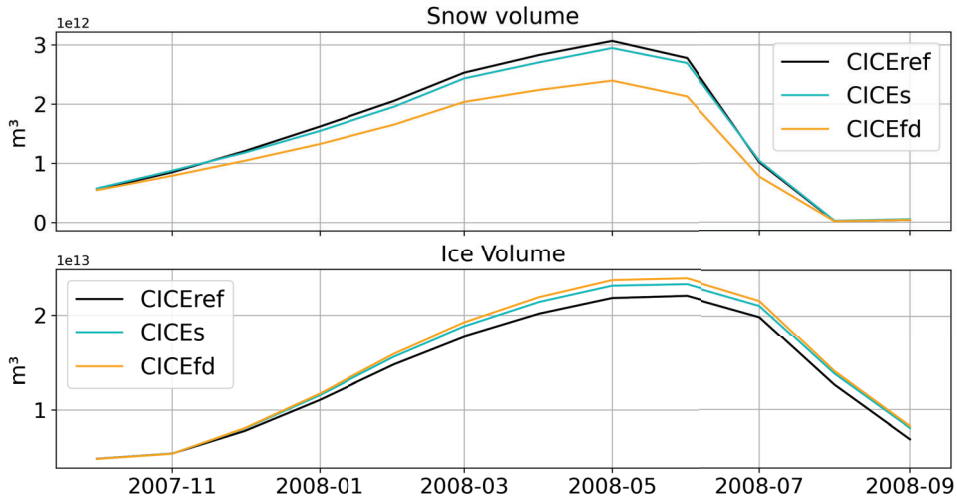

Fig. 3.4: Upper panel: Monthly mean snow volume for the runs CICEref, CICEs and CICEfd. Lower panel: Monthly mean ice volume from the runs CICEref, CICEs and CICEfd. Observe the difference scaling of the y-axes. Both graphs show the period September 2007 to September 2008.

Figure 3.4's upper panel shows the snow volume of all three runs. It is clear that the multiplication of the snow forcing by 1.22 is not exactly sufficient to account for the snow volume difference between the different form drag parametrisations. However, the remaining snow volume difference between CICEref and CICEs is small compared to the snow volume differences between CICEfd and CICEs. The ice volume shown in figure 3.4's lower panel indicates that the snow volume difference has an impact on the ice formation, but that the difference between the CICEref run and the CICEs run is larger than the difference between the CICEs run and the CICEfd run. To evaluate the ice growth and melt process, the different melt and growth components are plotted in figure 3.5. The growth rates, displayed in panels a) and e), show that the snow forcing leads to less bottom growth when comparing the two runs with constant drag (CICEs

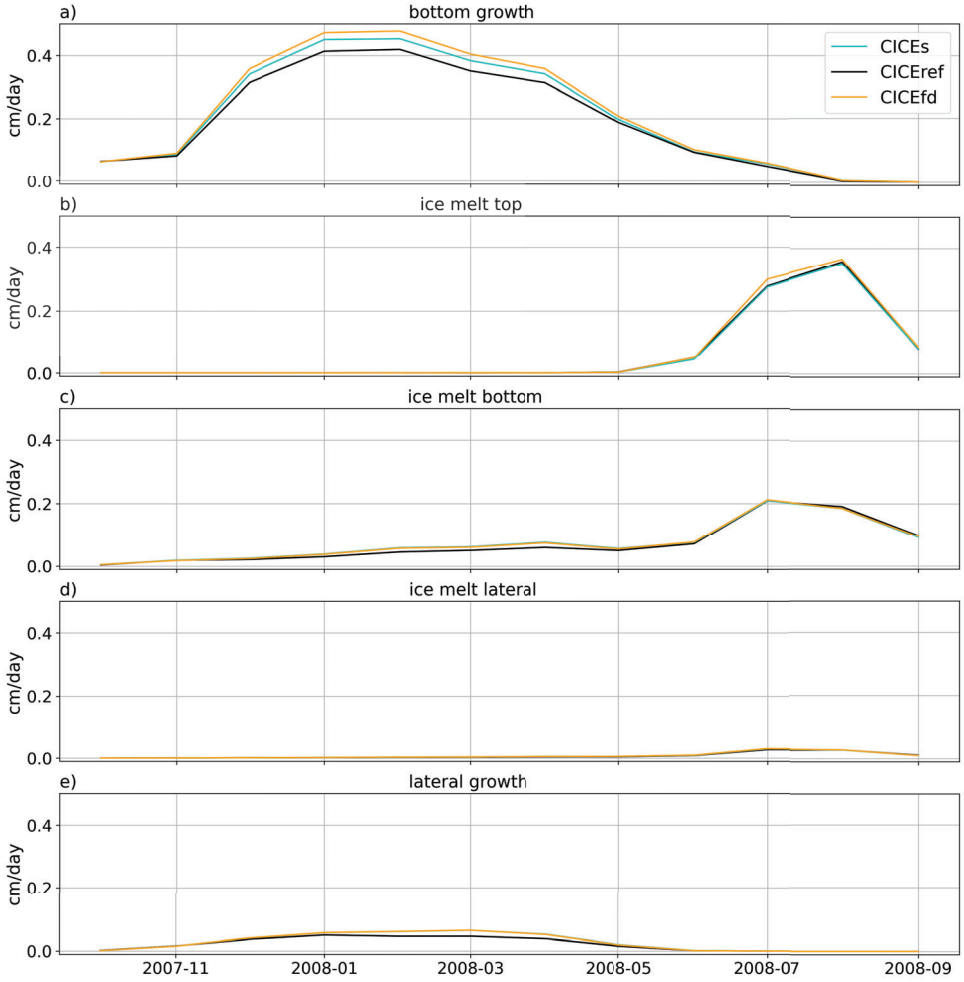

Fig. 3.5: Monthly mean ice melt and growth rates from the runs CICEref, CICEs and CICEfd in cm/day for the period September 2007 to September 2008. a) shows the ice bottom growth, b) the ice top melt, c) the ice bottom melt, d) the ice lateral melt and e) the ice lateral growth.

and CICEfd) but not to differences in lateral growth. The bottom growth rate in panel a) is clearly the strongest contribution to the overall larger ice volume in the runs CICEs and CICEfd. The largest differences between the melt rates are the bottom melt and the top melt, shown in panels b) and c). Both the CICEs and CICEfd show stronger

bottom melt from January to May than the CICEref run, indicating that the bottom melt is influenced by the drag parameterisation, but not by snow volume differences. In between the three runs, the top melt is only stronger in the CICEfd run, indicating that the snow layer prevents some of the top melt. Comparing the magnitude of growth and melt differences between the runs reveals that the growth differences are larger than the melt differences. As mentioned above, the ocean's drag coefficient is used to calculate the heat exchange coefficient. When form drag is used in CICE, the Stanton number is substituted with the neutral ocean drag coefficient. The value for the Stanton number is a constant that is set to 0.006 in the constant drag formulation following McPhee et al. (2008).

Tsamados et al. (2015) attribute the difference in ice volume between the runs to differences in summer melt. The results presented in figure 3.5 suggest that the difference in growth might be at least as important. Tsamados et al. (2015) however, analysed a longer run than the one displayed in figure 3.5. To make a clear statement, a study with longer model runs is needed. Further comparisons of the neutral ocean drag coefficient and the Stanton number are needed, as well as a run where the neutral ocean drag coefficient is set equal to the constant value of the Stanton number, to evaluate its influence on the total ice volume.

To understand the origin of the snow volume difference between CICEref, CICEfd and CICEs, the differences in snow melt and growth between the model runs CICEref, CICEfd and CICEs were analysed. The snow volume growth and melt depend on snow fall, snow melt and sublimation. Figure 3.6 shows the Arctic mean values for the three runs CICEref, CICEs and CICEfd. Figure 3.6 a) reveals that there is most snow fall in CICEs, which was expected since it is the run with increased snow forcing. The snow fall rate between the runs CICEref and CICEfd also differ slightly. This volume difference is most likely caused by the ice area differences between the model runs. Figure 3.6 c) shows that there is more sublimation in the constant form drag runs, which is likely caused by the form drag formulation that alters the latent and the sensible heat transfer.

The units are not given in cm/day as for the ice melt and growth, but in kg/m^2s. It should be noted that the y-axes differ and that the sublimation is negative if snow is sublimated and positive if snow is condensed. The sublimation values in figure 3.6 c) are about four orders above the snow fall, which is unrealistic. Evaluating single grid cells, it was found that the sublimation seems to accumulate instead of being calculated per second as the unit suggests. Other inconsistencies in conversion of units for the sublimation variables were found in the CICE code too, which might be the reason for the difference in magnitude. All inconsistencies were related only to diagnostic variables, and the intercomparison still gives indications about the differences between the form drag formulations. Namely, the form drag parametrisation in CICE reduces the sublimation of snow compared to the constant form drag formulation. Further work on the fate of snow is needed.

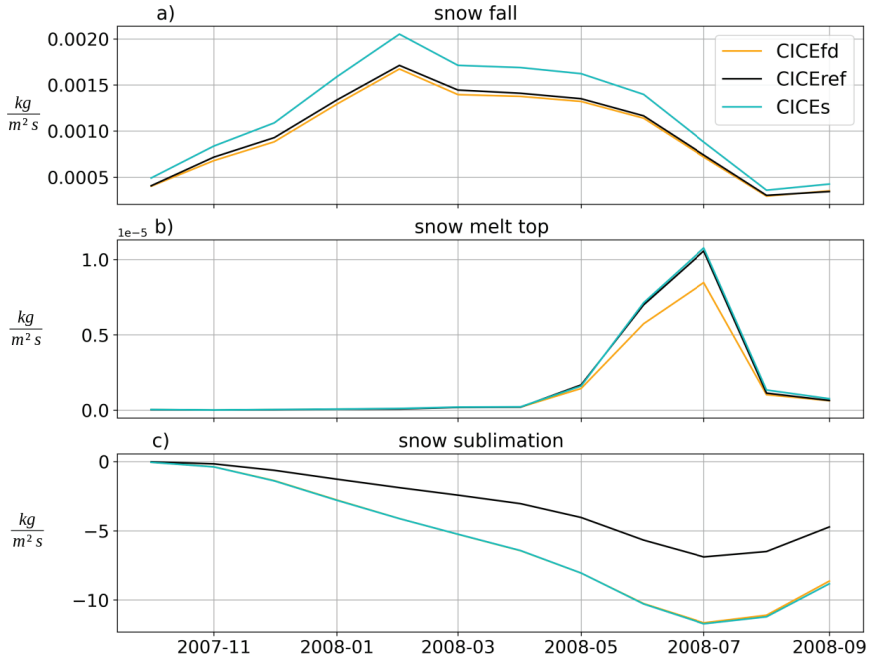

Fig. 3.6: Monthly mean snow melt and growth rates from the runs CICEref, CICEs and CICEfd in kg/m^2s for the period September 2007 to September 2008. a) shows the snow fall rate, b) the snow top melt and c) the snow sublimation rate. Be aware of different y-axes.

Implications for Assimilation

This work in progress aims to understand the origin of SIT and snow thickness differences between the constant and form drag parameterisation. The assimilation builds upon the assumption that the model simulation is unbiased, and the uncertainties are represented by internal variability. The sea ice volume plot in the upper panel of figure 3.3 shows that the sea ice volume in the CICEref run is systematically thinner than in the CICEfd run. Tracing back the origin of this thin bias in CICEref as done in figure 3.6 will in future work allow comparison of model growth and melt rates with observation studies, such as, for example, from observations taken during the MOSAiC campaign (Nicolaus et al., 2022). Paper 2 showed that the snow is a source of uncertainty in the FB to SIT conversion. Understanding the mechanisms behind the differences in the parameterisation will help users choose the best parameterisation for the FB SIT conversion in the FB assimilation scheme.

Chapter 4

Discussion

This thesis investigated different aspects of the relationship between FB and SIT, based on simulations with sea ice models and Cryosat-2 observations. In particular, this thesis has explored how radar FB can be modelled and assimilated to improve SIT estimates and explored different model values needed to derive radar FB.

In section 1, the findings from Paper 2 and 3 regarding the model variables used to derive radar FB from models are discussed. This discussion includes the snow depth, sea ice density and water density and SIT. The snow density is not further discussed, since it follows a spatial constant parameterisation, following Mallett et al. (2020), and no new work was conducted as part of this thesis.

In section 2, the FB assimilation from Paper 1 and choices made in the setup are discussed, as well as the resulting changes in FB and SIT.

1 Model Values to Derive Radar FB

The variables used to derive radar FB from model values are SIT, snow thickness, sea ice density and water density. These are the variables discussed in this section. Here only the model values are discussed, not the assimilation, which also influences the SIT. The SIT resulting from the assimilation is discussed subsequently in section 2.

1.1 Snow Thickness

The snow thickness was investigated in Paper 2, 3 and in the work in progress section. Paper 2 compared the model snow thickness against observations, and Paper 3 and the work in progress section explored how different model settings influence the snow volume.

Paper 2 finds that BGrun snow thickness agrees well with the ASD snow thickness product (Garnier et al., 2021) and better than the snow thickness from the AWI data. Paper 3 compared snow thicknesses from SI^3 and CICE with the ASD snow thickness product. It was shown that the SI^3 snow thickness in late winter agrees better with the ASD snow thickness than CICE snow thickness (BGrun). BGrun used the Tsamados et al. (2014) form drag parameterisation. In chapter 3 section 3.2, it was demonstrated that the form drag parameterisation has a large impact on the CICE snow volume, and that the constant neutral drag coefficient leads to snow thickness closer to the SI^3 snow thickness. Taking the results from Paper 3 and figure 3.3 into account, running CICE with the constant drag formulation would give snow thickness values closer to the ASD product. Before concluding that this would result in more realistic snow thickness values, two points raised in the discussion of Paper 2 have to be taken into consideration. First, the snow in CICE is not densifying while the snow in the Arctic in reality is (Mallett et al., 2020; Wagner et al., 2022), and second, the ASD snow product is based on Ku-band radar measurements, which are known to have biases in the snow penetration depth (King et al., 2018; Willatt et al., 2011).

Snow-on-sea-ice models, including densification processes, consider the effect of wind packing to alter the snow thickness and density (Petty et al., 2018) and the temperature and water vapour pressure (Liston et al., 2020). In this process, no snow mass is lost. This means that the product of H_s and ρ_s in the hydrostatic balance equation (equation 2.4) would give the same result no matter if the model includes snow densification or not, while altering H_s and ρ_s. If the model accounted for snow densification by increasing ρ_s and decreasing H_s over time, the CICE snow thickness would agree better with the thinner ASD product, but the modified snow thickness and snow density would not have any effect on the FB to SIT conversion.

The second point raised in the discussion of the snow validation in Paper 2 was the Ku-band radar penetration depth. Several studies have found that the CryoSat-2 Ku-band radar reflection horizon depends on snow depth, moisture content, snow salinity, and inhomogeneities, such as, for example, ice lenses (King et al., 2018; Kwok, 2014; Kwok et al., 2011; Nandan et al., 2017; Willatt et al., 2011). The ASD snow product also relies on Ku-band radar. All of these field studies, finding that Ku-band radar does not penetrate the entire snow pack, were conducted during the months March to May. The ASD product is calculated as the differences between the CryoSat-2 Ku-band radar and the Ka-band radar reflecting from the snow surface. If the Ku-band radar is reflected from within the snow pack and not from the snow-ice interface in late winter, it follows that the ASD product could underestimate the snow thickness in late winter. Therefore, it is plausible that, in late winter, CICE in Papers 3 and 2 might actually not be overestimating the snow thickness, but the ASD is underestimating it.

With the discussions of the ASD product in mind, it can be concluded that the snow thickness from the CICE form drag run agrees less with the ASD product in late winter but might be more realistic than the constant drag runs snow thickness. The

discussion also reveals that more Arctic-wide comprehensive snow thickness observations are needed.

Several other snow thickness products were available for comparison. The ASD product was chosen because it is independent of passive microwave observations and climatologies. The updated snow thickness climatology from Shalina and Sandven (2018) is not independent of the W99 snow climatology used in Hendricks et al. (2021). Further, the passive microwave snow product of Rostosky et al. (2018) is not independent of the Hendricks et al. (2021) snow product, which uses passive microwave snow thickness in the marginal seas. The only alternative radar observation-based snow thickness product is Lawrence et al. (2018). Its seasonal variability was found to be an outlier in Zhou et al. (2021) a study comparing different snow thickness products. It was found to be anomalously thick in early winter, and its seasonal cycle does not agree with any of the other snow products. Therefore, the ASD snow thickness product was the best suited product to independently compare model values and AWI values in Paper 2.

1.2 Sea Ice Density

Paper 2 finds that: the modelled sea ice density used in Paper 1 is generally lower than observations, higher than AWI sea ice density in MYI areas, lower than FYI AWI sea ice density and spacially not as variable as observations. The model sea ice density following equation 2.22 depends only on the sea ice brine content, which is weighted by its fraction and added to the baseline sea ice density of 882 kg/m^3. This means that the model sea ice density only varies with the brine content, while in reality sea ice density also depends on enclosed air bubbles, which can lead to large density variations (Timco and Frederking, 1996). Enclosed air bubbles are not simulated in CICE. MYI is lighter than FYI due to larger amount of air pockets resulting from brine drainage (Alexandrov et al., 2010; Shokr and Sinha, 2015; Timco and Frederking, 1996).

Therefore, Paper 2 introduces a new sea ice density parameterisation, dependent on the FYI fraction. This new parametrisation is found to be in better agreement with the in situ observations included in Paper 2 than the original parameterisation following equation 2.22 and than the AWI data values. The new parameterisation is only valid over the ice growth period. During melt season, some brine is washed out of the ice and substituted with air bubbles (Timco and Frederking, 1996). This leads to lower ice densities. In the updated model simulation, this is approximated by splitting ρ_{fresh} into FYI and MYI contributions, depending on the model variable's FYI area. FYI area is defined as the area fraction covered by newly formed ice since the previous September. This model parameterisation can not account for the washout of salt takes place over the entire melt period. For this reason, Paper 2 recommends using the newly derived sea ice density only during the sea ice growth period.

Paper 2 showed that sea ice density plays an important role in the conversion from FB to SIT, in line with earlier studies (Ji et al., 2021; Jutila et al., 2022; Kern et al.,

2015). The results from Paper 2, however, also contradict some of the earlier findings. For example, both Ji et al. (2021) and Jutila et al. (2022) state that the typical sea ice density values from Alexandrov et al. (2010) are underestimated, but the results from the MOSAiC in situ observation comparison in Paper 2 show that the Alexandrov et al. (2010) based CryoSat-2 values are higher than the in situ observations, contradicting this finding. Since the MOSAiC observations only cover one year, this might be an exception. This again highlights the need for more observations.

1.3 Water Density

Paper 2 found that the modelled water density does not reflect the World Ocean Atlas (WOA) surface water density spatial variability; yet neither does the commonly used signal value water density from the classical approach. Further, Paper 2 reveals that the commonly used error margin in the classical approach is too small, since it is based on seasonal variability and not on spatial variability. Paper 2 also found that the water density contributes to the smallest SIT differences when evaluating the contribution from snow thickness, sea ice density and water density. This aligns well with Kurtz et al. (2013), although, Paper 2 found that they underestimated the contribution of water density to the SIT error.

Similar to the snow and sea ice density observations are water density observations in the Arctic space. The advantage of using a climatology like WOA, especially in a 10-year average comparison as conducted in Paper 2, is that it is quality controlled and comprises major observation campaigns, such as, for example, the ice tethered profilers from the Woods Hole Institute of oceanography (Krishfield et al., 2008), or the Global Oceanographic Data Archaeology and Rescue (GODAR) Project (Levitus, 2012). There are other Arctic focused climatologies, such as, for example, the Polar Science Center Hydrographic Climatology (PHC3) (Steele et al., 2001) or the Arctic Ocean Atlas (AOA) (by L. Timokhov and Tanis., 1997), but both of them only include observations up to the late 1990s.

Zweng et al. (2019) investigated the WOA version 13, one prior to that used in Paper 2, and shows that there has been a large influx of data over the early 2000s. Since WOA18 includes data from five additional years covering the model period, it is a given that it has an even better data coverage than WOA13. AOA is a joint effort of US and Russia to make navel data accessible to scientists, by releasing a common climatology consisting of both their observations. PHC3 is based on WOA98, AOA and some additional data in the Canadian Arctic, which also are included in WOA18. Based on the fact that both AOA and PHC3 only include data up to the late 1990s and the period of interest in Paper 2 spans from 2010-2020, the WOA18 is a better choice for a 10-year mean comparison of the Arctic surface density than AOA or PHC3.

Paper 2 suggested a new uncertainty estimate of $\pm$ 2.6 kgm^{-3} for the water density, based on the standard deviation between the constant value used in the AWI data set

and the WOA. Ideally a variable water density should be used, reflecting the spatial, seasonal and interannual variability of Arctic surface waters. Paper 2 suggested that the ocean model could be used but recognises limitations in the spatial variability. These limitations were linked to the mixed layer, in line with earlier studies that found a too deep mixed layer depth in the Arctic (Hordoir et al., 2022). The area with the largest differences between the WOA and the model output is the Laptev Sea. This area is governed by high interannual variability, forced by river run off and atmospheric circulation (Hudson et al., 2024; Janout et al., 2020). A climatology like the WOA is not suited to evaluate the model's ability to simulate this variability. An alternative for future studies could be SMOS-derived sea surface salinity values, such as, for example, those used in Hudson et al. (2024).

In chapter 3 section 3.2, it was found that the freezing point used in the CICE–NEMO coupling was too low and that all runs included in this study were run with this freezing point. The test runs, correcting this error, showed (figure 3.2) that the resulting sea ice volume is slightly lower than the sea ice volume from CICEref. Comparing the CICEref and CICEtN sea ice areas (not shown) reveals even more significant differences in the summer months. The winter months difference is not as pronounced as the summer months difference. This means that more sea ice is formed in the CICEtN than in the CICEref, potentially altering the surface water conditions. The increase in growth could alter the surface salinity. This has not been investigated yet, but will be the topic for future work.

1.4 Sea Ice Thickness

Paper 3 found that the CICE SIT is within the expected accuracy compared to other model studies. Compared to the CS2SMOS SIT product, the modelled SIT is thinner during the entire winter in the central Arctic and thicker in the marginal seas in late winter. In the region where the model is thinner than the CS2SMOS product, the CRYOSat-2 component dominates. This thesis is investigating the uncertainties of this product, so it is not suitable for further comparison.

Overall, finding a suitable SIT comparison product, that was not derived from CryoSat-2 FB or did not depend on sea ice density assumptions, was challenging. The SMOS SIT product is only reliable for SIT below 1 m (Ricker et al., 2017). Other SIT products like the observation IceBridge SIT from Kurtz et al. (2013) or ICESat-2 SIT from Petty et al. (2020) could be used. Unfortunately, they also rely on sea ice density. The sea ice density used in Kurtz et al. (2013) and Petty et al. (2020) is set to a constant 915 kg/m^3. Jutila et al. (2022) retrieved their sea ice density observations in similar locations to those of the Operation IceBridge data. They showed that the sea ice density is highly variable in this area. Paper 2 indicated that the sea ice density has a significant impact on the SIT conversion, so using Operation IceBridge SIT for validation was not considered.

To validate the model with independent SIT observations, the BGEP and MOSAiC observations were chosen. Both of them are point measurements, but they are independent of assumptions of ice density, snow thickness and water density. One criticism of using point observations, such as, for example, the IMBs in the MOSAiC data set, is that they do not reflect the variability of SIT within the typical spatial coverage of models and satellite SIT products, since they are mounted on one specific ice floe (Wever et al., 2021). In contrast, one model grid cell, or 25 x 25 km averaged satellite observation, contains ice floes of different thicknesses, which respond differently to thermal forcing. This shortcome was addressed by averaging values of one day from the BGEP observation and observations from at least 9 IMBs for the MOSAiC observations. The variability of the observations was displayed by their STD in figure 6 and 8 in Paper 1. The variability of the BGEP observations originates from the observation platform being anchored below the ice and measuring the ice floe as it moves by the observation platform. In the MOSAiC observations, the variability originates from IMBs being deployed on different ice floes at distances spanning typical spatial scales of climate model resolution (Nicolaus et al., 2022). This unique spatial distribution of overall 16 IMBs in close proximity during the winter 2019/2020 makes the MOSAiC IMB data set a valuable observation data set to validate both model- and satellite-derived SIT.

The MOSAiC SIT comparison in Paper 1 figure 8 shows that the refRun is in the closest agreement with the observations. Still, the amount of ice growth is underestimated compared to the MOSAiC IMBs. According to the analysis in the work in progress section, the bottom growth causes the largest change in ice growth, with an increased ice growth in the CICEfd run. As mentioned in chapter 3 section 3.2, this difference in growth is caused by the dependants of the heat exchange coefficient on the neutral drag coefficient. For future assimilation runs, it should first be analysed if the change to a constant drag parameter will result in growth rates closer to the MOSAiC observations.

2 FB Assimilation

This section discusses, the Assimilation setup, the practical choices made (section 2.1) and the validation of the assimilation (section 2.2). Finally, the resulting FB and SIT from the assimilation are discussed and compared with observations and the AWI SIT (section 2.3).

2.1 Assimilation Setup

The assimilation framework presented in Paper 1 is based on an EnKF approach but was simplified to reduce computational costs and fit the timeframe of the project. The main simplifications made in comparison to other state-of-the-art assimilation setups are: running only one model realisation compared to running a full ensemble, and running

a univariate assimilation instead of a multivariate assimilation, as, for example, done in Liang et al. (2019); Lisæter et al. (2003); Mathiot et al. (2012). These simplifications will be discussed below. Additionally, this section discusses the observation and model error and the choices made to distribute mean grid cell SIT into the model SIT categories.

By running only one model realisation, the model error does not evolve and reduce in time, as it does in studies running a full ensemble (Liang et al., 2019; Wu and Zheng, 2017). Instead, the work presented here uses a 10-year historical run to calculate the model background error. The overestimation of the ice edge in the Greenland Sea and Barents Sea informed the decision for how to construct the error covariance matrix of the model ensemble error (see section 3) serving as the model background error in the Kalman gain (equation 2.11). Paper 3 found that the ice edge was significantly overestimated in the BGrun. Therefore, the different constructions of the background error covariance matrix listed in section 3.3 were introduced. The resulting RMSE from the different constructions of the background error covariance matrix in figure 2.3 shows close results for the one_p_m RMSE and the vary_sp RMSE, for an ensemble size of 80 ensemble members, which is the ensemble size used in the assimilation. The vary_sp setup was chosen because it was assumed that the one_p_m might overestimate the model error once the assimilation has improved the result. If this is the case, it has never been tested. Prior to a longer run, the model error should be reassessed.

In the first draft of Paper 1, the assimilation was run with a constant observation error of 15 cm. This was changed in the final submission to account for the actual error provided in the FB data product. Running the model with the data products error degraded the SIT results in the BGEP comparison and the MOSAiC comparison. The data product's own error is significantly lower than 15 cm. Figure 4.1 shows the mean AWI FB products error, which is particularly low in rings around the North Pole. These rings are where the overpasses of the considered CryoSat-2 overpasses intersect. This means that the error of the radar FB seems to depend mainly on the number of observations. This does not align with studies discussing the uncertainty of CryoSat-2 radar retrievals. Xia and Xie (2018) compared seven airborne FB observations that were colocated with FB derived with three different retrackers from CyroSat-2 overflights. They found that the TFMRA has a bias of -0.04 to 0.07 m and a RMSE of 0.05 to 0.19 m compared to the airborne FB observations. Landy et al. (2020) finds that the 50% TFMRA retracker used in the assimilated data and other retrackers tested leads to up to 12 cm differences in the retrieved radar FB. Based on this, the constant error of 15 cm is also not ideal.

For future assimilation studies, the observation error should be revised. Several studies show that the reflection from within the snow pack instead of at the ice-snow interface leads to overestimated radar FB (King et al., 2018; Nab et al., 2023; Willatt et al., 2011). Taking their findings into account, one option for an updated radar FB error could be to consider the model's snow depth. This could be done by for example varying the observational error as a function of the model snow thickness. Another

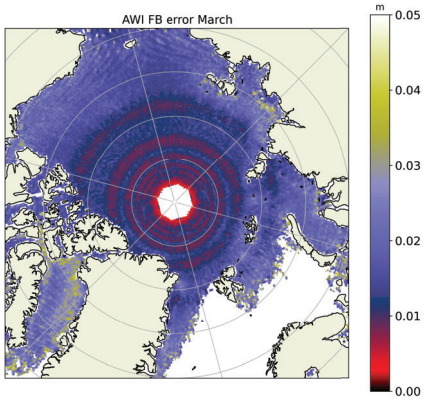

Fig. 4.1: Average AWI FB data error for March in meters. The average is calculated over the three years the assimilation was run in Paper 1.

option could be to compare different FB products derived from different retrackers and using their inter-product variability as observation error.

Many existing Kalman Filter assimilation setups use multivariate approaches (Liang et al., 2019; Lisæter et al., 2003; Mathiot et al., 2012; Mu et al., 2020; Yang et al., 2014), and studies suggest that multivariate approaches outperform univariate approaches (Cipollone et al., 2023; Liang et al., 2019; Mu et al., 2020). In a multivariate approach, the state vector $\boldsymbol{x}$ consists of several model state variables. For example, Liang et al. (2019) used SIC, SIT and the upper 1,000-m ocean temperature and Mathiot et al. (2012) used the full model state vector, only excluding sea-ice temperature and heat content for stability reasons. The multivariate approach has the advantage that the model state variables that are correlate are changed through these correlations. An example would be the sea surface temperature and the SIC and thickness in the marginal ice zone (Liang et al., 2019). If only the SIC is changed, as done in the work presented here, but, for example, not the sea surface temperature, the model's sea surface temperature might be too low and could cause the production of new ice where the assimilation just reduced the SIC. This artefact could be a reason for the low improvement of SIC (max 5%) shown in Paper 1 figure 3. In a multivariate approach, with a state vector containing SIC, FB and sea surface temperature, the temperature might have been adjusted through cross-correlations of the SIC and sea surface temperature field.

The assimilation setup developed herein had the goal of showing that assimilating FB can improve SIT, rather than developing an optimal assimilation system at the scale of Sakov et al. (2012), Fiedler et al. (2022) or Smith et al. (2021). Therefore, the univariate approach was a reasonable choice, also taking the time restriction into account. With the results from Paper 1 showing that the assimilation of FB can improve

the SIT, it could be a good next step to test the derived parameterisation of radar FB as an observation operator in a multivariate system.

The model simulates sea ice thickness at subgrid scale by calculating its distribution into five different thickness categories. The data assimilated, however, emerges as an average value per grid cell and a decision needs to be taken regarding how to distribute it into the thickness categories. In this work, each thickness category is altered by the same amount as the average grid cell SIT is altered (comp equation 2.23). A number of different approaches to this problem can be found in the literature. Chen et al. (2017a) save pre-observation distribution to calculate which category has to be altered, Gupta et al. (2021) use an approach of altering both the category SIT and SIC in an iterative process to match the new mean grid cell SIT and Williams et al. (2023) adopt the observation operator in the Kalman Filter to alter the category SIT and SIC by their relation to the mean grid cell SIT. All of these approaches result in improved SIT simulations, but no comparison between different approaches in an Arctic sea ice model has to the authors knowledge been performed to date.

Smith et al. (2016) discusses the drawback of the method used in Paper 1 to distribute the ice into the categories: if the model is thick or thin biased and therefore lacks ice in a certain category, the method used in Paper 1 will further enhance this bias, since a category in which no ice exist will not be changed. For example, if the model has a thin bias and no SIC in the thickest category, no thicker ice will be added. Smith et al. (2016) only assimilated SIC. Since Paper 1 also assimilated FB and the SIT is redistributed into according thickness categories after the assimilation, this effect is assumed to be counteracted. For the example from above, this means, the SIT in the thickest existing category will exceed its limits after the assimilation and be redistributed into the thicker category, which was prior to the assimilation empty.

Still, it can be assumed that the approach used in Paper 1 is suboptimal, due to an error introduced during the assimilation implementation. Currently, the SIC and SIT are changed independently, neglecting the fact that the change in SIC will change the SIT. The assimilation threshold of 80% for the FB assimilation is most likely the reason why this suboptimal update of SIC and SIT had no major impact on the simulated SIT. Ideally, the SIC and SIT would be changed in an iterative process, as suggested by Gupta et al. (2021). Efforts will be made to implement this approach into the model code.

2.2 Assimilation Validation

In Paper 1, the assimilation was validated against the assimilated data sets to prove that the runs fbRun and sicRun are closer to the respective assimilated observations, and finally, all model runs are compared to independent SIT observations. The SIC error of the fbRun is overall higher than the SIC error of the sicRun, but lower than the refRun SIC error (Paper 1 figure 3). In the independent SIT observation comparison in Paper 1

figure 6 and 8, the fbRun is closer to the observations than sicRun and refRun compared to the BGEP data, but not compared to the MOSAiC data. Paper 1 demonstrates that refRun and sicRun SIT at the locations where the MOSAiC measurements were obtained are in good agreement, and that the FB assimilation degrades the results of SIT. As discussed above, adjustments to the observation error and the construction of the model background error need to be tested, but the degradation could also result from biased observations as discussed in Paper 1.

Paper 1 validated refRun, sicRun and fbRun only against the assimilated data and against independent SIT observations. Non assimilated variables were not validated. A validation of independent variables ensures that the assimilation does not actually degrade the model results. To validate the assimilation system to additional independent data, the ice surface temperature from C3S (2024) was selected. C3S is an ice surface temperature data product available at 3h frequency, combining a multitude of satellite-based thermal infra-red observations. The ice surface temperature was selected for validation because a change of SIT will lead to a change of heat content in the model. The RMSE between the model runs and the observation data (figure 4.2) shows that all model runs have an ice surface temperature RMSE of about 5^o C. This error is most likely caused by the model's forcing data warm bias. ERA5 is known to be too warm in the Arctic (Tian et al., 2024; Wang et al., 2019). Another cause for the error in the surface temperature is that the model variable considered only consists of temperature contributions from the actual ice surface, while the satellite-based ice surface temperature is derived from a surface that might contain open ocean contributions (Nielsen-Englyst et al., 2023). The middle panel in figure 4.2 shows that the fbRun has the largest error, but the average RMSE of 0.1^o C is still within the data product's uncertainty of about 0.15^o C. Some outliers of 0.3 to 0.7^o C are visible for the refRun-fbRun difference RMSE. These outliers occur at times when the observations coinciding with the model values are lower for fbRun than for sicRun and refRun (compare peaks around September of the three years in middle with lower panel of figure 4.2). Still, overall, the RMSE of the fbRun is larger than the sicRun and refRun RMSE. This indicates that the FB assimilation degrades the sea ice temperature, even though the differences are low, compared to the overall bias of the model's sea ice temperature. A multivariate approach containing the full model state variables in the Kalman filter state vector might ensure that the ice temperature is not degraded. The only other existing FB assimilation study assimilating snow FB from IceSat that followed such a multivariate approach is Mathiot et al. (2012). However, they had to exclude the sea ice heat content and temperature due to stability issues, indicating that a multivariate state vector containing heat content, ice temperature and FB might be difficult to set up (Mathiot et al., 2012).

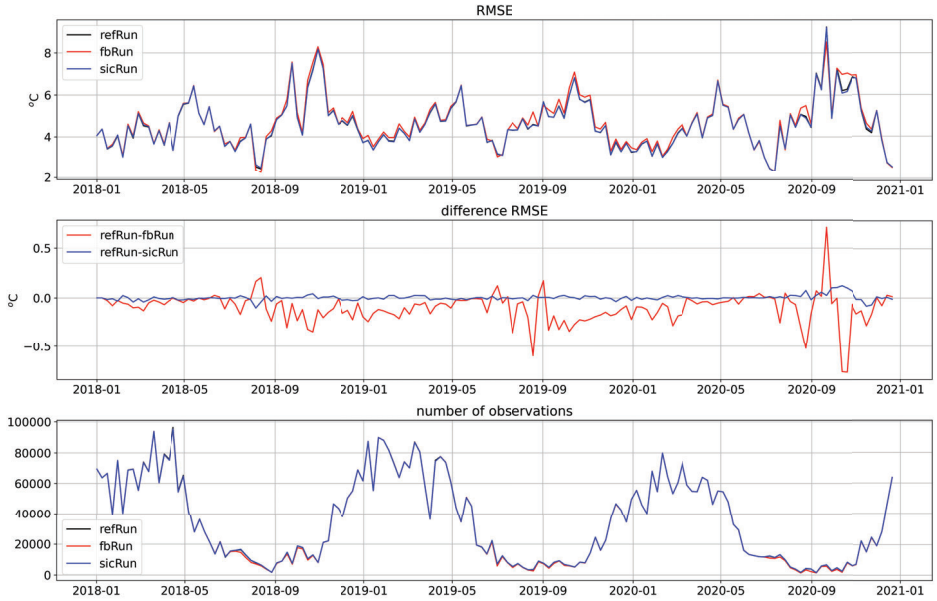

Fig. 4.2: Sea surface temperature errors of refRun, sicRun and fbRun. Upper panel: RMSE of the sea ice surface temperature of all runs. Observe that sicRun and refRun are almost equal and that the blue sicRun covers the black refRun. Middle Panel: Differences of the RMSE refRun and sicRun and fbRun, respectively. Lower panel: Number of grid points where observations were are available.

2.3 Sea Ice Thickness from Radar FB Assimilation

The SIT from the radar FB assimilation was discussed in Paper 1. Here it was compared to three other SIT products, the AWI CryoSat-2 SIT, the sea ice draft from the BGEP data and the sea ice thickness from an array of IMBs deployed during the MOSAiC expedition. The uncertainties in the SIT from the AWI CryoSat-2 product (and similar products) were the motivation to carry out the work in this thesis. So the comparison to the AWI CryoSat-2 SIT can not be seen as a validation for the assimilation. As discussed in section 1.4, finding independent SIT data to validate the assimilation is a challenge. In the following, the SIT will be discussed only at the locations where observations are available. This will not allow conclusions for the entire Arctic but at the locations where observations are available the causes for the SIT differences can be understood, and this understanding can lead to improvements of the assimilations which are valid for larger areas.

Paper 1 concludes that the better agreement between refRun and MOSAiC observations compared to the agreement between fbRun and MOSAiC observations is caused by

the assimilation of biased AWI FB data. This possibility can not be ruled out, but the results from Paper 2 also suggest another option: too low sea ice density. The C6N4$_{J21}$ sea ice density, which compares better to observation than the one used in fbRun, is higher than the refRun sea ice density in the Russian shelf region and eastern Arctic. A higher sea ice density would lead to a higher sea ice thickness, which would match the MOSAiC observations better. The first test run, running the assimilation with the C6N4$_{J21}$ sea ice density, showed promising results (blue line in figure 4.3). This run also shows a significantly overestimated SIT from February 2020. As discussed in Paper 1 and section 2.1, this might be due to biases in the FB that is assimilated. One point that supports this hypothesis is that the growth rate accelerates from February. This is unrealistic, since thick ice would be expected to grow slower (Maykut, 1982), as also shown by refRun and the observations.

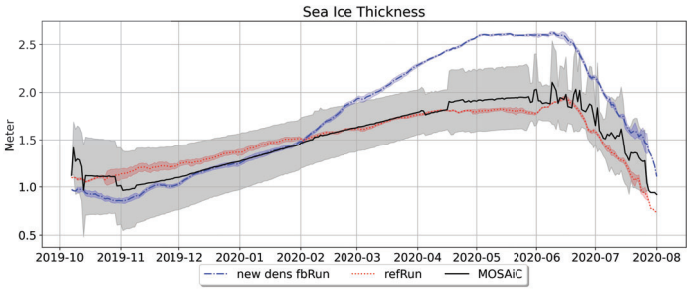

Fig. 4.3: SIT from the MOSAiC observations, model runs refRun and a run similar to fbRun differing only in sea ice density parameterisation, called "new dens fbRun". The sea ice density in this run is based on the sea ice density parameterization developed in Paper 2.

The snow might be another explanation for the SIT difference. The MOSAiC observations in late winter are located in the region defined as Russian Arctic west in Paper 2. Paper 2 here finds that the model snow volume in late winter is higher than the ASD snow thickness. Furthermore, this area overall is the one with the largest difference in snow volume between the model and the ASD snow product. An overestimated snow thickness will lead to an overestimated SIT, which might be another cause for the overestimated SIT in late winter for fbRun figure 4.3. The 2020 snow fall from the model forcing is found to be in good agreement with the snow fall measured (Wagner et al., 2022). The analysis of the work in progress section reveals that the same snow fall can lead to different snow volumes depending on the choice of the drag parameterisation. Which drag parameterisation is best suited to simulate the snow thickness still has to be investigated, as discussed in section 1.1.

Potential for new Insights into Radar FB Observation Biases

The discussion above and Paper 1 suggest that one reason for the large SIT difference between fbRun and the MOSAiC observations could be flawed FB observations. Many potential origins for radar FB errors exist, but two are widely discussed. These are: the retracker used to derive the FB and potential dislocation of the reflection horizon in the snow pack.

To evaluate if the retracker causes the SIT difference in late winter in the comparison with MOSAiC observations, the assimilation could be run with other FB products. Sallila et al. (2019) compared different CryoSat-2 SIT products. Most products use similar values for snow thickness, snow density, sea ice density and water density. Based on this, the authors attribute the SIT differences between the products mainly to the retrackers. From their comparison, it is clear that the AWI SIT is one of the thinner SIT products available. In Sallila et al. (2019) comparison, the only SIT product that is thinner in the region of the MOSAIC observations is the SIT product from Kwok and Cunningham (2015). This product uses a waveform centroid retracker. Landy et al. (2020) Lognormal Altimeter Retracker Model based FB would be another alternative to the AWI FB. They find that compared to the AWI FB base on the 50% TFMRA retracker, their retracking technique leads to thinner FB, which is closer to their validation data. This makes the FBs from Kwok and Cunningham (2015) and Landy et al. (2020) interesting products to assimilate as an alternative to the AWI FB.

Several studies have found that the radar signal can be reflected from within the snow pack under certain conditions. These conditions include thick, warm and wet snow (Giles and Hvidegaard, 2006; King et al., 2018; Willatt et al., 2011). The results from Paper 1 suggest that modelled radar FB is realistic in the regions where observations were available, and Paper 2 showed that the snow thickness is within the range of observations. To evaluate if thickness biases in the observed radar FB exist, the assimilated or modelled radar FB could be compared with the observed radar FB and correlated with, for example, model snow thickness and temperature. The aim with such a study would be to quantify the findings of (Giles and Hvidegaard, 2006; King et al., 2018; Willatt et al., 2011) that warm and thick snow leads to overestimated FB observation. It would allow quantifying the thickness biases found in past studies, without large-scale observation campaigns.

To minimise false conclusions due to model errors, the findings from past studies first would need to be verified with the model output. For example, sea ice thickness, snow thickness and FB observations used in King et al. (2018) are available from Rösel and King (2017). This data could be a good addition to the model verification against MOSAiC observations, to strengthen the point that radar FB from model values are realistic.

The results from Paper 1 suggest that the FB in the Beaufort Sea does not have a seasonal bias as discussed for the MOSAiC observations. At the locations where the BGEP sea ice draft observations were obtained, no pattern similar to the observed

increase in SIT difference between fbRun and MOSAiC observations is visible in late winter. If radar signal reflection from within the snow pack is the reason for the biases in the MOSAiC data, the BGEP observations suggest that such a bias is not uniform throughout the Arctic. This would be plausible, since snow fall varies greatly throughout the Arctic basin (Zhou et al., 2021).

Chapter 5

Conclusion

Overall, this thesis aimed to improve our understanding of Arctic sea ice thickness (SIT) and quantify and reduce the uncertainties of it by combining observations and sea ice models. To do so, the model values for sea ice density, snow thickness and water density were investigated and used to derive a model based radar FB. Further, these values were compared with values from a classically derived CryoSat-2 SIT product and the SIT differences resulting from changing the values for snow thickness, sea ice density and water density were analysed. Finally, a CryoSat-2 FB assimilation framework was developed consisting of the latest version of NEMO (ocean model) (Madec et al., 2017), CICE (Hunke et al., 2021c) (ice model) and PDAF (Nerger and Hiller, 2013) (a piece of software used to implement the Ensemble based Kalman Filters).

The main objectives of this study were to:

1. Understand the Parameterisation in the model and determine their influence on SIT and snow thickness.

2. Prove that model-derived sea ice density, snow thickness and water density values can substitute the values used in currently available CryoSat-2 SIT products.

3. Assess the SIT differences based on changing the snow thickness, sea ice density and water density used in available CryoSat-2 SIT products with modelled values.

4. Demonstrate that the assimilation of radar FB can improve SIT estimates.

Parametrisations potentially influencing the SIT and snow thickness were explored in the work in progress section (chapter 3 section 3.2). Here the blowing snow parameterisation from SI^3, the ocean freezing point and the drag Parameterisation were investigated. The parametrisation with the largest influence on snow thickness and SIT

is the drag parameterisation following Tsamados et al. (2014), due to its influence on the dynamics, the atmospheric boundary layer and on the ocean heat exchange coefficient. The form drag calculation following Lüpkes et al. (2012) has a significantly lower influence on the SIT and only influences the dynamics. To truly compare the two, a study should consider only the influence of the Tsamados et al. (2014) drag on the dynamics. A suggestion for such a study is detailed in the outlook.

The model values for sea ice density, snow thickness and water density were compared to observations in Paper 2. Paper 2 found that all model values are good substitutions for values typically used in available CryoSat-2 SIT products. The snow thickness is in agreement with the ASD snow thickness product (Garnier et al., 2021) but thicker in February and March in most regions. Compared to the W99- and microwave-based snow thickness used in Hendricks et al. (2021), it agrees better with the ASD snow thickness product except for the months February and March in the Russian Arctic West and in November in the Canadian Arctic (comp. Paper 2 table 1). The sea ice density used to derive radar FB in Paper 1 was found to be overall too low, and a new parameterisation was presented based on Jutila et al. (2022) sea ice density observations and the model value of FYI area. This parametrisation was found to be in good agreement with observations, but should only be used during ice growth season due to the definition of FYI area in the model. Overall, the newly-derived model values compare better to observations than the values used in Hendricks et al. (2021). Paper 2 also finds that the model water density is suited to substitute the constant value typically used in available CryoSat-2 SIT products. The limitation of the water density is too low spatial variability compared to the climatology used as validation data. Paper 2 suggests that this might be caused by mixing parameterisation and a too deep mixed layer. It was also found that the commonly neglected water density uncertainty in the error estimate of classically-derived CryoSat-2 SIT is based on inadequate assumptions. The uncertainty of water density in products using the classical approach is solely based on seasonal variability, but neglects spatial variability, which Paper 2 finds to add an extra uncertainty of $\pm$ 2.1 kg/m^3.

To assess the SIT difference that results from substituting the typical values used in available CryoSat-2 SIT products, the SIT difference was calculated based on 10 year mean values. These 10-year mean values were calculated for sea ice density, snow thickness and water density both from model and available CryoSat-2 SIT products in Paper 2. Based on this calculation, Paper 2 finds that the largest differences result from snow thickness and sea ice density, but that their SIT differences are of opposite signs at many locations. On average, Paper 2 finds, when substituting all values of sea ice density, snow thickness and water density leads to a difference of 0.12 m.

The final objective of this thesis was met in Paper 1, where the FB assimilation was presented. Paper 1 showed that the SIT from the three years of assimilation available (fbRun) is closer to the AWI SIT than the refRun. Since this thesis finds to several biases in the classically CryoSat-2-derived SIT products like the AWI SIT, the resulting

SIT also needed to be evaluated against independent observations. In the comparison to independent observations, the refRun compared better to the MOSAiC SIT observations and the fbRun better to the BGEP sea ice draft observations. Both refRun and fbRun compared better to the MOSAiC SIT observations than the AWI SIT. At the BGEP location, the AWI draft and fbRun draft compared similarly well to the observations and the refRun worse. To make a more certain statement, a longer assimilation run is needed. How such a run should be set up and which steps need to be taken to incorporate the findings of Paper 2 and the work in progress section is detailed in the outlook.

1 Outlook

From the work in progress section, it is evident that the form drag Parameterisation has the largest impact on the SIT and snow thickness. The results from chapter 3 section 3 show that the Lüpkes et al. (2012) and Tsamados et al. (2014) form drag formulations differ significantly. Their differences originate from the fact that Lüpkes et al. (2012) formulation only influences the dynamics, while the neutral drag parameter in Tsamados et al. (2014) also affects the bottom growth and snow sublimation. This means that investigating just the dynamically forced difference between the calculation of a form drag only depending on the SIC (Lüpkes et al., 2012) and the form drag depending on overall shape and size of the ice flow (Tsamados et al., 2014) is currently not possible. To conduct a study that systematically studies the differences between Lüpkes et al. (2012) and Tsamados et al. (2014), the following seven runs should be conducted:

1. SI3base: SI^3 run, everything equal to SI3ref, but constant drag coefficient equal to $Cd_a = 1.4e-3$ and $Cd_w = 5e-3$.

2. CICEbase: CICE run, everything equal to CICEref, but constant drag coefficient equal to $Cd_a = 1.4e-3$ and $Cd_w = 5e-3$.

3. CICEfdT: CICE run using Tsamados et al. (2014) form drag formulation.

4. SI3fdL: SI^3 run using Lüpkes et al. (2012) form drag formulation.

5. CICEdyn: CICE run using Tsamados et al. (2014) form drag formulation, but with the neutral drag coefficient used in the calculation of the atmospheric boundary layer stability set to $Cd_a = 1.4e-3$ and the Stanton number set to its original value, following McPhee et al. (2008).

6. CICEoc: like CICEdyn, but with the Stanton number equal to the neutral ocean drag parameter following Tsamados et al. (2014).

7. CICEatm: like CICEdyn, but with the neutral drag coefficient used in the calculation of the atmospheric boundary layer stability set to Tsamados et al. (2014) variable neutral drag coefficient Cd_a.

From the seven runs, the melt and growth rates as well as the ice transport and snow volume should be compared, to fully understand the origin of the difference between Lüpkes et al. (2012) and Tsamados et al. (2014) form drag parametrisations. The effect of FYI area in CICE should also be analysed to address the too low sea ice density in the Beaufort Sea found in Paper 2. Further, the snow volume and ice growth rates could be compared with MOSAiC in situ observations, to find the most realistic drag parametrisation to be used in future assimilation systems.

The three-year pilot study of FB assimilation in Paper 1 showed that FB assimilation can improve modelled SIT, at locations where observations were available. Degradation of the SIT at the MOSAiC locations are likely linked to biased FB observations assimilated. The assimilation study in this thesis, being over three years, is limited. An assimilation run spanning the entire CryoSat-2 observation period would be desirable. If the positive results from Paper 1 are reflected in this longer run, such a long run would allow assessing FB differences between CryoSat-2 and model, depending on snow depth and snow temperature. Such a study could quantify a relationship between FB biases and snow thickness and temperature, as found in observations (King et al., 2018; Kwok, 2014; Willatt et al., 2011). Prior to such a longer run, a sensitivity study tuning the model and observation errors should be conducted. This sensitivity study should examine the effect of the settings from one_p_m, vary_sp and same_w on a longer run with a focus on the radar FB. Further, it should be tested if the localization radius is ideal. Localisation is applied to avoid deficient long distance correlations, but if the localization radius is too small, it can introduce noise and even physical imbalance (Greybush et al., 2011; Kepert, 2009). The optimal localization radius depends on the size of the ensemble, the number of observations and state variables (Ying et al., 2018). Currently, the optimal localization radius is only determined for ensemble size of 80 ensembles and vary_sp ensemble construction. For the longer run, it should be determined how the optimal localization changes when changing the construction of the ensemble and the ensemble size. For the tuning study, the results from the above-detailed study of the form drag parameterisation should be taken into account, the new sea ice density should be used and the variable freezing point from chapter 3 section 3.2 should be implemented, as well as the iterative SIC and SIT distribution suggested by Gupta et al. (2021). The method by Gupta et al. (2021) is suggested, since it is already partly implemented. For in situ observation comparison for independent validation, the following data sets could be considered: the MOSAiC IMBs included in Paper 1 (Lei et al., 2021); BGEP data available for the entire CryoSat-2 period (Belter et al., 2019); monthly mean sea ice draft from upward-looking sonar in the Fram Strait (Sumata et al., 2021); daily sea ice draft from upward-looking sonar in the Laptev Sea covering the years 2013-2015 with breaks (Belter et al., 2019); SIT from drill holes from N-ICE2015 (Rösel and King, 2017)

taken in spring 2015 north-east of Svalbard. Such a large variety of observation data sets would allow the derived SIT to be evaluated at different locations and time scales within the Arctic Ocean. Finally, this longer run can be used to assess the model's skill in predicting the ice edge, following the methods of, for example, Lemieux et al. (2016) analysis of the model's persistence.

References

Abdalati, W., Zwally, H. J., Bindschadler, R., Csatho, B., Farrell, S. L., Fricker, H. A., Harding, D., Kwok, R., Lefsky, M., Markus, T., et al. (2010). The icesat-2 laser altimetry mission. *Proceedings of the IEEE*, 98(5):735–751.

Alexandrov, V., Sandven, S., Wahlin, J., and Johannessen, O. (2010). The relation between sea ice thickness and freeboard in the arctic. *The Cryosphere*, 4(3):373–380.

Assur, A. (1958). Arctic sea ice. *National Academy of Sciences-National Research Council. Chap. Composition of sea ice and its tensile strength*, pages 106–138.

Attema, E., Desnos, Y.-L., and Duchossois, G. (2000). Synthetic aperture radar in europe: Ers, envisat, and beyond. *Johns Hopkins APL technical digest*, 21(1):155–161.

Aubert, J. and Fournier, A. (2011). Inferring internal properties of earth's core dynamics and their evolution from surface observations and a numerical geodynamo model. *Nonlinear Processes in Geophysics*, 18(5):657–674.

Beaven, S., Lockhart, G., Gogineni, S., Hossetnmostafa, A., Jezek, K., Gow, A., Perovich, D., Fung, A., and Tjuatja, S. (1995). Laboratory measurements of radar backscatter from bare and snow-covered saline ice sheets. *International Journal of Remote Sensing*, 16(5):851–876.

Belter, H. J., Janout, M. A., Krumpen, T., Ross, E., Hölemann, J. A., Timokhov, L., Novikhin, A., Kassens, H., Wyatt, G., Rousseau, S., and Sadowy, D. (2019). Daily mean sea ice draft from moored Upward-Looking Sonars in the Laptev Sea between 2013 and 2015.

Bentsen, M., Evensen, G., Drange, H., and Jenkins, A. (1999). Coordinate transformation on a sphere using conformal mapping. *Monthly Weather Review*, 127(12):2733–2740.

Bitz, C. M., Holland, M. M., Weaver, A. J., and Eby, M. (2001). Simulating the ice-thickness distribution in a coupled climate model. *Journal of Geophysical Research: Oceans*, 106(C2):2441–2463.

Bitz, C. M. and Lipscomb, W. H. (1999). An energy-conserving thermodynamic model of sea ice. *Journal of Geophysical Research: Oceans*, 104(C7):15669–15677.

Björk, G. (1992). On the response of the equilibrium thickness distribution of sea ice to ice export, mechanical deformation, and thermal forcing with application to the arctic ocean. *Journal of Geophysical Research: Oceans*, 97(C7):11287–11298.

Blockley, E. W. and Peterson, K. A. (2018). Improving met office seasonal predictions of arctic sea ice using assimilation of cryosat-2 thickness. *The Cryosphere*, 12(11):3419–3438.

Bloom, S., Takacs, L., Da Silva, A., and Ledvina, D. (1996). Data assimilation using incremental analysis updates. *Monthly Weather Review*, 124(6):1256–1271.

Boetius, A., Albrecht, S., Bakker, K., Bienhold, C., Felden, J., Fernández-Méndez, M., Hendricks, S., Katlein, C., Lalande, C., Krumpen, T., et al. (2013). Export of algal biomass from the melting arctic sea ice. *Science*, 339(6126):1430–1432.

Briegleb, P. and Light, B. (2007). A delta-eddington mutiple scattering parameterization for solar radiation in the sea ice component of the community climate system model.

Budikova, D. (2009). Role of arctic sea ice in global atmospheric circulation: A review. *Global and Planetary Change*, 68(3):149–163.

Burgard, C., Notz, D., Pedersen, L. T., and Tonboe, R. T. (2020). The arctic ocean observation operator for 6.9 ghz (arc3o) – part 1: How to obtain sea ice brightness temperatures at 6.9 ghz from climate model output. *The Cryosphere*, 14(7):2369–2386.

by L. Timokhov, E. W. G. E. and Tanis., F. (1997). Environmental working group joint u.s.-russian atlas of the arctic ocean, version 1.

C3S (2024). Sea ice surface temperature daily data from 1982 to 2019 derived from satellite observations. Accessed on 25-03-2024.

Chen, Z., Liu, J., Song, M., Yang, Q., and Xu, S. (2017a). Impacts of assimilating satellite sea ice concentration and thickness on arctic sea ice prediction in the ncep climate forecast system. *Journal of Climate*, 30(21):8429–8446.

Chen, Z., Liu, J., Song, M., Yang, Q., and Xu, S. (2017b). Impacts of assimilating satellite sea ice concentration and thickness on arctic sea ice prediction in the ncep climate forecast system. *Journal of Climate*, 30(21):8429 – 8446.

Chenal, A., Testut, C.-E., Garnier, F., Laurent, P., and Gilles, G. (2022). Assimilation of cryosat-2 radar freeboard data in a global ocean-sea ice modelling system. In *EGU General Assembly Conference Abstracts*, pages EGU22–2061.

Cheng, S., Chen, Y., Aydoğdu, A., Bertino, L., Carrassi, A., Rampal, P., and Jones, C. K. R. T. (2023). Arctic sea ice data assimilation combining an ensemble kalman filter with a novel lagrangian sea ice model for the winter 2019–2020. *The Cryosphere*, 17(4):1735–1754.

Cipollone, A., Banerjee, D. S., Iovino, D., Aydogdu, A., and Masina, S. (2023). Bivariate sea-ice assimilation for global-ocean analysis–reanalysis. *Ocean Science*, 19(5):1375–1392.

Cohen, J., Screen, J. A., Furtado, J. C., Barlow, M., Whittleston, D., Coumou, D., Francis, J., Dethloff, K., Entekhabi, D., Overland, J., et al. (2014). Recent arctic amplification and extreme mid-latitude weather. *Nature geoscience*, 7(9):627–637.

Collow, T. W., Wang, W., Kumar, A., and Zhang, J. (2015). Improving arctic sea ice prediction using piomas initial sea ice thickness in a coupled ocean–atmosphere model. *Monthly Weather Review*, 143(11):4618 – 4630.

Commission, I. O. et al. (2015). The international thermodynamic equation of seawater–2010: calculation and use of thermodynamic properties.[includes corrections up to 31st october 2015].

Davis, C. H. (1997). A robust threshold retracking algorithm for measuring ice-sheet surface elevation change from satellite radar altimeters. *IEEE Transactions on Geoscience and Remote Sensing*, 35(4):974–979.

Dawson, G., Landy, J., Tsamados, M., Komarov, A. S., Howell, S., Heorton, H., and Krumpen, T. (2022). A 10-year record of arctic summer sea ice freeboard from cryosat-2. *Remote Sensing of Environment*, 268:112744.

Day, J., Hawkins, E., and Tietsche, S. (2014). Will arctic sea ice thickness initialization improve seasonal forecast skill? *Geophysical Research Letters*, 41(21):7566–7575.

Donlon, C., Berruti, B., Buongiorno, A., Ferreira, M.-H., Féménias, P., Frerick, J., Goryl, P., Klein, U., Laur, H., Mavrocordatos, C., et al. (2012). The global monitoring for environment and security (gmes) sentinel-3 mission. *Remote sensing of Environment*, 120:37–57.

Duarte, P., Meyer, A., Olsen, L. M., Kauko, H. M., Assmy, P., Rösel, A., Itkin, P., Hudson, S. R., Granskog, M. A., Gerland, S., Sundfjord, A., Steen, H., Hop, H., Cohen, L., Peterson, A. K., Jeffery, N., Elliott, S. M., Hunke, E. C., and Turner, A. K. (2017). Sea ice thermohaline dynamics and biogeochemistry in the arctic ocean: Empirical

and model results. *Journal of Geophysical Research: Biogeosciences*, 122(7):1632–1654.

Egbert, G. D. and Erofeeva, S. Y. (2002). Efficient inverse modeling of barotropic ocean tides. *Journal of Atmospheric and Oceanic technology*, 19(2):183–204.

Evensen, G. (1994). Sequential data assimilation with a nonlinear quasi-geostrophic model using monte carlo methods to forecast error statistics. *Journal of Geophysical Research: Oceans*, 99(C5):10143–10162.

Feltham, D., Untersteiner, N., Wettlaufer, J., and Worster, M. (2006). Sea ice is a mushy layer. *Geophysical Research Letters*, 33(14).

Fiedler, E. K., Martin, M. J., Blockley, E., Mignac, D., Fournier, N., Ridout, A., Shepherd, A., and Tilling, R. (2022). Assimilation of sea ice thickness derived from cryosat-2 along-track freeboard measurements into the met office's forecast ocean assimilation model (foam). *The Cryosphere*, 16(1):61–85.

Fofonoff, N. P. and Millard Jr, R. (1983). Algorithms for the computation of fundamental properties of seawater.

Garnier, F., Fleury, S., Garric, G., Bouffard, J., Tsamados, M., Laforge, A., Bocquet, M., Fredensborg Hansen, R. M., and Remy, F. (2021). Advances in altimetric snow depth estimates using bi-frequency saral and cryosat-2 ka–ku measurements. *The Cryosphere*, 15(12):5483–5512.

Gerland, S., Renner, A. H., Spreen, G., Wang, C., Beckers, J., Dumont, M., Granskog, M. A., Haapala, J., Haas, C., Helm, V., et al. (2012). In-situ calibration and validation of cryosat-2 observations over arctic sea ice north of svalbard. In *Proceedings paper (ESA-SP-712), ESA Earth Observation and Cryosphere Science Conference*, pages 13–16.

Giles, K. A. and Hvidegaard, S. M. (2006). Comparison of space borne radar altimetry and airborne laser altimetry over sea ice in the fram strait. *International Journal of Remote Sensing*, 27(15):3105–3113.

Glissenaar, I. A., Landy, J. C., Petty, A. A., Kurtz, N. T., and Stroeve, J. C. (2021). Impacts of snow data and processing methods on the interpretation of long-term changes in baffin bay early spring sea ice thickness. *The Cryosphere*, 15(10):4909–4927.

Greybush, S. J., Kalnay, E., Miyoshi, T., Ide, K., and Hunt, B. R. (2011). Balance and ensemble kalman filter localization techniques. *Monthly Weather Review*, 139(2):511 – 522.

Guemas, V., Blanchard-Wrigglesworth, E., Chevallier, M., Day, J. J., Déqué, M., Doblas-Reyes, F. J., Fučkar, N. S., Germe, A., Hawkins, E., Keeley, S., et al. (2016). A review on arctic sea-ice predictability and prediction on seasonal to decadal timescales. *Quarterly Journal of the Royal Meteorological Society*, 142(695):546–561.

Guerreiro, K. and Fleury, S. (2017). Legos altimetric sea ice thickness data product v1.

Guerreiro, K., Fleury, S., Zakharova, E., Kouraev, A., Rémy, F., and Maisongrande, P. (2017). Comparison of cryosat-2 and envisat radar freeboard over arctic sea ice: toward an improved envisat freeboard retrieval. *The Cryosphere*, 11(5):2059–2073.

Gupta, M., Caya, A., and Buehner, M. (2021). Assimilation of smos sea ice thickness in the regional ice prediction system. *International Journal of Remote Sensing*, 42(12):4583–4606.

Hendricks, S., Ricker, R., and Paul, S. (2021). Product user guide & algorithm specification: Awi cryosat-2 sea ice thickness (version 2.4).

Hersbach, H., Bell, B., Berrisford, P., Hirahara, S., Horányi, A., Muñoz Sabater, J., Nicolas, J., Peubey, C., Radu, R., Schepers, D., Simmons, A., Soci, C., Abdalla, S., Abellan, X., Balsamo, G., Bechtold, P., Biavati, G., Bidlot, J., Bonavita, M., De Chiara, G., Dahlgren, P., Dee, D., Diamantakis, M., Dragani, R., Flemming, J., Forbes, R., Fuentes, M., Geer, A., Haimberger, L., Healy, S., Hogan, R. J., Hólm, E., Janisková, M., Keeley, S., Laloyaux, P., Lopez, P., Lupu, C., Radnoti, G., de Rosnay, P., Rozum, I., Vamborg, F., Villaume, S., and Thépaut, J.-N. (2017). Complete era5: Fifth generation of ecmwf atmospheric reanalyses of the global climate. *Copernicus Climate Change Service (C3S) Data Store (CDS), accessed in 2021.*

Hibler, W. D. (1979). A dynamic thermodynamic sea ice model. *Journal of physical oceanography*, 9(4):815–846.

Holland, M. M., Bitz, C. M., Hunke, E. C., Lipscomb, W. H., and Schramm, J. L. (2006). Influence of the sea ice thickness distribution on polar climate in ccsm3. *Journal of Climate*, 19(11):2398–2414.

Hop, H., Vihtakari, M., Bluhm, B. A., Assmy, P., Poulin, M., Gradinger, R., Peeken, I., von Quillfeldt, C., Olsen, L. M., Zhitina, L., et al. (2020). Changes in sea-ice protist diversity with declining sea ice in the arctic ocean from the 1980s to 2010s. *Frontiers in Marine Science*, 7:243.

Hordoir, R., Skagseth, Ø., Ingvaldsen, R. B., Sandø, A. B., Löptien, U., Dietze, H., Gierisch, A. M., Assmann, K. M., Lundesgaard, Ø., and Lind, S. (2022). Changes in arctic stratification and mixed layer depth cycle: A modeling analysis. *Journal of Geophysical Research: Oceans*, 127(1):e2021JC017270.

Hudson, P. A., Martin, A. C. H., Josey, S. A., Marzocchi, A., and Angeloudis, A. (2024). Drivers of laptev sea interannual variability in salinity and temperature. *Ocean Science*, 20(2):341–367.

Hunke, E., Allard, R., Bailey, D. A., Blain, P., Craig, A., Dupont, F., DuVivier, A., Grumbine, R., Hebert, D., Holland, M., Jeffery, N., Lemieux, J.-F., Osinski, R., Rasmussen, T., Ribergaard, M., Roberts, A., Roy, F., Turner, M., and Worthen, D. (2021a). Cice-consortium/cice: Cice version 6.3.0.

Hunke, E., Allard, R., Bailey, D. A., Blain, P., Craig, A., Dupont, F., DuVivier, A., Grumbine, R., Hebert, D., Holland, M., Jeffery, N., Lemieux, J.-F., Osinski, R., Rasmussen, T., Ribergaard, M., Roberts, A., Turner, M., and Winton, M. (2021b). Cice-consortium/icepack: Icepack 1.2.5.

Hunke, E., Allard, R., Bailey, D. A., Blain, P., Craig, A., Dupont, F., DuVivier, A., Grumbine, R., Hebert, D., Holland, M., Jeffery, N., Lemieux, J.-F., Osinski, R., Rasmussen, T., Ribergaard, M., Roberts, A., Turner, M., Winton, M., and Rethmeier, S. (2021c). Cice version 6.2.0.

Hunke, E., Allard, R., Blain, P., Blockley, E., Feltham, D., Fichefet, T., Garric, G., Grumbine, R., Lemieux, J.-F., Rasmussen, T., et al. (2020). Should sea-ice modeling tools designed for climate research be used for short-term forecasting? *Current Climate Change Reports*, 6:121–136.

Hunke, E., Lipscomb, W., Jones, P., Turner, A., Jeffery, N., and Elliott, S. (2017). Cice, the los alamos sea ice model. Technical report, Los Alamos National Lab.(LANL), Los Alamos, NM (United States).

Hunke, E. C. and Dukowicz, J. K. (1997). An elastic–viscous–plastic model for sea ice dynamics. *Journal of Physical Oceanography*, 27(9):1849–1867.

Hunt, B. R., Kostelich, E. J., and Szunyogh, I. (2007). Efficient data assimilation for spatiotemporal chaos: A local ensemble transform kalman filter. *Physica D: Nonlinear Phenomena*, 230(1-2):112–126.

Huntemann, M., Heygster, G., Kaleschke, L., Krumpen, T., Mäkynen, M., and Drusch, M. (2014). Empirical sea ice thickness retrieval during the freeze-up period from smos high incident angle observations. *The Cryosphere*, 8(2):439–451.

Janout, M. A., Hölemann, J., Laukert, G., Smirnov, A., Krumpen, T., Bauch, D., and Timokhov, L. (2020). On the variability of stratification in the freshwater-influenced laptev sea region. *Frontiers in Marine Science*, 7:543489.

Ji, Q., Li, B., Pang, X., Zhao, X., and Lei, R. (2021). Arctic sea ice density observation and its impact on sea ice thickness retrieval from cryosat–2. *Cold Regions Science and Technology*, 181:103177.

Johannessen, O. M., Shalina, E. V., and Miles, M. W. (1999). Satellite evidence for an arctic sea ice cover in transformation. *Science*, 286(5446):1937–1939.

Joseph, J. H., Wiscombe, W., and Weinman, J. (1976). The delta-eddington approximation for radiative flux transfer. *Journal of Atmospheric Sciences*, 33(12):2452–2459.

Joshi, P., Oza, S. R., Gupta, U. K., Saini, S., Rajak, D. R., Bahuguna, I., Rajawat, A., and Kumar, R. (2020). Estimation of sea ice thickness from saral/altika in drifting orbit phase. *Marine Geodesy*, 43(3):302–323.

Jutila, A., Hendricks, S., Ricker, R., von Albedyll, L., Krumpen, T., and Haas, C. (2022). Retrieval and parameterisation of sea-ice bulk density from airborne multisensor measurements. *The Cryosphere*, 16(1):259–275.

Kalman, R. E. and Bucy, R. S. (1961). New results in linear filtering and prediction theory.

Kaminski, T., Kauker, F., Toudal Pedersen, L., Voßbeck, M., Haak, H., Niederdrenk, L., Hendricks, S., Ricker, R., Karcher, M., Eicken, H., et al. (2018). Arctic mission benefit analysis: impact of sea ice thickness, freeboard, and snow depth products on sea ice forecast performance. *The Cryosphere*, 12(8):2569–2594.

Kepert, J. D. (2009). Covariance localisation and balance in an ensemble kalman filter. *Quarterly Journal of the Royal Meteorological Society*, 135(642):1157–1176.

Kern, S., Khvorostovsky, K., Skourup, H., Rinne, E., Parsakhoo, Z., Djepa, V., Wadhams, P., and Sandven, S. (2015). The impact of snow depth, snow density and ice density on sea ice thickness retrieval from satellite radar altimetry: results from the esa-cci sea ice ecv project round robin exercise. *The Cryosphere*, 9(1):37–52.

Khohlov, G. P. (1978). Physico-chemical characteristics of the upper layers of different sea ice types in the area near of “np-22” drifting station. Trudy Arkticheskogo i Antarkticheskogo Instituta, 359, 4–12.

King, J., Skourup, H., Hvidegaard, S. M., Rösel, A., Gerland, S., Spreen, G., Polashenski, C., Helm, V., and Liston, G. E. (2018). Comparison of freeboard retrieval and ice thickness calculation from als, asiras, and cryosat-2 in the norwegian arctic to field measurements made during the n-ice2015 expedition. *Journal of Geophysical Research: Oceans*, 123(2):1123–1141.

Kinnard, C., Zdanowicz, C. M., Koerner, R. M., and Fisher, D. A. (2008). A changing arctic seasonal ice zone: Observations from 1870–2003 and possible oceanographic consequences. *Geophysical Research Letters*, 35(2).

Krishfield, R., Toole, J., Proshutinsky, A., and Timmermans, M.-L. (2008). Automated ice-tethered profilers for seawater observations under pack ice in all seasons. *Journal of Atmospheric and Oceanic Technology*, 25(11):2091 – 2105.

Kumar, R., Li, J., Hedstrom, K., Babanin, A. V., Holland, D. M., Heil, P., and Tang, Y. (2021). Intercomparison of arctic sea ice simulation in roms-cice and roms-budgell. *Polar Science*, 29:100716.

Kurtz, N., Farrell, S., Studinger, M., Galin, N., Harbeck, J., Lindsay, R., Onana, V., Panzer, B., and Sonntag, J. (2013). Sea ice thickness, freeboard, and snow depth products from operation icebridge airborne data. *The Cryosphere*, 7(4):1035–1056.

Kurtz, N. T. and Farrell, S. L. (2011). Large-scale surveys of snow depth on arctic sea ice from operation icebridge. *Geophysical Research Letters*, 38(20).

Kurtz, N. T., Galin, N., and Studinger, M. (2014). An improved cryosat-2 sea ice freeboard retrieval algorithm through the use of waveform fitting. *The Cryosphere*, 8(4):1217–1237.

Kwok, R. (2014). Simulated effects of a snow layer on retrieval of cryosat-2 sea ice freeboard. *Geophysical Research Letters*, 41(14):5014–5020.

Kwok, R. and Cunningham, G. (2015). Variability of arctic sea ice thickness and volume from cryosat-2. *Philosophical Transactions of the Royal Society A: Mathematical, Physical and Engineering Sciences*, 373(2045):20140157.

Kwok, R., Panzer, B., Leuschen, C., Pang, S., Markus, T., Holt, B., and Gogineni, S. (2011). Airborne surveys of snow depth over arctic sea ice. *Journal of Geophysical Research: Oceans*, 116(C11).

Laforge, A., Fleury, S., Dinardo, S., Garnier, F., Remy, F., Benveniste, J., Bouffard, J., and Verley, J. (2021). Toward improved sea ice freeboard observation with sar altimetry using the physical retracker samosa+. *Advances in Space Research*, 68(2):732–745.

Landy, J. C., Dawson, G. J., Tsamados, M., Bushuk, M., Stroeve, J. C., Howell, S. E., Krumpen, T., Babb, D. G., Komarov, A. S., Heorton, H. D., et al. (2022). A year-round satellite sea-ice thickness record from cryosat-2. *Nature*, 609(7927):517–522.

Landy, J. C., Petty, A. A., Tsamados, M., and Stroeve, J. C. (2020). Sea ice roughness overlooked as a key source of uncertainty in cryosat-2 ice freeboard retrievals. *Journal of Geophysical Research: Oceans*, 125(5):e2019JC015820.

Lannuzel, D., Tedesco, L., Van Leeuwe, M., Campbell, K., Flores, H., Delille, B., Miller, L., Stefels, J., Assmy, P., Bowman, J., et al. (2020). The future of arctic sea-ice biogeochemistry and ice-associated ecosystems. *Nature Climate Change*, 10(11):983–992.

Lawrence, I. R., Armitage, T. W., Tsamados, M. C., Stroeve, J. C., Dinardo, S., Ridout, A. L., Muir, A., Tilling, R. L., and Shepherd, A. (2021). Extending the arctic sea ice freeboard and sea level record with the sentinel-3 radar altimeters. *Advances in Space Research*, 68(2):711–723.

Lawrence, I. R., Tsamados, M. C., Stroeve, J. C., Armitage, T. W., and Ridout, A. L. (2018). Estimating snow depth over arctic sea ice from calibrated dual-frequency radar freeboards. *The Cryosphere*, 12(11):3551–3564.

Laxon, S., Peacock, N., and Smith, D. (2003). High interannual variability of sea ice thickness in the arctic region. *Nature*, 425(6961):947–950.

Laxon, S. W., Giles, K. A., Ridout, A. L., Wingham, D. J., Willatt, R., Cullen, R., Kwok, R., Schweiger, A., Zhang, J., Haas, C., et al. (2013). Cryosat-2 estimates of arctic sea ice thickness and volume. *Geophysical Research Letters*, 40(4):732–737.

Lei, R., Cheng, B., Hoppmann, M., and Zuo, G. (2021). Snow depth and sea ice thickness derived from the measurements of simba buoys deployed in the arctic ocean during the legs 1a, 1, and 3 of the mosaic campaign in 2019-2020. *PANGAEA. DOI: http://dx. doi. org/10.1594/PANGAEA*, 938244.

Lellouche, J.-M., Greiner, E., Bourdallé-Badie, R., Garric, G., Melet, A., Drévillon, M., Bricaud, C., Hamon, M., Le Galloudec, O., Regnier, C., et al. (2021). The copernicus global 1/12° oceanic and sea ice glorys12 reanalysis. *Frontiers in Earth Science*, 9:585.

Lemieux, J.-F., Beaudoin, C., Dupont, F., Roy, F., Smith, G. C., Shlyaeva, A., Buehner, M., Caya, A., Chen, J., Carrieres, T., Pogson, L., DeRepentigny, P., Plante, A., Pestieau, P., Pellerin, P., Ritchie, H., Garric, G., and Ferry, N. (2016). The regional ice prediction system (rips): verification of forecast sea ice concentration. *Quarterly Journal of the Royal Meteorological Society*, 142(695):632–643.

Levitus, S. (2012). The unesco-ioc-iode" global oceanographic data archeology and rescue"(godar) project and" world ocean database" project. *Data Science Journal*, 11:46–71.

Liang, X., Losch, M., Nerger, L., Mu, L., Yang, Q., and Liu, C. (2019). Using sea surface temperature observations to constrain upper ocean properties in an arctic sea ice-ocean data assimilation system. *Journal of Geophysical Research: Oceans*, 124(7):4727–4743.

Liang, Y.-c., Kwon, Y.-O., Frankignoul, C., Danabasoglu, G., Yeager, S., Cherchi, A., Gao, Y., Gastineau, G., Ghosh, R., Matei, D., et al. (2020). Quantification of the arctic sea ice-driven atmospheric circulation variability in coordinated large ensemble simulations. *Geophysical research letters*, 47(1):e2019GL085397.

Lipscomb, W. H. and Hunke, E. C. (2004). Modeling sea ice transport using incremental remapping. *Monthly weather review*, 132(6):1341–1354.

Lisæter, K. A., Rosanova, J., and Evensen, G. (2003). Assimilation of ice concentration in a coupled ice–ocean model, using the ensemble kalman filter. *Ocean Dynamics*, 53(4):368–388.

Liston, G. E., Itkin, P., Stroeve, J., Tschudi, M., Stewart, J. S., Pedersen, S. H., Reinking, A. K., and Elder, K. (2020). A lagrangian snow-evolution system for sea-ice applications (snowmodel-lg): Part i—model description. *Journal of Geophysical Research: Oceans*, 125(10):e2019JC015913.

Long, M., Zhang, L., Hu, S., and Qian, S. (2021). Multi-aspect assessment of cmip6 models for arctic sea ice simulation. *Journal of Climate*, 34(4):1515–1529.

Louet, J. and Bruzzi, S. (1999). Envisat mission and system. In *IEEE 1999 International Geoscience and Remote Sensing Symposium. IGARSS'99 (Cat. No. 99CH36293)*, volume 3, pages 1680–1682. IEEE.

Lüpkes, C., Gryanik, V. M., Hartmann, J., and Andreas, E. L. (2012). A parametrization, based on sea ice morphology, of the neutral atmospheric drag coefficients for weather prediction and climate models. *Journal of Geophysical Research: Atmospheres*, 117(D13).

Madec, G., Bourdallé-Badie, R., Bouttier, P.-A., Bricaud, C., Bruciaferri, D., Calvert, D., Chanut, J., Clementi, E., Coward, A., Delrosso, D., et al. (2017). Nemo ocean engine.

Mallett, R. D., Lawrence, I. R., Stroeve, J. C., Landy, J. C., and Tsamados, M. (2020). Brief communication: Conventional assumptions involving the speed of radar waves in snow introduce systematic underestimates to sea ice thickness and seasonal growth rate estimates. *The Cryosphere*, 14(1):251–260.

Mallett, R. D., Stroeve, J. C., Tsamados, M., Landy, J. C., Willatt, R., Nandan, V., and Liston, G. E. (2021a). Faster decline and higher variability in the sea ice thickness of the marginal arctic seas when accounting for dynamic snow cover. *The Cryosphere*, 15(5):2429–2450.

Mallett, R. D. C., Stroeve, J. C., Tsamados, M., Landy, J. C., Willatt, R., Nandan, V., and Liston, G. E. (2021b). Faster decline and higher variability in the sea ice thickness of the marginal arctic seas when accounting for dynamic snow cover. *The Cryosphere*, 15(5):2429–2450.

Martino, A. J., Neumann, T. A., Kurtz, N. T., and McLennan, D. (2019). Icesat-2 mission overview and early performance. In *Sensors, systems, and next-generation satellites XXIII*, volume 11151, pages 68–77. SPIE.

Maslowski, W., Clement Kinney, J., Higgins, M., and Roberts, A. (2012). The future of arctic sea ice. *Annual Review of Earth and Planetary Sciences*, 40(Volume 40, 2012):625–654.

Mathiot, P., König Beatty, C., Fichefet, T., Goosse, H., Massonnet, F., and Vancoppenolle, M. (2012). Better constraints on the sea-ice state using global sea-ice data assimilation. *Geoscientific Model Development*, 5(6):1501–1515.

Maykut, G. A. (1982). Large-scale heat exchange and ice production in the central arctic. *Journal of Geophysical Research: Oceans*, 87(C10):7971–7984.

Maykut, G. A. and Untersteiner, N. (1971). Some results from a time-dependent thermodynamic model of sea ice. *Journal of Geophysical Research*, 76(6):1550–1575.

McPhee, M., Morison, J., and Nilsen, F. (2008). Revisiting heat and salt exchange at the ice-ocean interface: Ocean flux and modeling considerations. *Journal of Geophysical Research: Oceans*, 113(C6).

Mélia, D. S. (2002). A global coupled sea ice–ocean model. *Ocean Modelling*, 4(2):137–172.

Meloni, M., Bouffard, J., Parrinello, T., Dawson, G., Garnier, F., Helm, V., Di Bella, A., Hendricks, S., Ricker, R., Webb, E., et al. (2020). Cryosat ice baseline-d validation and evolutions. *The Cryosphere*, 14(6):1889–1907.

Mignac, D., Martin, M., Fiedler, E., Blockley, E., and Fournier, N. (2022). Improving the met office's forecast ocean assimilation model (foam) with the assimilation of satellite-derived sea-ice thickness data from cryosat-2 and smos in the arctic. *Quarterly Journal of the Royal Meteorological Society*, 148(744):1144–1167.

Mu, L., Nerger, L., Tang, Q., Loza, S. N., Sidorenko, D., Wang, Q., Semmler, T., Zampieri, L., Losch, M., and Goessling, H. F. (2020). Toward a data assimilation system for seamless sea ice prediction based on the awi climate model. *Journal of Advances in Modeling Earth Systems*, 12(4):e2019MS001937. e2019MS001937 10.1029/2019MS001937.

Mu, L., Yang, Q., Losch, M., Losa, S. N., Ricker, R., Nerger, L., and Liang, X. (2018). Improving sea ice thickness estimates by assimilating cryosat-2 and smos sea ice thickness data simultaneously. *Quarterly Journal of the Royal Meteorological Society*, 144(711):529–538.

Nab, C., Mallett, R., Gregory, W., Landy, J., Lawrence, I., Willatt, R., Stroeve, J., and Tsamados, M. (2023). Synoptic variability in satellite altimeter-derived radar freeboard of arctic sea ice. *Geophysical Research Letters*, 50(2):e2022GL100696. e2022GL100696 2022GL100696.

Nakamura, K., Wakabayashi, H., Uto, S., Ushio, S., and Nishio, F. (2009). Observation of sea-ice thickness using envisat data from lÜtzow-holm bay, east antarctica. *IEEE Geoscience and Remote Sensing Letters*, 6(2):277–281.

Nandan, V., Geldsetzer, T., Yackel, J., Mahmud, M., Scharien, R., Howell, S., King, J., Ricker, R., and Else, B. (2017). Effect of snow salinity on cryosat-2 arctic first-year sea ice freeboard measurements. *Geophysical Research Letters*, 44(20):10–419.

Nerger, L. (2024). Offline mode: Implementation guide.

Nerger, L. and Hiller, W. (2013). Software for ensemble-based data assimilation systems—implementation strategies and scalability. *Computers & Geosciences*, 55:110–118.

Nerger, L., Janjić, T., Schröter, J., and Hiller, W. (2012). A regulated localization scheme for ensemble-based kalman filters. *Quarterly Journal of the Royal Meteorological Society*, 138(664):802–812.

Nicolaus, M., Perovich, D. K., Spreen, G., Granskog, M. A., von Albedyll, L., Angelopoulos, M., Anhaus, P., Arndt, S., Belter, H. J., Bessonov, V., Birnbaum, G., Brauchle, J., Calmer, R., Cardellach, E., Cheng, B., Clemens-Sewall, D., Dadic, R., Damm, E., de Boer, G., Demir, O., Dethloff, K., Divine, D. V., Fong, A. A., Fons, S., Frey, M. M., Fuchs, N., Gabarró, C., Gerland, S., Goessling, H. F., Gradinger, R., Haapala, J., Haas, C., Hamilton, J., Hannula, H.-R., Hendricks, S., Herber, A., Heuzé, C., Hoppmann, M., Høyland, K. V., Huntemann, M., Hutchings, J. K., Hwang, B., Itkin, P., Jacobi, H.-W., Jaggi, M., Jutila, A., Kaleschke, L., Katlein, C., Kolabutin, N., Krampe, D., Kristensen, S. S., Krumpen, T., Kurtz, N., Lampert, A., Lange, B. A., Lei, R., Light, B., Linhardt, F., Liston, G. E., Loose, B., Macfarlane, A. R., Mahmud, M., Matero, I. O., Maus, S., Morgenstern, A., Naderpour, R., Nandan, V., Niubom, A., Oggier, M., Oppelt, N., Pätzold, F., Perron, C., Petrovsky, T., Pirazzini, R., Polashenski, C., Rabe, B., Raphael, I. A., Regnery, J., Rex, M., Ricker, R., Riemann-Campe, K., Rinke, A., Rohde, J., Salganik, E., Scharien, R. K., Schiller, M., Schneebeli, M., Semmling, M., Shimanchuk, E., Shupe, M. D., Smith, M. M., Smolyanitsky, V., Sokolov, V., Stanton, T., Stroeve, J., Thielke, L., Timofeeva, A., Tonboe, R. T., Tavri, A., Tsamados, M., Wagner, D. N., Watkins, D., Webster, M., and Wendisch, M. (2022). Overview of the MOSAiC expedition: Snow and sea ice. *Elementa: Science of the Anthropocene*, 10(1):000046.

Nielsen-Englyst, P., Høyer, J. L., Kolbe, W. M., Dybkjær, G., Lavergne, T., Tonboe, R. T., Skarpalezos, S., and Karagali, I. (2023). A combined sea and sea-ice surface temperature climate dataset of the arctic, 1982–2021. *Remote Sensing of Environment*, 284:113331.

Notz, D., Jahn, A., Holland, M., Hunke, E., Massonnet, F., Stroeve, J., Tremblay, B., and Vancoppenolle, M. (2016). The cmip6 sea-ice model intercomparison project (simip): understanding sea ice through climate-model simulations. *Geoscientific Model Development*, 9(9):3427–3446.

Oggier, M., Salganik, E., Whitmore, L., Fong, A. A., Hoppe, C. J. M., Rember, R., Høyland, K. V., Divine, D. V., Gradinger, R., Fons, S. W., Abrahamsson, K., Aguilar-Islas, A. M., Angelopoulos, M., Arndt, S., Balmonte, J. P., Bozzato, D., Bowman, J. S., Castellani, G., Chamberlain, E., Creamean, J., D'Angelo, A., Damm, E., Dumitrascu, A., Eggers, S. L., Gardner, J., Grosfeld, L., Haapala, J., Immerz, A., Kolabutin, N., Lange, B. A., Lei, R., Marsay, C. M., Maus, S., Müller, O., Olsen, L. M., Nuibom, A., Ren, J., Rinke, A., Sheikin, I., Shimanchuk, E., Snoeijs-Leijonmalm, P., Spahic, S., Stefels, J., Torres-Valdés, S., Torstensson, A., Ulfsbo, A., Verdugo, J., Vortkamp, M., Wang, L., Webster, M., Wischnewski, L., and Granskog, M. A. (2023a). First-year sea-ice salinity, temperature, density, oxygen and hydrogen isotope composition from the main coring site (MCS-FYI) during MOSAiC legs 1 to 4 in 2019/2020.

Oggier, M., Salganik, E., Whitmore, L., Fong, A. A., Hoppe, C. J. M., Rember, R., Høyland, K. V., Gradinger, R., Divine, D. V., Fons, S. W., Abrahamsson, K., Aguilar-Islas, A. M., Angelopoulos, M., Arndt, S., Balmonte, J. P., Bozzato, D., Bowman, J. S., Castellani, G., Chamberlain, E., Creamean, J., D'Angelo, A., Damm, E., Dumitrascu, A., Eggers, L., Gardner, J., Grosfeld, L., Haapala, J., Immerz, A., Kolabutin, N., Lange, B. A., Lei, R., Marsay, C. M., Maus, S., Olsen, L. M., Müller, O., Nuibom, A., Ren, J., Rinke, A., Sheikin, I., Shimanchuk, E., Snoeijs-Leijonmalm, P., Spahic, S., Stefels, J., Torres-Valdés, S., Torstensson, A., Ulfsbo, A., Verdugo, J., Vortkamp, M., Wang, L., Webster, M., Wischnewski, L., and Granskog, M. A. (2023b). Second-year sea-ice salinity, temperature, density, oxygen and hydrogen isotope composition from the main coring site (MCS-SYI) during MOSAiC legs 1 to 4 in 2019/2020.

Ordoñez, A. C., Bitz, C. M., and Blanchard-Wrigglesworth, E. (2018). Processes controlling arctic and antarctic sea ice predictability in the community earth system model. *Journal of Climate*, 31(23):9771–9786.

OSISAF (2017). Global sea ice concentration climate data record v2. 0–multimission, eumetsat saf on ocean and sea ice.

OSISAF (2022). Global sea ice concentration interim climate data record release 3 - dmsp, eumetsat saf on ocean and sea ice.

Petty, A. A., Kurtz, N. T., Kwok, R., Markus, T., and Neumann, T. A. (2020). Winter arctic sea ice thickness from icesat-2 freeboards. *Journal of Geophysical Research: Oceans*, 125(5):e2019JC015764. e2019JC015764 2019JC015764.

Petty, A. A., Webster, M., Boisvert, L., and Markus, T. (2018). The nasa eulerian snow on sea ice model (nesosim) v1. 0: initial model development and analysis. *Geoscientific Model Development*, 11(11):4577–4602.

Pham, D. T. (2001). Stochastic methods for sequential data assimilation in strongly nonlinear systems. *Monthly weather review*, 129(5):1194–1207.

Ponsoni, L., Ribergaard, M. H., Nielsen-Englyst, P., Wulf, T., Buus-Hinkler, J., Kreiner, M. B., and Rasmussen, T. A. S. (2023). Greenlandic sea ice products with a focus on an updated operational forecast system. *Frontiers in Marine Science*, 10:138.

Posey, P. G., Metzger, E., Wallcraft, A., Hebert, D., Allard, R., Smedstad, O., Phelps, M., Fetterer, F., Stewart, J., Meier, W., et al. (2015). Improving arctic sea ice edge forecasts by assimilating high horizontal resolution sea ice concentration data into the us navy's ice forecast systems. *The Cryosphere*, 9(4):1735–1745.

Prather, M. J. (1986). Numerical advection by conservation of second-order moments. *Journal of Geophysical Research: Atmospheres*, 91(D6):6671–6681.

Quartly, G. D., Rinne, E., Passaro, M., Andersen, O. B., Dinardo, S., Fleury, S., Guillot, A., Hendricks, S., Kurekin, A. A., Müller, F. L., Ricker, R., Skourup, H., and Tsamados, M. (2019). Retrieving sea level and freeboard in the arctic: A review of current radar altimetry methodologies and future perspectives. *Remote Sensing*, 11(7).

Rabe, B., Karcher, M., Kauker, F., Schauer, U., Toole, J., Krishfield, R., Pisarev, S., Kikuchi, T., and Su, J. (2014). Arctic ocean basin liquid freshwater storage trend 1992–2012. *Geophysical Research Letters*, 41(3):961–968.

Rasmussen, T. A., Høyer, J. L., Ghent, D., Bulgin, C. E., Dybkjær, G., Ribergaard, M. H., Nielsen-Englyst, P., and Madsen, K. S. (2018). Impact of assimilation of sea-ice surface temperatures on a coupled ocean and sea-ice model. *Journal of Geophysical Research: Oceans*, 123(4):2440–2460.

Ricker, R., Hendricks, S., Helm, V., Skourup, H., and Davidson, M. (2014). Sensitivity of cryosat-2 arctic sea-ice freeboard and thickness on radar-waveform interpretation. *The Cryosphere*, 8(4):1607–1622.

Ricker, R., Hendricks, S., Kaleschke, L., Tian-Kunze, X., King, J., and Haas, C. (2017). A weekly arctic sea-ice thickness data record from merged cryosat-2 and smos satellite data. *The Cryosphere*, 11(4):1607–1623.

Ricker, R., Hendricks, S., Perovich, D. K., Helm, V., and Gerdes, R. (2015). Impact of snow accumulation on cryosat-2 range retrievals over arctic sea ice: An observational approach with buoy data. *Geophysical Research Letters*, 42(11):4447–4455.

Roach, L. A., Bitz, C. M., Horvat, C., and Dean, S. M. (2019). Advances in modeling interactions between sea ice and ocean surface waves. *Journal of Advances in Modeling Earth Systems*, 11(12):4167–4181.

Roach, L. A., Horvat, C., Dean, S. M., and Bitz, C. M. (2018). An emergent sea ice floe size distribution in a global coupled ocean-sea ice model. *Journal of Geophysical Research: Oceans*, 123(6):4322–4337.

Romanov, I. (2004). Morphometric characteristics of ice and snow in the arctic basin: Aircraft landing observations from the former soviet union, 1928–1989. *National Snow and Ice Data Center, Boulder, CO, digital media.[Available online at http://nsidc. org/data/g02140. html.]*.

Rösel, A. and King, J. (2017). N-ice2015 ice thickness, snow thickness, and freeboard from thickness drillings [data set]. *Norwegian Polar Institute*.

Rostosky, P., Spreen, G., Farrell, S. L., Frost, T., Heygster, G., and Melsheimer, C. (2018). Snow depth retrieval on arctic sea ice from passive microwave radiometers—improvements and extensions to multiyear ice using lower frequencies. *Journal of Geophysical Research: Oceans*, 123(10):7120–7138.

Rousset, C., Vancoppenolle, M., Madec, G., Fichefet, T., Flavoni, S., Barthélemy, A., Benshila, R., Chanut, J., Lévy, C., Masson, S., et al. (2015). The louvain-la-neuve sea ice model lim3. 6: global and regional capabilities. *Geoscientific Model Development*, 8(10):2991–3005.

Sakov, P., Counillon, F., Bertino, L., Lisæter, K. A., Oke, P. R., and Korablev, A. (2012). Topaz4: an ocean-sea ice data assimilation system for the north atlantic and arctic. *Ocean Science*, 8(4):633–656.

Salas Mélia, D. (2002). A global coupled sea ice–ocean model. *Ocean Modelling*, 4(2):137–172.

Saldo, R. (2022). Global sea ice concentration climate data records scientific validation report.

Sallila, H., Farrell, S. L., McCurry, J., and Rinne, E. (2019). Assessment of contemporary satellite sea ice thickness products for arctic sea ice. *The Cryosphere*, 13(4):1187–1213.

Schramm, J., Holland, M., Curry, J., and Ebert, E. (1997). Modeling the thermodynamics of a sea ice thickness distribution: 1. sensitivity to ice thickness resolution. *Journal of Geophysical Research: Oceans*, 102(C10):23079–23091.

Serreze, M. C., Barrett, A. P., Slater, A. G., Steele, M., Zhang, J., and Trenberth, K. E. (2007). The large-scale energy budget of the arctic. *Journal of Geophysical Research: Atmospheres*, 112(D11).

Shalina, E. V. and Sandven, S. (2018). Snow depth on arctic sea ice from historical in situ data. *The Cryosphere*, 12(6):1867–1886.

Shi, H., Sohn, B.-J., Dybkjær, G., Tonboe, R. T., and Lee, S.-M. (2020). Simultaneous estimation of wintertime sea ice thickness and snow depth from space-borne freeboard measurements. *The Cryosphere*, 14(11):3761–3783.

Shiklomanov, A., Déry, S., Tretiakov, M., Yang, D., Magritsky, D., Georgiadi, A., and Tang, W. (2021). River freshwater flux to the arctic ocean. *Arctic hydrology, permafrost and ecosystems*, pages 703–738.

Shokr, M. and Sinha, N. (2015). Ice physics and physical processes. *John Wiley and Sons„ Ltd: New York, NY, USA Sons, doi*, 10:9781119028000.

Shu, Q., Qiao, F., Liu, J., Song, Z., Chen, Z., Zhao, J., Yin, X., and Song, Y. (2021). Arctic sea ice concentration and thickness data assimilation in the fio-esm climate forecast system. *Acta Oceanologica Sinica*, 40:65–75.

Sievers, I., Gierisch, A. M., Rasmussen, T. A., Hordoir, R., and Stenseng, L. (2022). Arctic sea ice and snow from different ice models: A cice–si3 intercomparison study. *The Cryosphere Discussions*, pages 1–34.

Sievers, I., Rasmussen, T. A. S., and Stenseng, L. (2023a). Assimilating cryosat-2 freeboard to improve arctic sea ice thickness estimates. *The Cryosphere*, 17(9):3721–3738.

Sievers, I., Skourup, H., and Rasmussen, T. A. S. (2023b). The variability of cryosat-2 derived sea ice thickness introduced by modelled vs. empirical snow thickness, sea ice density and water density. *The Cryosphere Discussions*, 2023:1–25.

Simmonds, I. (2015). Comparing and contrasting the behaviour of arctic and antarctic sea ice over the 35 year period 1979-2013. *Annals of Glaciology*, 56(69):18–28.

Sissala, J. E., Sabatini, R. R., and Ackermann, H. J. (1972). Nimbus satellite data for polar ice survey. *Polar Record*, 16(102):367–373.

Smith, G. C., Liu, Y., Benkiran, M., Chikhar, K., Surcel Colan, D., Gauthier, A.-A., Testut, C.-E., Dupont, F., Lei, J., Roy, F., et al. (2021). The regional ice ocean prediction system v2: a pan-canadian ocean analysis system using an online tidal harmonic analysis. *Geoscientific Model Development*, 14(3):1445–1467.

Smith, G. C., Roy, F., Reszka, M., Surcel Colan, D., He, Z., Deacu, D., Belanger, J.-M., Skachko, S., Liu, Y., Dupont, F., Lemieux, J.-F., Beaudoin, C., Tranchant, B., Drévillon, M., Garric, G., Testut, C.-E., Lellouche, J.-M., Pellerin, P., Ritchie, H., Lu, Y., Davidson, F., Buehner, M., Caya, A., and Lajoie, M. (2016). Sea ice forecast

verification in the canadian global ice ocean prediction system. *Quarterly Journal of the Royal Meteorological Society*, 142(695):659–671.

Smolarkiewicz, P. (1996). A synchronous and iterative flux-correction formalism for coupled transport equations. *J. Comput. Phys*, 128:101.

Steele, M., Morley, R., and Ermold, W. (2001). Phc: A global ocean hydrography with a high-quality arctic ocean. *J. Climate*, 14:2079–2087.

Stroeve, J. and Notz, D. (2018). Changing state of arctic sea ice across all seasons. *Environmental Research Letters*, 13(10):103001.

Stroeve, J., Serreze, M., Drobot, S., Gearheard, S., Holland, M., Maslanik, J., Meier, W., and Scambos, T. (2008). Arctic sea ice extent plummets in 2007. *Eos, Transactions American Geophysical Union*, 89(2):13–14.

Stroeve, J. C., Serreze, M. C., Barrett, A., and Kindig, D. N. (2011). Attribution of recent changes in autumn cyclone associated precipitation in the arctic. *Tellus A: Dynamic Meteorology and Oceanography*, 63(4):653–663.

Sumata, H., de Steur, L., and Divine, D. V. (2021). Monthly mean sea ice draft from the fram strait arctic outflow observatory since 1990. *Norwegian Polar Institute*.

Tian, T., Yang, S., Høyer, J. L., Nielsen-Englyst, P., and Singha, S. (2024). Cooler arctic surface temperatures simulated by climate models are closer to satellite-based data than the era5 reanalysis. *Communications Earth & Environment*, 5(1):111.

Tian-Kunze, X., Kaleschke, L., Maaß, N., Mäkynen, M., Serra, N., Drusch, M., and Krumpen, T. (2014). Smos-derived thin sea ice thickness: algorithm baseline, product specifications and initial verification. *The Cryosphere*, 8(3):997–1018.

Tilling, R. L., Ridout, A., and Shepherd, A. (2018). Estimating arctic sea ice thickness and volume using cryosat-2 radar altimeter data. *Advances in Space Research*, 62(6):1203–1225.

Timco, G. and Frederking, R. (1996). A review of sea ice density. *Cold regions science and technology*, 24(1):1–6.

Tsamados, M., Feltham, D., Petty, A., Schroeder, D., and Flocco, D. (2015). Processes controlling surface, bottom and lateral melt of arctic sea ice in a state of the art sea ice model. *Philosophical Transactions of the Royal Society A: Mathematical, Physical and Engineering Sciences*, 373(2052):20140167.

Tsamados, M., Feltham, D. L., Schroeder, D., Flocco, D., Farrell, S. L., Kurtz, N., Laxon, S. W., and Bacon, S. (2014). Impact of variable atmospheric and oceanic form drag on simulations of arctic sea ice. *Journal of Physical Oceanography*, 44(5):1329–1353.

Tschudi, M. A., Stroeve, J. C., and Stewart, J. S. (2016). Relating the age of arctic sea ice to its thickness, as measured during nasa's icesat and icebridge campaigns. *Remote Sensing*, 8(6):457.

Turner, A. K. and Hunke, E. C. (2015). Impacts of a mushy-layer thermodynamic approach in global sea-ice simulations using the cice sea-ice model. *Journal of Geophysical Research: Oceans*, 120(2):1253–1275.

Turner, A. K., Hunke, E. C., and Bitz, C. M. (2013). Two modes of sea-ice gravity drainage: A parameterization for large-scale modeling. *Journal of Geophysical Research: Oceans*, 118(5):2279–2294.

Vancoppenolle, M., Fichefet, T., and Bitz, C. M. (2005). On the sensitivity of undeformed arctic sea ice to its vertical salinity profile. *Geophysical Research Letters*, 32(16).

Vancoppenolle, M., Rousset, C., Blockley, E., Aksenov, Y., Feltham, D., Fichefet, T., Garric, G., Guémas, V., Iovino, D., Keeley, S., Madec, G., Massonnet, F., Ridley, J., Schroeder, D., and Tietsche, S. (2023). Si3, the nemo sea ice engine.

Vernieres, G., Zhao, B., Cullather, R. I., Akella, S., Vikhliaev, Y. V., Kurtz, N. T., and Kovach, R. M. (2016). Assimilation of cryosat 2 arctic sea-ice freeboard in an ensemble of coupled geos5. *American Geophysical Union*, 2016:HE13A–06.

Villadsen, H., Deng, X., Andersen, O. B., Stenseng, L., Nielsen, K., and Knudsen, P. (2016). Improved inland water levels from sar altimetry using novel empirical and physical retrackers. *Journal of Hydrology*, 537:234–247.

Wadhams, P., Tucker III, W., Krabill, W. B., Swift, R. N., Comiso, J. C., and Davis, N. (1992). Relationship between sea ice freeboard and draft in the arctic basin, and implications for ice thickness monitoring. *Journal of Geophysical Research: Oceans*, 97(C12):20325–20334.

Wagner, D. N., Shupe, M. D., Cox, C., Persson, O. G., Uttal, T., Frey, M. M., Kirchgaessner, A., Schneebeli, M., Jaggi, M., Macfarlane, A. R., et al. (2022). Snowfall and snow accumulation during the mosaic winter and spring seasons. *The Cryosphere*, 16(6):2373–2402.

Walsh, J. E., Fetterer, F., Scott Stewart, J., and Chapman, W. L. (2017). A database for depicting arctic sea ice variations back to 1850. *Geographical Review*, 107(1):89–107.

Walsh, J. E., Hibler III, W. D., and Ross, B. (1985). Numerical simulation of northern hemisphere sea ice variability, 1951–1980. *Journal of Geophysical Research: Oceans*, 90(C3):4847–4865.

Wang, B., Sun, Z., Jiang, X., Zeng, J., and Liu, R. (2023). Kalman filter and its application in data assimilation. *Atmosphere*, 14(8).

Wang, C., Graham, R. M., Wang, K., Gerland, S., and Granskog, M. A. (2019). Comparison of era5 and era-interim near-surface air temperature, snowfall and precipitation over arctic sea ice: effects on sea ice thermodynamics and evolution. *The Cryosphere*, 13(6):1661–1679.

Wang, J., Min, C., Ricker, R., Shi, Q., Han, B., Hendricks, S., Wu, R., and Yang, Q. (2022). A comparison between envisat and icesat sea ice thickness in the southern ocean. *The Cryosphere*, 16(10):4473–4490.

Wang, Q., Wekerle, C., Danilov, S., Koldunov, N., Sidorenko, D., Sein, D., Rabe, B., and Jung, T. (2018). Arctic sea ice decline significantly contributed to the unprecedented liquid freshwater accumulation in the beaufort gyre of the arctic ocean. *Geophysical Research Letters*, 45(10):4956–4964.

Warren, S. G., Rigor, I. G., Untersteiner, N., Radionov, V. F., Bryazgin, N. N., Aleksandrov, Y. I., and Colony, R. (1999). Snow depth on arctic sea ice. *Journal of Climate*, 12(6):1814–1829.

Wever, N., Leonard, K., Maksym, T., White, S., Proksch, M., and Lenaerts, J. T. M. (2021). Spatially distributed simulations of the effect of snow on mass balance and flooding of antarctic sea ice. *Journal of Glaciology*, 67(266):1055–1073.

Willatt, R., Laxon, S., Giles, K., Cullen, R., Haas, C., and Helm, V. (2011). Ku-band radar penetration into snow cover on arctic sea ice using airborne data. *Annals of Glaciology*, 52(57):197–205.

Williams, N., Byrne, N., Feltham, D., Van Leeuwen, P. J., Bannister, R., Schroeder, D., Ridout, A., and Nerger, L. (2023). The effects of assimilating a sub-grid-scale sea ice thickness distribution in a new arctic sea ice data assimilation system. *The Cryosphere*, 17(6):2509–2532.

Wingham, D., Francis, C., Baker, S., Bouzinac, C., Brockley, D., Cullen, R., de Chateau-Thierry, P., Laxon, S., Mallow, U., Mavrocordatos, C., et al. (2006). Cryosat: A mission to determine the fluctuations in earth's land and marine ice fields. *Advances in Space Research*, 37(4):841–871.

Wu, G. and Zheng, X. (2017). The error covariance matrix inflation in ensemble kalman filter. In de Oliveira Serra, G. L., editor, *Kalman Filters*, chapter 2. IntechOpen, Rijeka.

Xia, W. and Xie, H. (2018). Assessing three waveform retrackers on sea ice freeboard retrieval from cryosat-2 using operation icebridge airborne altimetry datasets. *Remote Sensing of Environment*, 204:456–471.

Xie, J., Counillon, F., and Bertino, L. (2018). Impact of assimilating a merged sea-ice thickness from cryosat-2 and smos in the arctic reanalysis. *The Cryosphere*, 12(11):3671–3691.

Yang, C.-Y., Liu, J., and Xu, S. (2020). Seasonal arctic sea ice prediction using a newly developed fully coupled regional model with the assimilation of satellite sea ice observations. *Journal of Advances in Modeling Earth Systems*, 12(5):e2019MS001938.

Yang, Q., Losa, S. N., Losch, M., Tian-Kunze, X., Nerger, L., Liu, J., Kaleschke, L., and Zhang, Z. (2014). Assimilating smos sea ice thickness into a coupled ice-ocean model using a local seik filter. *Journal of Geophysical Research: Oceans*, 119(10):6680–6692.

Ying, Y., Zhang, F., and Anderson, J. L. (2018). On the selection of localization radius in ensemble filtering for multiscale quasigeostrophic dynamics. *Monthly Weather Review*, 146(2):543 – 560.

Zhang, J. and Rothrock, D. (2001). A thickness and enthalpy distribution sea-ice model. *Journal of Physical Oceanography*, 31(10):2986–3001.

Zhang, J. and Rothrock, D. A. (2003). Modeling global sea ice with a thickness and enthalpy distribution model in generalized curvilinear coordinates. *Monthly Weather Review*, 131(5):845 – 861.

Zhang, J., Schweiger, A., Webster, M., Light, B., Steele, M., Ashjian, C., Campbell, R., and Spitz, Y. (2018). Melt pond conditions on declining arctic sea ice over 1979–2016: Model development, validation, and results. *Journal of Geophysical Research: Oceans*, 123(11):7983–8003.

Zhang, S., Xuan, Y., Li, J., Geng, T., Li, X., and Xiao, F. (2021). Arctic sea ice freeboard retrieval from envisat altimetry data. *Remote Sensing*, 13(8):1414.

Zhou, L., Stroeve, J., Xu, S., Petty, A., Tilling, R., Winstrup, M., Rostosky, P., Lawrence, I. R., Liston, G. E., Ridout, A., et al. (2021). Inter-comparison of snow depth over arctic sea ice from reanalysis reconstructions and satellite retrieval. *The Cryosphere*, 15(1):345–367.

Zuo, H., Balmaseda, M. A., Tietsche, S., Mogensen, K., and Mayer, M. (2019). The ecmwf operational ensemble reanalysis–analysis system for ocean and sea ice: a description of the system and assessment. *Ocean science*, 15(3):779–808.

Zweng, M., Seidov, D., Boyer, T., Locarnini, M., Garcia, H., Mishonov, A., Baranova, O., Weathers, K., Paver, C., Smolyar, I., et al. (2019). World ocean atlas 2018, volume 2: Salinity.

Zygmuntowska, M., Rampal, P., Ivanova, N., and Smedsrud, L. H. (2014). Uncertainties in arctic sea ice thickness and volume: new estimates and implications for trends. *The Cryosphere*, 8(2):705–720.

Appendix

The Cryosphere, 17, 3721–3738, 2023
https://doi.org/10.5194/tc-17-3721-2023

The Cryosphere
Open Access
EGU

Assimilating CryoSat-2 freeboard to improve Arctic sea ice thickness estimates

Imke Sievers[1,3], **Till A. S. Rasmussen**[1], **and Lars Stenseng**[2]

[1]Nationalt Center for Klimaforskning, Danish Meteorological Institute, Lyngbyvej 100, 2100 Copenhagen, Denmark
[2]DTU Space, Technical University of Denmark, Elektrovej Bygning 328, 2800 Kongens Lyngby, Denmark
[3]Electronic Systems, Aalborg University, A. C. Meyers Vænge 15, 2450 Copenhagen, Denmark

Correspondence: Imke Sievers (imksie@dmi.dk)

Received: 23 December 2022 – Discussion started: 4 January 2023
Revised: 7 July 2023 – Accepted: 28 July 2023 – Published: 1 September 2023

Abstract. In this study, a new method to assimilate freeboard (FB) derived from satellite radar altimetry is presented with the goal of improving the initial state of sea ice thickness predictions in the Arctic. In order to quantify the improvement in sea ice thickness gained by assimilating FB, we compare three different model runs: one reference run (refRun), one that assimilates only sea ice concentration (SIC) (sicRun), and one that assimilates both SIC and FB (fbRun). It is shown that estimates for both SIC and FB can be improved by assimilation, but only fbRun improved the FB. The resulting sea ice thickness is evaluated by comparing sea ice draft measurements from the Beaufort Gyre Exploration Project (BGEP) and sea ice thickness measurements from 19 ice mass balance (IMB) buoys deployed during the Multidisciplinary drifting Observatory for the Study of Arctic Climate (MOSAiC) expedition. The sea ice thickness of fbRun compares better than refRun and sicRun to the longer BGEP observations more poorly to the shorter MOSAiC observations. Further, the three model runs are compared to the Alfred Wegener Institute (AWI) weekly CryoSat-2 sea ice thickness, which is based on the same FB observations as those that were assimilated in this study. It is shown that the FB and sea ice thickness from fbRun are closer to the AWI CryoSat-2 values than the ones from refRun or sicRun. Finally, comparisons of the abovementioned observations and both the fbRun sea ice thickness and the AWI weekly CryoSat-2 sea ice thickness were performed. At the BGEP locations, both fbRun and the AWI CryoSat-2 sea ice thickness perform equally. The total root-mean-square error (RMSE) at the BGEP locations equals 30 cm for both sea ice thickness products. At the MOSAiC locations, fbRun's sea ice thickness performs significantly better, with a total 11 cm lower RMSE.

1 Introduction

With declining sea ice in the Arctic, marine traffic is increasing (Cao et al., 2022). This increases the demand for accurate sea ice predictions to ensure safety on shipping routes. Data assimilation is a commonly used tool to improve the initial state of sea ice predictions (Chen et al., 2017; Mu et al., 2018; Fiedler et al., 2022). In data assimilation, models and observations are combined using a number of approaches. For all approaches, the variables that are assimilated need to be observable and need to affect the model variable that the assimilation aims to improve. Stroeve and Notz (2015) list sea ice volume and ocean heat content as the two model variables with the largest impact on Arctic sea ice forecast. Ocean heat content is difficult to observe on an Arctic-wide scale, but sea ice concentration (SIC) and sea ice thickness can be observed from satellites (Kwok, 2010; Laxon et al., 2013; Ivanova et al., 2014; OSI SAF, 2017; Hendricks et al., 2021). While satellite-observed SIC has rather good accuracy and has been available since the late 1970s, satellite sea ice thickness observations have only been available since the early 2000s and come with large uncertainties (Laxon et al., 2003; Kwok, 2010). Several studies have found that sea ice thickness, in contrast to SIC, has a longer memory (Day et al., 2014; Stroeve and Notz, 2015; Dirkson et al., 2017). Longer memory here means that the change introduced by initial sea ice thickness persists longer than the change in-

troduced by SIC. This makes the sea ice thickness the more suitable variable to assimilate when aiming for an improved initial estimate of the Arctic sea ice, which also has an impact on the skill of the forecast at longer timescales (Day et al., 2014).

Arctic-wide sea ice observations can only be obtained through remotely sensed data from satellites. However, for sea ice thickness, it is possible to observe the portion of the sea ice above the sea surface, which is referred to as freeboard (FB). The longest record of FB observations from a satellite with a polar orbit can be obtained from the European Space Agency (ESA) satellite CryoSat-2, which has been in orbit since 2010 (Drinkwater et al., 2004). Using an advanced radar altimeter, data from CryoSat-2 can be used to estimate FB as the difference between the observed height of the sea ice surface and the water level in leads between sea ice floes. To derive sea ice thickness from FB, a number of assumptions need to be made, which will be discussed below. These assumptions lead to a large uncertainty in the resulting sea ice thickness estimate. Therefore, we propose a method that assimilates FB directly, instead of using sea ice thickness derived from FB.

Most existing sea ice thickness products use FB measurements to calculate sea ice thickness assuming hydrostatic balance. The hydrostatic balance equation relates sea ice thickness to FB, snow density, snow thickness, sea ice density and seawater density. In this relation, FB is measured, and the other parameters are derived from climatologies or empirical values derived from in situ observations (Ricker et al., 2014; Kwok and Cunningham, 2015; Tilling et al., 2018). The abovementioned uncertainties in satellite-derived sea ice thickness largely originate from the uncertainty in these parameters (Alexandrov et al., 2010). According to Alexandrov et al. (2010), sea ice density introduces the largest error when calculating sea ice thickness from FB under the assumption of hydrostatic balance. Sea ice density depends on the ice age, where younger sea ice has a higher salinity due to more brine being enclosed in it. Over time, brine is expelled into the ocean below. During the melt season, salt is washed out by meltwater (Cox and Weeks, 1974), making multi-year ice (MYI) less saline and therefore less dense than first-year ice (FYI). Enclosed gas is another parameter that makes sea ice density estimates uncertain. FYI sea ice density uncertainty is typically around $23.0\,\mathrm{kg\,m^{-3}}$, and for MYI, the uncertainty is around $35.7\,\mathrm{kg\,m^{-3}}$ (Alexandrov et al., 2010). This high uncertainty originates from the difficulty of measuring sea ice density and the limited availability of density measurements. The density varies within the ice column depending on whether the ice is below or above sea level. On top of that, the harsh environment adds extra challenges to performing exact measurements (Timco and Frederking, 1996). Despite the variation in sea ice density, most products use fixed values of $917\,\mathrm{kg\,m^{-3}}$ for FYI and $882\,\mathrm{kg\,m^{-3}}$ for MYI (Sallila et al., 2019). The second-largest error contributor to sea ice thickness, according to Alexandrov et al. (2010), is FB. Uncertainties in FB originate from uncertainties in the sea surface height, the location of the backscattering horizon, speckle noise (Ricker et al., 2014), the retracking of the radar waveform (Landy et al., 2019), and uncertainties in snow height and density used to calculate the reduction in radar wave propagation speed in the snowpack (Mallett et al., 2020). The uncertainty introduced by the snow thickness has been extensively discussed (Kurtz and Farrell, 2011; Kwok et al., 2011; Laxon et al., 2013; Kern et al., 2015; Garnier et al., 2021). Historically, snow thickness has been derived from the Warren et al. (1999) snow climatology (W99), which was calculated from Russian drift stations for the period 1954–1991. Most of the included measurements were obtained on thick MYI. However, Kurtz and Farrell (2011) showed that W99 is less reliable over FYI compared to MYI, and Laxon et al. (2013) proposed a method to differentiate MYI and FYI snow thickness and snow density from W99. This method is now more commonly used in sea ice thickness products than the pure W99 climatology (Sallila et al., 2019). Another alternative to W99 is to use a snow model to calculate the local snow thickness, depending on precipitation. For example, Fiedler et al. (2022) showed results using snow thickness from the Forecast Ocean Assimilation Model (FOAM; Blockley et al., 2014), which is a global coupled sea ice–ocean model, or Landy et al. (2022) used SnowModel-LG (Liston et al., 2020).

W99 also includes a snow density climatology, which was commonly used in the calculation of sea ice thickness until 2020 (Sallila et al., 2019). Mallett et al. (2020) found that approximating the snow density by a linear function improves the sea ice thickness estimate by about 10 cm. Recent sea ice thickness products, for example in Hendricks et al. (2021), have started to use the proposed seasonal linear approximation of snow density, with good results. Seawater density only varies very little throughout the Arctic. Most CryoSat-2 sea ice thickness products use a single value of $1024\,\mathrm{kg\,m^{-3}}$, which is the density at the freezing point of Arctic surface water. The influence of the uncertainty in this value on the hydrostatic balance equation is negligible (Kurtz et al., 2013).

The uncertainties in sea ice density, freeboard (FB), snow density and seawater density all contribute to the overall error in sea ice thickness calculated from FB. To account for these errors, error estimates are used in data assimilation methods such as Kalman filters. Kalman filters rely on knowledge of the model uncertainties and observational uncertainties, as well as the assumption that they are unbiased and Gaussian distributed. Based on these assumptions, the Kalman filter aims to derive the best estimate. The accuracy of the resulting state estimate improves with better uncertainty estimates. The errors in CryoSat-2-derived sea ice thickness not only are due to the sources mentioned above, but also depend on how FYI and MYI are defined. The sea ice density; snow thickness; and, in some cases, snow density are calculated based on this ice type. The ice type is typically derived from the Ocean and Sea Ice Satellite Application Facility

(OSI SAF) ice type data (Sallila et al., 2019), which distinguish between FYI, MYI and ambiguous ice types (Aaboe et al., 2021). Ye et al. (2023) assessed different sea ice type products, including the OSI SAF ice type data product, and compared them to the National Snow and Ice Data Center (NSIDC) sea ice age data (Tschudi et al., 2020). They found that the OSI SAF ice type data have for FYI a bias of 0.42×10^6 to 0.6×10^6 km^2 and for MYI a bias of -0.54×10^6 to -0.35×10^6 km^2. This comparison only considers FYI and MYI areas and compares them to satellite-obtained ice age products. Ambiguous areas are not considered. In most CryoSat-2 sea ice thickness products, a small transitioning area with a linear transition from MYI to FYI is assumed (Laxon et al., 2013; Tilling et al., 2018; Hendricks et al., 2021). However, the ice-chart-based sea ice type data product G10033 (Fetterer and Stewart, 2020) suggests large areas of mixed ice types. These areas are notably larger and less homogeneous than the areas suggested by the linear transition between MYI and FYI based on the OSI SAF sea ice type. This means that sea ice density, snow thickness and snow density errors are systematically underestimated or overestimated in these areas of ambiguous ice type.

As the FB error estimate is part of the sea ice thickness error estimate, it is fair to conclude that the FB error is better constrained than the sea ice thickness error. This is not to say that FB errors are unbiased. However, by choosing to assimilate FB, error contributions originating from snow thickness, snow density, sea ice density and sea ice type when converting FB to sea ice thickness are eliminated. Consequently, it follows that the FB data would be more suitable for assimilation than the derived sea ice thickness, as a lower uncertainty will increase the weight of the observed CryoSat-2 FB.

The challenge of this approach is that FB is not a sea ice model state variable but a diagnostic variable. Even though FB is not a state variable, it is related to sea ice thickness, which is a state variable and can be calculated from FB under the assumptions that a change in FB is caused only by modeled sea ice thickness and modeled snow thickness and that snow density and ice density are realistic.

In this study, we present an approach to assimilating FB directly into the sea ice model CICE (Hunke et al., 2021a). We aim to answer the following questions: does FB assimilation have a significant impact on the modeled sea ice thickness? And how does the modeled sea ice thickness after assimilation of FB compare to sea ice thickness (SIT) from a conventional CryoSat-2 sea ice thickness product? To transform FB into the model state variable sea ice thickness, we use parametrization and assumptions from the model and the forcing data. The method is implemented into CICE, but it should be applicable to any other model. This study mainly focuses on CryoSat-2 measurements, but the approach presented could also be applied to ICESat FB data (Martino et al., 2019) with small adjustments. Several studies have mentioned approaches to assimilate FB (Vernieres et al., 2016; Kaminski et al., 2018; Fiedler et al., 2022), but none has included a description of how the FB assimilation was implemented. Kaminski et al. (2018) conducted a study using the quantitative network design approach to quantify how beneficial it would be to assimilate radar FB, among other variables. The study concludes that assimilation of radar FB can improve sea ice volume simulations on the same order of magnitude as sea ice thickness assimilation. The quantitative network design approach builds upon error propagation and the sea ice thickness errors used in the analysis, which originate from the Alfred Wegener Institute (AWI) CryoSat-2 sea ice thickness products. As discussed above, this error estimate includes no contribution from ice type data and might be underestimated. To our knowledge, this is the first paper presenting detailed descriptions of an assimilation method using FB instead of sea ice thickness.

2 Methods and data

The following section presents all data sets, software and methods used to derive the sea ice thickness data sets evaluated in this study. The model setup is presented in Sect. 2.1, the assimilation setup is presented in Sect. 2.2, the observational data are presented in Sect. 2.3 and 2.4, and Sect. 2.5 presents the observation data sets which are used for validation.

2.1 Model setup

The FB assimilation is implemented in a coupled sea ice (CICE v6.2; Hunke et al., 2021a) and ocean model (NEMO v4.0; Madec et al., 2017). The coupling is based on Smith et al. (2021); however both NEMO and CICE have been updated to more recent versions. NEMO is set up following (Hordoir et al., 2022).

CICE is a multicategory sea ice model that consists of a dynamical solver, an advection scheme and a thermodynamic column physics model called Icepack. CICE and Icepack (Hunke et al., 2021b) are developed independently but are by default linked (Hunke et al., 2021b, a). The model is run with five thickness categories with category bounds that follow a World Meteorological Organization (WMO) standard setup. The upper bounds for the five categories (n) are as follows: $n=1$, 0.3 m; $n=2$, 0.7 m; $n=3$, 1.2 m; $n=4$, 2 m; and $n=5$, 999 m. In the presented study, CICE was implemented close to the default setup except that form drag calculations, following Tsamados et al. (2014), were enabled.

The model domain is pan-Arctic, as shown by the red area in Fig. 1 (large parts are covered by the blue and orange visualization). The lateral boundaries are located outside the Arctic sea-ice-covered region such that sea ice boundary conditions are not required. The lateral ocean boundaries are forced with monthly GLORYS12 data, which consist of salinity, temperature, and u and v velocities (Lellouche et al., 2021). The ocean model includes tides, the tidal forc-

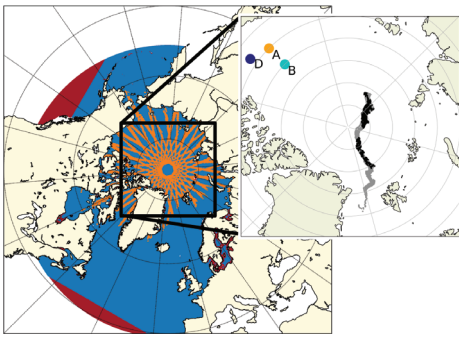

Figure 1. The red area indicates the model domain (large parts are covered by the blue and orange visualization) described in Sect. 2.1, the blue area shows the OSI SAF SIC data coverage and the orange lines give example coverage of 1 week of CryoSat-2 data (here from 3 March 2020). The zoomed-in area shows the location of the three moorings described in Sect. 2.5, marked with corresponding letters, and the gray and black track indicates the drift path of the ice mass balance buoys also described in Sect. 2.5. The gray indicates the full data set used in Fig. 8 and the black the subset used in Fig. 7.

ing at the open boundaries originates from the TPXO 7.2 harmonic tidal constituents (Egbert and Erofeeva, 2002), and river runoff is based on a climatology from Dai and Trenberth (2002). The model is forced with 3-hourly ERA5 atmospheric forcing data, which consist of 2 m temperature, 2 m specific humidity, 10 m wind, incoming shortwave and longwave radiation, total precipitation, snowfall, and air pressure at sea level (Hersbach et al., 2017). The model runs discussed in this study are restarted from the same initial run, which runs from 1995 to 2020 and was initialized from ORAS5 (Zuo et al., 2019) ocean temperature and salinity fields. The years 2010–2020 of the initial run were used to calculate the model background error discussed in Sect. 2.2. The three other runs discussed in the following text are refRun, sicRun and fbRun: refRun consists of the initial run from 1 January 2018 to 31 December 2020; sicRun and fbRun are started from the same restart file as refRun on 1 January 2018 but assimilate (i) SIC and (ii) SIC and FB respectively. They both also cover the period 1 January 2018 to 31 December 2020. All model output discussed in the following sections is calculated based on daily means.

In order to be able to assimilate radar FB from CryoSat-2, a new variable for radar FB needs to be introduced in CICE. For this we combined Eq. (4) from Alexandrov et al. (2010) with Eq. (12) from Tilling et al. (2018) as follows:

$$\mathrm{FBr} = \frac{\mathrm{hi}(\rho_\mathrm{w} - \rho_i) - \rho_\mathrm{s} h_\mathrm{s}}{\rho_\mathrm{w}} - (h_\mathrm{s}(\frac{c}{\mathrm{cs}} - 1)). \quad (1)$$

Here, h_i is the modeled sea ice thickness from CICE, ρ_w is the modeled surface water density from NEMO, h_s is the modeled snow thickness from CICE, c is the speed of light in vacuum ($3 \times 10^8\,\mathrm{m\,s^{-1}}$) and c_s the speed of light in snow. The variable cs is calculated following Eq. (2):

$$\mathrm{cs} = c(1 + 0.51\rho_\mathrm{s})^{-1.5}. \quad (2)$$

Mallett et al. (2020) compared constant ρ_s values to the seasonal linear variation in ρ_s derived by Warren et al. (1999) and concluded that a seasonally varying ρ_s can improve FB-derived sea ice thickness estimates by up to 10 cm. The original value used in CICE is constant and equals $330\,\mathrm{kg\,m^{-3}}$. In this study it was substituted with the derived relation from Mallett et al. (2020) following Eq. (3):

$$\rho_\mathrm{s} = 6.5 \times t + 274.51, \quad (3)$$

where t is time counted in months since October. The relation in Eq. (3) is only used in the radar FB calculation for the assimilation and nowhere else in the sea ice model. CICE uses constant ρ_i values, but for the radar FB calculation, a variable sea ice density was needed, since ρ_i has significant impact on Eq. (1) (Alexandrov et al., 2010; Kern et al., 2015). Sea ice density is dependent on the air bubbles enclosed in the sea ice and on the brine content (Timco and Frederking, 1996). Brine content in sea ice results from the brine rejection during freeze-up and drains over time. If the brine channels are not filled with water, they remain as air bubbles in the ice (Timco and Frederking, 1996). CICE calculates the salinity content in sea ice and the density of sea ice without accounting for a changing number of air pockets. To calculate the sea ice density, we divide the sea ice volume in one grid cell into fresh ice and brine, calculate the percentage of the fresh ice and brine, and weight a fresh ice density (ρ_i0) and the brine density (ρ_b) with this.

$$\rho_i = \mathrm{aice_b} \times \rho_\mathrm{b} + (1 - \mathrm{aice_b}) \times \rho_\mathrm{i0} \quad (4)$$

Here, $\mathrm{aice_b}$ is the amount of brine as a percentage of the total ice volume. The variable ρ_i0 was set to $882\,\mathrm{kg\,m^{-3}}$ following Alexandrov et al. (2010) values for MYI sea ice density. In the following text, FB stands for the radar FB.

2.2 Assimilation setup

Kalman-filter-based assimilation is a widely used technique that employs an ensemble of model forecasts to estimate the state of a system using available observations. The method involves three main steps: a forecasting step, a filtering step and a re-sampling step. The forecast is performed by the model. During the filtering step, the ensemble members are adjusted based on knowledge of the model background error, observation error, model states and observations to obtain the best possible estimate of the system state. In the re-sampling step, the best estimate from the filtering step is used to update the ensemble members. This process is repeated iteratively in order to improve the accuracy of the state estimate. For the filtering step, we use the Local Error Subspace

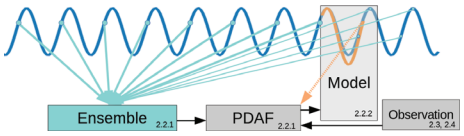

Figure 2. General setup of the assimilation routine. The dark-blue curve indicates the initial model run and the orange curve the assimilated run, with the dashed orange arrow indicating the model state at the assimilation time. The thick turquoise arrows indicate the 8 d chosen around the assimilation date and the thin turquoise arrows the 4 (or 3) d chosen ± 2 months around the assimilation date (described in Sect. 2.2.1). The numbers in the lower corners indicate in which section of the paper the different elements are described.

Transform Kalman Filter (LESTKF) (Nerger et al., 2012), which is included in the Parallel Data Assimilation Framework (PDAF) (Nerger and Hiller, 2013). LESTKF has, prior to this study, successfully been used to assimilate SIC and sea ice thickness, for example by Chen et al. (2017). In this study, PDAF is used offline, which means that the assimilation scheme runs independently of the ocean and sea ice model. The consequence is that the ocean and sea ice model needs to be restarted when the model and the assimilation exchange information. PDAF was run separately for SIC and FB. Figure 2 illustrates the data flow between the different components. The numbers noted in the lower corner of each component correspond to each of the following sections, describing which part of the assimilation is handled in which program.

2.2.1 PDAF

PDAF inputs consist of the model state, model ensemble, observations and observation uncertainties in the model grid. The spread of the ensemble is used to calculate the model background error used in the filtering step. In this study, we only run one model realization and calculate the model background error in the Kalman filter from a static ensemble, similarly to the setups in BAL MFC (Nord et al., 2021) and SAM2 (Tranchant et al., 2006). Using a static ensemble has the advantage of lower computational cost. To calculate the model background error based on a static ensemble, a free model run of the model used in the assimilation is needed. In our case the free model ran from 1995 to 2020, but only the years 2010–2020 were used to construct the static ensemble as the earlier years were considered spinup. The justification of using a static ensemble is based on the assumption that the model error on a certain day in a year is reflected by the interannual model variability of this same day. Knowing the biases of the model allows for the correction of this assumption. In our case, the model overestimates the ice extent, which we found when comparing the 10-year initial run to OSI SAF (Saldo, 2022) SIC observations. Thus, the background error based on the same date in several years would not result in a large enough spread to weight the observations correctly. The ensemble used to calculate the model background error consists of 80 members, and it is constructed as follows: each of the 10 years from the free run contributes 8 d.

- In 8 years, a period of 8 consecutive days is chosen, starting from the date 3 d prior the assimilation time step and ending 4 d past it.
- In 2 years, a period of 3 consecutive days from the date 2 months prior to the assimilation time and a period of 4 consecutive days from 2 months past the assimilation time are chosen.

After the ensemble members were chosen, they are averaged. This average is then subtracted from each member, and the resulting variation is added to the model state at the assimilation date. These 80 ensemble members are then used to calculate the model error. For the observation error, we use the error estimates provided in the data sets.

2.2.2 Integration of increments

The physical model in Sect. 2.1 utilizes the Kalman filter increment, which is the correction that adjusts the model state to the optimal state based on observations and model states. This increment is obtained as the difference between the model state input to PDAF and the analyzed state. The model state is corrected towards the analyzed state by subtracting the increment from the model state. To ensure stability, the increment is divided by the number of time steps (number of model time steps in one assimilation time step), which results in the fractal increment or the amount of change needed per model time step (following Eq. 5). This fractal increment is hereafter subtracted at each time step from the model value. This method is called incremental analysis updating and was introduced by Bloom et al. (1996). For SIC, this method is straightforward, since the observations are also what we aim to assimilate.

$$\mathrm{inc} = \frac{\mathrm{var}_0 - \mathrm{new}_{\mathrm{ice}}}{\mathrm{time}_r} \tag{5}$$

FB needs to be converted into sea ice thickness, and if this were to be done separately at each time step, the changing sea ice density and snow thickness could potentially influence the resulting sea ice thickness. Similarly to SIC, the FB increment is subtracted from the model state at t_0. To convert FB to sea ice thickness, Eq. (1) was rewritten as follows:

$$\mathrm{new}_{\mathrm{ice}} = \frac{\rho_{\mathrm{s}} h_{\mathrm{s}} + \rho_{\mathrm{w}} (\mathrm{FB}_{\mathrm{new}} + \mathrm{corr})}{\rho_{\mathrm{w}} - \rho_i}. \tag{6}$$

The variable $\mathrm{new}_{\mathrm{ice}}$ is now subtracted from the modeled sea ice thickness and linearly spread following Eq. (5).

At each time step, we have the fractional increment of SIC and sea ice thickness to be subtracted from the model state. The model used in this study is a multicategory model. Therefore, the grid cell average increment must be spread over the five model categories. To achieve this, Eq. (7) was used. Here $\mathrm{var}_{\mathrm{old}}$ is the SIC at the current time step, $\mathrm{var}_{\mathrm{old}}(n)$ is the SIC in n categories, inc is the SIC increment and n is the thickness category.

$$\mathrm{var}(n) = \mathrm{var}_{\mathrm{old}}(n) - \mathrm{var}_{\mathrm{old}}(n)\frac{\mathrm{inc}}{\mathrm{var}_{\mathrm{old}}} \tag{7}$$

In the case where SIC and FB are negative after the assimilation, they are rounded to 0. In cases where the SIC ends up above 1, SIC is rounded to 1. FB is only assimilated if SIC is above 80 % and if sea ice thickness is above 0.05 m. These thresholds were chosen not only for stability, but also because thin FB is not measured accurately (Wingham et al., 2006; Ricker et al., 2014) and because FB is calculated from the model's ice volume per unit area of ice. In areas with lower concentrations, this can lead to SIT and FB values that are unrealistically high. To avoid overestimation of FB following this artifact, a high SIC threshold was chosen for the FB assimilation.

2.3 CryoSat-2 radar altimetry freeboard and sea ice thickness

The observed FB assimilated in this study is level-3 weekly gridded CryoSat-2 radar FB downloaded from the Alfred Wegener Institute (AWI) sea ice portal (version 2.4; Hendricks et al., 2021). This comprises gridded, along-track data on the EASE2-Grid with a 25 km resolution. The radar FB is defined as the elevation of a retracked point above instantaneous sea surface height without snow range correction. The data product is derived from the CryoSat-2 Baseline-E data, the mean sea surface model DTU21 and the threshold first-maximum retracker algorithm (TFMRA) (Ricker et al., 2014).

With the onset of melt at the beginning of summer, melt ponds are formed on the sea ice surface. The radar signature from melt ponds is comparable to the signature from leads, which can result in ambiguous determination of the sea surface height. This ambiguity results in a larger bias in the FB measurements, and FB data are therefore only assimilated from November to March, when we do not expect melt ponds. The uncertainty in FB given in the AWI data set ranges on average from 0 to 0.07 m in the chosen month. The data set was bi-linearly interpolated to the model grid with help of Climate Data Operators (CDO; Schulzweida, 2022). An example of the FB data assimilated per assimilation time step (1 week) is indicated by the orange lines in Fig. 1.

The data set also contains sea ice thickness derived by assuming hydrostatic balance, which is the method referred to as the classical approach. In order to obtain sea ice thickness from FB, hydrostatic balance is assumed, and sea ice thickness is calculated as described in Eq. (6). In the AWI CryoSat-2 data set, the snow thickness from Warren et al. (1999) snow climatology was applied over MYI, and NSIDC AMSR2 snow depth (Hendricks et al., 2021) was applied over FYI. The snow density is calculated following Eq. (3) from Mallett et al. (2020), and the sea ice density is set to $916.7\,\mathrm{kg\,m^{-3}}$ for FYI and to $882.0\,\mathrm{kg\,m^{-3}}$ for MYI. MYI and FYI are distinguished with the help of OSI SAF ice type data. For a more detailed description of the data set, see Hendricks et al. (2021).

2.4 OSI SAF data

Ocean and Sea Ice Satellite Application Facility (OSI SAF) SIC is assimilated in this study. It is based on passive microwave measurements of the Special Sensor Microwave Imager/Sounder (SSMIS), which is onboard a polar-orbiting satellite. The OSI SAF algorithm combines SSMIS microwave measurements with numerical weather prediction (NWP) model output from ECMWF in order to calculate SIC. Passive microwave measurements are independent of visible light, which makes this sensor type especially suitable in polar regions. The data set used is the climate data record (CDR) OSI-430-a, which is gridded on a 25×25 km grid once a day. The data can be downloaded from the Norwegian Meteorological Institute FTP servers: ftp://osisaf.met.no/reprocessed/ice/conc/v3p0 (last access: 12 January 2023). The presented data set was chosen after examining the error estimates in the different data products. The comparison showed that the CDR is the only data set that has no large error fluctuations over open-water areas. More details on the error estimate can be found in Saldo (2022). Studies have found that the summer melt ponds lead to underestimated SIC in satellite passive microwave measurements (Kern et al., 2016; Ivanova et al., 2013; Rösel and Kaleschke, 2012). This is the reason we decided to only assimilate SIC during the months November to March.

For the assimilation, the data set was bi-linearly interpolated onto the model grid using CDO (Schulzweida, 2022). The resulting SIC data coverage assimilated is indicated by the blue area in Fig. 1.

2.5 Validation data

Two in situ sea ice observation data sets are used for validation. The Beaufort Gyre Exploration Project (BGEP) upward-looking sonar (ULS) sea ice draft data set and 19 ice mass balance (IMB) buoys deployed during the Multidisciplinary drifting Observatory for the Study of Arctic Climate (MOSAiC) campaign measuring sea ice thickness. The advantage of these observations is that they are independent of the assimilated data; however each observation has limitations in terms of time and space.

The BGEP ULS sea ice draft data set can be downloaded from https://www2.whoi.edu/site/beaufortgyre/data/

mooring-data/ (last access: 28 June 2023). The ULS data are obtained from three locations named moorings A, B and D, marked with orange, turquoise and dark-blue dots in Fig. 1. The data cover 2 years, from October 2018 to November 2020. The instruments are located 50–85 m below the water surface and measure the ice draft with a frequency of 2 s over a 2×2 m area. The signal is filtered and averaged over 10 s intervals in order to correct for tilting errors. Tilting error refers to the error that results from the movement of the ULS when ocean currents move the instrument and so influence the distance to the sea ice. The error is assumed to be random; hence averaging the data will eliminate it. The sea ice draft accuracy is ± 5 cm.

For the comparison of BGEP observations and model and AWI data, the model and AWI draft was calculated as sea ice thickness minus sea ice FB. To compare the BGEP data with the three model runs, the daily average and standard deviation (SD) were calculated from the differences of all 10 s measurements and the model daily output. For the comparison, only the grid cell which would cover the respective buoy was considered. Since the resulting daily mean and SD were still too variable, they were further smoothened by a 7 d running mean. For the comparison of the fbRun, AWI and BGEP draft, only weeks in which the AWI data cover the BGEP locations were considered. The model values are weekly means of the respective buoy covering the grid cell.

To be able to compare sea ice in situ measurements from more locations, the IMB buoy deployed during the MOSAiC campaign are used (Lei et al., 2021). In contrast to the stationary measurements from the BGEP, the measurements drift along the black trajectory in Fig. 1, from the center of the Arctic towards Greenland. The IMB buoy includes a thermistor string reaching from the snowpack top to the ice–ocean interface at the bottom. A thermometer and a heating element are located each 2 cm. The ice–snow, ice–water and snow–air interfaces are measured by heating the thermistor string up and measuring the thermal response. More information on the instrument can be found in Jackson et al. (2013). The IMB buoys measure the thickness of only one ice flow, unlike the BGEP upward-looking sonar, and the data have a temporal frequency of one measurement per day. To ensure that the comparison between the buoys and the gridded AWI sea ice thickness and model output is reliable, 19 IMB buoys were considered. However, not all buoys were active at the same time. All buoys were interpolated to the model grid by the nearest-neighbor method.

For a comparison of the different model runs vs. the IMB measurements, a minimum of eight active buoys per day were chosen. The limit of eight buoys was chosen to account for the spatial coverage of the active buoys and at the same time secure a sufficient number of days in which at least eight buoys were active.

For the IMB sea ice thickness vs. assimilated sea ice thickness and the AWI sea ice thickness comparison, the IMB buoy coverage of 1 week was projected onto the model grid, choosing the nearest neighbor. For the model data, only grid points covered by the AWI data and the IMB buoys were chosen, and weekly averages were calculated for all three products. No threshold of a minimum number of active buoys was chosen, as this would have limited the available data too much.

3 Results

3.1 Freeboard and sea ice concentration RMSE

To verify that the assimilation improves the modeled FB and SIC, the root-mean-square errors (RMSEs) between the assimilated data sets and the model variables were computed after each assimilation time step. The calculation of RMSE includes all observed data points of the assimilation time step. RMSE for FB is calculated on the available satellite tracks (marked orange in Fig. 1), which change every week, and the co-located model values. The same approach is used for SIC (the blue area in Fig. 1) and the corresponding model data.

The results are shown in the upper panels of Figs. 3 and 4, and they are based on mean weekly model output data at the location where the corresponding observations exist. The lower panels in both figures show the difference between refRun and sicRun or fbRun. Positive values indicate that the assimilation has improved the SIC or FB, and negative values indicate that the variable was degraded by the assimilation. Degradation can occur when an assimilation variable disturbs the physical balance of the model and during a period of free run, when it is in the process of reestablishing its physical balance.

The results (Fig. 3, upper panel) show that the reference run (black) had the highest RMSE of all and that the RMSE increased the most over the assimilation period. This indicates that the assimilation improved the modeled sea ice concentration. The RMSE for the assimilated runs (sicRun in turquoise and fbRun in orange) also increased over the assimilation period but to a lesser extent than for the reference run. The lower panel in Fig. 3 shows a steady increase in the difference between the reference run and the assimilated runs, reflecting the degree to which assimilation improved sea ice concentration.

The increase in RMSE over the season is a result of the chosen area for calculating RMSE and the definition of the metric itself. RMSE weights larger errors more heavily than smaller errors. The FB differences are only calculated over areas with sea ice, while the SIC data include larger areas that are seasonally either ice-free or ice-covered. For SIC, the area with the largest error, which is weighted most, is the ice edge at the Atlantic side, which increases over winter, accounting for the observed seasonal increase in SIC RMSE from November to March in Fig. 3. Other assimilation studies have chosen to calculate RMSE only over ice areas with

sea ice concentration above 15 % (Chen et al., 2017), but to be consistent, we chose to calculate RMSE over the entire area.

The lower panel in Fig. 3 also shows negative values in October for the last 2 years, indicating that the assimilated runs agree less with the assimilated data compared to the reference run at the beginning of the assimilation period. The RMSE difference in the lower panel falls below 0 at the beginning of all assimilation periods after the initial one. As noted earlier, this can occur if the physical balance of the model is disturbed by assimilation.

The upper panel of Fig. 4 displays the RMSE of all FB values assimilated at the corresponding time. The black line represents refRun, while the turquoise line represents sicRun. Both have almost equal FB RMSE throughout the assimilation period, ranging between 7 and 14 cm. The black refRun covers the turquoise sicRun in the upper panel. On the other hand, the FB RMSE for fbRun shows a clear drop within the first month of the assimilation period, reducing to about 5 to 6 cm. The lower panel in Fig. 4 shows that the RMSE differences are all above 0, even at the beginning of a new assimilation period in November.

It is expected that the SIC RMSE in Fig. 3 and the FB RMSE in Fig. 4 show improvements, as the observation values are used within the assimilation scheme; however this demonstrates that the assimilation works.

3.2 CryoSat-2 AWI sea ice thickness

To demonstrate that the sea ice thickness estimated through the FB assimilation method provides comparable results to other sea ice thickness products derived from CryoSat-2, the sea ice thickness of fbRun was compared to the AWI sea ice thickness. The AWI sea ice thickness was selected because it is derived from the same FB values as the FB data assimilated in fbRun. Any differences between the two data sets therefore indicate the impact of the FB assimilation introduced here in contrast to the method of directly converting FB to sea ice thickness.

Table 1 presents the correlation coefficients and biases for sea ice thickness and FB in refRun and fbRun compared to the AWI data. All spatially coinciding data points of the model runs and the AWI data were considered over the entire period from 1 January 2018 to 31 December 2020. In general, the lowest correlations and highest biases are found in October, as no data had been assimilated yet and the assimilation period started in November.

The sea ice thickness biases are negative for all months and runs, indicating that the modeled sea ice thickness and FB are thinner than the AWI data's FB and sea ice thickness. The sea ice thickness biases for both runs are smallest in January, and the FB biases are smallest in January and February. Overall, the FB biases are thinner than the SIT biases, which is no surprise as FB is typically on the order of about 10 % of sea ice thickness (Alexandrov et al., 2010).

Comparing the correlation coefficients of refRun and fbRun for both the FB and the sea ice thickness shows that the difference between the FB correlation coefficients is higher than the difference between the sea ice thickness correlation coefficients. This indicates that the FB assimilation brings the modeled FB closer to the assimilated FB data but that the difference in deriving the SIT from the FB data also impacts the resulting SIT.

Figure 5 displays bivariate and univariate kernel density estimates (KDEs) for sea ice thickness (panels a and b) and FB (panels c and d) for fbRun (in orange) and refRun (in blue) compared to the AWI data. The months of October and December were displayed as they represent the lowest and highest sea ice thickness correlation (see Table 1).

The KDE for both variables of fbRun changes from October to December, indicating higher correlation coefficients and smaller biases in December, which is a result both of thin and thick sea ice and of FB getting thicker. However, the thicker FB and sea ice thickness values are still thinner than the AWI data variables, while the thin FB and sea ice thickness values are thicker than the AWI values. This could be a result of the assimilation discarding negative FB values in the model, while the AWI data set includes negative FB values.

For the month following December (not displayed), the center of the sea ice thickness KDE (at about 1 m in Fig. 5b) falls, month by month, further below the black regression line, while the thick sea ice thickness compared to refRun shows similar improvements to the December plot. This indicates that the decreasing correlation and increasing bias (Table 1) originate from fbRun's sea ice thickness and FB becoming thinner compared to the AWI data sets values, while the thick sea ice compares equally well to the AWI sea ice thickness.

3.3 Upward-looking sonar data

The BGEP upward-looking sonar sea ice draft is independent of the satellite-derived FB data, and it is used for the comparison of the modeled sea ice draft, which is calculated as described in Sect. 2.5. The BGEP data are not available for the complete period from 1 January 2018 to 31 December 2020; hence only data from October 2018 to December 2020 are used.

The BGEP ULS data, model data and AWI sea ice draft data are provided at different spatial and temporal coverage levels. To compare the different data sets, we split the comparison into two parts in order to account for these differences. In Fig. 6 the model drafts from all three model runs are compared to the BGEP ULS drafts based on mean daily differences, whereas, Fig. 7 compares the AWI draft and the fbRun draft with the BGEP ULS drafts based on mean weekly differences only at locations covered by the AWI data.

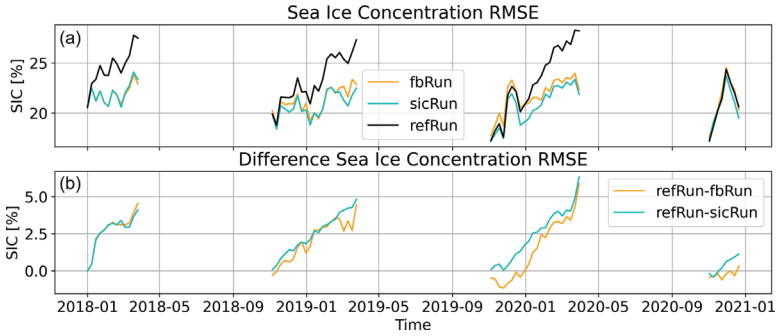

Figure 3. **(a)** Weekly SIC RMSE calculated at the observation data location, averaged over the corresponding assimilation time step. The orange plot shows the fbRun RMSE, the black the refRun RMSE and the turquoise the sicRun RMSE. **(b)** The differences in the top-panel RMSEs of refRun − fbRun in orange and refRun − sicRun in turquoise. The date format is year-month.

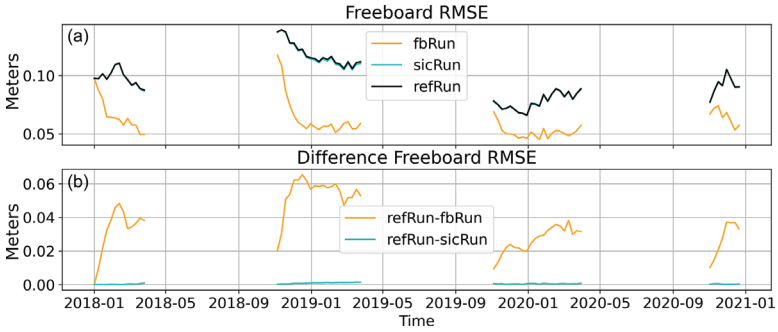

Figure 4. **(a)** Weekly FB RMSE calculated at the observation data location, averaged over the corresponding assimilation time step. The orange plot shows the fbRun RMSE, the black the refRun RMSE and the turquoise the sicRun RMSE. The black plot indicating refRun covers the turquoise plot indicating sicRun most of the time. **(b)** The differences in the top-panel RMSEs of refRun − fbRun in orange and refRun − sicRun in turquoise. The date format is year-month.

The differences between the BGEP upward-looking sonar ice draft and the model sea ice draft are shown in Fig. 6. The dashed line shows fbRun, the solid line refRun and the solid line with circle markers sicRun. The gray-shaded areas indicate the assimilation period.

For all three moorings, fbRun shows the values in closest agreement with the observations throughout the entire period displayed. This is also reflected by the lower RMSE listed in Table 2. The runs refRun and the sicRun are almost in perfect agreement except for on a few days, for example in October 2019 at BGEP moorings A and D. The RMSE between the BGEP data and fbRun is with 0.41 m, 23 cm lower than the RMSE of refRun and sicRun. Periods in summer, when the observation SD is 0 m, indicate periods with no ice present in the observations. Gaps indicate periods where no data are available. The BGEP observations are all ice-free in summer 2019, while only fbRun at BGEP mooring A reaches the point of being ice-free in late September continuing until the beginning of November 2019.

Figure 7 shows the mean differences between the AWI sea ice draft and the fbRun sea ice draft. To do so, the AWI data set was interpolated to the model grid and only data points covered by all three data sets (AWI CryoSat-2, fbRun and BGEP) were considered. Instead of daily averages as shown in Fig. 6, weekly averages were calculated, since the AWI sea ice draft is provided in weekly time steps. The dashed lines in Fig. 7 show the AWI data and the solid lines the fbRun data. The gray background shows the assimilation period. Colors are chosen per mooring according to Fig. 1. The resulting differences between the fbRun and the AWI CryoSat-2 sea

Table 1. Monthly mean correlation coefficient and mean bias between the weekly AWI sea ice thickness (SIT) and FB and the fbRun SIT and FB for the entire assimilation period from 1 January 2018 to 31 December 2020. Only grid points covered by both the AWI FB data and the model were considered.

	October	November	December	January	February	March	April
Correlation coefficient SIT fbRun	0.56	0.81	0.83	0.81	0.78	0.75	0.72
Correlation coefficient SIT refRun	0.40	0.49	0.45	0.44	0.44	0.51	0.50
Bias SIT fbRun	−0.52	−0.38	−0.17	−0.15	−0.18	−0.18	−0.22
Bias SIT refRun	−0.65	−0.56	−0.38	−0.23	−0.26	−0.28	−0.34
Correlation coefficient FB fbRun	0.30	0.68	0.79	0.76	0.78	0.78	0.74
Correlation coefficient FB refRun	0.06	0.09	−0.2	0.2	0.05	0.16	0.19
Bias FB fbRun	−0.03	−0.02	0.01	0.01	0	−0.01	−0.02
Bias FB refRun	−0.04	−0.04	−0.02	−0.01	−0.01	−0.02	−0.03

Table 2. RMSE calculated between the BGEP ULS draft measurement and the model runs fbRun, sicRun and refRun and the MOSAiC IMB sea ice thickness and the model runs. The RMSE and biases were calculated for all three mooring locations together, the assimilation period marked gray in Fig. 6 and the free-run period.

	BGEP ULS total	MOSAiC IMB
RMSE fbRun	0.41 m	0.20 m
RMSE sicRun	0.64 m	0.09 m
RMSE refRun	0.64 m	0.10 m

Table 3. The mean RMSE of the weekly mean differences shown in Fig. 7. The RMSE was calculated on average for each mooring and both the fbRun ice draft and the AWI CryoSat-2 ice draft.

	BGEP moorings A, B, D	MOSAiC IMB
fbRun	0.30 m	0.23 m
AWI CryoSat-2	0.30 m	0.34 m

ice draft are shown in Fig. 7. Both the AWI sea ice draft and the fbRun sea ice draft differ by about ±50 to 90 cm from the mooring data. There is no clear bias or seasonality in either difference, and they do not always follow the same pattern, except in winter 2019/20, when both data sets begin with a negative bias and end with a positive bias with the exception of a few weeks in the AWI CryoSat-2 draft at the end of the assimilation period.

The RMSEs between the BGEP moorings' sea ice draft, the fbRun sea ice draft and AWI CryoSat-2 sea ice draft were calculated. They are listed in Table 3. The RMSEs of the data products compared to the mooring data are both 0.3 m.

3.4 MOSAiC IMB data

The MOSAiC data cover a different spatial area than the BGEP observations. Data are interpolated to daily and weekly means respectively in order to have the same frequency as the data that they are being compared to. Details are described in Sect. 2.5.

In Fig. 8, the daily sea ice thicknesses from the MOSAiC IMB buoys and the three model runs are plotted for days when at least eight buoys were active. The shaded area around each line indicates 1 SD of the respective displayed data. The MOSAiC IMB data set has the largest SD, and all model runs lies within this SD for most of the observation period, with the exception of fbRun's sea ice thickness in October 2019, April 2020 and June 2020. Overall, the modeled, assimilated and observed sea ice thicknesses grow over the same period from October 2019 to April 2020, and all four sea ice thicknesses also start to decline at about the same time in June 2020. The observed sea ice thickness starts to be more variable at the beginning of June 2020, which is not reflected in the model data. The variability in the observation data is most likely caused by the reduced number of buoys that are active during this time and the sea ice being more mobile as it starts to melt. Both the refRun and the sicRun sea ice thicknesses compare better than fbRun to the MOSAiC observation. This is also reflected in the RMSE calculated for fbRun, sicRun and refRun in comparison to the MOSAiC sea ice thickness in Table 3. A one-sided t test was performed, comparing the differences between the different model runs and the MOSAiC IMB sea ice thickness. The one-sided t test showed that sicRun's and refRun's sea ice thickness RMSE was significantly lower than fbRun's RMSE.

Figure 9 shows the weekly mean sea ice thickness from the MOSAiC IMB buoys and the three model runs. The average is calculated as described in Sect. 2.5. The dash-dotted yellow line represents the AWI sea ice thickness, the dashed turquoise line represents the fbRun sea ice thickness and the solid black line represents the MOSAiC sea ice thickness. The transparent shaded background in each corresponding color indicates 1 SD. All three sea ice thicknesses increase over the displayed period. The AWI sea ice thickness increases the most from approximately 0.6 to 2.3 m with a sharp drop in the last week of April. The MOSAiC data display less growth and start slightly thicker than both the fbRun

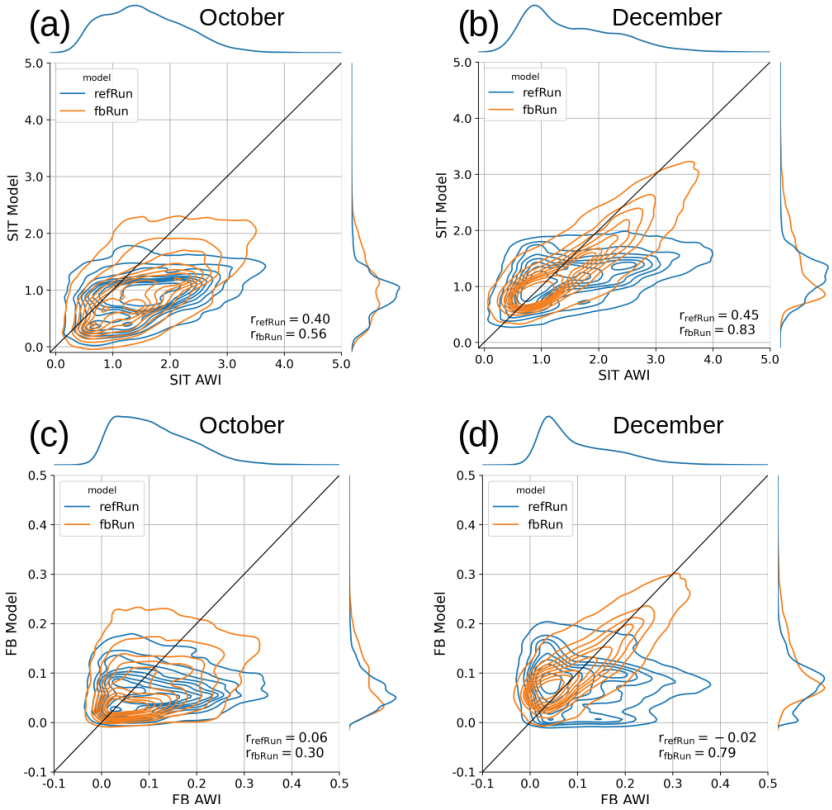

Figure 5. The bivariate and univariate kernel density estimate (KDE) for sea ice thickness and FB for the model runs fbRun and refRun in comparison to the AWI sea ice thickness and FB. Panels **(a)** and **(b)** show the sea ice thickness in October and December, and panels **(c)** and **(d)** show the FB for October and December. The months October and December were chosen because October is the month with the lowest sea ice thickness correlation between fbRun and AWI (as listed in Table 1). The correlation coefficients r are displayed in the lower-right corner of each plot. The black line indicates $r = 1$, and the unit is meters.

and AWI sea ice thickness at around 0.8 m in October 2019 and reach around 1.8 m in April 2020.

When comparing the sea ice thickness for fbRun from Figs. 8 and 9a, it is apparent that the fbRun sea ice thickness follows a similar pattern. However, this is not the case for the MOSAiC sea ice thickness. Comparing the sea ice thickness for the MOSAiC IMB data from Figs. 8 and 9a, the data in Fig. 9a appear to be more abundant. This difference is caused by the number of buoys considered. The buoys considered in Fig. 9 depend on the sparse AWI data coverage, while Fig. 8 considers at least eight buoys per day. This leads to larger jumps from week to week of the MOSAiC sea ice thickness in Fig. 9 compared to Fig. 8. This is also evident by the low SD at the beginning of March and in mid-April 2020 in Fig. 9.

Table 3 lists the RMSE calculated between the AWI and the MOSAiC sea ice thickness and between fbRun and MOSAiC sea ice thickness. The RMSE calculated for the AWI sea ice thickness is 11 cm greater than the RMSE calculated for the fbRun sea ice thickness. A one-sided t test was performed to determine the statistical significance of the difference, which showed that the fbRun RMSE is significantly smaller than the AWI RMSE.

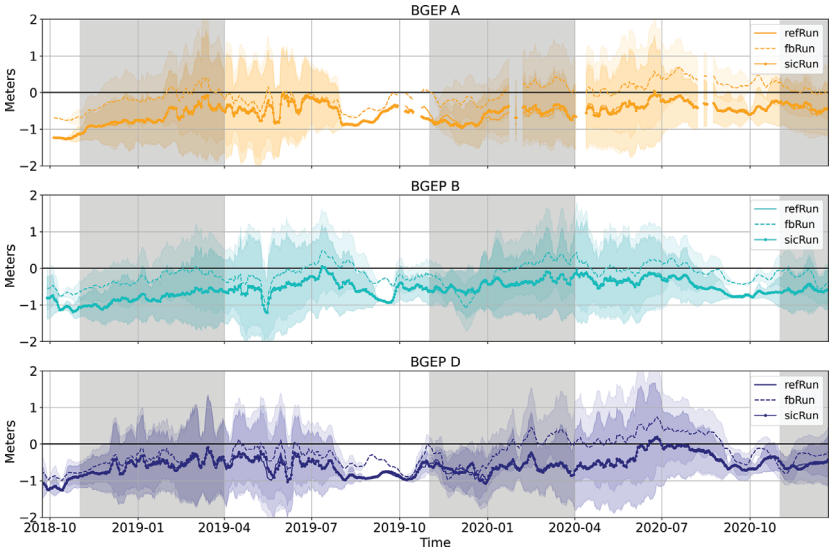

Figure 6. Daily mean sea ice draft differences and SD between BGEP observations and all three model runs. The shaded colored area shows 1 SD calculated for each day from the 10 s record. The SD appears darker where the SDs from different model runs overlap. The gray-shaded area indicates the assimilation period. The dashed line shows observed sea ice draft minus fbRun sea ice draft, the solid line the equivalent for refRun and the solid line with circle markers the equivalent for sicRun only. Panel **(a)** shows data from mooring A, panel **(b)** data from mooring B and panel **(c)** data from mooring D. The sites are marked in the corresponding colors in Fig. 1. The date format is year-month.

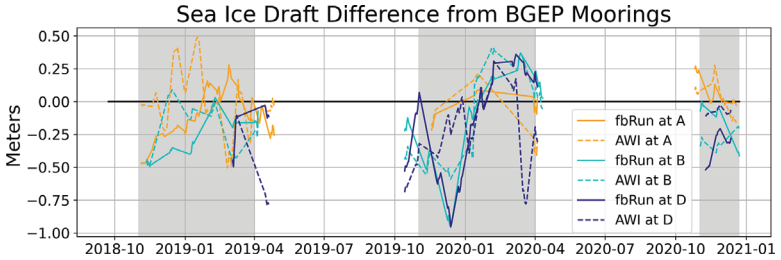

Figure 7. The weekly mean difference between the BGEP upward-looking sonar sea ice draft measurements and sea ice draft calculated from the AWI sea ice data set (dashed lines) and the fbRun sea ice data (solid lines). The color indicates the location in Fig. 1. Positive values indicate that the BGEP draft is thicker. The date format is year-month.

In Fig. 9b, the radar FB for the refRun, fbRun and AWI data are shown. The fbRun and AWI data FB in Fig. 9a and the respective sea ice thicknesses in Fig. 9b do not entirely follow the same pattern. The AWI FB starts out thinner than fbRun's FB, while the AWI sea ice thickness is thicker than fbRun's sea ice thickness throughout the entire displayed period. This indicates that the difference is caused by the difference in snow thickness and sea ice density. The AWI data are the FB values that were assimilated, and the fbRun FB is approximately between refRun's and AWI data values, showing the effect of the assimilation. It is clear from Fig. 8 that refRun and sicRun are closer to MOSAiC IMB data; however Fig. 9 shows that the fbRun follows the evolution of the observed radar FB better. This shows that the assimilation acts as expected, but in this area there is a discrepancy between the in situ observations from MOSAiC IMB buoys and the

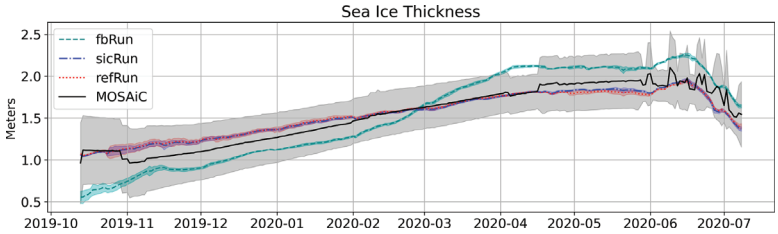

Figure 8. Daily mean sea ice thickness averaged over all grid cells covered by at least eight active buoys per day. The solid black line indicates the MOSAiC IMB-buoy-measured sea ice thickness, the dotted red line the refRun sea ice thickness, the dash-dotted blue line the sicRun sea ice thickness and the dashed turquoise line the fbRun sea ice thickness. The shaded areas around each of the plots indicate 1 SD of each daily averaged sea ice thickness data set. The date format is year-month.

remotely sensed AWI FB observations. The relation between the FB from refRun and fbRun follows a similar pattern to the sea ice thickness in Fig. 8, since the sea ice density, snowfall and water density values are not significantly influenced by the assimilation.

4 Discussion

To show the effect of the assimilation, the RMSE between the assimilated SIC and FB observations and the modeled SIC and FB was calculated for refRun, sicRun and fbRun. Figures 3 and 4 show that SIC and FB are improved as expected in each winter season when satellite-derived FB and SIC are assimilated. Further, the correlation coefficient between the AWI FB data (which was assimilated) and the fbRun FB data is higher than the correlation coefficient of the refRun and the AWI FB data. Sea ice thickness correlations and biases of fbRun in Table 1 also indicate a closer agreement with the AWI data when compared to refRun's correlations and biases. This shows that the FB assimilation has an effect on the modeled sea ice thickness.

The RMSE between the assimilated SIC and FB observations and the modeled SIC and FB was calculated for refRun, sicRun and fbRun, as shown in Figs. 3 and 4. The results show that assimilation of satellite-derived sea ice concentration and freeboard data has a positive effect on the model performance, with improved sea ice concentration and freeboard values in each winter season. The sea ice thickness, FB correlations and biases of fbRun in Table 1 suggest closer agreement with the AWI data than with refRun's correlations and biases. This again shows that the FB assimilation has an effect on the modeled sea ice thickness.

The comparisons to independent sea ice thickness observations indicate that the fbRun sea ice thickness is improved in the Beaufort Sea but not in the central Arctic. In contrast, refRun and sicRun perform significantly better in the central Arctic. Notably, the in situ observations in the Beaufort Sea cover more than 2 years, while those in the central Arctic only cover 9 months. The RMSE plots in Fig. 4 show that refRun's RMSE during the winter of 2019/20 is lower than in the prior month. Moreover, the calculation of the mean sea ice thickness difference between refRun and fbRun at the location of the MOSAiC IMB data in October for other years showed that 2019 was the year with the largest differences. This indicates that the sea ice thickness in this region is highly variable and suggests that the better performance of refRun and sicRun in winter 2019/20 might not be representative of all years. The FB values in Fig. 9b could suggest that the assimilated FB data cause the thinner ice for the fbRun sea ice thickness in Fig. 8. The assimilation begins in November, when fbRun's sea ice thickness is already thinner than refRun's and sicRun's sea ice thickness. Thus, the thinner sea ice in Fig. 8 is a result of the assimilation in the previous year. To be able to compare the year 2019 with other years, the mean sea ice thickness differences between refRun and fbRun were calculated at the location of the MOSAiC IMB data in October. The mean difference between refRun and fbRun is 28 cm for October 2018, 50 cm for October 2019 and 2 cm for October 2020. The MOSAiC year is clearly the one with the largest difference.

Considering refRun's RMSE in other years, the interannual variability in sea ice thickness in the examined region, the fact that the observations in the Beaufort Sea span a significantly longer time, and the fact that the BGEP ULS fbRun RMSE is over 20 cm lower than the refRun RMSE and only 10 cm higher for the MOSAiC IMB locations, we argue that fbRun's sea ice thickness is overall improved in comparison to sicRun's and refRun's sea ice thickness. Nevertheless, the difference between the Beaufort Sea and the central Arctic in the observations and the model runs underlines the need for more long-term in situ observations.

Dirkson et al. (2017) and Day et al. (2014) show that SIC has a shorter memory than sea ice thickness. The facts that FB improves sea ice thickness, as shown in Fig. 6, and that FB values are still improved after summer in all years (in

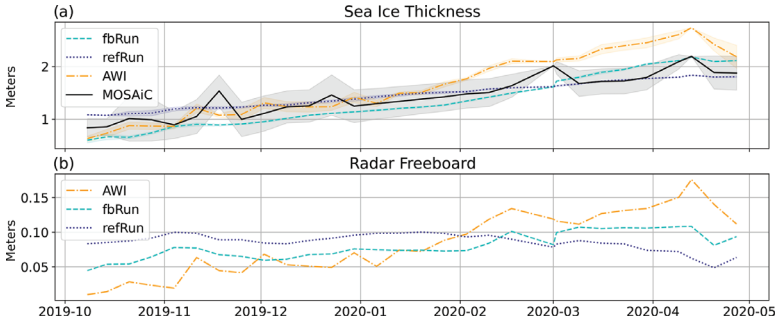

Figure 9. **(a)** Weekly mean sea ice thickness averaged over all grid cells covered by the CryoSat-2 flight pass considered in the AWI data set. The mean sea ice thickness is displayed with 1 SD for sea ice thickness from MOSAiC (solid black), AWI (dash-dotted yellow), fbRun (dashed turquoise) and refRun (dotted dark blue). **(b)** Same as **(a)** but for radar freeboard and without MOSAiC observations. The dash-dotted yellow line shows AWI radar FB, the dashed turquoise line fbRun radar FB and the dotted dark-blue line refRun radar FB. The date format is year-month.

contrast to SIC), as shown in the lower panel of Fig. 4, suggest that FB also keeps the memory as opposed to SIC.

The AWI sea ice thickness could be a typical CryoSat-2 product that could be assimilated in order to improve the modeled sea ice thickness. Based on the RMSEs in Table 2, which show that the FB assimilation gives better values compared to the MOSAiC data, and similar results in the Beaufort Sea, the method presented in this study shows the perspective of assimilating FB instead.

We discussed that the thinner fbRun sea ice thickness in October in Figs. 9 and 8 is not caused by assimilating the also thinner AWI FB, as the assimilation starts in November. In contrast, the significantly larger increase in fbRun's sea ice thickness later in the year is a direct result of assimilating thick FB: in the second half of the 2019/20 winter season, the AWI sea ice thickness (Fig. 9a) was clearly thicker than the MOSAiC sea ice thickness. While it is not as clear for fbRun's sea ice thickness in Fig. 9a, Fig. 8 clearly shows that fbRun's sea ice thickness is also thicker than the MOSAiC sea ice thickness. The increase in fbRun's sea ice thickness during late February to early April 2020 (Fig. 8) follows the increase in AWI FB (yellow line in Fig. 9b) starting at the end of January 2020. Since the AWI FB is assimilated in fbRun, this increase is caused by the assimilation. However, this assimilation leads to sea ice that is too thick, as seen in Fig. 8. This overestimation of sea ice thickness is likely due to an overestimation of FB in the AWI data, as found by King et al. (2018) in their field campaign in April. Other studies (Giles and Hvidegaard, 2006; Willatt et al., 2011; Ricker et al., 2015) suggest similar biases in the radar backscattering horizon for deep snow and high moisture content. Giles and Hvidegaard (2006) and King et al. (2018) both conducted field studies in March and April, months when the assimilated AWI FB (Fig. 7b) is highest, near the final MOSAiC location. The resulting overestimation of sea ice thickness in the AWI data and the comparable thinner assimilated sea ice thickness from fbRun comprise a good example of the advantage of assimilating FB instead of sea ice thickness.

The increase in biases and the decrease in correlations shown in Table 1 exhibit a similar pattern to the FB and sea ice thickness at the MOSAiC IMB locations discussed above. This similar behavior could indicate that the pattern displayed in Fig. 7 is not restricted to the observation area and suggests that the FB assimilation could correct the error introduced by the wrongly located scattering horizon in the CryoSat-2 FB retrievals to some extent. However, the thickness comparison of fbRun and AWI data to the BGEP data set (Figs. 6 and 7) does not show the same seasonal pattern in thickness as that discussed above for the MOSAiC observation. This might indicate regional differences in the scattering horizon or that the assimilation does not correct for the effect everywhere in the same manner. Further studies are needed to investigate this.

5 Conclusions

In this study, a method to assimilate FB is described, and the results from a 3-year assimilation run are evaluated. The presented method builds upon calculating an increment using modeled FB and then converting the changed FB into the sea ice thickness. The method uses parameters from the sea ice model for the sea ice density, snow density and snow thickness instead of the prescribed values used in the AWI sea ice thickness product, which it is compared to. First, it was shown that the FB assimilation improves the modeled FB (Fig. 4) and that the assimilation affects the sea ice thickness (Table 1). Figure 6 shows that the sea ice thickness of

the run assimilating FB is improved in the Beaufort Sea. The comparison to MOSAiC IMB sea ice thickness data from the central Arctic does not give the same results. Here refRun and sicRun perform better, but we can show that the poorer performance of the assimilation is to some extent due to too thick FB being assimilated. CryoSat-2 FB is known to have a thick bias in late winter due to uncertainties in the backscattering horizon of the radar signal (Giles and Hvidegaard, 2006; Willatt et al., 2011; Ricker et al., 2015). The seasonality of the biases and correlations listed in Table 1 as well as the observation comparison in Fig. 9 indicates that the assimilation has some skill in mitigating this bias. One of the two main objectives was to determine if the FB assimilation improves sea ice thickness. Even though fbRun is worse compared to the MOSAiC IMB observations than refRun, it is in closer agreement with the longer observation record at the BGEP locations.

To compare our method to sea ice thickness data from a more classical approach, we have chosen the weekly sea ice thickness product from the AWI sea ice portal (Hendricks et al., 2021). This sea ice thickness is derived from the same FB as that assimilated in fbRun. Overall, the AWI CryoSat-2 sea ice thickness and FB is thicker than fbRun's sea ice thickness and FB (Table 1). When comparing the two sea ice thicknesses to independent sea ice measurements from the BGEP upward-looking sonar data, we can show that the FB-assimilated sea ice thickness and AWI sea ice thickness result in similar RMSEs. The comparison to sea ice thickness observations from MOSAiC IMB buoys deployed during the MOSAiC in the central Arctic results in significantly lower RMSE for the sea ice thickness from the FB assimilation.

5.1 Outlook

The presented method builds upon modeling the most influential variables of Eq. (6). These are the snow thickness, the snow density and the sea ice density (Alexandrov et al., 2010). The snow density used in this study does not differ from the snow density used in the AWI data product. The results in Fig. 7 show that the modeled variables result in similar results at the BGEP locations and better results in the central Arctic compared to the empirical values used in the AWI sea ice thickness product. Both the snow thickness and the sea ice density differ, and no clear conclusion can be drawn at this point as to whether the AWI values or the model values are more correct. As the aim of this study was to present the method on how to assimilate FB and a validation of the resulting sea ice thickness, a detailed discussion of the model parameters and the resulting influence on the sea ice thickness when compared to more traditional approaches is not included. A study with a focus on this is currently in preparation.

Code availability. The CICE code is available from https://github.com/CICE-Consortium/CICE/releases/tag/CICE6.2.0 (last access: 12 April 2021) and https://doi.org/10.5281/zenodo.4671172 (Hunke et al., 2021). The NEMO code is available from here: https://doi.org/10.5281/zenodo.3878122 (Madec et al., 2017). The PDAF code can be downloaded from this home page: https://pdaf.awi.de/register/index.php (last access: 20 January 2022, Nerger and Hiller, 2013). Additional CICE routines for the FB assimilation are available upon request to the contact author.

Data availability. The BGEP data were collected and made available by the Beaufort Gyre Exploration Program based at the Woods Hole Oceanographic Institution (https://www2.whoi.edu/site/beaufortgyre/, BGEP, 2022) in collaboration with researchers from Fisheries and Oceans Canada at the Institute of Ocean Sciences. The AWI FB and SIT are available at https://epic.awi.de/id/eprint/53331/ (Hendricks et al., 2021). The MOSAiC IMB data are accessible through PANGAEA (https://doi.org/10.1594/PANGAEA.938244,, Lei et al., 2021). The assimilate SIC data are the Global Sea Ice Concentration Climate Data Record v3.0 – Multimission and are available at https://doi.org/10.15770/EUM_SAF_OSI_0014 (OSI SAF, 2022).

Author contributions. IS conceived the assimilation setup, implemented it and wrote the manuscript draft. TASR edited and reviewed the manuscript and advised on matters related to the assimilation setup and CICE. LS edited and reviewed the manuscript and advised on CryoSat-2-related matters.

Competing interests. The contact author has declared that none of the authors has any competing interests.

Disclaimer. The model input contains Copernicus Climate Change Service information (2021), and neither the European Commission nor ECMWF is responsible for any use that may be made of the Copernicus information or data it contains.

Publisher's note: Copernicus Publications remains neutral with regard to jurisdictional claims in published maps and institutional affiliations.

Acknowledgements. The BGEP data were collected and made available by the Beaufort Gyre Exploration Program based at the Woods Hole Oceanographic Institution (https://www2.whoi.edu/site/beaufortgyre/, last access: 29 June 2022) in collaboration with researchers from Fisheries and Oceans Canada at the Institute of Ocean Sciences.

We thank Lars Nerger for his help during the implementation process of PDAF.

We would also like to thank William Gregory and the anonymous reviewer for their comments, helping us improve the presented study significantly.

Financial support. This study is a collaboration between the Danish Meteorological Institute, Aalborg University and the Technical University of Denmark. It is funded by the Danish state through the National Centre for Climate Research and the Act of Innovation foundation in Denmark through the MARIOT project (grant number 9090 00007B).

Review statement. This paper was edited by Vishnu Nandan and reviewed by William Gregory and one anonymous referee.

References

Aaboe, S., Down, E. J., and Eastwood, S.: Product User Manual for the Global sea-ice edge and type Product, Norwegian Meteorological Institute: Oslo, Norway, https://osisaf-hl.met.no/sites/osisaf-hl/files/user_manuals/osisaf_cdop3_ss2_pum_sea-ice-edge-type_v3p1.pdf (last access: 30 August 2023), 2021.

Alexandrov, V., Sandven, S., Wahlin, J., and Johannessen, O. M.: The relation between sea ice thickness and freeboard in the Arctic, The Cryosphere, 4, 373–380, https://doi.org/10.5194/tc-4-373-2010, 2010.

BGEP (Beaufort Gyre Exploration Program): https://www2.whoi.edu/site/beaufortgyre/, Woods Hole Oceanographic Institution last access: 29 June 2022.

Blockley, E. W., Martin, M. J., McLaren, A. J., Ryan, A. G., Waters, J., Lea, D. J., Mirouze, I., Peterson, K. A., Sellar, A., and Storkey, D.: Recent development of the Met Office operational ocean forecasting system: an overview and assessment of the new Global FOAM forecasts, Geosci. Model Dev., 7, 2613–2638, https://doi.org/10.5194/gmd-7-2613-2014, 2014.

Bloom, S., Takacs, L., Da Silva, A., and Ledvina, D.: Data assimilation using incremental analysis updates, Mon. Weather Rev., 124, 1256–1271, 1996.

Cao, Y., Liang, S., Sun, L., Liu, J., Cheng, X., Wang, D., Chen, Y., Yu, M., and Feng, K.: Trans-Arctic shipping routes expanding faster than the model projections, Global Environ. Chang., 73, 102488, https://doi.org/10.1016/j.gloenvcha.2022.102488, 2022.

Chen, Z., Liu, J., Song, M., Yang, Q., and Xu, S.: Impacts of assimilating satellite sea ice concentration and thickness on Arctic sea ice prediction in the NCEP Climate Forecast System, J. Climate, 30, 8429–8446, 2017.

Cox, G. F. and Weeks, W. F.: Salinity variations in sea ice, J. Glaciol., 13, 109–120, 1974.

Dai, A. and Trenberth, K. E.: Estimates of freshwater discharge from continents: Latitudinal and seasonal variations, J. Hydrometeorol., 3, 660–687, 2002.

Day, J., Hawkins, E., and Tietsche, S.: Will Arctic sea ice thickness initialization improve seasonal forecast skill?, Geophys. Res. Lett., 41, 7566–7575, 2014.

Dirkson, A., Merryfield, W. J., and Monahan, A.: Impacts of sea ice thickness initialization on seasonal Arctic sea ice predictions, J. Climate, 30, 1001–1017, 2017.

Drinkwater, M. R., Francis, R., Ratier, G., and Wingham, D. J.: The European Space Agency's earth explorer mission CryoSat: measuring variability in the cryosphere, Ann. Glaciol., 39, 313–320, 2004.

Egbert, G. D. and Erofeeva, S. Y.: Efficient inverse modeling of barotropic ocean tides, J. Atmos. Ocean. Tech., 19, 183–204, 2002.

Fetterer, F. and Stewart, J. S.: U.S. National Ice Center Arctic and Antarctic Sea Ice Concentration and Climatologies in Gridded Format, Version 1, Boulder, Colorado USA, National Snow and Ice Data Center [data set], https://doi.org/10.7265/46cc-3952, 2020.

Fiedler, E. K., Martin, M. J., Blockley, E., Mignac, D., Fournier, N., Ridout, A., Shepherd, A., and Tilling, R.: Assimilation of sea ice thickness derived from CryoSat-2 along-track freeboard measurements into the Met Office's Forecast Ocean Assimilation Model (FOAM), The Cryosphere, 16, 61–85, https://doi.org/10.5194/tc-16-61-2022, 2022.

Garnier, F., Fleury, S., Garric, G., Bouffard, J., Tsamados, M., Laforge, A., Bocquet, M., Fredensborg Hansen, R. M., and Remy, F.: Advances in altimetric snow depth estimates using bi-frequency SARAL and CryoSat-2 Ka–Ku measurements, The Cryosphere, 15, 5483–5512, https://doi.org/10.5194/tc-15-5483-2021, 2021.

Giles, K. A. and Hvidegaard, S. M.: Comparison of space borne radar altimetry and airborne laser altimetry over sea ice in the Fram Strait, Int. J. Remote Sens., 27, 3105–3113, 2006.

Hendricks, S., Ricker, R., and Paul, S.: Product User Guide & Algorithm Specification: AWI CryoSat-2 Sea Ice Thickness (version 2.4), https://epic.awi.de/id/eprint/53331/ (last access: 21 October 2021) 2021.

Hersbach, H., Bell, B., Berrisford, P., Hirahara, S., Horányi, A., Muñoz Sabater, J., Nicolas, J., Peubey, C., Radu, R., Schepers, D., Simmons, A., Soci, C., Abdalla, S., Abellan, X., Balsamo, G., Bechtold, P., Biavati, G., Bidlot, J., Bonavita, M., De Chiara, G., Dahlgren, P., Dee, D., Diamantakis, M., Dragani, R., Flemming, J., Forbes, R., Fuentes, M., Geer, A., Haimberger, L., Healy, S., Hogan, R. J., Hólm, E., Janisková, M., Keeley, S., Laloyaux, P., Lopez, P., Lupu, C., Radnoti, G., de Rosnay, P., Rozum, I., Vamborg, F., Villaume, S., and Thépaut, J.-N.: Complete ERA5: Fifth generation of ECMWF atmospheric reanalyses of the global climate, Copernicus Climate Change Service (C3S) Data Store (CDS) [data set], https://doi.org/10.1002/qj.3803, 2017.

Hordoir, R., Skagseth, Ø., Ingvaldsen, R. B., Sandø, A. B., Löptien, U., Dietze, H., Gierisch, A. M., Assmann, K. M., Lundesgaard, Ø., and Lind, S.: Changes in Arctic Stratification and Mixed Layer Depth Cycle: A Modeling Analysis, J. Geophys. Res.-Oceans, 127, e2021JC017270, https://doi.org/10.1029/2021jc017270, 2022.

Hunke, E., Allard, R., Bailey, D. A., Blain, P., Craig, A., Dupont, F., DuVivier, A., Grumbine, R., Hebert, D., Holland, M., Jeffery, N., Lemieux, J.-F., Osinski, R., Rasmussen, T., Ribergaard, M., Roberts, A., Turner, M., Winton, M., and Rethmeier, S.: CICE-Consortium/CICE: CICE Version 6.2.0 (6.2.0), Zenodo [code], https://doi.org/10.5281/zenodo.4671172, 2021.

Hunke, E., Allard, R., Bailey, D. A., Blain, P., Craig, A., Dupont, F., DuVivier, A., Grumbine, R., Hebert, D., Holland, M., Jeffery, N., Lemieux, J.-F., Osinski, R., Rasmussen, T., Ribergaard, M., Roberts, A., Turner, M., and Winton, M.: CICE-Consortium/Icepack: Icepack 1.2.5, Zenodo, https://doi.org/10.5281/zenodo.4671132, 2021b.

Hunke, E., Allard, R., Bailey, D. A., Blain, P., Craig, A., Dupont, F., DuVivier, A., Grumbine, R., Hebert, D., Holland, M., Jeffery,

N., Lemieux, J.-F., Osinski, R., Rasmussen, T., Ribergaard, M., Roberts, A., Turner, M., Winton, M., and Rethmeier, S.: CICE Version 6.2.0, https://github.com/CICE-Consortium/CICE/tree/CICE6.2.0 (last access: 12 April 2021), 2021a.

Ivanova, N., Tonboe, R., and Pedersen, L.: SICCI Product Validation and Algorithm Selection Report (PVASR)–Sea Ice Concentration, Technical Report, https://doi.org/10.13140/2.1.2204.0649, 2013.

Ivanova, N., Johannessen, O. M., Pedersen, L. T., and Tonboe, R. T.: Retrieval of Arctic Sea Ice Parameters by Satellite Passive Microwave Sensors: A Comparison of Eleven Sea Ice Concentration Algorithms, IEEE T. Geosci. Remote, 52, 7233–7246, https://doi.org/10.1109/TGRS.2014.2310136, 2014.

Jackson, K., Wilkinson, J., Maksym, T., Meldrum, D., Beckers, J., Haas, C., and Mackenzie, D.: A novel and low-cost sea ice mass balance buoy, J. Atmos. Ocean. Tech., 30, 2676–2688, 2013.

Kaminski, T., Kauker, F., Toudal Pedersen, L., Voßbeck, M., Haak, H., Niederdrenk, L., Hendricks, S., Ricker, R., Karcher, M., Eicken, H., and Gråbak, O.: Arctic Mission Benefit Analysis: impact of sea ice thickness, freeboard, and snow depth products on sea ice forecast performance, The Cryosphere, 12, 2569–2594, https://doi.org/10.5194/tc-12-2569-2018, 2018.

Kern, S., Khvorostovsky, K., Skourup, H., Rinne, E., Parsakhoo, Z. S., Djepa, V., Wadhams, P., and Sandven, S.: The impact of snow depth, snow density and ice density on sea ice thickness retrieval from satellite radar altimetry: results from the ESA-CCI Sea Ice ECV Project Round Robin Exercise, The Cryosphere, 9, 37–52, https://doi.org/10.5194/tc-9-37-2015, 2015.

Kern, S., Rösel, A., Pedersen, L. T., Ivanova, N., Saldo, R., and Tonboe, R. T.: The impact of melt ponds on summertime microwave brightness temperatures and sea-ice concentrations, The Cryosphere, 10, 2217–2239, https://doi.org/10.5194/tc-10-2217-2016, 2016.

King, J., Skourup, H., Hvidegaard, S. M., Rösel, A., Gerland, S., Spreen, G., Polashenski, C., Helm, V., and Liston, G. E.: Comparison of freeboard retrieval and ice thickness calculation from ALS, ASIRAS, and CryoSat-2 in the Norwegian Arctic to field measurements made during the N-ICE2015 expedition, J. Geophys. Res.-Oceans, 123, 1123–1141, 2018.

Kurtz, N. T., Farrell, S. L., Studinger, M., Galin, N., Harbeck, J. P., Lindsay, R., Onana, V. D., Panzer, B., and Sonntag, J. G.: Sea ice thickness, freeboard, and snow depth products from Operation IceBridge airborne data, The Cryosphere, 7, 1035–1056, https://doi.org/10.5194/tc-7-1035-2013, 2013.

Kurtz, N. T. and Farrell, S. L.: Large-scale surveys of snow depth on Arctic sea ice from Operation IceBridge, Geophys. Res. Lett., 38, L20505, https://doi.org/10.1029/2011GL049216, 2011.

Kwok, R.: Satellite remote sensing of sea-ice thickness and kinematics: a review, J. Glaciol., 56, 1129–1140, 2010.

Kwok, R. and Cunningham, G.: Variability of Arctic sea ice thickness and volume from CryoSat-2, Philos. T. Roy. Soc. A, 373, 20140157, https://doi.org/10.1098/rsta.2014.0157, 2015.

Kwok, R., Panzer, B., Leuschen, C., Pang, S., Markus, T., Holt, B., and Gogineni, S.: Airborne surveys of snow depth over Arctic sea ice, J. Geophys. Res.-Oceans, 116, C11018, https://doi.org/10.1029/2011JC007371, 2011.

Landy, J. C., Tsamados, M., and Scharien, R. K.: A facet-based numerical model for simulating SAR altimeter echoes from heterogeneous sea ice surfaces, IEEE T. Geosci. Remote, 57, 4164–4180, 2019.

Landy, J. C., Dawson, G. J., Tsamados, M., Bushuk, M., Stroeve, J. C., Howell, S. E., Krumpen, T., Babb, D. G., Komarov, A. S., Heorton, H. D., Belter, B. S., Jakob, H., and Yevgeny, A.: A year-round satellite sea-ice thickness record from CryoSat-2, Nature, 609, 517–522, 2022.

Laxon, S., Peacock, N., and Smith, D.: High interannual variability of sea ice thickness in the Arctic region, Nature, 425, 947–950, 2003.

Laxon, S. W., Giles, K. A., Ridout, A. L., Wingham, D. J., Willatt, R., Cullen, R., Kwok, R., Schweiger, A., Zhang, J., Haas, C., Hendricks, S., Krishfield, R., Kurtz, N., Farrell, S., and Davidson, M.: CryoSat-2 estimates of Arctic sea ice thickness and volume, Geophys. Res. Lett., 40, 732–737, 2013.

Lei, R., Cheng, B., Hoppmann, M., and Zuo, G.: Snow depth and sea ice thickness derived from the measurements of SIMBA buoys deployed in the Arctic Ocean during the Legs 1a, 1, and 3 of the MOSAiC campaign in 2019–2020, PANGAEA [data set], https://doi.org/10.1594/PANGAEA.938244, 2021.

Lellouche, J.-M., Greiner, E., Bourdallé-Badie, R., Garric, G., Melet, A., Drévillon, M., Bricaud, C., Hamon, M., Le Galloudec, O., Regnier, C., Candela, T., Testut, C.-E., Gasparin, F., Ruggiero, G., Benkiran, M., Drillet, Y., and Le Traon, P.-Y.: The Copernicus global 1/12° oceanic and sea ice GLORYS12 reanalysis, Front. Earth Sci., 9, 585, https://doi.org/10.3389/feart.2021.698876, 2021.

Liston, G. E., Itkin, P., Stroeve, J., Tschudi, M., Stewart, J. S., Pedersen, S. H., Reinking, A. K., and Elder, K.: A Lagrangian snow-evolution system for sea-ice applications (SnowModel-LG): Part I–Model description, J. Geophys. Res.-Oceans, 125, e2019JC015913, https://doi.org/10.1029/2019JC015913, 2020.

Madec, G., Bourdallé-Badie, R., Chanut, J., Clementi, E., Coward, A., Ethé, C., Iovino, D., Lea, D., Lévy, C., Lovato, T., Martin, N., Masson, S., Mocavero, S., Rousset, C., Storkey, D., Vancoppenolle, M., Müeller, S., Nurser, G., Bell, M., and Samson, G.: NEMO ocean engine, Zenodo [code], https://doi.org/10.5281/zenodo.3878122, 2017.

Mallett, R. D. C., Lawrence, I. R., Stroeve, J. C., Landy, J. C., and Tsamados, M.: Brief communication: Conventional assumptions involving the speed of radar waves in snow introduce systematic underestimates to sea ice thickness and seasonal growth rate estimates, The Cryosphere, 14, 251–260, https://doi.org/10.5194/tc-14-251-2020, 2020.

Martino, A. J., Neumann, T. A., Kurtz, N. T., and McLennan, D.: ICESat-2 mission overview and early performance, in: Sensors, systems, and next-generation satellites XXIII, 11151, 68–77, SPIE, 2019.

Mu, L., Yang, Q., Losch, M., Losa, S. N., Ricker, R., Nerger, L., and Liang, X.: Improving sea ice thickness estimates by assimilating CryoSat-2 and SMOS sea ice thickness data simultaneously, Q. J. Roy. Meteor. Soc., 144, 529–538, 2018.

Nerger, L. and Hiller, W.: Software for ensemble-based data assimilation systems–Implementation strategies and scalability, Comput. Geosci., 55, 110–118, 2013.

Nerger, L., Janjić, T., Schröter, J., and Hiller, W.: A regulated localization scheme for ensemble-based Kalman filters, Q. J. Roy. Meteor. Soc., 138, 802–812, 2012.

Nord, A., Kärnä, T., Lindenthal, A., Ljungemyr, P., Maljutenko, I., Falahat, S., Ringgaard, I. M., Korabel, V., Kanarik, H., Verjovkina, S., Jandt, S., with support of the whole BAL MFC team: New coupled forecasting system for the baltic sea area, in: 9th EuroGOOS International conference, Ifremer; EuroGOOS AISBL, May 2021, Brest, France, 238–244, hal-03328374v2f, 2021.

OSI SAF: Global Sea Ice Concentration Climate Data Record v2.0 – Multimission, EUMETSAT SAF on Ocean and Sea Ice [data set], https://doi.org/10.15770/EUM_SAF_OSI_0008, 2017.

OSI SAF: OSISAF: Global Sea Ice Concentration Climate Data Record v3.0 – Multimission, EUMETSAT SAF on Ocean and Sea Ice [data set], https://doi.org/10.15770/EUM_SAF_OSI_0014, 2022.

Ricker, R., Hendricks, S., Helm, V., Skourup, H., and Davidson, M.: Sensitivity of CryoSat-2 Arctic sea-ice freeboard and thickness on radar-waveform interpretation, The Cryosphere, 8, 1607–1622, https://doi.org/10.5194/tc-8-1607-2014, 2014.

Ricker, R., Hendricks, S., Perovich, D. K., Helm, V., and Gerdes, R.: Impact of snow accumulation on CryoSat-2 range retrievals over Arctic sea ice: An observational approach with buoy data, Geophys. Res. Lett., 42, 4447–4455, 2015.

Rösel, A. and Kaleschke, L.: Influence of melt ponds on microwave sensors' sea ice concentration retrieval algorithms, in: 2012 IEEE International Geoscience and Remote Sensing Symposium, July 2012, Munich, Germany, 3261–3264, https://doi.org/10.1109/IGARSS.2012.6350608, 2012.

Saldo, R.: Global Sea Ice Concentration Climate Data Records Scientific Validation Report, https://osisaf-hl.met.no/sites/osisaf-hl/files/user_manuals/osisaf_cdop3_ss2_pum_sea-ice-edge-type_v3p1.pdf (last access: 30 August 2023), 2022.

Sallila, H., Farrell, S. L., McCurry, J., and Rinne, E.: Assessment of contemporary satellite sea ice thickness products for Arctic sea ice, The Cryosphere, 13, 1187–1213, https://doi.org/10.5194/tc-13-1187-2019, 2019.

Schulzweida, U.: CDO User Guide, Zenodo, https://doi.org/10.5281/zenodo.7112925, 2022.

Smith, G. C., Liu, Y., Benkiran, M., Chikhar, K., Surcel Colan, D., Gauthier, A.-A., Testut, C.-E., Dupont, F., Lei, J., Roy, F., Lemieux, J.-F., and Davidson, F.: The Regional Ice Ocean Prediction System v2: a pan-Canadian ocean analysis system using an online tidal harmonic analysis, Geosci. Model Dev., 14, 1445–1467, https://doi.org/10.5194/gmd-14-1445-2021, 2021.

Stroeve, J. and Notz, D.: Insights on past and future sea-ice evolution from combining observations and models, Global Planet. Change, 135, 119–132, 2015.

Tilling, R. L., Ridout, A., and Shepherd, A.: Estimating Arctic sea ice thickness and volume using CryoSat-2 radar altimeter data, Adv. Space Res., 62, 1203–1225, 2018.

Timco, G. and Frederking, R.: A review of sea ice density, Cold Reg. Sci. Technol., 24, 1–6, 1996.

Tranchant, B., Testut, C.-E., Ferry, N., and Brasseur, P.: SAM2: The second generation of Mercator assimilation system, European Operational Oceanography: Present and Future, p. 650, ISBN 92-894-9788-2, 2006.

Tsamados, M., Feltham, D. L., Schroeder, D., Flocco, D., Farrell, S. L., Kurtz, N., Laxon, S. W., and Bacon, S.: Impact of variable atmospheric and oceanic form drag on simulations of Arctic sea ice, J. Phys. Oceanogr., 44, 1329–1353, 2014.

Tschudi, M. A., Meier, W. N., and Stewart, J. S.: An enhancement to sea ice motion and age products at the National Snow and Ice Data Center (NSIDC), The Cryosphere, 14, 1519–1536, https://doi.org/10.5194/tc-14-1519-2020, 2020.

Vernieres, G., Zhao, B., Cullather, R. I., Akella, S., Vikhliaev, Y. V., Kurtz, N. T., and Kovach, R. M.: Assimilation of Cryosat 2 Arctic Sea-Ice Freeboard in an Ensemble of Coupled GEOS5, American Geophysical Union, 2016, HE13A–06, 2016.

Warren, S. G., Rigor, I. G., Untersteiner, N., Radionov, V. F., Bryazgin, N. N., Aleksandrov, Y. I., and Colony, R.: Snow depth on Arctic sea ice, J. Climate, 12, 1814–1829, 1999.

Willatt, R., Laxon, S., Giles, K., Cullen, R., Haas, C., and Helm, V.: Ku-band radar penetration into snow cover on Arctic sea ice using airborne data, Ann. Glaciol., 52, 197–205, 2011.

Wingham, D., Francis, C., Baker, S., Bouzinac, C., Brockley, D., Cullen, R., de Chateau-Thierry, P., Laxon, S., Mallow, U., Mavrocordatos, C., Phalippou, L., Ratier, G., Rey, L., Rostan, F., Viau, P., and Wallis, D.: CryoSat: A mission to determine the fluctuations in Earth's land and marine ice fields, Adv. Space Res., 37, 841–871, 2006.

Ye, Y., Luo, Y., Sun, Y., Shokr, M., Aaboe, S., Girard-Ardhuin, F., Hui, F., Cheng, X., and Chen, Z.: Inter-comparison and evaluation of Arctic sea ice type products, The Cryosphere, 17, 279–308, https://doi.org/10.5194/tc-17-279-2023, 2023.

Zuo, H., Balmaseda, M. A., Tietsche, S., Mogensen, K., and Mayer, M.: The ECMWF operational ensemble reanalysis–analysis system for ocean and sea ice: a description of the system and assessment, Ocean Sci., 15, 779–808, https://doi.org/10.5194/os-15-779-2019, 2019.

Impact assessment of snow thickness, sea ice density and water density in CryoSat-2 derived sea ice thickness

Imke Sievers[1], Henriette Skourup[2], and Till A. S. Rasmussen[1]

[1]Danish Meteorological Institut, Sankt Kjelds Plads 11, 2100 Copenhagen East, Denmark
[2]DTU Space, Danish Technical University, Elektrovej Building 327, 2800 Kongens Lyngby, Denmark

Correspondence: Imke Sievers (imksie@dmi.dk)

Abstract. Sea ice thickness is an essential climate variable, which is often derived from satellite altimetry freeboard estimates, e.g. CryoSat-2. In order to convert freeboard to sea ice thickness, assumptions are needed for snow thickness, snow density, sea ice density and water density. These parameters are difficult to observe co-located in time and space with the satellite derived freeboard measurements. For this reason, most available CryoSat-2 sea ice thickness products rely on climatologies based on outdated observations and empirical values. Model and observation based alternatives of sea ice density and snow thickness values have been suggested over the past years, but their combined influence on the freeboard to sea ice thickness conversion has not been analyzed.

This study, evaluates model based spatially varying snow thickness, sea ice density and water density with in situ observations and the associated parameters used in the classical CryoSat-2 sea ice thickness production. Further, this study calculates the mean sea ice thickness differences resulting from substituting the parameters used in a classical CryoSat-2 sea ice thickness product with model based values. The evaluation shows that the model derived snow thickness, sea ice density and water density compare better to observations than the associated parameters used in the CryoSat-2 sea ice thickness product. Furthermore, we find that the model based snow thickness and sea ice density separately lead to the largest sea ice thickness differences, but that, to some extent, their differences cancel out when both parameters are used in combination. For the water density, we find the average and maximum sea ice thickness difference to be small in comparison to the sea ice thickness differences introduced by the snow thickness and sea ice density, but not negligible as currently stated in most studies. Based on our findings, we recommend to either use a water density climatology, or an uncertainty value of 2.6 kgm^{-3} instead of the commonly used value of 0 to 0.5 kgm^{-3} in CryoSat-2 freeboard to sea ice thickness conversion.

1 Introduction

Observing sea ice thickness (SIT) on an Arctic wide scale has been impossible before the satellite era. Laxon et al. (2003) published the first study that calculated SIT from freeboard (FB) observations derived from satellite radar altimetry. They based the derivation on an assumption of hydrostatic balance and estimates of the mass of snow and ice. Equation 1 from Tilling et al. (2018) is currently often used to derive SIT from radar FB, following similar assumptions.

$$SIT = \frac{(FB_r + 0.25 * H_s)\rho_w}{(\rho_w - \rho_i)} + \frac{H_s \rho_s}{(\rho_w - \rho_i)} \quad (1)$$

FB_r is the radar freeboard, H_s is the snow thickness, ρ_s is the snow density, ρ_i is the ice density and ρ_w is the water density. These variables are difficult to observe co-located in time and space with satellite derived FB estimates. For this reason, most current CryoSat-2 based SIT products use, with adaptations of snow thickness and sea ice density estimates, the approach introduced by Laxon et al. (2003), which was based on using climatologies and empirical values.

The first of these adaptations was introduced by Alexandrov et al. (2010) for the sea ice density. While Laxon et al. (2003) used a constant sea ice density, Alexandrov et al. (2010) allowed the sea ice density to differentiate between multi-year ice (MYI) and first year ice (FYI). The second adaptation was introduced to the snow thickness. Laxon et al. (2003) used values from Warren et al. (1999), which is known as the Warren climatology, or simply W99. The W99 climatology is based on observations in the central Arctic collected during the time period 1954–1991 on primarily MYI (Warren et al., 1999). Since then, the Arctic sea ice cover has obtained dramatic changes towards a larger coverage of FYI (Maslanik et al., 2011). In line with this, Kurtz and Farrell (2011) pointed out that W99 snow thickness is biased towards snow on thick ice i.e., MYI and that the snow thickness should be reduced on the thinner FYI. Different approaches have since then been used to modify the W99 snow thickness over FYI. For example, Tilling et al. (2018) and Guerreiro et al. (2017) reduced the snow thickness from W99 by 50% on FYI, whereas e.g. Hendricks et al. (2021) used auxiliary satellite products to estimate the snow thickness over FYI. The approach of differentiating the snow thickness and sea ice density based on satellite derived ice types will here be referred to as the classical approach.

The snow thickness and sea ice density values used in the classical approach have been discussed heavily over the recent years. According to Kern et al. (2015), these are the variables with the largest impact on the conversion from FB to SIT. Mallett et al. (2021b) showed that inclusion of seasonal variability in the snow thickness product used in the FB to SIT conversion can lead to up to 100% faster decline of sea ice in the marginal seas. For this analysis, they used the SnowModel-LG (Liston et al., 2020) forced by ERA5 (Hersbach et al., 2017) to simulate the seasonal variability. Later, Landy et al. (2022) used the same snow model in their FB to SIT conversion and finally Fiedler et al. (2022) used the modeled snow thickness in their sea ice thickness assimilation. However, both Landy et al. (2022) and Fiedler et al. (2022) use the bi-modal sea ice densities introduced by Alexandrov et al. (2010).

Alternative approaches to derive sea ice density for FB to SIT conversion have been explored by e.g., Jutila et al. (2022a) and Ji et al. (2021). Ji et al. (2021) showed that sea ice densities from a climatology derived from sea ice density observations from 2011-2015 improved the SIT estimates in the Beaufort Sea compared to using the fixed values from Alexandrov et al. (2010). However, the observations used in this climatology are sparse with significantly more observations close to the validation site in the Beaufort Sea, which means that more validation is needed before relying on the derived method. Jutila et al. (2022a) uses airborne observations to derive bulk sea ice densities and finds that sea ice in the Arctic has become denser since Alexandrov et al. (2010). They also derive a negative exponential relationship between the bulk density and the FB, but acknowledge that more research is needed in order to use this relationship in FB to SIT retrievals. Based on the study by Jutila et al. (2022a), Hendricks et al. (2021) recognizes that the Alexandrov et al. (2010) sea ice densities within their SIT product are probably biased low, but that a change in one variable should go hand in hand with a review of other variables, which might be biased too. Changing only one of the variables in eq. 1 could introduce a significant bias.

A multi-variable evaluation has to our knowledge not been carried out to date. One challenge with such an approach is the lack of available Arctic wide sea ice density observations. Even though Jutila et al. (2022a) suggests a method to derive sea ice density from FB, they acknowledge that the method is not mature enough to be used routinely in the FB to SIT conversion for the entire Arctic. Sievers et al. (2023) introduced a new FB assimilation method, including a FB to SIT conversion in which snow thickness, sea ice density and water density model values were used to derive the SIT from FB. The values from this modeling approach allow for an Arctic wide comparison to the classically used values of snow thickness, sea ice density and water density, as they are available on similar temporal and spatial resolution as the typically used satellite derived FB values.

The model values from Sievers et al. (2023) include Arctic wide varying water densities, which are typically assumed to be constant in the classical FB to SIT conversion, see Laxon et al. (2003); Alexandrov et al. (2010); Tilling et al. (2018); Guerreiro et al. (2017); Kurtz et al. (2013). Most of these studies cite Laxon et al. (2003) or Alexandrov et al. (2010) as their water density source. Alexandrov et al. (2010) states that the surface water density only varies with 2 kgm^{-3} throughout the Arctic, which is not reflected in our model results. Laxon et al. (2003) uses the water density from Wadhams et al. (1992) that changes with the season but not in space. It is known that the surface salinity varies throughout the Arctic (Zweng et al., 2019) and that this governs the density. Wadhams et al. (1992) also emphasizes that water density could have a significant influence on the FB to SIT conversion but has since not gotten much attention, which means that it might be about time to revise the assumption that water density can be considered constant.

This study aims at analyzing how on average the geographical variability of sea ice density, snow thickness and water density influences the derived SIT. First, we compare the modeled and classical approach values for sea ice density, snow thickness and water density against in situ observations. Since we find that the model sea ice density from Sievers et al. (2023) is not varying enough, we introduce an improved model derived sea ice density. The detailed derivation of the improved model sea ice density is added in the appendix. Secondly, the impact of using the different snow thicknesses, sea ice density and water density values in the FB to SIT conversion is evaluated. For this, the SIT difference resulting from each parameter separately is calculated, as well as their combined impact on the SIT.

The snow thickness, sea ice density and water density values from the classical approach are taken from Hendricks et al. (2021) in this study. This data set was chosen, because it provides all variables used to derive SIT from FB. Sallila et al. (2019) compared different CryoSat-2 derived SIT products, also listing their approach to derive sea ice density and snow thickness. Their analysis shows that the publicly available SIT products derived via the classical approach are using similar values for snow thickness and sea ice density, hence it can be assumed that Hendricks et al. (2021) data set provides a good representation of typical values used.

As mentioned above, observations on similar time and spatial scales as the CryoSat-2 observations are currently not available for snow thickness, sea ice density and water density. Therefore, different methods for the validation of each of the parameters were introduced. They are presented in section 2.4. The variable with the closest temporal and spatial coverage to CryoSat-2 FB is the snow thickness. Over the past years, multiple efforts have been made to derive new Arctic winter snow thickness products. The efforts comprise microwave based snow thickness products (Rostosky et al., 2018), radar based snow thickness products (Garnier et al., 2021; Lawrence et al., 2018) and model based approaches (Liston et al., 2020; Petty et al., 2018). For

the comparison in section 3.1 we decided to utilize the radar based snow product Garnier et al. (2021), due to its independence from the CryoSat-2 snow thickness including W99 and the microwave based Rostosky et al. (2018) snow product, and it's more realistic seasonal cycle compared to Lawrence et al. (2018). Since we compare 10-year averages in the SIT comparison, we chose to compare the surface water density to the World Ocean Atlas climatology from 2018 (Zweng et al., 2019) in section 3.3. Most in situ observations that could have been used instead are included in the climatology. The sea ice density observations are the most sparse, which is why we included two data set for the sea ice density observation comparison in section 3.2: the airborne observation from Jutila et al. (2022a) and the ice core based observations from (Oggier et al., 2023a, b).

2 Data and Methods

2.1 Model setup

The model system is a coupled ocean and sea ice model, which is described in Sievers et al. (2023). The ocean model is NEMO (v4.2, Madec et al. (2017)) and it closely follows the tuning from Hordoir et al. (2022). The sea ice component is CICE v6.2 (Hunke et al., 2021). The model setup used in this study will be called C6N4 in the following.

In CICE snow-ice formation is applied, and melt ponds are included. The CICE surface water density is calculated from sea surface salinity following Feltham et al. (2006). The coupling is performed every time step, and both the ocean and the ice components are run with a 600-second time step and on a 10 km x 10 km gird. The model run analyzed ran from 2010-01-01 to 2020-12-31 and was initialized by a 15-year spin up simulation.

The atmospheric forcing applied is ERA5 (Hersbach et al., 2017) with a frequency of 3 hours. The snow thickness is calculated by CICE based on the snow forcing from ERA5. We found that the atmospheric boundary layer scheme and the atmospheric drag formulation impacts the snow thickness. This study use the CICE default atmospheric boundary layer and the form drag formulation from Tsamados et al. (2014).

The sea ice density parameterization requires temporal evolving sea ice salinity, which is only available in the mushy thermodynamics (Turner et al., 2013). Two sea ice density parameterization are investigated. The sea ice density originally used in Sievers et al. (2023) model C6N4 is shown in equation 2.

$$\rho_i = a_b * \rho_b + (1. - a_b) * \rho_{fresh} \tag{2}$$

where a_b is the fraction of brine contained in sea ice and ρ_b the density of the brine, following Assur (1958). ρ_{fresh} is the sea ice density excluding brine, and is to $882 kgm^{-3}$ in C6N4. The second model approach for calculating the sea ice density, here called C6N4$_{J21}$, is achieved by letting ρ_{fresh} depend on the model variable first year ice area fraction (FYI_{frac}):

$$\rho_{fresh} = \rho_{myi} * (1. - FYI_{frac}) + \rho_{fyi} * FYI_{frac} \tag{3}$$

where $\rho_{myi} = 890 kgm^{-3}$ is the sea ice density of MYI and $\rho_{fyi} = 907 kgm^{-3}$ the sea ice density of FYI, in both cases excluding brine. The values for ρ_{myi} and ρ_{fyi} were determined by the least square fit analysis of data from Jutila et al. (2022a).

Since the sea ice density is only a diagnostic variable, it has no impact on the snow thickness and water density, which are the same as in C6N4. More details on the derivation of ρ_{myi} and ρ_{fyi} are listed in the appendix.

2.2 Snow Thickness, Sea Ice Density and Water Density from the Classical Approach

The weekly gridded along-track CryoSat-2 derived SIT data product version 2.4 developed at the Alfred Wegener Institute (AWI) (Hendricks et al., 2021) includes all values used in equation 1 for deriving the SIT from radar FB at the corresponding location. It also only differs on minor details from other CryoSat-2 FB derived SIT data sets (Sallila et al., 2019), which is why it is here used as a representation for the classical FB to SIT approach.

The sea ice density values used are 916.7 $\pm$ 35.7kgm^{-3} for FYI and 882.0 $\pm$ 23.0 kgm^{-3} for MYI following Alexandrov et al. (2010). The ice type data is the OSISAF daily ice type product OSI-403-d (SAF, 2017). The snow thickness is a combination of the W99 snow climatology and a product that uses the Advanced Microwave Scanning Radiometer 2 (AMSR2) in the marginal seas. The snow thickness products are weighted depending on location. In the central Arctic extending to the Russian, the Greenlandic and Canadian coasts the W99 climatology is dominating. In the marginal seas of the Canadian Archipelago, the Fram Strait, the Barents Sea and the Bering Sea the AMSR2 snow thickness is dominating. Following Kurtz and Farrell (2011) they reduce the W99 snow thickness by 50% over FYI. The value used for the water density is 1024 kgm^{-3}, and its uncertainties are neglected. The data comes on an Equal-Area Scalable Earth Grid version 2 (EASE2-Grid) with a 25 km resolution. For model comparison, the data was bilinearly interpolated to the model grid. In the following text, this data set will be referred to as CS2$_{AWI}$.

2.3 Validation data

2.3.1 Snow thickness

To validate the snow thickness, the altimeter based snow thickness product (ASD) published by Garnier et al. (2021) from Laboratoire d'Etudes en Géophysique et Océanographie Spatiales (LEGOS) was used. The ASD product is based on the assumption of different penetration depth of different radar wavelengths. It is derived by subtracting the SARAL/Altika Ka-band and CryoSat-2 Ku-band radar height measurements from one another. It is available on a monthly basis on a 12.5 km grid.

Garnier et al. (2021) found that the ASD data product compares better to NASA Operation IceBridge airborne snow thickness observations than both the W99 climatology and the AMSR2 based data product. The ASD data product covers the Arctic up to 81.5 °N, which sets the limit for the comparison in section 3.1.

2.3.2 Sea ice density

Airborne observations (Jutila et al., 2022a) of sea ice bulk densities are used as the baseline for sea ice densities. The density was calculated based on the Archimedes' principle, following:

$$\rho_i = \rho_w(1 - \frac{H_{fs}}{h_{tot} - H_s}) + (\rho_w - \rho_s)\frac{H_s}{H_{tot} - H_s} \quad (4)$$

ρ_w equals 1024 kgm^{-3} and ρ_s 300 kgm^{-3}. The values for H_s (snow thickness), H_{tot} (total snow and ice thickness) and H_{fs} (snow freeboard) are based on airborne observations in the beginning of April 2017 and April 2019. The locations of the field campaign in 2017 are marked on figure 1 by blue dots and stars, and by red dots and stars for the 2019 campaign. H_s was measured with a snow radar (Jutila et al., 2022b), h_{tot} was measured with an electromagnetic induction sounding instrument also called the EM-Bird (Haas et al., 2009) and H_{fs} was measured with a near-infrared, line-scanning Riegl VQ-580 airborne laser scanner. More details about each of the measurements can be found in Jutila et al. (2022a). The resulting data includes an error estimate, which was used to filter the data. No values with error larger than 30 kgm^{-3} were used.

A second sea ice density data set, used for comparison, was obtained primarily in the central Arctic (figure 1 black dots). This data set was collected during the Multidisciplinary drifting Observatory for the Study of Arctic Climate (MOSAiC) expedition, where sea ice density from FYI and second year ice cores was obtained (Oggier et al., 2023a, b). The sea ice density values were calculated using the method of hydrostatic weighing. For this method, the mass of the ice core is measured both in air and in an unspecified liquid (Oggier et al., 2023a, b). The locations of the coring sites were interpolated to the model grid using the nearest neighbor method. The time the measurements were taken range from October 2019 to August 2020.

2.3.3 Water density

The surface water density was calculated from the salinity of the World Ocean Atlas 2018 (WOA) data set described in Zweng et al. (2019). The WOA consists of quality controlled observations interpolated to a standardized depth grid. It is the largest freely available gridded data set of oceanographic observations (Boyer et al., 2018). The data set used in this study is the 0.25° data set spanning the years 1955 to 2017 and the averaged monthly subsets for October to March. The density was calculated following the salt water density calculation from Feltham et al. (2006) utilizing only the surface values from WOA.

2.4 Validation methods

Reference observations of ice conditions in the Arctic are sparsely distributed both in time and geographic coverage. The reference measurements included in this study have different spatial and temporal resolutions, and thus different methods have been used to validate the model and CS2$_{AWI}$ values of snow thickness, sea ice density and water density. Where the latter two have been compared using conventional methods such as the root-mean-square differences (RMSD), the snow thickness and SIT comparison methods need a more detailed description, which is included in section 2.4.1 and 2.5.

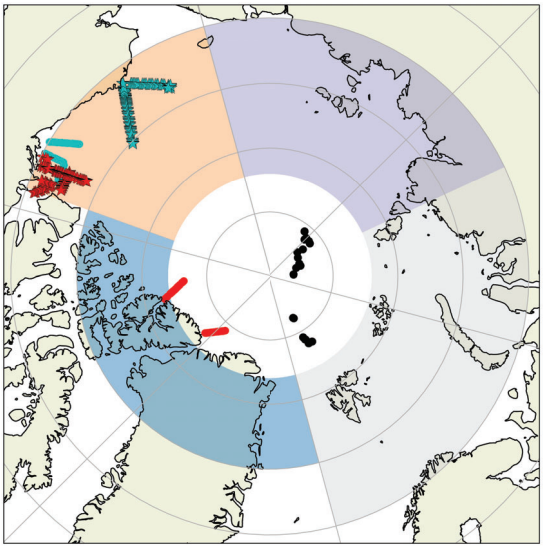

Figure 1. The map shows the locations of the observations from the IceBird campaign from April 2017 (turquoise stars and dots), April 2019 (red stars and dots) and the four areas considered in figure 2. The blue region is the Canadian Arctic, the orange region the Beaufort Sea, the purple region the Russian Arctic East and the gray region the Russian Arctic West. The black dots indicate the locations of the MOSAiC sea ice density measurement shown in figure 4

.

2.4.1 Snow thickness

The snow thickness data sets from C6N4, CS2$_{AWI}$ and ASD have different spatial and temporal resolutions. The C6N4 data is provided on an Arctic wide 10x10 km grid at a weekly frequency, the CS2$_{AWI}$ data includes approx. 100 orbit passes per week gridded on a 25 x 25 km EASE2 grid covering up to 88°N, and the ASD data is provided with a monthly frequency on a 12.5 km EASE2 grid, covering only up to 81.5°N. To ensure a fair comparison, probability density functions (PDF) of each month's snow data were calculated for each of the three data sets. The data was divided into 4 regions, covered by all three data sets (figure 1), which enables the discussion of regional differences. The area under the PDF is always one, allowing a direct comparison of data sets with different resolutions. To evaluate, how well the model and CS2$_{AWI}$ data agree with the ASD data, a measure here called "disagreement" (Dis) is introduced,

$$Dis = \int PDF_{ASD} + \int PDF_{model} - \int PDF_{overlap} \tag{5}$$

Where the PDF_{ASD} is the PDF of the ASD data set, PDF_{model} PDF of the model and $PDF_{overlap}$ the area where the two PDFs overlap. For the disagreement between ASD and CS2$_{AWI}$, PDF_{model} would be substituted by PDF_{CS2} in equation 5 If both curves are perfectly overlapping Dis=0 and if there is no overlap between the curves Dis=2. Dis is dimensionless.

2.5 SIT comparison

One objective of this study is to evaluate SIT differences resulting from using different sea ice density, snow thickness and water density in the production of the CS2$_{AWI}$ and the C6N4 data. To evaluate this, first the CS2$_{AWI}$ data was bilinearly interpolated onto the model grid and the model data was averaged to weekly means to match the temporal resolution of the CS2$_{AWI}$ data. Following this, all grid points covered by less than 50 satellite overpasses, in the CS2$_{AWI}$ data set from 2010-01-01 to 2020-12-31 were discarded, and only grid points and time steps covered by both the CS2$_{AWI}$ data product and C6N4 were kept for further analysis. In a second step, where gird cells fulfilled the above-mentioned criteria, the mean snow thickness, sea ice density and water density values for the model and CS2$_{AWI}$ data were calculated, followed by their differences as model – CS2$_{AWI}$ resulting in $\Delta\rho_i$, ΔH_s and $\Delta\rho_w$. Finally, the average snow thickness, sea ice density and water density for each grid cell fulfilling the above-mentioned criteria was calculated from all model and CS2$_{AWI}$ values represented in the following by $\overline{\rho_i}$, $\overline{H_s}$ and $\overline{\rho_w}$. The mean difference and mean values are used to determine the mean SIT difference when calculating the SIT. For the SIT differences resulting from snow thickness (ΔSIT_{H_s}), sea ice density (ΔSIT_{ρ_i}) and water density (ΔSIT_{ρ_w}) the following equations were used:

$$\Delta SIT_{H_s} = \left(\frac{FB\bar{\rho}_w}{(\bar{\rho}_w - \bar{\rho}_i)} + \frac{(\bar{H}_s + \Delta H_s)\rho_s}{(\bar{\rho_w} - \bar{\rho}_i)}\right) - \left(\frac{FB\bar{\rho_w}}{(\bar{\rho_w} - \bar{\rho}_i)} + \frac{\bar{H}_s\rho_s}{(\bar{\rho_w} - \bar{\rho}_i)}\right) \tag{6}$$

$$\Delta SIT_{\rho_i} = \left(\frac{FB\bar{\rho}_w}{(\bar{\rho}_w - (\bar{\rho}_i + \Delta\rho_i))} + \frac{\bar{H}_s\rho_s}{(\bar{\rho_w} - (\bar{\rho}_i + \Delta\rho_i))}\right) - \left(\frac{FB\bar{\rho_w}}{(\bar{\rho_w} - \bar{\rho}_i)} + \frac{\bar{H}_s\rho_s}{(\bar{\rho_w} - \bar{\rho}_i)}\right) \tag{7}$$

$$\Delta SIT_{\rho_w} = \left(\frac{FB(\bar{\rho}_w + \Delta\rho_w)}{((\bar{\rho}_w + \Delta\rho_w) - \bar{\rho}_i)} + \frac{\bar{H}_s\rho_s}{((\bar{\rho}_w + \Delta\rho_w) - \bar{\rho}_i)}\right) - \left(\frac{FB\bar{\rho_w}}{(\bar{\rho_w} - \bar{\rho}_i)} + \frac{\bar{H}_s\rho_s}{(\bar{\rho_w} - \bar{\rho}_i)}\right) \tag{8}$$

for the combined SIT difference:

$$\Delta SIT = \left(\frac{FB(\bar{\rho}_w + \Delta\rho_w)}{((\bar{\rho}_w + \Delta\rho_w) - (\bar{\rho}_i + \Delta\rho_i))} + \frac{(\bar{H}_s + \Delta H_s)\rho_s}{((\bar{\rho_w} + \Delta\rho_w) - (\bar{\rho}_i + \Delta\rho_i))}\right) - \left(\frac{FB\bar{\rho_w}}{(\bar{\rho_w} - \bar{\rho}_i)} + \frac{\bar{H}_s\rho_s}{(\bar{\rho_w} - \bar{\rho}_i)}\right) \tag{9}$$

The mean FB values are calculated from CS2$_{AWI}$ data only, and the ρ_s values are equal in both data sets.

3 Results

The results are split into two sections. In section 3.1, 3.2 and 3.3 the snow thickness, sea ice density and water density from C6N4 and CS2$_{AWI}$ data are compared to observations for validation. In section 3.4, the differences in SIT resulting from the 10-year mean snow thickness, sea ice density and water density values of the two data sets are analyzed. First for each parameter isolated and finally for all three combined.

3.1 Snow thickness

The PDF of the snow thicknesses from C6N4, CS2$_{AWI}$ and ASD are displayed in figure 2 for the months November to March. Compared to the CS2$_{AWI}$ and ASD snow thicknesses, the C6N4 values are thinner in November and have the largest

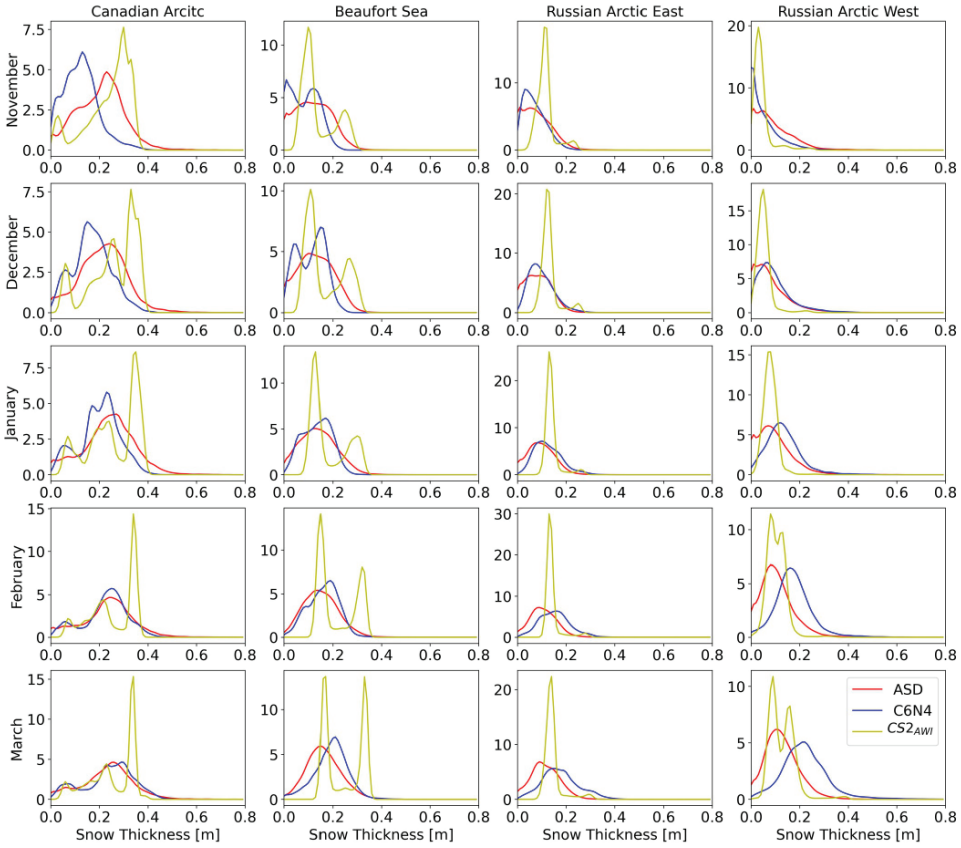

Figure 2. Probability density functions (PDF) for snow thickness in regions defined in figure 1, where all three data sets exist.

accumulation over winter. The CS2$_{AWI}$ snow thickness PDFs show two or even three distinct peaks due to the thinner snow cover over FYI and thicker over MYI. In the Canadian Arctic, three peaks are visible. This is due to the diverse snow conditions

in the Canadian Archipelago, the northern Baffin Bay and Fram Strait that are all included within the region (figure 1). Overall, the PDFs in figure 2 show that the snow cover of C6N4 is in better agreement with the ASD snow thickness compared to the agreement of the CS2$_{AWI}$ and the ASD. To quantify this, the disagreement between the CS2$_{AWI}$ and the ASD PDFs and the disagreement between the C6N4 and the ASD PDFs were calculated and displayed in table 1.

Table 1. Overview of the disagreement between the PDFs in figure 2 using the ASD observations as reference. The disagreement is based on equation 5, and it ranges from 0. to 2., where 0 is best.

Month	Canadian Arctic		Beaufort Sea		Russian Arctic East		Russian Arctic West	
	C6N4	CS2$_{AWI}$	C6N4	CS2$_{AWI}$	C6N4	CS2$_{AWI}$	C6N4	CS2$_{AWI}$
November	0.91	0.58	0.45	0.87	0.30	0.98	0.48	0.98
December	0.54	0.71	0.42	0.84	0.24	1.11	0.22	0.86
January	0.46	0.65	0.25	0.98	0.33	1.28	0.50	0.88
February	0.22	0.78	0.26	1.18	0.61	1.38	0.87	0.62
March	0.26	0.74	0.46	1.24	0.67	1.15	0.94	0.57

Overall, the disagreement between the C6N4 and ASD is lower than the disagreement between the ASD and CS2$_{AWI}$. The C6N4 snow thickness is in best agreement with the ASD data in the Beaufort Sea and the Russian Arctic East. The large disagreement in the Beaufort Sea (figure 2) is caused by the presence of the large peak indicating thick MYI snow ($\sim$ 0.3-0.4 m) in the CS2$_{AWI}$ data, which is not reflected in the ASD data set, nor in the C6N4 data. It is only in November in the Canadian Arctic and in February and March in the Russian Arctic West that CS2$_{AWI}$ data match better with the ASD data, when it is compared to C6N4.

3.2 Sea ice density

The relation between the sea ice density retrievals from the IceBird measurements of Jutila et al. (2022a) and the C6N4, C6N4$_{J21}$ and CS2$_{AWI}$ data is displayed in figure 3. According to Jutila et al. (2022a), the observations from 2017 were only obtained over FYI locations, while the 2019 observations cover both MYI and FYI. To distinguish the data sets from 2017 and 2019, they are here shown in two separate panels. All IceBird measurements originating from the same day and grid cell were averaged to one value. Grid cells with less than 10 IceBird measurements were excluded (0.9 % of the data) from the analysis. The RMSD between the IceBird and CS2$_{AWI}$, and IceBird and C6N4/C6N4$_{J21}$ data are listed in table 2 for each year separately.

In both 2017 and 2019 there appears to be clustering of the modeled data and the CS2$_{AWI}$ data in figure 3. The flight tracks of the IceBird campaigns in both years (figure 1) are situated at two different locations. The clustering is a result of the different representations of sea ice densities in C6N4 and the CS2$_{AWI}$ data at the different locations. The locations are marked by stars and dots in figure 1. The large stars and dots in figure 3 show the average values for the two regions of each year.

Comparing C6N4 and C6N4$_{J21}$ with the IceBird observations in figure 3, C6N4$_{J21}$ appears to be in better agreement with the IceBird observations than C6N4. From the RMSD in table 2, it is also clear that the C6N4$_{J21}$ sea ice densities are in closer

agreement with the observations than C6N4. In 2019 both the eastern and western average values (large red stars and dots in figure 3b) from C6N4$_{J21}$ compare especially well to the IceBird values, which was to be expected, since the 2019 values were used to derive the C6N4$_{J21}$ sea ice density. In 2017 the C6N4$_{J21}$ sea ice density also compares better to the IceBird values than the C6N4 sea ice density, but the 2017 C6N4$_{J21}$ RMSD is 4 kgm^{-3} higher than in 2019. Especially in the western Beaufort sea (large red star in figure 3a) the values have not improved as much as in 2019 or the 2017 eastern Beaufort Sea values (large red dot in figure 3a). The close agreement between the averaged sea ice density from C6N4$_{J21}$ and the IceBird data in

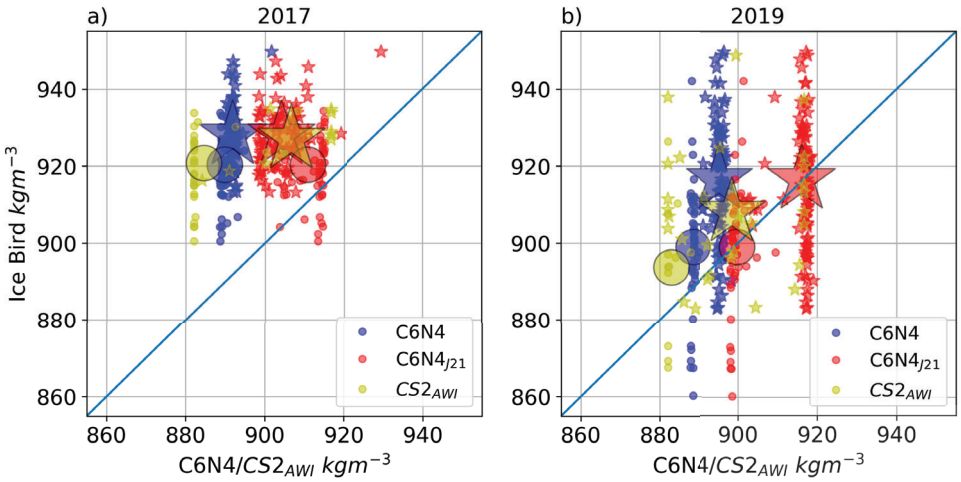

Figure 3. The IceBird sea ice density plotted against CS2$_{AWI}$, C6N4 and C6N4$_{J21}$ sea ice densities for 2017 and 2019 campaigns. The stars and dots represent the averaged Western and Eastern observation sites, as defined in figure 1.

2019, and the fact that the 2019 IceBird data were used to derive the sea ice density parameterization in C6N4$_{J21}$, calls for a comparison with independent reference observations. Such a comparison has been made between the sea ice core based sea ice density measured from the MOSAiC expedition and the C4N6, C4N6$_{J21}$ model based estimates. All the MOSAiC density measurements and density estimates are plotted against time in figure 4 and the resulting RMSD are listed in table 3. From figure 4 and table 3 it is clear that the C6N4$_{J21}$ sea ice densities are in closer agreement with the observations than the C6N4 values, supporting the findings of the IceBird comparison. Figure 4 also shows that both model estimates result in overall lower sea ice density values, with a slight seasonality of decreasing density over the winter, which is not reflected in the observations. Since this is visible in both C6N4$_{J21}$ and C6N4 sea ice density, the reason for this seasonality must be linked to the sea ice brine content, since this is the only factor varying C6N4 sea ice density. The best agreement between C6N4$_{J21}$ and MOSAiC

observations is in April, which is also the month that the observations (Jutila et al., 2022a) used to derive ρ_{myi} and ρ_{fyi} in equation 3 were collected.

Table 2. RMSD between C6N4, C6N4$_{J21}$, CS2$_{AWI}$ and the IceBird sea ice density. The values in brackets indicate the model values only considering data points covered by all three data sets.

	2017			2019		
	C6N4	C6N4$_{J21}$	CS2$_{AWI}$	C6N4	C6N4$_{J21}$	CS2$_{AWI}$
RMSD	35 (33)	21 (17)	35	25 (20)	17 (18)	22

In the 2019 plot (figure 3b), the mean IceBird values (large stars and dots location on the y-axis) differ significantly between the CS2$_{AWI}$ (yellow) and the model data (blue and red). This is due to the different number of data points covered by the observation and CS2$_{AWI}$ data and the observation and C6N4 data. To compare the CS2$_{AWI}$ with the model values, only data point should be taken into account which are covered by a all three datasets. This reduces the comparison data significantly. For comparison, the CS2$_{AWI}$ data coincides only with $\sim$ 40 observation points, while the model coincides with 130-140 observation points, depending on the year. To compare the CS2$_{AWI}$ data with the modeled sea ice density and the observations, the RMSD was calculated for all data points covering all three data sets. The RMSD are listed in the brackets in table 2 and 3. Overall, the RMSD between the C6N4$_{J21}$ and the IceBird data are lower than the ones between CS2$_{AWI}$ and IceBird data. For the MOSAiC data, the C6N4$_{J21}$ RMSD is also lower than the CS2$_{AWI}$ RMSD, but not as significant as in the IceBird data comparison.

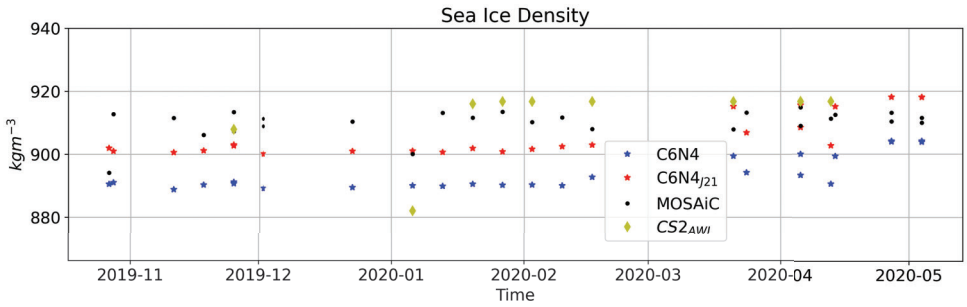

Figure 4. C6N4, C6N4$_{J21}$ and CS2$_{AWI}$ sea ice density estimates and MOSAiC FYI and second year ice core sea ice density.

While the CS2$_{AWI}$ data was biased low in comparison to the IceBird data in figure 3, the CS2$_{AWI}$ data is biased high in comparison to the MOSAiC data (figure 4). Most of the CS2$_{AWI}$ data points here are classified as FYI, and also many of the observations are taken on a FYI ice flow (Oggier et al., 2023a). Jutila et al. (2022a) concludes that the sea ice densities values

Table 3. RMSD between the MOSAiC sea ice density observations and model and CS2$_{AWI}$ values. The values in the brackets indicate the results for model values in locations where only CS2$_{AWI}$ data exists (yellow rhombuses in figure 4).

	C6N4	C6N4$_{J21}$	CS2$_{AWI}$
RMSD	17.3 (17.8) kgm^{-3}	8.1 (7.7) kgm^{-3}	8.2 kgm^{-3}

following Alexandrov et al. (2010) are biased low for both FYI and MYI. The results displayed in figure 4 suggest that this might not be the case for the FYI values everywhere in the Arctic.

3.3 Water density

To evaluate the model and CS2$_{AWI}$ surface water densities, the model's 10-year mean and the CS2$_{AWI}$ approach using a single value of 1024 kgm^{-3} were compared to the WOA climatology, which is based on observations. The water 10-year mean densities of WOA, CS2$_{AWI}$ and the C6N4 simulation are displayed for November to March in figure 5.

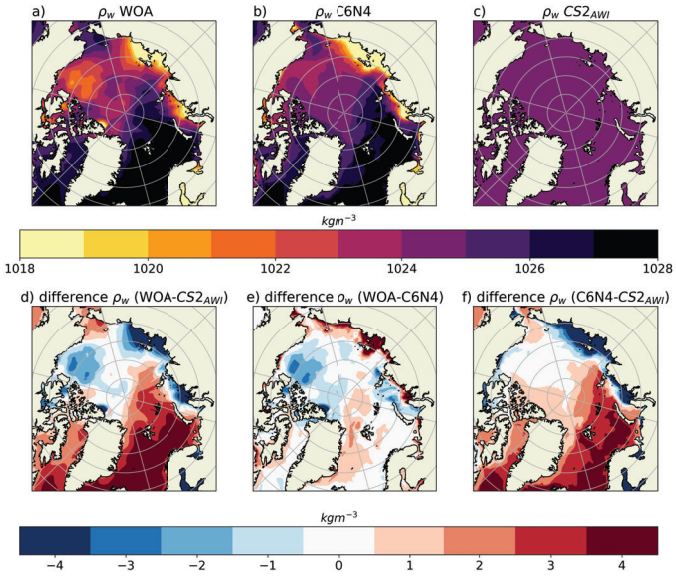

Figure 5. From left to right: Maps of the WOA, C6N4 and CS2$_{AWI}$ water densities (top row), and difference maps of WOA–CS2$_{AWI}$, WOA–C6N4, and CS2$_{AWI}$-C6N4 water densities (bottom row).

Overall, the pattern of dense water in the Atlantic sector, low density water in the Russian shelf area and a negative density gradient from the Fram Strait towards the Beaufort Sea are present in both the model and the WOA density maps. The WOA–C6N4 surface water density differences (figure 5e) reveal areas with the highest differences located in the Russian shelf area. The WOA–CS2$_{AWI}$ surface water density differences (figure 5d) also show the largest differences here, but of opposite sign than WOA–C6N4. The model simulated lower densities than the WOA suggests, and the CS2$_{AWI}$ value is higher than WOA. In the rest of the Arctic, the WOA–C6N4 and WOA–CS2$_{AWI}$ differences are of similar sign, but locally of different magnitude. In the Beaufort Sea both WOA–C6N4 and WOA–CS2$_{AWI}$ differences are of about the same magnitude and in the Atlantic sector the WOA–CS2$_{AWI}$ differences is larger than the WOA–C6N4 differences. In the Lincoln Sea, a strong negative anomaly is shown in both differences. Apart from this, the WOA–CS2$_{AWI}$ difference is here lower than the WOA–C6N4 differences. Overall, the C6N4 is in better agreement with the WOA, except in the Lincoln Sea. C6N4 show less variability when compared to the WOA data. The standard deviation (STD) between the C6N4 and the WOA water densities for the entire Arctic is 1.6 kgm^{-3} and the STD between the WOA and the CS2$_{AWI}$ water densities is 2.1 kgm^{-3}.

3.4 Sea Ice Thickness difference analysis

The individual influence of sea ice density, snow thickness and water density on the FB to SIT conversion are displayed in figure 6. Both the snow thickness differences between C6N4 and CS2$_{AWI}$ (figure 6c) and the sea ice density differences between C6N4$_{J21}$ and CS2$_{AWI}$ (figure 6k) result in significant SIT differences, as seen in figure 6d and figure 6l, respectively. The largest SIT difference results from the sea ice density differences between C6N4$_{J21}$ and CS2$_{AWI}$. On average, it amounts to 0.14 m, but reaches maximum values of 1.16 m (table 4) close to the north coast of Greenland. The water density results in the lowest SIT difference (on average 0.01 m), but the maximum value of 0.33 m is not negligible.

Table 4. Maximum (D$_{max}$) and root-mean-square difference (RMSD) of the SIT differences calculated by the 10-year mean model and CS2$_{AWI}$ differences for snow thickness, sea ice density, water density and all three combined.

	C6N4–CS2$_{AWI}$	C6N4–CS2$_{AWI}$	C6N4$_{J21}$–CS2$_{AWI}$	C6N4–CS2$_{AWI}$	C6N4$_{J21}$–CS2$_{AWI}$	C6N4–CS2$_{AWI}$
	Snow Thickness	Sea ice density	Sea ice density	Water density	Combined	Combined
D$_{max}$	0.55 m	0.49 m	1.16 m	0.33 m	0.94 m	0.61 m
RMSD	0.17 m	0.11 m	0.21 m	0.01 m	0.12 m	0.17 m

Figure 6 also shows that the impact of the specific variables on the SIT differences are not necessarily mapped one-to-one for all parameters. The snow thickness differences in figure 6c for example almost translate one-to-one to the resulting SIT differences in figure 6d. For example, both in the Lincoln Sea and north of Svalbard, does a H_s anomaly of about 0.1 m translate to a SIT anomaly of about 0.2 m. This is not the case for the sea ice density, which is particularly visible when comparing figure 6g and h. In this case, the sea ice density anomaly in the Lincoln Sea of about 5 kgm^{-3} causes the same SIT anomaly in the Lincoln Sea as the sea ice density anomaly of about -20 kgm^{-3} on the East Siberian Shelf.

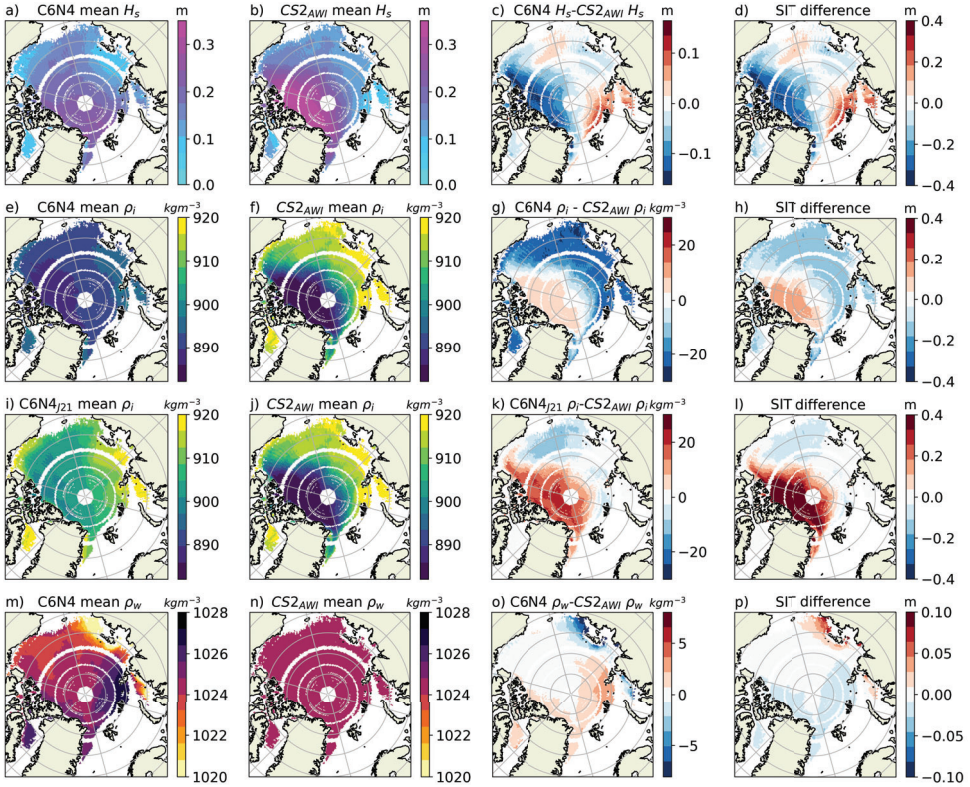

Figure 6. The rows show from top to bottom; the snow thickness, the C6N4 sea ice density, the C6N4$_{J21}$ sea ice density and the water density. Each column shows from left to right; the 10-year model mean, the 10-year CS2$_{AWI}$ mean, their differences and the resulting SIT differences of the respective parameters. Be aware of the different color scales of the SIT differences in p and o.

310 The influence of all combined differences are shown in figure 7 for the two different cases using C6N4 (figure 7a) and C6N4$_{J21}$ (figure 7b), respectively. Both plots show up to 0.4 m differences, but of opposing signs and in different locations, indicating that the change of sea ice density from C6N4 to C6N4$_{J21}$ has a significant impact on the FB to SIT conversion. The largest differences SIT between the C6N4 data and the CS2$_{AWI}$ data is located in the eastern Beaufort Sea and is mainly caused by lower snow thickness and sea ice density in the C6N4 data (compare figure 6c and g). The largest differences between the

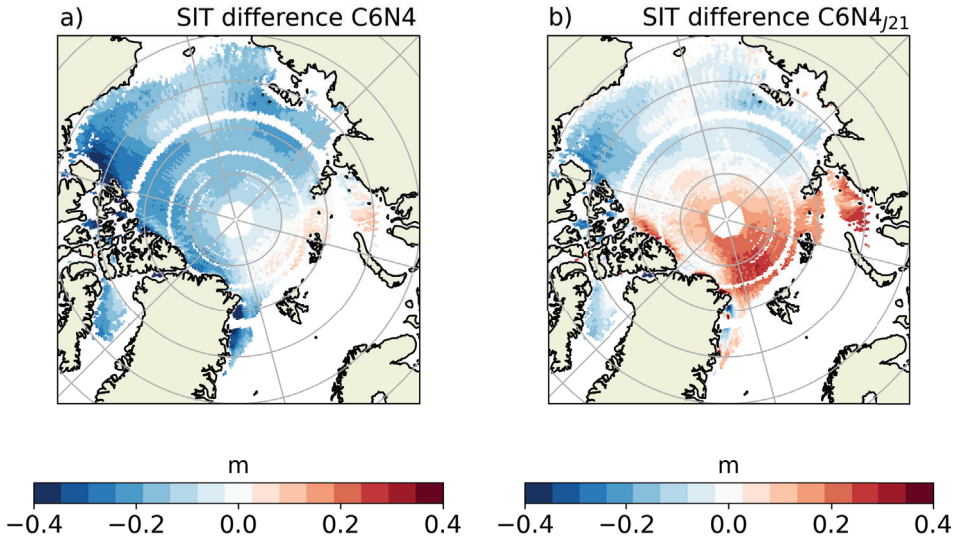

Figure 7. SIT differences resulting from all variables combined differences. a) shows the SIT differences using C6N4 and b) using C6N4$_{J21}$ sea ice density.

C6N4$_{J21}$ data and the CS2$_{AWI}$ data is located north of Svalbard and mainly caused by higher snow thickness and sea ice density in the model (compare figure 6c and k).

3.4.1 Water density derived SIT differences

To evaluate whether the differences in water density between the WOA and the model and the WOA and the CS2$_{AWI}$ data, leads to significant differences in SIT, we calculated the SIT differences using different water density differences ($\Delta\rho_w$) as input for equation 8. The results are presented in figure 8. For figure 8a $\Delta\rho_w$ was calculated from mean values of WOA–CS2$_{AWI}$ and for figure 8b from WOA–C6N4. Both SIT difference plots show maximum values in the Lincoln Sea. These maxima are caused by anomalous low surface salinity in the WOA data. The observation density in this area is sparse, and the climatology might be biased to a certain year with anomalous low salinity here. For the further analysis, this region is excluded.

The SIT difference calculated from the WOA–CS2$_{AWI}$ density has a more wide-spread variation than is the case for the one calculated from WOA–C6N4, including regions with both positive and negative biases. Since the CS2$_{AWI}$ water density is constant, this was to be expected. Both the C6N4 and CS2$_{AWI}$ water density lead to thicker ice in the Beaufort Sea and thinner ice in the Fram Strait and Greenland Sea, with the bias towards thinner ice being less pronounced in the C6N4 comparison. In

the Russian shelf region, the CS2$_{AWI}$ data leads to thicker ice and the C6N4 data to no difference, except for a small area of thinner ice, west of the Anzhu Islands. The RMSD between WOA–CS2$_{AWI}$ amounts to 0.02 m and between WOA–C6N4 to

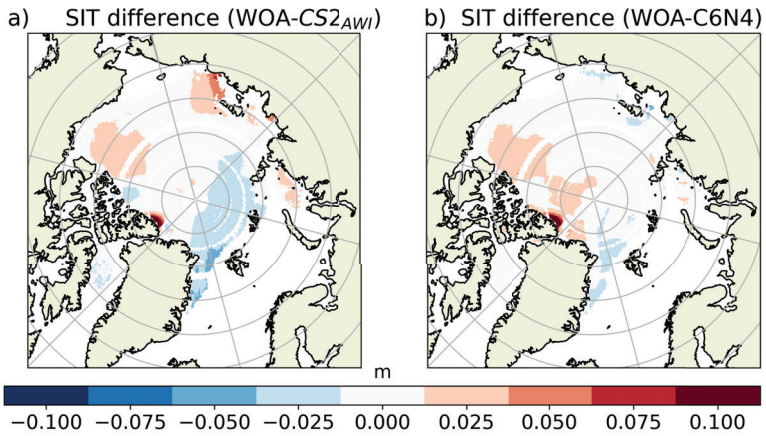

Figure 8. SIT differences resulting from varying equation 5 by the difference between the WOA–CS2$_{AWI}$ (left) and WOA–C6N4 (right) water densities.

0.01 m SIT difference with a maximum of 0.13 m for the CS2$_{AWI}$ data and 0.16 m for the C6N4 data.

4 Discussion

4.1 Snow thickness

The snow thicknesses of C6N4, CS2$_{AWI}$ and ASD are compared in figure 2 and table 1. The best agreement is found between the C6N4 and the ASD snow thicknesses, whereas the CS2$_{AWI}$ snow thickness is in general too thick. The CS2$_{AWI}$ snow thickness consist of a combination of two snow products, i.e., the W99 climatology and the AMSR2 snow thickness product. The included areas in this study primarily use the W99 climatology except for the marginal seas of the Greenland Sea, Barents Sea and the Baffin Bay. Here, the snow thickness was derived from microwave data (Hendricks et al., 2021). The snow thickness comparison in figure 2 does not include any snow observations in the central Arctic, as the ASD snow product only covers up to 81.5°N. Zhou et al. (2021) compares eight different snow thickness products, to W99 and finds that W99 is significantly thicker than any of them. This is in good agreement with our results.

The PDFs in figure 2 show that the C6N4 snow thickness, when compared to the ASD snow thickness product, overall is thinner in the beginning of winter and thicker by the end of winter. The snow is thinner in the beginning of the winter in C6N4,

because most of the snow in the model is melted away during the summer. There are three possible reasons for the thicker snow by the end of winter.

First, C6N4 does not include snow densification, which is the process where wind and temperature reduces the volume over time without changing the mass (Liston et al., 2020). When C6N4 is run with FB assimilation, the value of 0.25 in equation 1 is substituted with a term depending on the snow density, which densifies over winter according to a linear function introduced by Mallett et al. (2021a). This snow densification term is only used during the assimilation and does not influence the snow thickness anywhere else in the model (Sievers et al., 2023). To avoid overestimation of the C6N4 snow thickness in late winter, the densification used in the assimilation following Mallett et al. (2021a) could be applied to scale the snow thickness.

The second reason for the difference in snow thickness in late winter could be that the Ku-band radar, which is used to determine the snow-ice interface in the ASD product, does not penetrate the entire snowpack (Willatt et al., 2011; Kwok, 2014; Ricker et al., 2015; King et al., 2018). In situ observations that can be used to evaluate the Arctic wide snow thickness products are limited in time and space, thus a consistent validation of this will remain a challenge.

A third reason that may bias the C6N4 snow thickness is regional biases in the snowfall from ERA5, which could be overestimated in certain regions. Stroeve et al. (2020) compared two snow model runs forced with ERA5 and NASA's Modern Era Retrospective-Analysis for Research and Applications, Version 2 (MERRA-2) (Gelaro et al., 2017). They find that the modelled snow thickness from both atmospheric forcing data sets are thicker compared to W99 in a similar region, slightly further west. They attribute this difference to a storm that brought more snow into the region in the year they evaluated, but they also mention that the snow fall rate might have changed over the past decades due to changes in the atmospheric circulation as a result of the decreased summer sea ice extent (Stroeve et al., 2011). The in situ observations from the MOSAiC expedition can provide some insight of the evaluation of at least one winter season. Wagner et al. (2022) compared snowfall rates during the MOSAiC expedition to ERA5 and finds good agreement between the observed and ERA5 snowfall rates. C6N4 is forced by ERA5 snowfall. Further, (Kwok et al., 2020) finds that snow thickness estimates from combined CryoSat-2 and IceSat data compares well with reconstructed snowfall from ERA5. However, they also use the CryoSat-2 radar measurements, which might lead to underestimation of snow thickness, as mentioned above. All of these studies (Stroeve et al., 2011; Zhou et al., 2021; Wagner et al., 2022; Kwok et al., 2020) support the thicker modelled snow in the Russian Arctic west area to be more realistic than both the ASD product and the $CS2_{AWI}$ snow thickness.

Overall, table 1 shows that the snow thickness from C6N4 agrees better with the ASD data product than the $CS2_{AWI}$ snow thickness. A few exceptions are found in the Canadian Arctic and the Russian Arctic West for specific months, where the $CS2_{AWI}$ and the ASD snow products agrees better. In the Russian Arctic West, the C6N4 snow thickness increasingly disagrees with the ASD snow thickness in the late winter months. As mentioned above, this could be a result of either the Ku-band radar not penetrating the entire snowpack or the snow in C6N4 not including snow densification. The in situ measurements on which King et al. (2018) base their findings, that the Ku-band radar does not penetrate the entire snowpack, are taken north of Svalbard, a region included in our region called "Russian Arctic West" (figure 1). In November in the Canadian Arctic, the difference most likely deems from the overestimation of summer snow melt in C6N4. This region is typically covered by ice that has survived several winters. The snow thickness from the snow model in Stroeve et al. (2020) supports the snow thickness

of about 0.20-0.25 m from the ASD product in November in the Canadian Arctic. Overall, we conclude that there is enough evidence that the C6N4 snow thickness is more realistic than the CS2$_{AWI}$ data snow thickness.

4.2 Sea ice density

According to figure 3 the C6N4 sea ice density is too low and has too little spatial variability compared to the airborne IceBird observations. Figure 4 also shows that the C6N4 sea ice density is also too low when compared to MOSAiC observations. The 10-year mean C6N4 sea ice density in figure 6e shows that similarly low values are calculated for the entire Arctic. In fact, all observations are denser than the C6N4 sea ice density. The formula used to calculate the sea ice density (equation 2) accounts for the amount of brine, but not the fact that the amount of enclosed air bubbles in the ice changes during melt season, leading to lower sea ice density in MYI (Timco and Frederking, 1996). The C6N4 value for ρ_{fresh} is 882 kgm^{-3}, which reflects a typical density for MYI (Alexandrov et al., 2010) and explains the comparable low sea ice density in the C6N4 run.

The C6N4$_{J21}$ sea ice density parameterization varies ρ_{fresh} depending on the FYI area fraction in each grid cell. Based on the RMSD, the resulting sea ice density is in better agreement with the IceBird data. This was expected as ρ_{fyi} and ρ_{myi} from equation 3 were fitted to the 2019 IceBird data. It is also closer to the MOSAiC observations (figure 4), which are independent of the IceBird data sea ice density observations. This shows that overall the C6N4$_{J21}$ density parametrization performs better than the simpler approach used in C6N4.

The 2017 averaged values (figure 3a) show that the eastern Beaufort Sea (dots) sea ice is denser than in the western Beaufort Sea (stars). This is reflected in the C6N4 and CS2$_{AWI}$ data, but not in the C6N4$_{J21}$ data, where the opposite is the case. Jutila et al. (2022a) states that the 2017 data exclusively consists of FYI. C6N4$_{J21}$ and CS2$_{AWI}$ however also include MYI data, just in different locations: CS2$_{AWI}$ mostly in the western Beaufort Sea and C6N4$_{J21}$ mostly in the eastern Beaufort Sea. The denser western Beaufort Sea values in C6N4 must be caused by the brine content, since no destination of MYI and FYI is included in this simulation. The lower C6N4$_{J21}$ densities in western Beaufort Sea (stars in figure 3a) indicate that the model here falsely classifies ice as MYI. The 10-year mean sea ice density in figure 6i indicates that on average, the model simulates more MYI in this region. Since the observations only cover one year, no conclusion can be drawn whether the model in general simulates too much MYI in the western Beaufort Sea. The wrongly classified MYI in the C6N4$_{J21}$ seems to stem from too much MYI exported into the western Beaufort gyre. Hunke (2014) found that the drag parameterization form Tsamados et al. (2014) increases the MYI export into this region. This drag parameterization is also the one used in the presented model set up. This means that the drag parameterization is one of the first model settings that should be examined to determine the reason for the excessive MYI export into the western Beaufort gyre. In the CS2$_{AWI}$ data (figure 3a yellow stars and dots), the majority of the eastern Beaufort sea values were classified as MYI, but also some western Beaufort Sea values. The results in figure 3 show that both the CS2$_{AWI}$ and C6N4$_{J21}$ assume MYI, where the observations only suggest FYI. In the CS2$_{AWI}$ data, this classification is based on passive microwave based ice type data. Our results suggest that the classification is not reliable. Another study evaluating different satellite sea ice type datasets comes to the same conclusion (Ye et al., 2023). They find that the ice type data used in the CS2$_{AWI}$ FB to SIT conversion has a MYI area bias of up to -0.54 x$10^6 km^2$ and FYI area bias up

to 0.60 x$10^6 km^2$. More accurate classification of MYI and FYI would influence both the snow thickness and sea ice density, which are also the parameters found to be the most important in the FB to SIT conversion.

Comparing the RMSD of the C6N4$_{J21}$ and the CS2$_{AWI}$ sea ice densities shows that overall, the C6N4$_{J21}$ densities are in better agreement with observations than the CS2$_{AWI}$ densities (comp. values in brackets in table 2 and 3). As discussed above, for 2017 the reason for the too low sea ice density values is FYI, which is classified as MYI. But other studies have also suggested that the Alexandrov et al. (2010) values in general are too low (Ji et al., 2021; Jutila et al., 2022a). Ji et al. (2021) does not specify, if it is both the values for MYI and FYI that are biased low according to their results. But Jutila et al. (2022a) finds that the both MYI and FYI values from Alexandrov et al. (2010) are biased low. Figure 4 however suggests that the CS2$_{AWI}$ FYI sea ice densities are actually slightly higher than the MOSAiC observations. There are two distinct differences between the IceBird observations and the MOSAiC observations: The location and the observation method. The physical conditions under which ice is formed vary throughout the Arctic. This might lead to differences in density, which is however only a speculation and will need further investigation. Timco and Frederking (1996) reviewed sea ice density observation methods and found that the method used to obtain the IceBird observations is the least reliable and the method used to obtain the MOSAiC observations is the most reliable.

The sea ice density that is derived for C6N4$_{J21}$ is rather simple, which impose at least three limitations. These limitations are:

1) the model track the FYI area as a fraction of the grid cell area. For estimating the bulk sea ice density, the volume of MYI and FYI is needed. The calculation of volume assumes that the ice thickness is the same for FYI and MYI, which introduces a bias towards too large a volume of FYI.

2) FYI area is defined as ice area formed since the previous September. This means that every September, all the remaining ice is classified as MYI, including also ice younger than one year. This results in a jump in sea ice density that is nonphysical. The physical explanation for lower densities in summer are the inclusion of air bubbles where brine has washed out (Timco and Frederking, 1996). This happens gradually throughout the melt season and not as a jump in September. With these limitations in mind, we recommend using the here derived sea ice density parameterization only during ice growth season.

3) the observation method and limited time. Timco and Frederking (1996) reviewed different methods to derive sea ice density and found the method used in Jutila et al. (2022a) to be the least reliable. This might explain some of the variability shown in figure 3. Another limitation of the observations is that they are only available in April, but the parameterization was derived for the entire winter. Figure 4 shows that the C6N4$_{J21}$ sea ice density indeed agrees best with the MOSAiC observations in April. The April model values in figure 4 are though also more variable than in the winter month, and further observation comparisons have to be carried out to come to a final conclusion.

4.3 Water density

Following WOA (Figure 5) the general pattern of dense water on the Atlantic side of the Arctic and lighter water in the Russian shelf area and the Beaufort Sea is replicated by C6N4, however this spatial water density gradient is less pronounced in C6N4.

Particularly, the Beaufort Sea surface water is lighter and in the Fram Strait region denser in WOA. The $CS2_{AWI}$ water density is represented by a single value with no spatial variations.

Evaluating C6N4 mixed layer depth (MLD) we found that it is overall too deep, similar to the MLD in Hordoir et al. (2022), who's mixing parametrization were closely followed in our model setup. This overestimated MLD is a result of enhanced mixing, which also explains the too high Beaufort Sea water densities, which is a result of the low density surface water getting mixed with denser subsurface water. The largest differences in between the WOA climatology and the C6N4 data is found in the Laptev Sea. The Laptev Sea surface salinity is highly dependent on river run-off and atmospheric forced transport of the river run-off to different locations each year (Janout et al., 2020). A climatology, like the WOA, will not reflect this inter-annual variability, whereas an ocean model potentially could. In most regions of the Arctic, there are less than 50 water density observations on a 1x1 degree grid for a period covering 150 years (Zweng et al., 2018). Even though, the WOA climatology is compiling a large part of all existing oceanographic observations (Zweng et al., 2018), one has to keep in mind that the coverage is extremely sparse. Keeping all limitations in mind, C6N4 compares better to the WOA data set than the constant value used in the $CS2_{AWI}$ data set. In area like the Laptev Sea, where the surface salinity is subject to large inter-annual variability due to wind forcing, models could even be more suited than climatologies. If using modeled surface density, a thorough analysis of the region's fresh water distribution should be carried out.

The C6N4 water density was calculated following Feltham et al. (2006), which calculates the density only depending on the salinity. This is currently the default in CICE. For consistency, the WOA water density was calculated following a similar approach by Feltham et al. (2006). The oceanographic standard would have been to use the salinity and temperature dependent TEOS-10 (Commission et al., 2015). We tested if using TEOS-10 had any impact on the results in the SIT difference, or the overall STD calculation between the $CS2_{AWI}$ and WOA data, and found this not to be the case.

4.4 Evaluation of Sea Ice Thickness differences

Currently available SIT products (Hendricks et al., 2021; Tilling et al., 2018; Guerreiro et al., 2017; Kurtz et al., 2013) use similar approaches as the $CS2_{AWI}$ data product to derive their sea ice density, snow thickness and water density. Differences mainly accruing in the snow thickness reduction over FYI or satellite data product used to derive ice type (Sallila et al., 2019). Since the values are similar, the $CS2_{AWI}$ data can in the following discussion be used as a general representation of the classical approach for CryoSat-2 SIT data. The above discussion of C6N4, $C6N4_{J21}$, $CS2_{AWI}$ and observations for snow thickness, sea ice density and water density shows that all model variables compare better to observations than the values used in $CS2_{AWI}$.

The largest SIT differences (figure 6b and table 4), result from the snow thickness differences and the $C6N4_{J21}$ sea ice density differences. The snow and the sea ice density that influences the SIT calculation has been discussed by other studies (Zygmuntowska et al., 2014; Kern et al., 2015; Ji et al., 2021; Jutila et al., 2022a). Kern et al. (2015) finds that both snow thickness and sea ice density contribute equally to the SIT uncertainty, while Zygmuntowska et al. (2014) finds that the snow contributes with 70 % and the sea ice density with 30-35 %. Even though this study does not analyze the exact contribution from each parameter in percentage, we find that the sea ice density differences on average influence the sea ice thickness more

than the snow thickness (comp. RMSD table 4), when the values from the classical approach are substituted with the modelled values. This might however depend on the snow thickness used in the comparison (Zhou et al., 2021).

The differences in SIT are compared variable by variable in figure 6d, h, l and p, and the combined SIT differences are shown in figure 7b. The single value SIT differences in figure 6 result in higher SIT differences than the combined ones in figure 7b. This is due to the opposite signs in the SIT differences of snow and sea ice density (figure 6d and l) canceling each other out in the combined SIT difference. Here, our results show that only substituting W99 snow thickness, or only Alexandrov et al. (2010) sea ice density, introduce biases.

The effect of varying the water density on the SIT are normally neglected, see e.g. (Alexandrov et al., 2010; Kurtz et al., 2013; Guerreiro et al., 2017; Tilling et al., 2018; Hendricks et al., 2021). The SIT difference analysis between the C6N4 and CS2$_{AWI}$ suggests that the water density can lead to up to 0.33 m difference with a RMSD of 0.01 m, which is little in comparison to the SIT differences initiated by snow thickness and sea ice density, but still not negligible in certain areas. The SIT RMSD between WOA–CS2$_{AWI}$ amounts to 0.02 m and for WOA–C6N4 0.01 m. The average value shows that in general, the C6N4 value result in lower SIT difference, which is also shown in figure 8. The maximum though is higher for the WOA–C6N4 difference. The higher maximum value could be due to the nature of the WOA climatology. This maximum is located close to the Lena river delta. As discussed above, this is a region with high inter-annual sea surface salinity variability (Janout et al., 2020; Zhuk and Kubryakov, 2021) and low observational converge (Zweng et al., 2018). As also mentioned above, an analysis of the inter-annual variability of sea surface salinity of C6N4 in this area is needed to draw any final conclusion about its ability to model the right location of river discharge.

All existing SIT data products that use the hydrostatic balance equation to derive SIT are either neglecting the error contribution from water density (Kurtz et al., 2013; Tilling et al., 2018; Hendricks et al., 2021) or are using values of 0.5 kgm^{-3} (Guerreiro et al., 2017) as the uncertainty with reference to Alexandrov et al. (2010) or Laxon et al. (2003). Alexandrov et al. (2010) refers to three data sources (i.e: Gorshkov (1980); Pavlov and Stanovoy (1998); Timokhov and Tanis (1997)) for their assumptions which were not accessible for us, and Laxon et al. (2003) refers to Wadhams et al. (1992). Wadhams et al. (1992) evaluated the seasonal variability of the Arctic surface water density and finds that it varies by about 0.5 kgm^{-3}, but they did not take the spatial variability into account. Figure 5 shows that the WOA water density varies by up to 10 kgm^{-3} in space. Our results show that, using a climatology like the WOA or model value would give more realistic water density estimates than the commonly used single value. If a single value is used for the water density in equation 1, the spatial variability should be accounted for in the uncertainty estimate. We suggest, in this case, to use 2.6 kgm^{-3} calculated as the sum of the STD between the WOA and CS2$_{AWI}$ density of 2.1 kgm^{-3} and 0.5 kgm^{-3} to account for the seasonal variability, as suggested by Wadhams et al. (1992). Figure 8 shows that using a variable water density can improve the SIT, which is why we suggest that data products deriving SIT via the hydrostatic balance equation should use a data product like the WOA climatology. As discussed above, the WOA climatology is also associated with its own uncertainties, but these are still smaller than those related to a single value of water density.

Even though the model values were found to be closer to the validation data, our analysis indicates that more work should be invested in validation of the ocean component. Particularly, the migration of river discharge should be validated. Further,

we found that the mixing seems to be too strong, which results in a too deep mixed layer. Furthermore, the ice transport in the Beaufort Sea should be investigated. Our results show that MYI is present where observations indicate only FYI in the Beaufort sea. The drag parameterization seems to be a good first subject of interest to improve this.

The analysis focused on 10-year mean values. One additional benefit of using model values would be to include the inter-annual variability. This could lead to significantly higher SIT differences compared to the ones found in this study

5 Conclusions

The aim of this study was; 1) To evaluate whether sea ice model values, as used in Sievers et al. (2023) (C6N4) can substitute the commonly used W99 snow thickness, the Alexandrov et al. (2010) sea ice density and the Arctic wide constant water density values in the classically satellite derived FB to SIT conversion. 2) Evaluating how much changing the snow thickness, sea ice density and water density would impact the SIT difference for each variable separately and combined.

We found that the C6N4 snow thickness and water density compares better to observations than the CS2$_{AWI}$ values, but that the C6N4 sea ice density does not. Therefore, this study introduced an improved sea ice density parameterization (eq. 3) C6N4$_{J21}$, which we find compares better to observations than the Alexandrov et al. (2010) sea ice type based densities used in the CS2$_{AWI}$ approach.

Analyzing the SIT differences resulting from the snow thickness, sea ice density and water density separately, we find that the snow thickness and sea ice density differences between the CS2$_{AWI}$ and C6N4$_{J21}$ lead to the largest SIT differences. The areas with the largest differences for both values are located north of Greenland and Canada, and are of opposite sign. In the combined SIT difference (figure 7b) their effects cancel out. The combined SIT differences analysis shows that only substituting snow thickness, or sea ice density, introduces a bias. This underlines the value of the derived C6N4$_{J21}$ sea ice density, which can be easily combined with approaches of substituting the snow thickness with model values, as done by for example Landy et al. (2022) and Fiedler et al. (2022).

In contrast to other studies (e.g., Kurtz et al. (2013); Tilling et al. (2018); Hendricks et al. (2021)), we find that the water density introduced uncertainty is not negligible, but on average leads to 0.02 m difference in the SIT to FB conversion and can in extreme cases lead to up to 0.13 m in SIT difference, comparing CS2$_{AWI}$ constant value and WOA values. To our knowledge, all public available CryoSat-2 SIT products assume a water density uncertainty of 0 to 0.5 kgm^{-3} which is based on assumptions only taking into account the seasonal variability of water density (Wadhams et al., 1992), but not the spatial variability. We suggest changing the sea ice density uncertainty to 2.6 kgm^{-3} to account for both the seasonal and spatial variations, or using water density values from climatologies like the WOA, or as in this study ocean model values. The value of 2.6 kgm^{-3} is derived from the STD between the CS2$_{AWI}$ constant value and the WOA.

Appendix A: Deriving Sea Ice Density C6N4$_{J21}$

C6N4 sea ice density varies only by the amount of brine enclosed in the ice (equation 2). Figure **??** and **??** show that the resulting sea ice density is not variable enough and too light. The value of ρ_{fresh} in equation 2 represents with 882 kgm^{-3} typical MYI values. Enclosed air bubbles are the main reason for older ice to be less dense than newly formed ice (Timco and Frederking, 1996). The sea ice model is not capable of simulating enclosed air bubbles, so we need an alternative method to derive ρ_{fresh}, for example by using MYI and FYI volume per grid cell, following approaches used in the classical approach.Also FYI and MYI volume is not calculated by the model. However, the model does calculate the percentage of the FYI area coverage per grid cell (FYI_{frac}), where FYI_{frac} is defined as the area fraction of ice formed since last September. Equation 3 was introduced to substitute the constant ρ_{fresh} value of 882 kgm^{-3} in equation 2, with ρ_{myi} and ρ_{fyi} values weighted by FYI_{frac}. We here use the sea ice density observations from Jutila et al. (2022a) to minimize the root-mean-square error (RMSE) between observation and model values for different ρ_{myi} and ρ_{fyi}:

$$\rho_{i,RMSE} = \sqrt{\sum_{i=1}^{n} \frac{(\rho_{i,model} - \rho_{i,J21})^2}{n}} \tag{A1}$$

where $\rho_{i,model}$ was calculated following:

$$\rho_{i_{model}} = a_b * \rho_b + (1. - a_b) * (\rho_{myi} * (1. - FYI_{frac}) + \rho_{fyi} * FYI_{frac}) \tag{A2}$$

similarly to the ρ_b in equation 2, ρ_b is the model calculated sea ice enclosed brine density and a_b the percentage of brine of the total volume of ice. The sea ice density values for ρ_{myi} and ρ_{fyi} used as input to estimate the RMSE error matrix are:

$$\rho_{myi} = [870, 875, 880, 885, 890, 895, 897] \qquad \rho_{fyi} = [900, 905, 907, 910, 914, 917, 919, 921]$$

The values for ρ_{myi} and ρ_{fyi} were chosen under the following assumptions; (a) MYI is typically less dense than FYI due to the presence of enclosed air bubbles in MYI (Timco and Frederking, 1996), (b) taking into considerations observed values from the literature (Jutila et al., 2022a; Alexandrov et al., 2010; Timco and Frederking, 1996) and (c) the densities for MYI and FYI need to lay within the observed ranges, excluding extreme outliers, because the resulting value will reflect a bulk value for an area covering 10 km^2.

The 2019 observations from Jutila et al. (2022a) were used for this calculation because they include a similar amount of FYI and MYI value from the same source. The observations were interpolated to the model grid by the nearest neighbor method, and all values on the same day and the same grid cell were averaged. All observation values, with an associated error larger than 30 kgm^{-3}, were excluded from the analysis. The considered observations have an average error of 22.62 kgm^{-3}.

The error matrix of the RMSE between the observations and model values, using all combinations of ρ_{myi} and ρ_{fyi}, are visualized in Figure A1. The lowest RMSE were found for $\rho_{myi} = 890kg/m^3$ and $\rho_{fyi} = 907kg/m^3$, indicated by the darkest blue area in figure A1. We use these densities for MYI and FYI as input for ρ_{myi} and ρ_{fyi} in the C6N4$_{J21}$ sea ice density in equation 3.

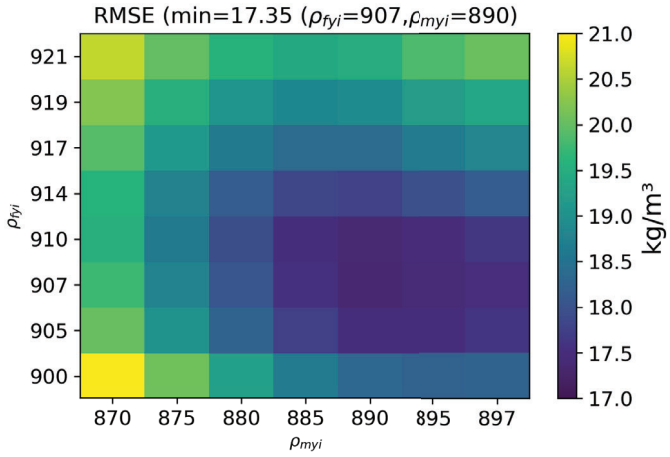

Figure A1. Error matrix of the calculated sea ice density RMSE following equation A1 for all tested ρ_{myi} and ρ_{fyi}.

https://doi.org/10.5194/tc-2022-84
Preprint. Discussion started: 28 April 2022

The Cryosphere Discussions

Arctic sea ice and snow from different ice models: A CICE–SI3 intercomparison study

Imke Sievers[1,3], Andrea M. U. Gierisch[1], Till A. S. Rasmussen[1], Robinson Hordoir[4,5], and Lars Stenseng[2]

[1]Danish Meteorological Institut, Lyngbyvej 100, Copenhagen East, Denmark
[2]DTU Space, Danish Technical University, Elektrovej Bygning 327, 2800 Kongens Lyngby, Denmark
[3]Aalborg University,A. C. Meyers Vænge 15, 2450 Copenhagen, Denmark
[4]Institute of Marine Research, Bergen, Norway
[5]Bjerknes Centre for Climate Research, Bergen, Norway

Correspondence: Imke Sievers (imksie@dmi.dk)

Abstract. Sea-ice models fill many purposes; they are used in global climate models or for short-term forecasts to plan shipping routes. No matter what their output is used for, understanding the cause for their variability is crucial.

In the this study two commonly used sea-ice models, CICE and SI3 were compared after running both models with similar boundary condition, on the same grid, with the same forcing and initialised with the same data, with the aim to understand how the two models differ from each other when forced equally. The set-up also allows linking certain model biases observed in both models to the external forcing. We found that the models compare well to sea ice concentration, sea ice thickness and snow thickness observations, with small regional differences, which could be linked to different model processes. The processes with the highest influence are the drag formulation, the albedo, and the treatment of snow. We find that the treatment of snow has a significant influence on the difference in sea ice thickness between the models, even though their forcing is equal.

1 Introduction

The interest in forecasts of Arctic sea ice conditions on multiple time scales has increased. On short time scales (up to days) forecasts are of importance for search and rescue and maritime safety (Wagner et al., 2020). As the forecast length is extended towards seasonal the variability in the Arctic sea ice cover is of interest when planning shipping routes and other maritime activities (Stocker et al., 2020; Stewart et al., 2020). On long time scales (decades and more) forecast of the Arctic sea ice cover are of interest for the climate science community as it plays a central role in the global climate system as changes in the sea ice cover changes the albedo of the poles and thereby provides a positive feedback to the climate system (Kashiwase et al., 2017). Validation of model systems are primarily based on remotely sensed data as in-situ data is difficult to obtain in the Arctic. Long records of sea ice concentration (SIC) are often based on remotely sensed passive microwave data, which extends back to the 1970s. In addition to validation, these data sets provide time series of the historical evolution of the sea ice cover. Within this time period sea ice extend has retreated and the fraction of multi-year sea ice has reduced (Tonboe et al., 2016). Hindcast from sea-ice models aim to reproduce and predict these changes. One example is Collow et al. (2015), who show

https://doi.org/10.5194/tc-2022-84
Preprint. Discussion started: 28 April 2022

the same trend for sea ice volume as what is seen in the remotely sensed data records. However, two model simulations rarely result in the exact same result.

Several studies have examined the cause of these differences. The influencing parameters can in general be grouped into external and internal parameters. External parameters are for example atmospheric forcing, lateral boundary conditions or initial conditions. Atmospheric forcing for example influences sea ice by adding heat, precipitation and radiation. Wang et al. (2018) compared the widely used atmospheric reanalysis ERA-Interim with its successor ERA5, which has on average a 2° C higher warm bias. Forcing a 1-D thermodynamic model with both dataset resulted in an unexpected low difference since ERA5s precipitation is higher and insulated the sea ice from heat loss. Another example of an external parameter for differences are the initial conditions. They are especially interesting for short-term predictions. When cold starting a model run the initial SIC and thickness are often depending on the ocean and atmosphere temperature and are constant. To avoid over or underestimated ice they are often set to a value realistic in the area of interest. Dirkson et al. (2017) and Day et al. (2014) run simulations where observed SIC and thickness were used as initial conditions and show that the skill of the model increases significantly when a realistic sea ice thickness (SIT) is used.

Internal parameters are for example the model grid, time steps, number of sea ice categories or the way thermodynamic and dynamic processes are discretized. Kiss et al. (2020) compares three global ocean-sea-ice models on three different fine grid resolutions and finds that different resolutions favour the representation of different process. They for example find that models run on coarser girds miss certain sea ice characteristic features as for example leads. Another example of internal cause for resulting model differences is the dynamical solver chosen to solve the momentum equation of sea ice. Losch et al. (2010) compares a line-successive-over-relaxation (LSOR) an a elastic-viscous-plastic (EVP) scheme finding that the resulting sea ice velocities differ by several cm/s resulting in a freshwater export difference of 200 km^3 yr^{-1}.

Many solutions as, for example the dynamical solver, the grid size, and the number of sea ice categories increase the computational cost. Many sea-ice models, which are commonly used, come with a limited set of options for internal parameters as for example the dynamical solver, or the way albedo is calculated from the radiative forcing. This leads to many different sea-ice model set ups, which when compared to one another still show to have comparable skill (Long et al., 2021), however they still show a certain amount of variability in Arctic sea ice conditions. In order to set up an ideal sea-ice model, the external and the internal parameters and forcing should reflect the reality, as close as possible, however it can be hard to differentiate the sources that introduces the bias between the external and internal parameters. In order to study the internal parameters only the external forcing can be set to be the same.

In this study, we want to investigate this variability. This is done by using two state of the art sea-ice models which are commonly used to simulate Arctic sea ice at different time scales such as climate models (Long et al., 2021), short term sea ice predictions (Dupont et al., 2015) and in sea ice reanalysis (Lellouche et al., 2021). In order to focus the analysis on the sea-ice models the two models were run on the same grid, with the same atmospheric forcing, coupled to the same ocean model, forced by the same boundary conditions and started from the same ocean and sea ice initial conditions to eliminate sources influencing the sea ice predictability. The models are CICE and SI3. SI3 is the default sea-ice model included in NEMO after version 4.0.

https://doi.org/10.5194/tc-2022-84
Preprint. Discussion started: 28 April 2022

Since CICE can be run stand-alone or coupled to an ocean model, CICE was coupled to NEMO. To our knowledge this study is the first coupling NEMO4 to CICE and this study also serves as a validation study.

Snow plays an important role in the sea ice thermodynamics as it acts as an insulating layer between the atmosphere and the sea ice. It has a high albedo which ensures that the incoming radiation is reflected. It also plays a part in sea ice dynamic processes as it alters the surface roughness of sea ice. During the last year snow on sea ice gained more and more attention. New satellite based snow observation data products were released as for example the Ka/Ku band snow product from LEOGS (Garnier et al., 2021) or the snow depth resulting from a combination of Cryosat2 and ICESat2 sea ice freeboards by Kacimi and Kwok (2022). The increased understanding has also reached the modelling community with the result that snow becomes more and more important (Blanchard-Wrigglesworth et al., 2015). For these reasons we decided to include the snow volume in this study to contribute to the understanding which role snow plays in sea ice models.

The aim of this study is to compare the two models under as similar conditions as possible and investigate the significant differences which may appear. In addition, if there are significant differences we want to identify and discuss their causes. Based on this we want to make a statement about where the sea-ice modelling community might need to put a focus for further improvement.

Section two describes the data, methods including the models used in this study. Section three describes the results and highligths the differences between the two ice models, whereas section four discuss the results and section five concludes this study.

2 Data and Models

The two coupled ocean and sea ice model systems consist of the same ocean model, which is described in section 2.1, and two different sea ice models, which are introduced in section 2.2, together with their setup and input data. In section 2.3 the observational data which was used for the evaluation is described.

2.1 Ocean model

The ocean model NEMO (Madec et al., 2017) is widely used in the modelling community for both regional (Le Sommer et al., 2019) and global ocean simulations, climate prediction, hind casts (Hazeleger et al., 2012) and modelling of marginal seas (Hordoir et al., 2019) to only name a few applications. The set up used in this paper closely follows Hordoir et al. (2022) and uses similar forcing and namelist settings. Changes were made to the namelist due to a version update and the atmospheric forcing differs. The setup includes tides and runs without ocean surface restoring. The forcing consists of 3-hourly atmospheric data from ERA5 (Hersbach et al., 2017) (2-m temperature, 2-m specific humidity, 10-m wind, incoming short/long wave radiation, total precipitation, snowfall and sea level pressure). At the lateral boundaries it is forced monthly with GLORYS salinity, temperature, u- and v-velocities and sea surface height fields (Lellouche et al., 2021). The tidal forcing consists of TPXO 7.2 harmonic tidal constituents at open boundaries (Egbert and Erofeeva, 2002). For the river runoff a climatology from

https://doi.org/10.5194/tc-2022-84
Preprint. Discussion started: 28 April 2022

Dai and Trenberth (2002) was used. The initial fields for salinity, temperature, SIC and SIT for ocean and ice are ORAS5 reanalysis (Zuo et al., 2019).

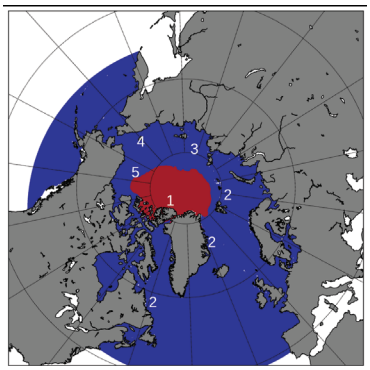

Figure 1. The model domain of the coupled NEMO-CICE and NEMO-SI3 models (area in blue and red). The red area refers to the thick ice mask used in figure 9 and the blue area to the thin ice mask used in figure 9. The thin ice mask also includes open water and its southern borders mark the end of the model domain. The numbers indicate different areas discussed in section 4. Number 1 indicates the Lincoln Sea and Canadian Archipelago, 2 the Atlantic ice edge, 3 the Russian shelf, 4 the Chukchi Sea and 5 the Beaufort sea.

2.2 Sea ice models

Both sea-ice models are coupled to NEMO. The sea-ice models CICE (Hunke et al., 2021a) and SI3 (NEMO-Sea-Ice-Working-Group, 2022) both are eulerian multi category sea-ice models solving dynamics, and thermodynamics of sea ice numerically. Both models use Elastic-Viscous-Plastic (EVP) rheology run with the same time step, and are coupled and forced at the same frequency. The models were run from 2008 to 2020 starting from the same initial conditions. The model output analysed in the following sections includes data from 2010-2020, excluding a 2 year spin up phase. The albedo was tuned in both models. Since the calculation of the albedo differs in both models this could not be made coherently. The tuned parameters are attached in the supplementary material along with their models namelists.

2.2.1 SI3

SI3 (Sea-Ice Integrated Initiative) is the NEMO default sea-ice model from version 4.0. It was developed to unify the former three main sea-ice models used in combination with NEMO in the past: CICE, GELATO and LIM (Madec et al., 2017). SI3 uses constant drag coefficients for ocean ice and atmosphere ice drag. The parameters can be found in the namelist in the appendix. The albedo calculation follows (Shine and Henderson-Sellers, 1985) and distinguishes in between five different surface types which which all can be tuned via namelist parameters, which can be found in the appendix. The albedo parameters were tuned

https://doi.org/10.5194/tc-2022-84
Preprint. Discussion started: 28 April 2022

to fit the Pan-Arctic Ice Ocean Modeling and Assimilation System (PIOMAS) (Schweiger et al., 2011a) total sea ice volume. For this study we use NEMO-SI3 version 4.0.4 revision r13658.

2.2.2 CICE

CICE is a portable sea-ice model, which can be used standalone, however it is recommended to run as part of a coupled system either global or regional. The model consists of one dynamical part solving advection of sea ice and changes in thickness and a thermodynamic model solving the changes in thickness due to thermodynamic processes. The code for both parts is frequently updated and maintained by the CICE consortium and can be found on github (Hunke et al., 2021a).

In this set up we use form drag formulation which calculates the drag coefficients depending on SIC, flow size, melt pond, ridges and freeboard as described by Tsamados et al. (2015). The albedo is calculated depending on the suns incident angle and sea ice surface type following Briegleb and Light (2007). The different surfaces types are snow, ice and melt ponds. For the calculation of the surface albedo different process are taken into account. For a more detailed description we refer to Hunke et al. (2021b). The albedo parameters were tuned to fit PIOMAS (Schweiger et al., 2011a) total sea ice volume.

CICE is coupled to NEMO based on a set up used in Smith et al. (2021). Changes made from Smith et al. (2021) to the present setup are the update of the model versions from NEMOv3.6 to NEMOv4 and CICEv4 to CICEv6.2. As a difference to the standard setting the freezing and the melt temperature has been differentiated in order to account for salinity difference of sea ice and the ocean.

2.3 Observations

The model simulations are compared with remote sensing observations of SIC, SIT and snow depth on sea ice. Therefore monthly averages of model output were interpolated to the observation grids. All averages were calculated over the period 2010-2020.

2.3.1 OSISAF Sea ice concentration

The Ocean and Sea Ice Satellite Application Facility (OSISAF) SIC is based on passive microwave data from satellite measurements. Brightness temperature measurements retrieved by SSMIS instruments are processed with help of ECMWF atmospheric reanalyses on a daily basis by DMI and MET Norway. The advantage of using brightness temperatures to retrieve SIC is the independence of cloud cover and daylight in the Arctic, resulting in a year round data product. The data is gridded in a resolution of 10x10km covering the entire Arctic. It has an accuracy of $\pm$ 10% in the Arctic with the largest bias in summer due to meltponds (OSISAF, 2017).

2.3.2 CS2SMOS Sea Ice Thickness

The CS2SMOS SIT product is an optimal interpolated sea ice product combining weekly averaged CryoSat2 SIT with daily SMOS SIT developed by the Alfred Wegener Institue (AWI). The combination of these two products utilise their combined

https://doi.org/10.5194/tc-2022-84
Preprint. Discussion started: 28 April 2022

strength; the thick sea ice from Cryosat and the thin sea ice from SMOS (Mu et al., 2018b). Data comes on a 25x25km EASE2 grid with a time step of one week. More information about the data set can be found in Ricker et al. (2017).

2.3.3 Ka/Ku Snow Thickness

The Ka/Ku snow depth product combines altimeter data from SARAL and from CryoSat2. It uses the difference in penetration depths from Ka-band and Ku-band altimeters to determine how much snow lays on top of sea ice. This is possible because the Ku-band radar is reflected at the snow–ice interface, while the Ka-band radar is reflected at the snow surface. The data product comes in monthly time steps covering the time period November to April 2013-2019. The data is distributed on a 12.5km x 12.5km EASE2 grid and covers the Arctic up to 81.5N (Garnier et al., 2021).

3 Results

This section will describe comparisons of the two model systems and SIC, SIT and snow thickness with each other and with observations.

3.1 Sea Ice Concentration

Figure 2 shows the 10 year mean OSISAF SIC compared to 10 year mean modelled SIC for March and September. In general, the differences are slightly larger in CICE compared to SI3, but this difference is small in comparison to the model-observation differences. In March, the largest differences are found in the North Atlantic and Barent Sea. In September, both models show a higher SIC in the Beaufort Sea and a lower SIC in the central Arctic close to the Russian shelf. The negative bias of the models in the Beaufort Sea is stronger pronounced in CICE. The positive bias in SI3 in the Central Arctic/Russian shelf region is stronger pronounced in SI3.

Figure 3 shows the difference between SI3 and CICE and the SIC for the respective month September and March. In March, the differences are mainly in the Atlantic sector with more SIC in CICE. At the maximum CICE exceeds SI3 SIC by 60% just north of Iceland. In average CICEs SIC exceeds SI3s by about 25% in the region where the models differ from each other. In September, CICEs SIC is larger than SI3s close to the ice edge. Here the maximum of this difference lies with 50% more SIC in CICE compared to SI3 in the northern Laptev Sea. The central Arctic and the area north of Greenland SI3 has up to 20% higher SIC than CICE.

3.2 Sea Ice Thickness

To compare the models with the CS2SMOS all the monthly SIT model data was interpolated onto the CS2SMOS grid. Only data points covered by CS2SMOS were considered for the comparison and all data above 88° N was excluded, since CS2SMOS is an optimal interpolation and not CryoSat2 nor SMOS covers latitudes above 88° N. Data from each month in which CS2SMOS is available was summed up over the total covered area and is shown for both models and CS2SMOS in figure 4.

https://doi.org/10.5194/tc-2022-84
Preprint. Discussion started: 28 April 2022

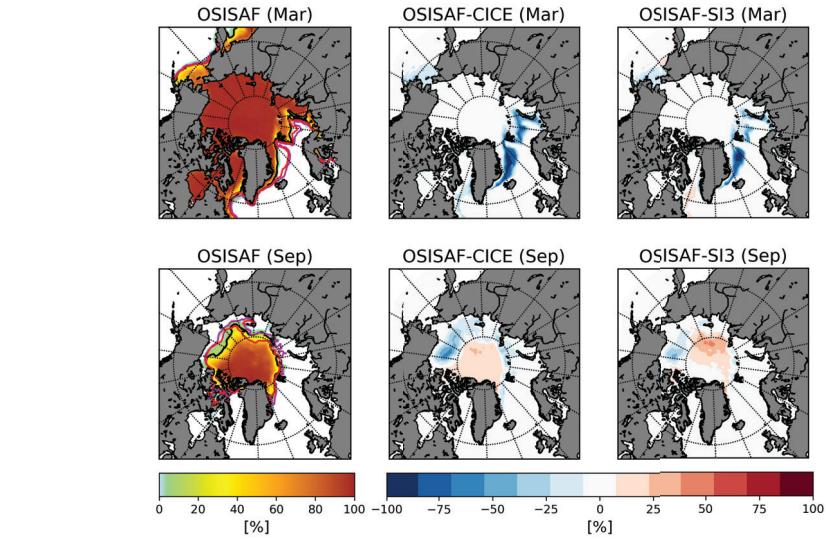

Figure 2. Monthly SIC climatology and differences for the period 2010-2020. March is shown in the upper row and September in the lower row. Left panel displays OSISAF observation, the middle the difference of OSISAF and CICE and on the right OSISAF minus SI3. The black line shows the 15% SIC contour from OSISAF, the red line from SI3 and the purple line from CICE for the respective month.

3.2.1 Model Satellite Comparison

Figure 4 shows that in most years CS2SMOS starts the winter season with a larger sea ice volume compared to the models. In most years, when the freeze up begins CICE models the sea ice cover to be thinner than the ice cover from SI3. Throughout the rest of the winter season, the modeled sea ice volume grows faster compared to the CS2SMOS sea ice volume. While CS2SOMS stop increasing the sea ice volume in April, both models keep on producing sea ice until the end of the season. CICE slows down the sea ice production slightly earlier than SI3. This is especially true from 2012 to 2016.

To get a better understanding of the regional differences between models and observations monthly difference maps of 10 year averages for October and March are plotted along with a reference CS2SMOS SIT in figure 5. The figure shows that the overall lower sea ice volume in October, also shown in figure 4 originates from a difference in the central Arctic. Overall, this difference is stronger between CICE and CS2SMOS than between SI3 and CS2SMOS. In March, both models show a thicker ice cover than CS2SMOS in coastal areas (Canadian Archipelago, Hudson Bay, Russian shelf seas) and at the ice margins around western Greenland. The SIT differences in the central Arctic is approximately the same as in October. In the Beaufort Sea region, both models display more ice than CS2SMOS for all months. This difference is strongest pronounced

https://doi.org/10.5194/tc-2022-84
Preprint. Discussion started: 28 April 2022

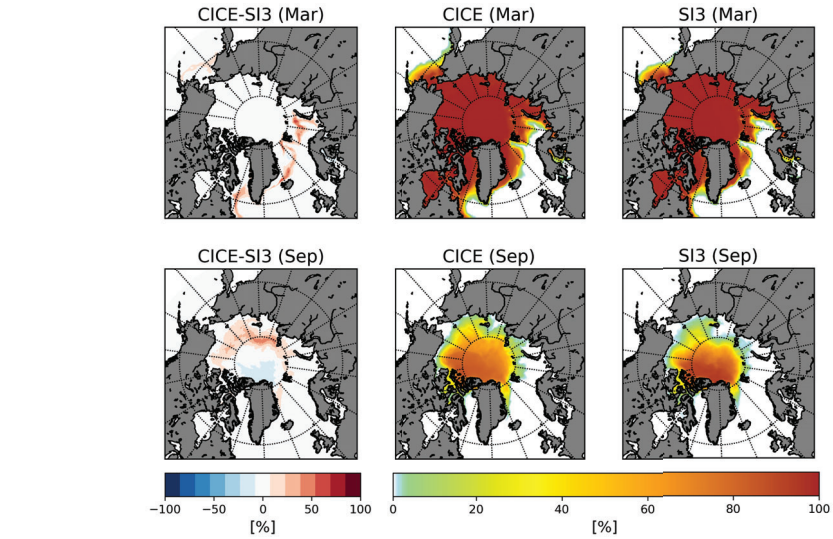

Figure 3. Monthly SIC climatology and differences for the period 2010-2020. First column shows the difference in SIC between the two model setups in March (top) and September (bottom) and the respective SIC for CICE and SI3 (second and third column) in 10 year monthly mean for March (upper row) and September (lower row).

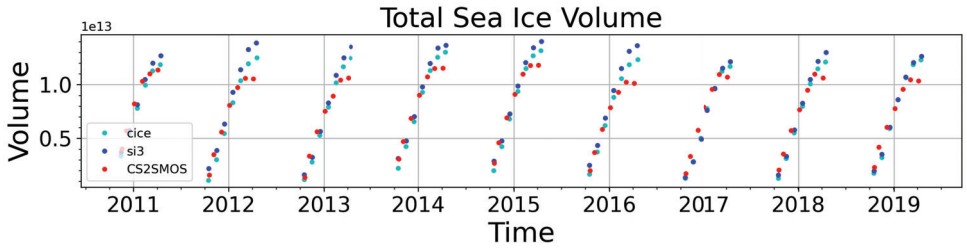

Figure 4. Sea ice volume variation of CICE (light blue), SI3 (dark blue) and CS2SMOS (red) for October - April 2010 to 2019

175 in SI3 compared to CICE. SI3 shows a thicker ice cover just north of Greenland for all months. In CICE, this area is in both March and October close to C2SMOS SIT. Both models display a more homogeneous SIT throughout the Arctic compared to

https://doi.org/10.5194/tc-2022-84
Preprint. Discussion started: 28 April 2022

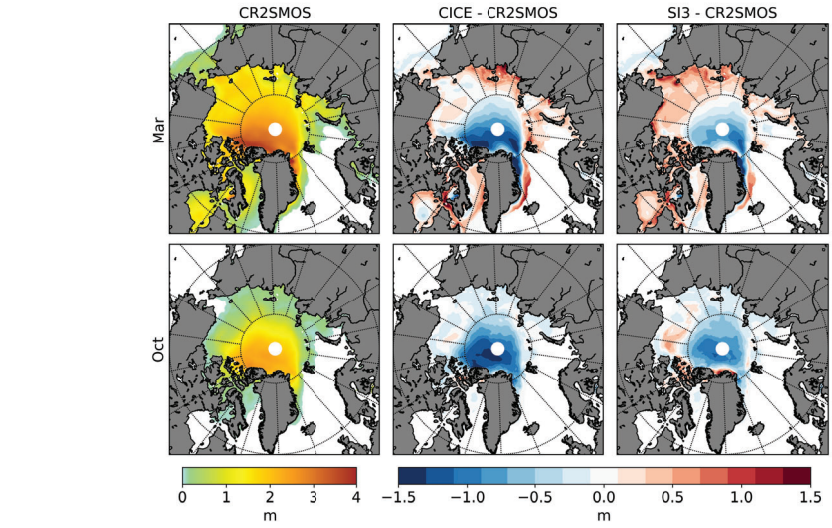

Figure 5. Monthly SIT climatology and differences for the period 2010-2020 for March and October. The left column shows CR2SMOS SIT the middle CICE-CR2SMOS and the right SI3-CR2SMOS.

observations with less thick ice in the central Arctic and thicker sea ice towards the margins. In general, the locations in which the models differ from CS2SMOS are similar.

Figure 6 compares the ice thickness of the two model systems. CICE SIT is in general thinner than the SI3 SIT in the regions north of Greenland and in the Beaufort Sea. In March, CICE SIT is over all thinner than SI3s SIT in most regions. This is shown in 6 upper left panel. Only close to the ice edge, in the Atlantic sector and in the Laptev Sea CICE sea ice is up to 0.7m thicker than SI3. SI3 is up 1m thicker than CICE in Chucki Sea, north of Greenland and the Canadian archipelago. In September SI3 SIT (lower left panel 6) is thicker in the region north of Greenland, the Canadian archipelago and the Beaufort sea and CICE is thicker than SI3 on the Russian shelf break.

3.3 Snow

Modeled and observed snow thickness distributions are shown in figure 7. The Ka/Ku data product only covers the Arctic up until 81.5° N, which excludes a larger part of the multiyear sea ice, see figure 1. To compare data sets, monthly model data was interpolated onto the Ka/Ku grid and all data points not covered by the satellite observations were excluded. The resulting monthly thickness distribution for the period 2013-2019 is shown in figure 7 as a probability density function (PDF). Both

https://doi.org/10.5194/tc-2022-84
Preprint. Discussion started: 28 April 2022

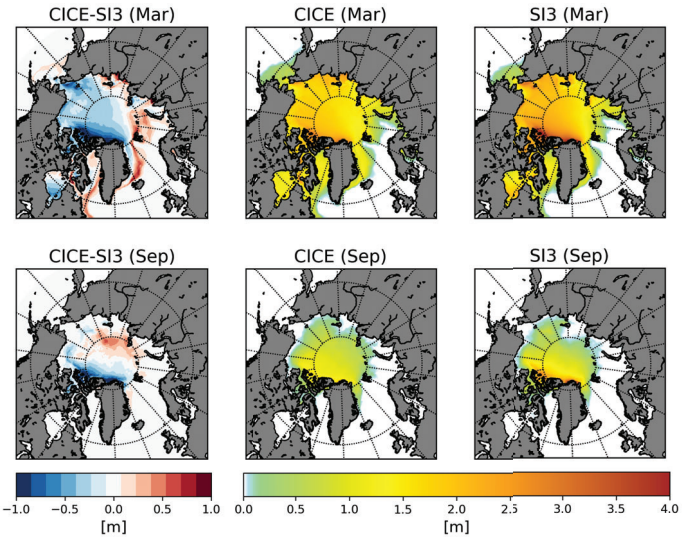

Figure 6. Arctic wide CICE and SI3 SIT comparisons for March (upper row) and September (lower row). The left panels show CICE-SI3 SIT, the middle CICE and the right SI3 SIT.

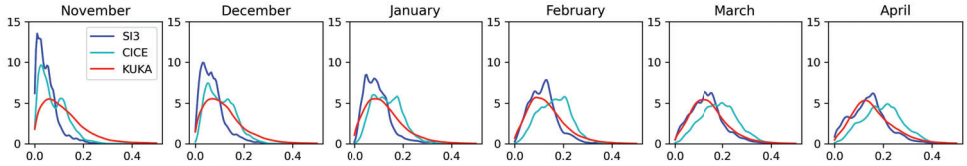

Figure 7. Pdfs of the snow thickness distribution for CICE (turquoise), SI3 (blue) and Ka/Ku (red) snow thicknesses. a) The pdf for the entire area covered by the Ka/Ku data product , b) for the Canadian Arctic marked as yellow in fig 1 and c) for the Russian Arctic marked as green in fig 1 for the month November, December, January, February, March and April. Note the different x-axis for a).

190 models have a limited snow cover which is only a few cm thick in November, whereas the snow thickness in the observations is around 10cm. The dominant snow thickness increases over the winter season in the models. In April, the dominant snow thickness in CICE is about 22cm and 18cm in SI3. The dominant snow thickness in the observations (red line) moves from approximately 8cm in November to about 15cm in April. CICE agrees more with the observed snow thickness distribution in

https://doi.org/10.5194/tc-2022-84
Preprint. Discussion started: 28 April 2022

the beginning of the season, whereas SI3 agrees more with observations in the end of the season. Especially in March and April
195 SI3 shows good agreement with observations. Overall, the models show a more noisy distribution than the observations.

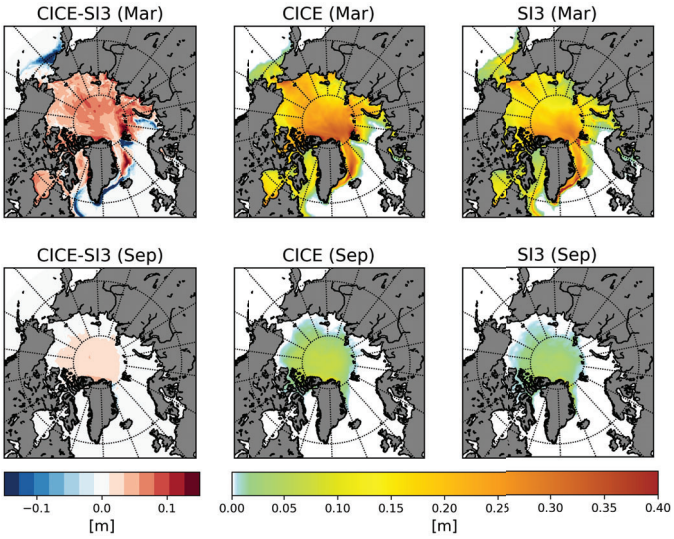

Figure 8. March (lower panel) and September (upper panel) monthly Arctic wide snow thickness climatologies calculated over the period 2010-2020. The left column shows the difference CICE-SI3 snow thickness the middle CICE and the right SI3 total snow thickness.

Figure 8 shows the snow cover of both models (CICE: middle, SI3: right) in March and September and their differences (left). In September, CICE has a 5cm snow cover in most of the central Arctic while SI3 only shows a few cm in small patches in the central Arctic and off the coast of north Greenland and the Canadian Archipelago. In March CICE and SI3 build up a snow cover of up to 40cm. In CICE, this maximum is located between Iceland, Greenland, and north of Svalbard. In SI3 the
200 maximum is located south west of Svalbard and along the ice edge southeast of Greenland. The difference map for March shows that overall CICE has a 8-10cm thicker snow cover than SI3 in almost the entire Arctic. Only close to the ice edge, SI3 has up to 15cm more ice than CICE.

3.4 Regional sea ice and snow volume comparison

Analyses of the modelled total sea ice volume and total snow volume development throughout the year show a seasonal and
205 regional difference between the models. This seasonality is shown in 9. The curves in 9 were calculated by subtracting CICE total Arctic sea ice and snow volume from SI3. Figure 9 upper panel shows the total Arctic snow volume and sea ice volume

https://doi.org/10.5194/tc-2022-84
Preprint. Discussion started: 28 April 2022

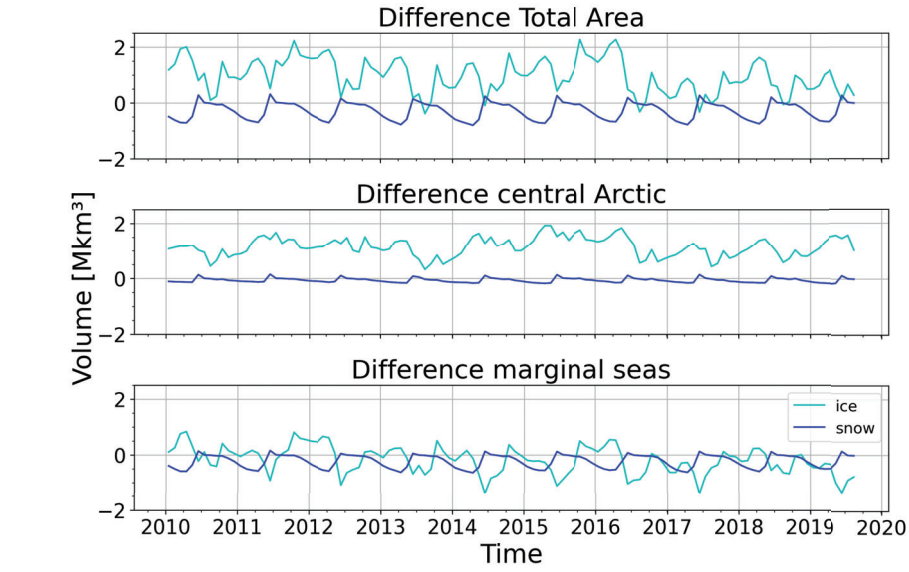

Figure 9. The modelled total sea ice volume difference and snow difference. The turquoise line indicates the ice volume difference calculated as SI3-CICE the blue line snow volume. The upper panel shows the total Arctic ice and snow volume, the middle panel the ice and snow volume difference from thick ice dominated areas (blue mask in figure 1) and the lower panel from thin ice dominated areas (red mask in figure 1).

differences in between the models (Snow blue, Ice turquoise). Both curves display a certain seasonality. Overall, SI3 has a higher sea ice volume than CICE and CICE has a higher snow volume than SI3. The sea ice volume difference peaks each year in the beginning of the freeze-up in September and in the end of the freeze-up in April. The snow volume difference curve has its maximum (higher snow volume in SI3) in June and a minimum (higher snow volume in CICE) in April. The minimum in snow volume difference coincides with the end of freeze-up maximum difference in ice thickness. The correlation between the two volumes differences is -0.5, which means that the snow and ice differences are anticorrelated.

Since the SIT differences in figure 6 left column are differing more in areas covered by thin ice and stays about the same in areas covered by thick multiyear ice (the region north of Greenland and the Canadian Archipelago), the data was divided into thin ice volume and thick ice volume, to be analysed separately. The thin ice areas is indicated by the blue region and the thick ice region by the red region in figure 1. The middle panel in figure 9 shows the snow and ice volume differences for the thick ice covered regions and the lower one the thin ice dominated regions sea ice and snow volume differences.

https://doi.org/10.5194/tc-2022-84
Preprint. Discussion started: 28 April 2022

The thick ice region difference (middle panel figure 9) shows clearly that SI3 has a thicker ice cover in this region overall as found in figure 6. The snow difference is minimal, but there is a clear peak in June (more snow in SI3) as in both other graphs and a slight decrease (towards more snow in CICE) of the snow volume difference throughout the winter season. The sea ice volume also shows a slight seasonality, but by far not as clear as in the upper panel. The correlation was calculated to -0.13. The bottom panel shows the thin ice dominated areas sea ice and snow volume difference. There is a clear seasonality in both sea ice and snow volume difference as already seen in the total area differences in the upper panel. The minimum in sea ice differences (more ice in CICE) occurs each June together with the maximum snow difference (more snow in SI3). The ice volume peaks twice during a year. Once in October and once in April. The peak in April coincides with a minimum in snow volume (more snow in CICE) and the peak in October with the end of the melting season when there is almost no snow in either of the models. The correlation was calculated to -0.56.

3.5 Ice-Ocean and Atmosphere-Ocean drag

The models use different drag formulations to calculate the ocean and atmosphere forcing on sea ice. CICE uses a formulation which computes the drag depending on on SIC, flow size, melt pond, ridges and freeboard, while SI3 uses the same drag coefficient Arctic wide. This drag coefficients are 0.0014 for the atmospheric drag and 0.005 for the ocean drag. Figure 10 shows the difference between CICE and SI3 mean 10 year ocean and atmosphere drag for March and September. In September the atmospheric drag in SI3 is higher in the central Arctic. At the margins and in the coastal regions around Greenland as well as in the Kara Sea CICE drag coefficients exceed SI3s constant value. The September ocean drag is everywhere higher in CICE than in SI3, with maximal values of up to 0.008 in the coastal regions around Greenland and Canada, on the East Siberian shelf and in the Kara and Barents Sea. In March the both the atmosphere and ocean drag in SI3 exceeds CICE drag coefficient in most regions. Only close to the ice edge and close to the coast CICEs drag coefficient is higher than SI3s. The variable ice drag formulation in CICE is higher in the marginal ice zones and the ridged areas north of Greenland and Canada, which means that the ice is more vulnerable to the external forcing.

4 Discussion

Overall, the models compare better to each other than to observations. The models were forced by the same data only the models numerical formulation differ. This links the model observation differences to external forcing and input data and the model differences to the model internal biases.

The differences between the model output and the observational data sets are in good agreement with other model comparison studies. Long et al. (2021) compared NSIDC SIC climatologies from 1979-2014 with the SIC climatologies from all CMIP6 participating models sea ice components. The bias that was found by Long et al. (2021) (figure 1 in Long et al. (2021)) are in many cases bigger than the biases displayed in figure 2. This is expected as the resolution is generally lower within the CMIP6 runs. The models sea ice extent is higher than OSISAF sea ice extent both in March and September. In March the area where the models exceed OSISAF observations at the Atlantic ice edge is over estimated in several ice models (Long et al., 2021) and

https://doi.org/10.5194/tc-2022-84
Preprint. Discussion started: 28 April 2022

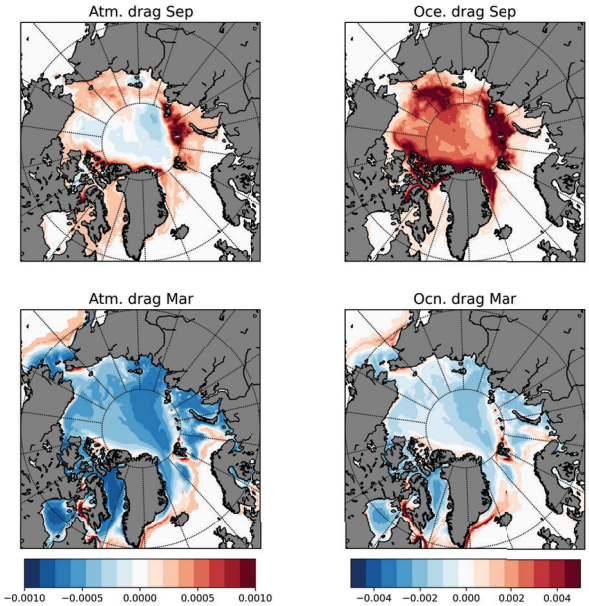

Figure 10. 10 year mean ocean and atmosphere drag difference (CICE-SI3) for March and September.

will further be discussed in section 4.1. In summer OSISAF is known to under estimate the ice edge due to melt ponds on ice (Kern et al., 2016). This might lead to some of the September ice edge differences we see in figure 3.

Comparisons of CS2SMOS data with PIOMAS show similar variability as we find (Wang et al., 2016; Parrinello et al., 2018; Mu et al., 2018a). Mu et al. (2018a) finds that PIOMAS mean SIT in March over a period of 5 years differs by 23cm. Similar calculations for our data sets (averaged over the same region, but over 10 years) show that the SI3 average SIT differs about 12cm from CS2SMOS mean March SIT and CICE by only 7cm. This could indicate that the variability and/or trend is smaller in the models compared to PIOMAS. However, PIOMAS should be seen as a point of reference and not the truth as it is also based on a model run, assimilating SIC and sea surface temperature (Zhang and Rothrock, 2003). In general the ice volume from CS2SOMS is not an exact metric either as it also has its uncertainties (Ricker et al., 2017).

Differences between models and observations were not only found in spacial distribution (figures 2 and 5), but also in the seasonal ice growth as shown in figure 4, which shows the over all sea ice volume per month. The winter growth of CICE and SI3 continues until April, while CS2SMOS sea ice growth slows down in March. Figure 4 also shows that the models over all produce more sea ice than observed. The data shown in figure 4 was masked to only cover the area included in the CS2SMOS

https://doi.org/10.5194/tc-2022-84
Preprint. Discussion started: 28 April 2022

data set. As figure 2 shows the models overestimate the ice edge, which means that there is a significant amount of data not included in figure 4, which is thinner than the included data and melts off first. Hence the apparent sea ice growth from March to April in figure 4 is likely caused by the chosen data points not reflecting the entire ice volume and exclude data point where the models lose ice from March to April. Figure 4 also shows that the models overestimate the total seasonal ice volume growth and melt. Most years the models start into the winter season with less ice than observed and end with more ice than observed. One reason for too much ice loss over the summer season could be the melt of almost all snow in the models. As Figure 7 shows, the Ka/Ku snow product in November has a significant thicker snow layer than SI3 and a slightly thicker snow layer than CICE.

The negative correlation of snow and ice volume differences shown in figure 9 underlines how important the snow layer is for correct sea ice simulation. A large amount of the differences between the models is as figure 9 shows, caused by different treatment of snow, specially in the thin ice region marked blue in figure 1. In the thick ice region the ice-snow difference anticorrelation is with -0.13 significantly lower than the thin ice-snow difference anticorrelation of -0.56. This lower anticorrelation is probably due to the inter-annual variability in the ice differences, which is dominating the variability of the curve. For the snow the main variability still originates from the seasonal cycle. Even though the models are in good agreement with oneanother compared to the differences they show to observations, there are differences between the model. SI3 agrees better with observations in regards to sea ice extent, snow thickness distribution as well as sea ice volume, to a certain extent. CICE performs slightly better according to observations in regards to early winter snow thickness distribution and March sea ice volume.

4.1 Regional differences

In the following section we take a closer look at the differences in the areas (1) Lincoln Sea and Canadian Archipelago, (2) the Atlantic ice edge, (3) Laptev Sea and Siberian shelf, (4) the Chukchi Sea an (5) the Beaufort Sea and where they might originate from. The areas are indicated by their numbers in figure 1. Finally, the parameters, which were found to have the largest effects on the differences in between the models, are discussed.

In area 1, the region north of Greenland and the Canadian Archipelago both models have too little sea ice compared to observations (figure 5) in both March and September. CICE SIT is here about 1 m thinner than SI3 throughout the year (figure 6). CICE agrees better with the CS2SMOS product just off the north coast of Greenland in the Lincoln sea. Moore et al. (2019) Links the sea ice accumulation in region 1 to wind driven ice transport into this region. The sea ice velocities and drag coefficients in winter are lower in CICE than in SI3 (monthly averaged plots of total speed are added in the appendix). This links the difference in drag formulation to the over all thinner ice in CICE compared to SI3. In the Lincoln (region just north off the cost of Greenland) sea SI3 overestimates sea ice, CICE shows realistic values in all seasons. In figure 10 CICE displays a higher drag coefficient in both month and for both atmospheric drag and ocean drag. Tsamados et al. (2015) finds that form drag improves the SIT in this region. Our results agree with this.

The overall pattern with larger ice extend in the Barents sea and east of Greenland is known from other models (Long et al., 2021). The overestimation in the Barents sea sea ice extent is according to Li et al. (2017) forced by a lack of oceanic

https://doi.org/10.5194/tc-2022-84
Preprint. Discussion started: 28 April 2022

heat. Since both models show the same pattern in this area and are forced by the same ocean model this is a plausible cause for the model-observation differences. Long et al. (2021) explains the overestimation in East Greenland sea ice extent with the simplicity of the sea-ice model SIS in comparison to CICE. In our study SI3 is the simpler formulated sea-ice model, but performs slightly better than CICE. The general over estimation of the west Greenlandic ice edge is also found in both models which suggests that the formulation of the sea-ice model might not play that big of a role here. Since both models are forced by the same ocean this could hint that the overestimation in this area is also caused by oceanic biases, as mentioned above as a reason for the Barents sea overestimation. The strength of the East Greenlandic current and the front between this and the Atlantic ocean could also cause the bias. This is however only speculation and needs to be investigated further. As mentioned above there is some difference in between CICE and SI3 sea ice extent west of Greenland. As figure 10 shows the drag coefficients of CICEs exceeds the values of SI3. The regions with more SIC in March in figure 3 coincides well with the regions with a significantly higher drag coefficient in CICE located at the ice edge (see figure 10).

SI3 sea ice extent is further north in the Russian shelf region (region 3 in figure 1) than OSISAF and CICE. In the summer month, when little new sea ice is formed SI3 displays stronger north west directed ice velocities (figures in appendix) in this region, which could explain the difference in sea ice extent in between the models. This would also explain the thicker ice during this month in CICE shown in figure 6. Since both models are forced by the same wind fields this difference originates most likely from the difference in drag formulation. Figure 10 shows that the atmospheric drag coefficient in this region are higher in SI3 in September. The ocean drag coefficients are however larger in this region in CICE. Atmospheric circulation is expected to govern the ice drift (Uotila, 2001; Hakkinen et al., 2008), explaining the higher sea ice velocities even though SI3 ocean drag exceeds CICE. The Russian shelf region is shallow and both models calculate grounded ice differently. This could be another reason leading to the differences here. Both modelled SIT in the shelf region differ in lager areas compared to CS2SMOS (Figure 5) than compared to one another. Watts et al. (2021) finds that the ocean heat transport could be the reason that grows and melt is not properly resolved in most models. The remaining difference between the models could be explained by differing formulations for grounded and land fast ice.

In March SI3 has up to a meter more ice in the Chukchi sea (region 4 in figure 1) than CICE. Comparing the models to the CS2SMOS product CICE agrees better with observations than SI3 in this region. Petty et al. (2016) describe how a faster spinning Beaufort gyre accumulates more ice in the Chukchi Sea. Comparing average sea ice velocities in the Beaufort Sea shows that SI3 sea ice velocities (figures in appendix) in this region are higher than CICEs in most month. CICE drag coefficients in March (lower row in figure 10) are also higher than SI3s. Since both models are force by the same ocean and atmosphere data this is a strong evidence that the difference in drag formulation in the models lead to thicker ice in the Chukchi Sea in SI3.

In the Beaufort Sea CICEs SIT is over all thinner than SI3s. Both models have thicker sea ice in the Beaufort Sea (region 5 in figure 1) than observed (figure 4), with a better agreement between CICE and CS2SMOS. The mean sea ice velocities in the Beaufort gyre are during all month higher in SI3 than in CICE. The drag coefficients in figure 10 however are only higher SI3 in March. The resulting higher sea ice velocities in summer are most likely resulting from the lower SIC in SI3 (3). The SIC differences in summer are most likely caused by the albedo differences. The spin of the Beaufort gyre highly depends on the

https://doi.org/10.5194/tc-2022-84
Preprint. Discussion started: 28 April 2022

sea ice motion forced by winds. This relation is known as the Ice-Ocean Governor (Meneghello et al., 2018) and is known to control the sea surface height in the Beaufort sea. In our results, a faster spinning ice field in the Beaufort Sea also leads to a thicker sea ice cover. How this influences the underlying ocean out of the scope of this study.

Overall the drag coefficient plays an important role in the differences in between the models. In many region (Lincoln Sea, Russian shelf area, Chukchi Sea and Beaufort Sea) the from drag formulation most likely leads to a model result closer to the observations. Over all CICE, which is the model using the formdrag has a thinner ice layer than SI3 which as Castellani et al. (2018) points out might be caused by the form drag. Comparing the albedo values of the two models shows that CICE calculates in general lower albedo values in summer than SI3. This is most likely an other reason for the generally lower sea ice volume in CICE.

Another reason for the lower sea ice volume in CICE is the different treatment of snow. Especially in late winter, the overall snow cover is thinner in SI3 than in CICE (figure 7, 9, 8). Figure 7 shows how the snow grows faster and thicker over the winter month in CICE than in SI3. The blue curve in figure 9 shows that CICE total snow volume in March exceeds SI3 snow volume by about 0.8 Mkm^2. The March snow climatology in figure 8 shows the special distribution of the differences. SI3 agrees better with observations in the last month as figure 7 shows. SI3s snow scheme included a reduction of the snow cover due to blowing snow and ridging and rafting. In the presented set up this means that the snow over ridges and rafts is reduced by 50% and a blowing snow parameter of 0.66 for a blowing snow parametrisation following Ledley (1985). Over all this parametrisation leads to a better agreement with observations.

5 Conclusions

We compared the sea-ice models CICE and SI3 under equal forcing, grid set up and coupled to the same ocean model. By this we aim to get a better understanding of how much variability is cased by the choice of sea-ice models and identify model processes that drive differences in resulting sea ice predictions, which could help better interpret there results in general. This study also presents a new sea ice ocean model set up with NEMO4 coupled to the sea-ice model CICE version 6.2. The results show that the set up performs comparable to other sea-ice models.

Overall the models compare well to observations and their differences are in a range similar to other model comparisons (Wang et al., 2016; Parrinello et al., 2018; Mu et al., 2018a; Long et al., 2021). The biggest differences between the models were found in the total sea ice volume. SI3 produces thicker sea ice than CICE. CICE on the other hand shows a larger sea ice extent in any season. OSISAF sea ice observations agree better with SI3. Both models differ significantly from CR2SOMS SIT retrievals and produce more ice throughout the winter season. Both models differ in snow thickness from observations and from each other. The differences in between the models are not as significant as the difference both models show in respect to the Ka/Ku snow product.

Several processes could be link to the discussed model differences. These are the drag formulation, the albedo calculation and the treatment of snow. The formdrag formulation in CICE results in better sea ice simulations locally in the Chukchi sea, Beaufort Sea as well as in the Russian shelf region, but might cause an overestimation of the ice edge and an overall thinner SIT

https://doi.org/10.5194/tc-2022-84
Preprint. Discussion started: 28 April 2022

as also found by Castellani et al. (2018). The tuning in this study was done by comparing models total Arctic sea ice volume to PIOMAS (Schweiger et al., 2011b) total sea ice volume. The resulting albedo differs significantly with SI3 reflecting a large amount of the short wave radiation, which was linked to the overall thicker sea ice cover. The tuning in the models was done manually testing varying each of the albedo parameters one by one and comparing the result to total sea ice volume. With the snow and ice layer changing through out the seasons and several parameters at play which have different effect in different regions depending on the season it would be advisable to use a more sophisticated tuning method as for example Panteleev et al. (2020) or Massonnet et al. (2014).

The third and most significant differences is resulting from different treatment of snow. Both models are forced by the same atmospheric forcing what means that the same amount of snow arrives at the ice surface. As figure 9 shows the development of the snow through out the year is significantly different and correlates negatively with the differences in SIT especially over newly formed ice. The negative correlation in between the differences is significant and differences in both SIT and SIC in the models output can be linked to the snow thickness differences. The comparison to the Ka/Ku snow thickness observations shows that the snow thickness is differing more from observations than from each other. Our results show that better representation of the snow layer in models will also improve the sea ice prediction.

Data availability. sea-ice model output data can be provided upon request.

Appendix A: Sea Ice velocity

https://doi.org/10.5194/tc-2022-84
Preprint. Discussion started: 28 April 2022

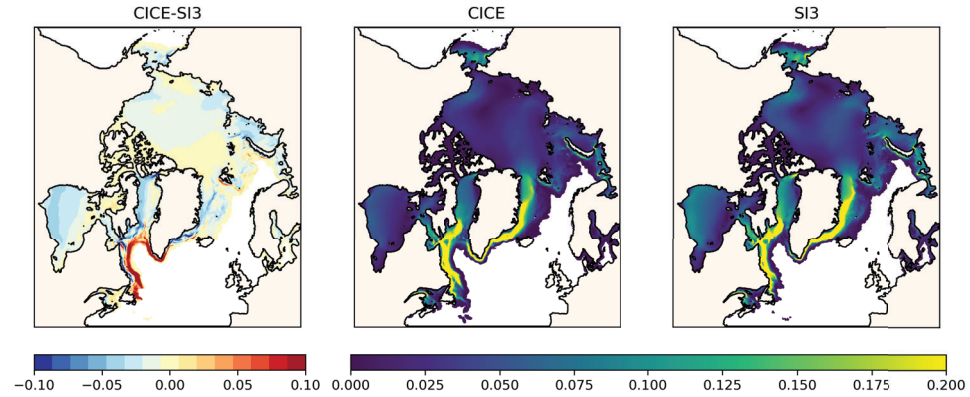

Figure A1. 10 year mean sea ice velocities for January from model output. Left panel: CICE-SI3 differences, middle panel: CICE total velocities, right panel: SI3 total velocities.

https://doi.org/10.5194/tc-2022-84
Preprint. Discussion started: 28 April 2022

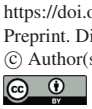

The Cryosphere Discussions
Open Access
EGU

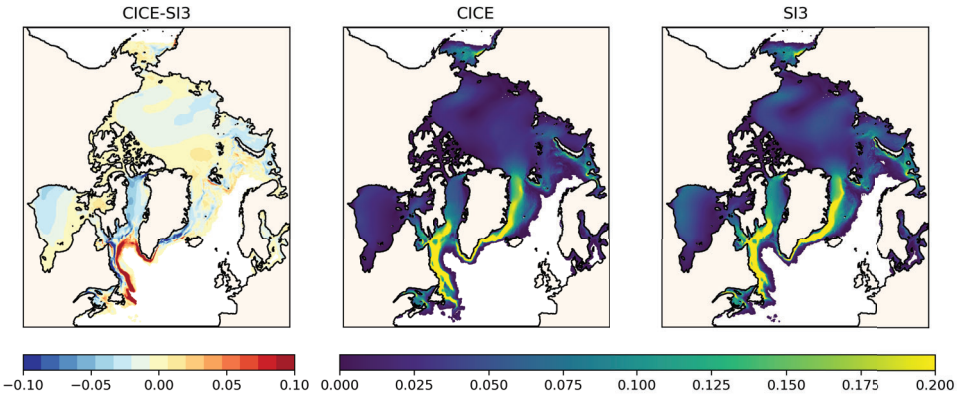

Figure A2. 10 year mean sea ice velocities for February from model output. Left panel: CICE-SI3 differences, middle panel: CICE total velocities, right panel: SI3 total velocities.

https://doi.org/10.5194/tc-2022-84
Preprint. Discussion started: 28 April 2022

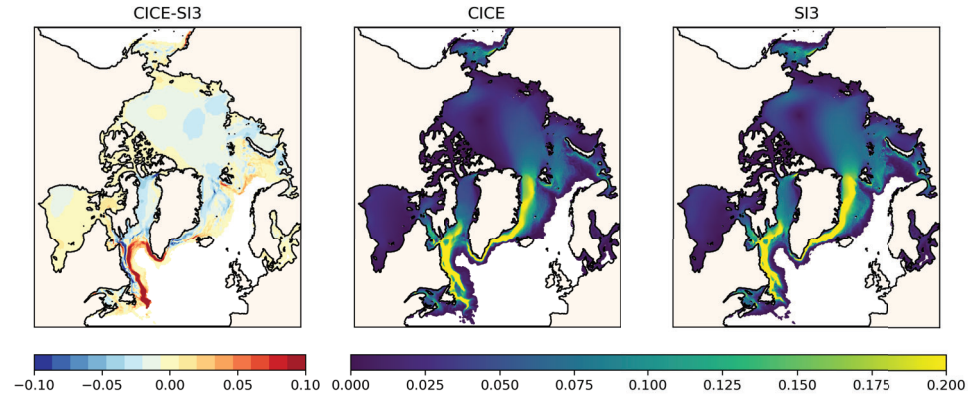

Figure A3. 10 year mean sea ice velocities for March from model output. Left panel: CICE-SI3 differences, middle panel: CICE total velocities, right panel: SI3 total velocities.

https://doi.org/10.5194/tc-2022-84
Preprint. Discussion started: 28 April 2022

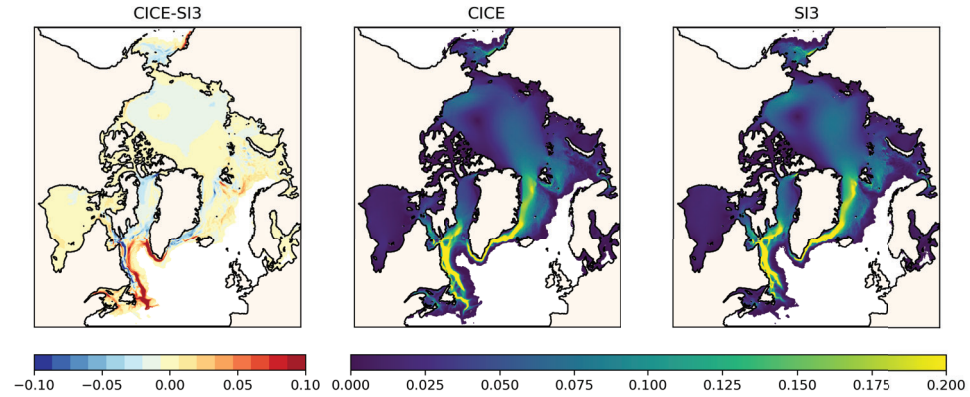

Figure A4. 10 year mean sea ice velocities for April from model output. Left panel: CICE-SI3 differences, middle panel: CICE total velocities, right panel: SI3 total velocities.

https://doi.org/10.5194/tc-2022-84
Preprint. Discussion started: 28 April 2022

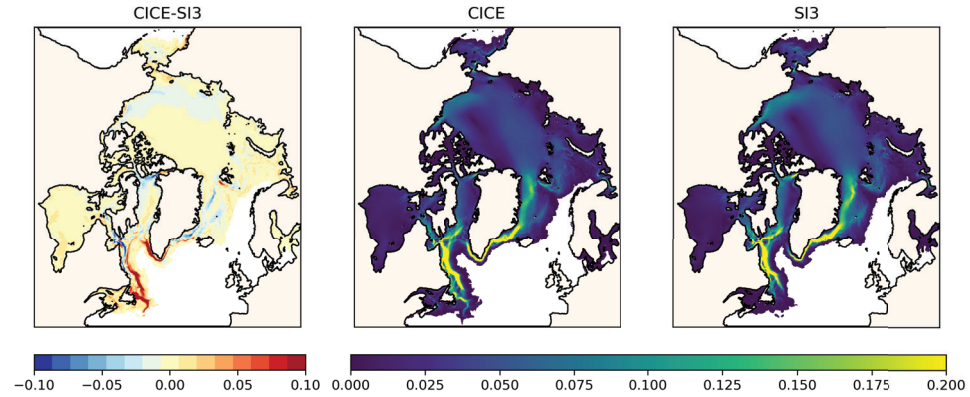

Figure A5. 10 year mean sea ice velocities for May from model output. Left panel: CICE-SI3 differences, middle panel: CICE total velocities, right panel: SI3 total velocities.

https://doi.org/10.5194/tc-2022-84
Preprint. Discussion started: 28 April 2022

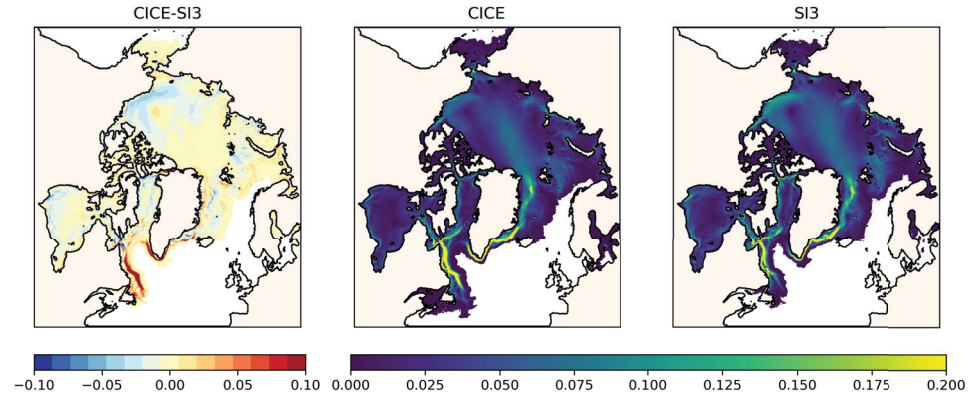

Figure A6. 10 year mean sea ice velocities for June from model output. Left panel: CICE-SI3 differences, middle panel: CICE total velocities, right panel: SI3 total velocities.

https://doi.org/10.5194/tc-2022-84
Preprint. Discussion started: 28 April 2022

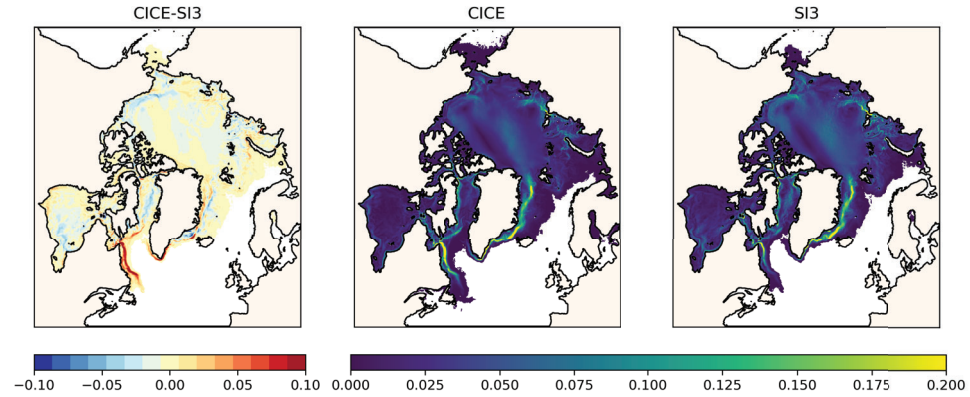

Figure A7. 10 year mean sea ice velocities for July from model output. Left panel: CICE-SI3 differences, middle panel: CICE total velocities, right panel: SI3 total velocities.

https://doi.org/10.5194/tc-2022-84
Preprint. Discussion started: 28 April 2022

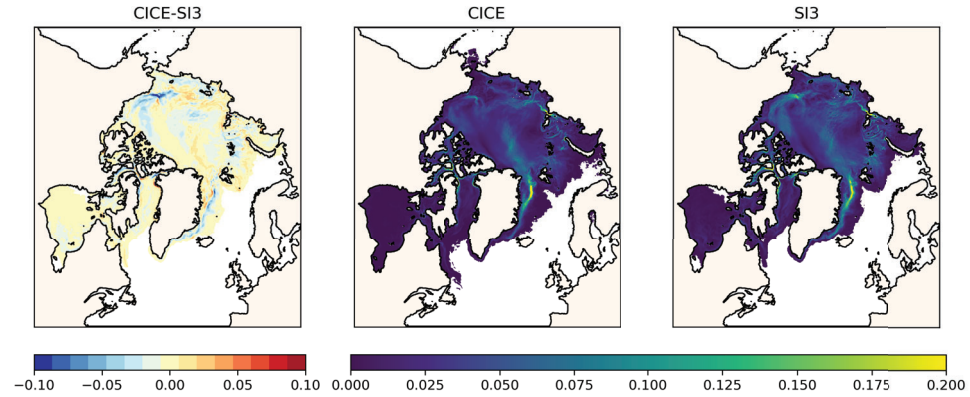

Figure A8. 10 year mean sea ice velocities for August from model output. Left panel: CICE-SI3 differences, middle panel: CICE total velocities, right panel: SI3 total velocities.

https://doi.org/10.5194/tc-2022-84
Preprint. Discussion started: 28 April 2022

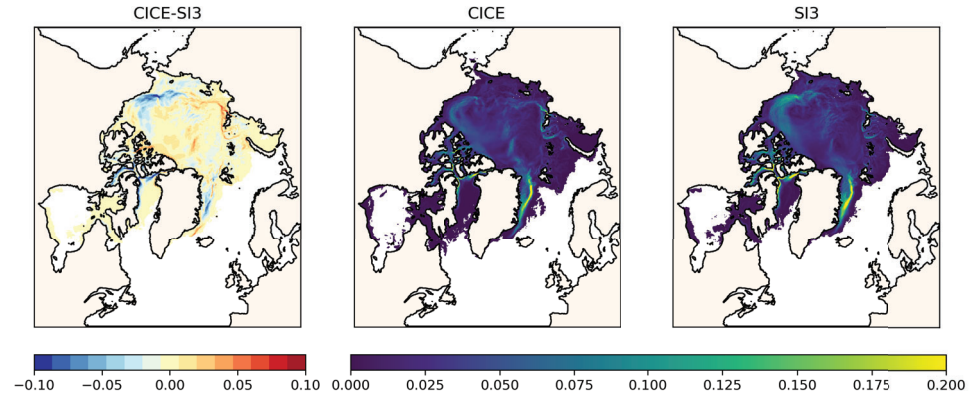

Figure A9. 10 year mean sea ice velocities for September from model output. Left panel: CICE-SI3 differences, middle panel: CICE total velocities, right panel: SI3 total velocities.

https://doi.org/10.5194/tc-2022-84
Preprint. Discussion started: 28 April 2022

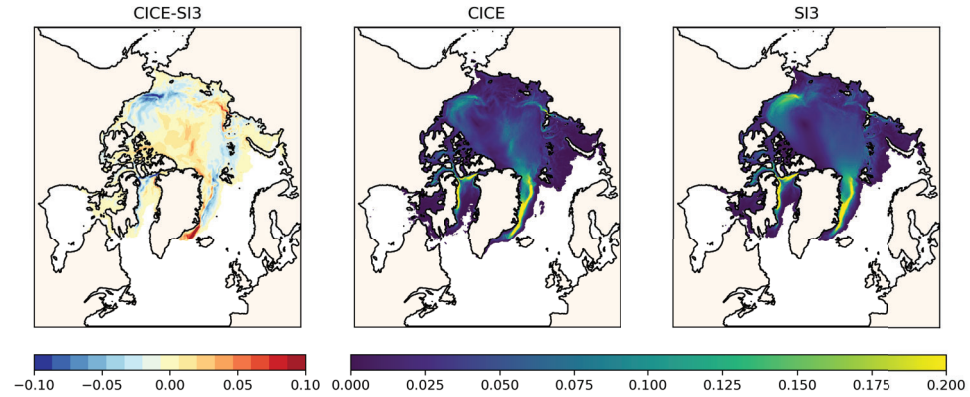

Figure A10. 10 year mean sea ice velocities for October from model output. Left panel: CICE-SI3 differences, middle panel: CICE total velocities, right panel: SI3 total velocities.

https://doi.org/10.5194/tc-2022-84
Preprint. Discussion started: 28 April 2022

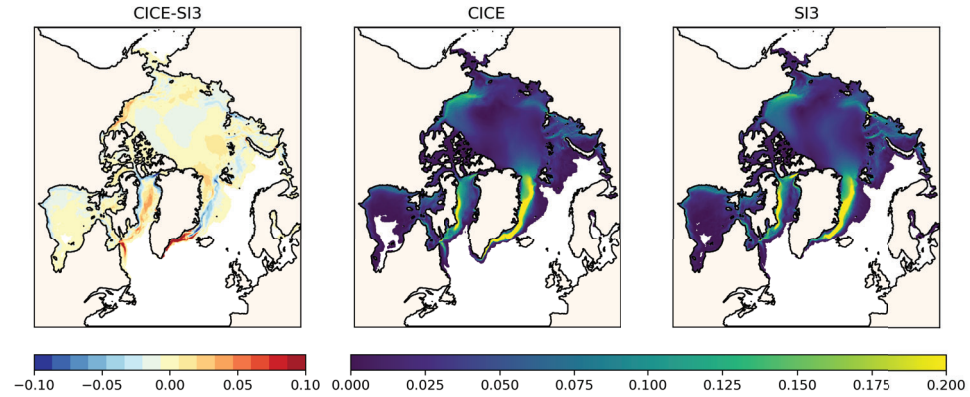

Figure A11. 10 year mean sea ice velocities for November from model output. Left panel: CICE-SI3 differences, middle panel: CICE total velocities, right panel: SI3 total velocities.

https://doi.org/10.5194/tc-2022-84
Preprint. Discussion started: 28 April 2022

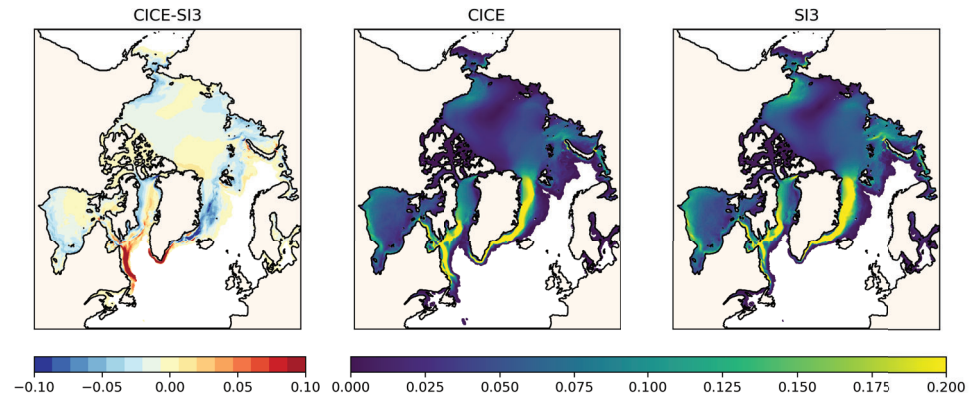

Figure A12. 10 year mean sea ice velocities for December from model output. Left panel: CICE-SI3 differences, middle panel: CICE total velocities, right panel: SI3 total velocities.

Author contributions. IS ran the CICE model experiment, wrote the manuscript draft and analysed the model output, ANG ran the SI3 model experiment, ANG and TAR, contributed to the introduction and method section of the manuscript, RH set up of the ocean model, ANG, TAR, RH and LS edited and reviewed the manuscript.

Competing interests. To the knowledge of the authors there are no competing interest

Acknowledgements. This study is a collaboration between the Danish Meteorological Institute, Aalborg University and the Danish Technical University. It is funded by the Danish State through the National centre for Climate Research.

The model input contains Copernicus Climate Change Service information (2021) and neither the European Commission nor ECMWF is responsible for any use that may be made of the Copernicus information or data it contains.

https://doi.org/10.5194/tc-2022-84
Preprint. Discussion started: 28 April 2022

References

Blanchard-Wrigglesworth, E., Farrell, S. L., Newman, T., and Bitz, C. M.: Snow cover on Arctic sea ice in observations and an Earth System Model, Geophysical Research Letters, 42, 10,342–10,348, https://doi.org/https://doi.org/10.1002/2015GL066049, 2015.

Briegleb, B. and Light, B.: A Delta-Eddington multiple scattering parameterization for solar radiation in the sea ice component of the Community Climate System Model, NCAR technical note, pp. 1–108, 2007.

Castellani, G., Losch, M., Ungermann, M., and Gerdes, R.: Sea-ice drag as a function of deformation and ice cover: Effects on simulated sea ice and ocean circulation in the Arctic, Ocean Modelling, 128, 48–66, 2018.

Collow, T. W., Wang, W., Kumar, A., and Zhang, J.: Improving Arctic Sea Ice Prediction Using PIOMAS Initial Sea Ice Thickness in a Coupled Ocean–Atmosphere Model, Monthly Weather Review, 143, 4618 – 4630, https://doi.org/10.1175/MWR-D-15-0097.1, 2015.

Dai, A. and Trenberth, K. E.: Estimates of freshwater discharge from continents: Latitudinal and seasonal variations, Journal of hydrometeorology, 3, 660–687, 2002.

Day, J., Hawkins, E., and Tietsche, S.: Will Arctic sea ice thickness initialization improve seasonal forecast skill?, Geophysical Research Letters, 41, 7566–7575, 2014.

Dirkson, A., Merryfield, W. J., and Monahan, A.: Impacts of sea ice thickness initialization on seasonal Arctic sea ice predictions, Journal of Climate, 30, 1001–1017, 2017.

Dupont, F., Higginson, S., Bourdallé-Badie, R., Lu, Y., Roy, F., Smith, G. C., Lemieux, J.-F., Garric, G., and Davidson, F.: A high-resolution ocean and sea-ice modelling system for the Arctic and North Atlantic oceans, Geoscientific Model Development, 8, 1577–1594, 2015.

Egbert, G. D. and Erofeeva, S. Y.: Efficient inverse modeling of barotropic ocean tides, Journal of Atmospheric and Oceanic technology, 19, 183–204, 2002.

Garnier, F., Fleury, S., Garric, G., Bouffard, J., Tsamados, M., Laforge, A., Bocquet, M., Fredensborg Hansen, R. M., and Rémy, F.: Advances in altimetric snow depth estimates using bi-frequency SARAL/CryoSat-2 Ka/Ku measurements, The Cryosphere Discussions, 2021, 1–40, https://doi.org/10.5194/tc-2021-79, 2021.

Hakkinen, S., Proshutinsky, A., and Ashik, I.: Sea ice drift in the Arctic since the 1950s, Geophysical Research Letters, 35, 2008.

Hazeleger, W., Wang, X., Severijns, C., Ştefănescu, S., Bintanja, R., Sterl, A., Wyser, K., Semmler, T., Yang, S., Van den Hurk, B., et al.: EC-Earth V2. 2: description and validation of a new seamless earth system prediction model, Climate dynamics, 39, 2611–2629, 2012.

Hersbach, H., Bell, B., Berrisford, P., Hirahara, S., Horányi, A., Muñoz Sabater, J., Nicolas, J., Peubey, C., Radu, R., Schepers, D., Simmons, A., Soci, C., Abdalla, S., Abellan, X., Balsamo, G., Bechtold, P., Biavati, G., Bidlot, J., Bonavita, M., De Chiara, G., Dahlgren, P., Dee, D., Diamantakis, M., Dragani, R., Flemming, J., Forbes, R., Fuentes, M., Geer, A., Haimberger, L., Healy, S., Hogan, R. J., Hólm, E., Janisková, M., Keeley, S., Laloyaux, P., Lopez, P., Lupu, C., Radnoti, G., de Rosnay, P., Rozum, I., Vamborg, F., Villaume, S., and Thépaut, J.-N.: Complete ERA5: Fifth generation of ECMWF atmospheric reanalyses of the global climate, Copernicus Climate Change Service (C3S) Data Store (CDS), accessed in 2021, 2017.

Hordoir, R., Axell, L., Höglund, A., Dieterich, C., Fransner, F., Gröger, M., Liu, Y., Pemberton, P., Schimanke, S., Andersson, H., Ljungemyr, P., Nygren, P., Falahat, S., Nord, A., Jönsson, A., Lake, I., Döös, K., Hieronymus, M., Dietze, H., Löptien, U., Kuznetsov, I., Westerlund, A., Tuomi, L., and Haapala, J.: Nemo-Nordic 1.0: a NEMO-based ocean model for the Baltic and North seas – research and operational applications, Geoscientific Model Development, 12, 363–386, https://doi.org/10.5194/gmd-12-363-2019, 2019.

https://doi.org/10.5194/tc-2022-84
Preprint. Discussion started: 28 April 2022

Hordoir, R., Skagseth, Ø., Ingvaldsen, R. B., Sandø, A. B., Löptien, U., Dietze, H., Gierisch, A. M., Assmann, K. M., Lundesgaard, Ø., and Lind, S.: Changes in Arctic Stratification and Mixed Layer Depth Cycle: A Modeling Analysis, Journal of Geophysical Research: Oceans, 127, e2021JC017 270, 2022.

Hunke, E., Allard, R., Bailey, D. A., Blain, P., Craig, A., Dupont, F., DuVivier, A., Grumbine, R., Hebert, D., Holland, M., Jeffery, N., Lemieux, J.-F., Osinski, R., Rasmussen, T., Ribergaard, M., Roberts, A., Turner, M., Winton, M., and Rethmeier, S.: CICE Version 6.2.0, https://github.com/CICE-Consortium/CICE/tree/CICE6.2.0, 2021a.

Hunke, E., Allard, R., Bailey, D. A., Blain, P., Craig, A., Dupont, F., DuVivier, A., Grumbine, R., Hebert, D., Holland, M., Jeffery, N., Lemieux, J.-F., Osinski, R., Rasmussen, T., Ribergaard, M., Roberts, A., Turner, M., Winton, M., and Rethmeier, S.: CICE-Consortium/CICE: CICE Version 6.2.0, https://doi.org/10.5281/zenodo.4671172, 2021b.

Kacimi, S. and Kwok, R.: Arctic snow depth, ice thickness and volume from ICESat-2 and CryoSat-2: 2018-2021, Geophysical Research Letters, p. e2021GL097448, 2022.

Kashiwase, H., Ohshima, K. I., Nihashi, S., and Eicken, H.: Evidence for ice-ocean albedo feedback in the Arctic Ocean shifting to a seasonal ice zone, Scientific Reports, 8170, https://doi.org/10.1038/s41598-017-08467-z, 2017.

Kern, S., Rösel, A., Pedersen, L. T., Ivanova, N., Saldo, R., and Tonboe, R. T.: The impact of melt ponds on summertime microwave brightness temperatures and sea-ice concentrations, The Cryosphere, 10, 2217–2239, 2016.

Kiss, A. E., Hogg, A. M., Hannah, N., Boeira Dias, F., Brassington, G. B., Chamberlain, M. A., Chapman, C., Dobrohotoff, P., Domingues, C. M., Duran, E. R., et al.: ACCESS-OM2 v1. 0: a global ocean–sea ice model at three resolutions, Geoscientific Model Development, 13, 401–442, 2020.

Le Sommer, J., Molines, J., Albert, A., Brodeau, L., Ajayi, A., Gomez Navarro, L., Cosme, E., Penduff, T., Barnier, B., Verron, J., et al.: NATL60: A North Atlantic ocean circulation model dataset based on NEMO for preparing SWOT altimeter mission, in prep, preparation for Geoscientific Model Development, 2019.

Ledley, T. S.: Sensitivity of a thermodynamic sea ice model with leads to time step size, Journal of Geophysical Research: Atmospheres, 90, 2251–2260, 1985.

Lellouche, J.-M., Greiner, E., Bourdallé-Badie, R., Garric, G., Melet, A., Drévillon, M., Bricaud, C., Hamon, M., Le Galloudec, O., Regnier, C., et al.: The Copernicus global 1/12° oceanic and sea ice GLORYS12 reanalysis, Frontiers in Earth Science, 9, 585, 2021.

Li, D., Zhang, R., and Knutson, T. R.: On the discrepancy between observed and CMIP5 multi-model simulated Barents Sea winter sea ice decline, Nature Communications, 8, 1–7, 2017.

Long, M., Zhang, L., Hu, S., and Qian, S.: Multi-Aspect Assessment of CMIP6 Models for Arctic Sea Ice Simulation, Journal of Climate, 34, 1515–1529, 2021.

Losch, M., Menemenlis, D., Campin, J.-M., Heimbach, P., and Hill, C.: On the formulation of sea-ice models. Part 1: Effects of different solver implementations and parameterizations, Ocean Modelling, 33, 129–144, https://doi.org/https://doi.org/10.1016/j.ocemod.2009.12.008, 2010.

Madec, G., Bourdallé-Badie, R., Bouttier, P.-A., Bricaud, C., Bruciaferri, D., Calvert, D., Chanut, J., Clementi, E., Coward, A., Delrosso, D., et al.: NEMO ocean engine, 2017.

Massonnet, F., Goosse, H., Fichefet, T., and Counillon, F.: Calibration of sea ice dynamic parameters in an ocean-sea ice model using an ensemble Kalman filter, Journal of Geophysical Research: Oceans, 119, 4168–4184, 2014.

Meneghello, G., Marshall, J., Campin, J.-M., Doddridge, E., and Timmermans, M.-L.: The ice-ocean governor: Ice-ocean stress feedback limits Beaufort Gyre spin-up, Geophysical Research Letters, 45, 11–293, 2018.

https://doi.org/10.5194/tc-2022-84
Preprint. Discussion started: 28 April 2022

Moore, G., Schweiger, A., Zhang, J., and Steele, M.: Spatiotemporal variability of sea ice in the arctic's last ice area, Geophysical Research Letters, 46, 11 237–11 243, 2019.

Mu, L., Losch, M., Yang, Q., Ricker, R., Losa, S. N., and Nerger, L.: Arctic-wide sea ice thickness estimates from combining satellite remote sensing data and a dynamic ice-ocean model with data assimilation during the CryoSat-2 period, Journal of Geophysical Research: Oceans, 123, 7763–7780, 2018a.

Mu, L., Yang, Q., Losch, M., Losa, S. N., Ricker, R., Nerger, L., and Liang, X.: Improving sea ice thickness estimates by assimilating CryoSat-2 and SMOS sea ice thickness data simultaneously, Quarterly Journal of the Royal Meteorological Society, 144, 529–538, 2018b.

NEMO-Sea-Ice-Working-Group: Sea Ice modelling Integrated Initiative (SI^3) – The NEMO sea ice engine, https://doi.org/10.5281/zenodo.1471689, 2022.

OSISAF: Global Sea Ice Concentration Climate Data Record v2. 0–Multimission, EUMETSAT SAF on Ocean and Sea Ice, 2017.

Panteleev, G., Yaremchuk, M., Stroh, J. N., Francis, O. P., and Allard, R.: Parameter optimization in sea ice models with elastic–viscoplastic rheology, The Cryosphere, 14, 4427–4451, 2020.

Parrinello, T., Shepherd, A., Bouffard, J., Badessi, S., Casal, T., Davidson, M., Fornari, M., Maestroni, E., and Scagliola, M.: CryoSat: ESA's ice mission–Eight years in space, Advances in Space Research, 62, 1178–1190, 2018.

Petty, A. A., Hutchings, J. K., Richter-Menge, J. A., and Tschudi, M. A.: Sea ice circulation around the Beaufort Gyre: The changing role of wind forcing and the sea ice state, Journal of Geophysical Research: Oceans, 121, 3278–3296, 2016.

Ricker, R., Hendricks, S., Kaleschke, L., Tian-Kunze, X., King, J., and Haas, C.: A weekly Arctic sea-ice thickness data record from merged CryoSat-2 and SMOS satellite data, The Cryosphere, 11, 1607–1623, https://doi.org/10.5194/tc-11-1607-2017, 2017.

Schweiger, A., Lindsay, R., Zhang, J., Steele, M., Stern, H., and Kwok, R.: Uncertainty in modeled Arctic sea ice volume, Journal of Geophysical Research: Oceans, 116, 2011a.

Schweiger, A., Lindsay, R., Zhang, J., Steele, M., Stern, H., and Kwok, R.: Uncertainty in modeled Arctic sea ice volume, Journal of Geophysical Research: Oceans, 116, 2011b.

Shine, K. and Henderson-Sellers, A.: The sensitivity of a thermodynamic sea ice model to changes in surface albedo parameterization, Journal of Geophysical Research: Atmospheres, 90, 2243–2250, 1985.

Smith, G. C., Liu, Y., Benkiran, M., Chikhar, K., Surcel Colan, D., Gauthier, A.-A., Testut, C.-E., Dupont, F., Lei, J., Roy, F., et al.: The Regional Ice Ocean Prediction System v2: a pan-Canadian ocean analysis system using an online tidal harmonic analysis, Geoscientific Model Development, 14, 1445–1467, 2021.

Stewart, E. J., Liggett, D., Lamers, M., Ljubicic, G., Dawson, J., Thoman, R., Haavisto, R., and Carrasco, J.: Characterizing polar mobilities,to understand the role of weather, water, ice and climate (WWIC) information, Polar Geography, 43, https://doi.org/10.1080/1088937X.2019.1707319, 2020.

Stocker, A. N., Renner, A. H., and Knol-Kauffman, M.: Sea ice variability and maritime activity around Svalbard in the period 2012–2019, Scientific reports, 10, 1–12, 2020.

Tonboe, R. T., Eastwood, S., Lavergne, T., Sørensen, A. M., Rathmann, N., Dybkjær, G., Pedersen, L. T., Høyer, J. L., and Kern, S.: The EUMETSAT sea ice concentration climate data record, The Cryosphere, 10, 2275–2290, https://doi.org/10.5194/tc-10-2275-2016, 2016.

Tsamados, M., Feltham, D., Petty, A., Schroeder, D., and Flocco, D.: Processes controlling surface, bottom and lateral melt of Arctic sea ice in a state of the art sea ice model, Philosophical Transactions of the Royal Society A: Mathematical, Physical and Engineering Sciences, 373, 20140 167, 2015.

Uotila, J.: Observed and modelled sea-ice drift response to wind forcing in the northern Baltic Sea, Tellus A, 53, 112–128, 2001.

https://doi.org/10.5194/tc-2022-84
Preprint. Discussion started: 28 April 2022

Wagner, P. M., Hughes, N., Bourbonnais, P., Stroeve, J., Rabenstein, L., Bhatt, U., Little, J., Wiggins, H., and Fleming, A.: Sea-ice information and forecast needs for industry maritime stakeholders, Polar Geography, 43, 160–187, https://doi.org/10.1080/1088937X.2020.1766592, 2020.

Wang, C., Graham, R. M., Wang, K., Gerland, S., and Granskog, M. A.: Comparison of ERA5 and ERA-Interim near surface air temperature and precipitation over Arctic sea ice: Effects on sea ice thermodynamics and evolution, in: AGU Fall Meeting Abstracts, vol. 2018, pp. C33F–1626, 2018.

Wang, X., Key, J., Kwok, R., and Zhang, J.: Comparison of Arctic sea ice thickness from satellites, aircraft, and PIOMAS data, Remote Sensing, 8, 713, 2016.

Watts, M., Maslowski, W., Lee, Y. J., Kinney, J. C., and Osinski, R.: A spatial evaluation of Arctic sea ice and regional limitations in CMIP6 historical simulations, Journal of Climate, 34, 6399–6420, 2021.

Zhang, J. and Rothrock, D. A.: Modeling global sea ice with a thickness and enthalpy distribution model in generalized curvilinear coordinates, Monthly Weather Review, 131, 845–861, 2003.

Zuo, H., Balmaseda, M. A., Tietsche, S., Mogensen, K., and Mayer, M.: The ECMWF operational ensemble reanalysis–analysis system for ocean and sea ice: a description of the system and assessment, Ocean science, 15, 779–808, 2019.